Impact of the unsteady aerothermal environment on the turbine blades temperature

Elena Collado Morata

THESE

En vue de l'obtention du

DOCTORAT DE L'UNIVERSITÉ DE TOULOUSE

Délivré par Institut National Polytechnique de Toulouse
Discipline ou spécialité : Énergétique et Transferts

Par Elena Collado Morata
Soutenue le : 29 Octobre 2012

Impact of the unsteady aerothermal environment on the turbine blades temperature

---

JURY

S. Moreau	Rapporteur
E. Van der Weide	Rapporteur
I. Trébinjac	Examinateur
B. Nkonga	Examinateur
L. Pons	Invité
M. Dumas	Invité
N. Gourdain	Co-directeur de thèse
L.Y.M. Gicquel	Directeur de thèse

École doctorale : Mécanique, Energétique, Génie civil, Procédés
Unité de recherche : CERFACS
Directeur de Thèse : Laurent Gicquel
Co-Directeur de Thèse : Nicolas Gourdain

Acknowledgements

No man is an island, entire of itself;
every man is a piece of the continent,
a part of the main.

Meditation 17, John Donne

C'est la soutenance qui marque le point culminant de la thèse. Merci sincèrement aux rapporteurs, M. Van der Weide et M. Moreau, de s'être investis autant dans la relecture du manuscrit. Je remercie également le reste du jury pour leur disponibilité et surtout pour leurs questions pertinentes qui ouvrent maintes perspectives pour la suite de cette étude. Je pensais que ça allait être un chemin de croix, mais ce fut en réalité un plaisir d'échanger avec vous!

Pendant ces 3 ans de thèse, je me suis un peu sentie comme d'Artagnan, entourée de 3 Mousquetaires dont j'avais tout à apprendre. Laurent, mon directeur de thèse, puits de savoir scientifique (espaces de Sobolev et traces, comprises) mais surtout humain, il a su me *canaliser* avec les bons mots. Quand je serai grande, j'aimerais être comme lui! Méfiez-vous quand il vous dit qu'il ne sait pas. Après, il vous donne une idée que vous mettrez 3 mois à comprendre! Nico, mon co-directeur, son enthousiasme est contagieux. Merci pour ta générosité! Et qu'aurais-je fais sans le senzalationnel Florent Duchaine? Ni pale, ni couplage. C'est bien la question que je me suis souvent posée, bien plus que celle de déterminer la température de pale à 5K près! MERCI Florent.

Guillaume Bonneau, Jean-Phillipe Ousty, Laurence Vial, sans qui cette thèse n'aura jamais vu le jour, et Lorenzo Pons, merci pour vos commentaires toujours constructifs et votre accueil à Bordes. Si je viens à Pau, c'est que j'ai eu une très bonne image de Turbomeca grâce vous!

J'aimerais aussi remercier la CSG team, ONG du CERFACS, pour leur aide inébranlable et leur sourire à preuve de segmentation fault et surtout pour leurs conseils pratiques pour la virée en Inde! Merci aussi à toute la dream-team de l'administration, les fous rires avec Chantal et Michelle, vous êtes les *coupables* de la bonne ambiance qui règne au CERFACS! Merci à Marie et Nicole qui m'ont vraiment aidé le dernier mois quand je leur écrivais en détresse pour préparer la soutenance à distance.

Elodie, ma coach de squash, collègue, copine puis amie, et toi aussi Anne, les supernanas, c'est nous!!! Elodie F., arrivée sur le tard a subi mes sauts d'humeur de la fin, merci à toutes les 3 pour les brunchs, spetacles et surtout les apéros après une longue journée de rédaction place de l'Olivier. Merci aussi à Joris, pour les pauses ... mais surtout pour le chocolat!!! Y Nacho, mi sombra ;) A ver cuando escribimos esas ecuaciones Duran-Collado? Et, bien sûr, Petit Flageolet, mon co-bureau d'amour et "Rêmi" Le Franzen, espion dévoué, pour tes mails loufouques en espagnol et tout le reste ... je ne peux citer tout le monde car on me reprocherait de faire des remerciements plus longs que mon intro de thèse! Merci à tous les stagiaires, thésards, post-docs et seniors, ... de toujours avoir une épaule compatissante dans les moments de doute et un sourire encourageant quand on arrive à faire tourner notre petit code.

Et oui, il y a une vie en dehors de la thèse, Luis, Javi, Cris, Ivan, Emilia, Miguel, gracias por animarme de lejos, por vuestros mails incongruentes que me hacían reír, las vacas, los findes en España y tantas otras cosas. Gracias a la familia de los Buiges-Vila por el apoyo y sobretodo por el vino!!! Aussi, remercier la troupe de Toulouse pour leur joie de vivre contagieuse et tous ces moments passés pendant cette thèse et depuis bien avant au bord de la Garonne. Merci aux Monjarret qui sont venus au complet ... la *familia* continue de s'agrandir.

Ronan, mon décodeur d'articles matheux, je n'aurais pas réussi à comprendre les lemmes et théorèmes sans toi. Surtout merci de m'avoir supporté, dans les 2 sens du terme, pendant ces 3 ans. J'espère que ta thèse se passera aussi bien que la mienne!!! Y sobretodo espero que pueda ayudarte tanto y tan bien como tu me has ayudado. Qué habría hecho sin ti? Le dedico esta tesis a mis padres, que no tienen ni idea de lo que es el numero de Reynolds, pero sin los cuales todo esto no hubiera sido posible. Gracias por apoyarme siempre.

Contents

1

General introduction

Contents

1.1 Scientific and industrial context

The cooperation and exchange of ideas between the public and private research sectors is crucial for the advance of research, especially in such a specialized field as aeronautics. In an attempt to reduce the historical barriers between those two worlds, the French education ministry has created the CIFRE (Conventions Industrielles de Formation par la Recherche) thesis. By this mean, the French research community can come together to promote shared interests and seek solutions to address the issues that interfere with advancement of the aeronautical field. This alliance provides a process for debate among all relevant participants so that academic researchers propose original solutions to the technical problems of the industrials partners. This CIFRE thesis originates from a cooperation between TURBOMECA and the European Centre for Research and Advanced Training in Scientific Computation (CERFACS) laboratory.

The thesis presented here inherits from this particular background. This introduction describes the specific problem of turbine blades in the helicopter engines, which are the final industrial target. Indeed, including its joint programs with other manufacturers, TURBOMECA is the world leading

provider of helicopter engines. Going through the state-of-the-art and todays methods applied in engine design, the aim is to show that a new technological step has to be achieved in Computational Fluid Dynamics (CFD) in order to provide industrial constructors with a reliable tool to predict more precisely temperature on turbine blades.

1.1.1 The temperature problem

Current gas engines are at the paradigm of advanced technology. However, due to the limitation of fuel reserves and the increase of the environmental concern as well as operating cost restraints, improvements must be achieved in gas turbine components even if those (compressor, combustion chamber and turbine) already operate close to their maximum thermodynamic efficiency. Decrease of the fuel consumption and extension of the engine life time are two of the major improvements that must be accomplished to lower operating cost and to limit the global warming impact.

The Gordian knot of this thesis is the temperature of the turbine blades, which drives the life time of this component. The ideal Brayton cycle can be used to understand the significance of this temperature, Fig. 1.1 (a):

- ◇ The flow entering the engine undergoes first an isentropic compression in the compressor receiving the work $\dot{W}_{comp}$.
- ◇ Then, an isobaric combustion takes place in the combustion chamber, the flow receiving a heat $\dot{Q}_{comb}$ released by chemical reactions.
- ◇ Finally, the flow expands isentropically in the turbine, the work $\dot{W}_{turb}$ being generated.

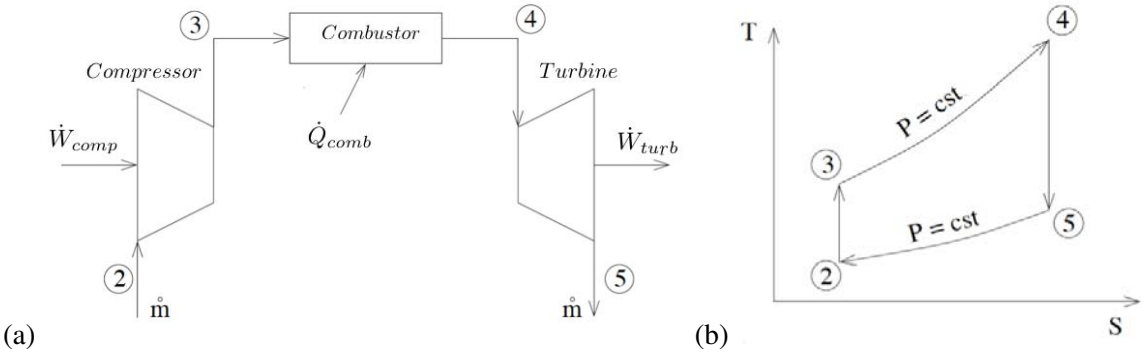

Figure 1.1: Ideal Brayton cycle: (a) simplified gas turbine and (b) associated temperature-entropy diagram, $\dot{W}_{comp}$ is the work used to drive the compressor, $\dot{Q}_{comb}$ the heat created by combustion and $\dot{W}_{turb}$ the work generated by the turbine, source Mattingly [117].

In real engines, pressure and thermal losses induce irreversibilities which move us away from the ideal cycle. Nevertheless, the aim of this little exercise is to point out the major development axis in

engine design. The engine performance is driven by its mass flow rate $\dot{m}$ and the difference between $\dot{W}_{turb}$-$\dot{W}_{comp}$, which is proportional to the area between curves 3-4 and 2-5 of Fig. 1.1 (b). This balance is called the net power, $\dot{W}_{net}$, which is controlled mainly by the combustion chamber exit temperature T_4. Additionally, the thermal efficiency of the cycle can be defined as:

$$\eta_t = \frac{\dot{W}_{net}}{\dot{Q}_{comb}} = 1 - \left(\frac{p_3}{p_2}\right)^{-\frac{\gamma-1}{\gamma}}.$$

When the compression ratio increases so does the thermal efficiency. In the real system, an inflection point exists and at this point, $\dot{W}_{net}$ begins to decrease with $\frac{p_3}{p_2}$. Therefore, an arrangement must be found between the production of work $\dot{W}_{net}$ and the pressure ratio (thermal efficiency) in real engines. Another limitation to take into account is the one regarding T_4. The temperature at the exit of the combustion chamber can not be increased infinitely since the blades in the downstream turbine could not physically bare such environment. This specific problem will be looked at in detail in the following paragraphs.

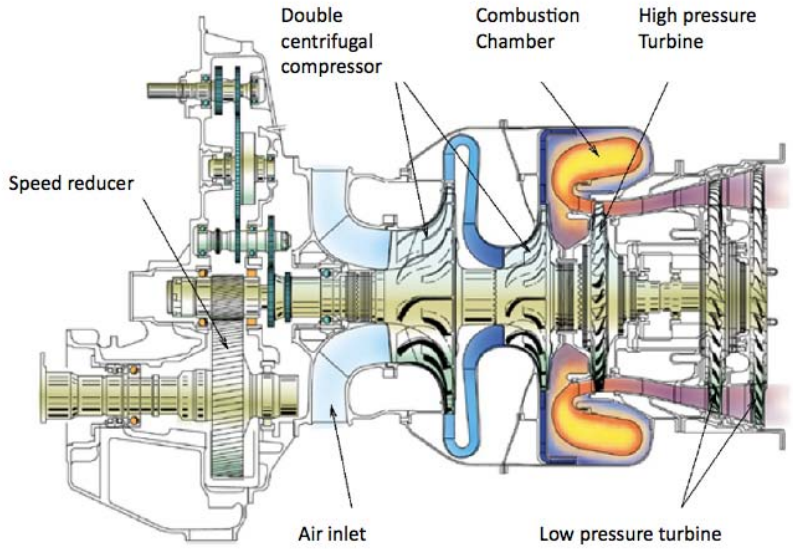

Figure 1.2: Cross-section of Ardiden III turboshaft.

After the middle of the last century, helicopter industry adopted the gas turbine neglecting piston engines, that had been used since the 30s. In helicopter industry, the gas turbine is a turboshaft, a form of gas turbine which is optimized to produce free turbine shaft power rather than jet thrust, i.e. $\dot{W}_{net}$ is used to produce mechanical energy provided to the rotor of the helicopter. The turboshaft

engine is made of two major modules: the gas generator and the power section. The gas generator consists of the compressor, combustion chamber and at least one stage of turbine. The power section includes additional stages of turbines, a gear reduction system and the shaft output. The gas generator creates the hot expanding gases to drive the power section. In most designs, the gas generator and power section are mechanically separated so that they may each rotate at different speeds. In this thesis, only a part of the gas generator is studied. A usual example of the turboshaft principle is the TURBOMECA Ardiden III engine. The general layout of this turboshaft is presented in Fig. 1.2. Fresh air goes in before undergoing two stages of compression, both of them usually being centrifugal stages. The annular combustion chamber is designed as a reverse-flow combustor and at the end of the engine, a high pressure turbine drives the compressor and a free low pressure turbine is united to the speed reducer via a coaxial branch (left part of Fig. 1.2).

Figure 1.3: Picture of a coloration, technique in which the temperature seen by the blades corresponds to a color scale, courtesy of TURBOMECA.

In this last 60 years, the gas turbines have encountered significant improvements in global performance, power, life span and reduction of pollutants, etc. The enhancement of efficiency and pressure ratio $\frac{P_3}{P_2}$ of the compressor, the advancement of combustion chamber efficiency and pressure loss reductions, the gains of turbine efficiency and the increase of the inlet temperature bared by the blades thanks to material research and cooling techniques have contributed to the progressive amelioration of the whole gas turbine performance. However, the actual thermal design of high-pressure turbine blades represents one of the most difficult engineering tasks in the whole turboshaft conception as the improvement of the propulsive performance is inhibited by several technological issues focused on this component. The main difficulty is the hot streak flow temperature issued by combustion taking place upstream the blades. The maximum temperature withstood by the blades can be increased by

cooling techniques or the use of more resistant materials. But the ultimate aim is to know with precision what temperature the blades are seeing. Independently of the technological achievements, this can be accomplished by better understanding and control of the flow field around the blades. In this case, fluid mechanics simulation tools play an important role in the conception process. Experimental campaigns do not provide a temperature with sufficient accuracy, as one can see in Fig. 1.3. No magnitude on the temperature is given deliberately, this figure shows nevertheless that experimental campaigns are quite rough in the prediction of blades temperature. However, it is commonly accepted that a difference of 15° in the blade temperature can divide the blade life span towards thermal fatigue by two [166]. Therefore, accurate predictions of the blades temperature is of paramount importance. Part I of this dissertation specifically deals with this issue and proposes the qualification of LES methods to predict the heat flux on a fixed turbine, a necessary step prior to any other.

As mentioned before, the main cycle components (compressor, combustion chamber and turbine) are the key factors to improve the overall efficiency and power of the turboshaft. But the separate improvement of single components is limited due to the interaction between them. Changes in one component may have impact on the other and lead to efficiency losses. For example, increasing the combustion temperature will increase the Brayton cycle efficiency, but will also cause higher thermal stress and thus shorter lifetime of the high pressure turbine. With this in mind and the increasing compactness of new engines, the need to take the interaction phenomena into account becomes obvious. This thesis captures one of the numerous interfaces within an engine: the combustor-turbine interface and the aero-thermal combustor-turbine interactions associated.

1.1.2 Aero-thermal combustion chamber-turbine interaction

Two components of the turboshaft are involved if focusing on the combustion chamber-turbine interface: the combustion chamber and the turbine. The design problems confronted by these two components are different.

The combustion chamber

In the combustion chamber, thermal energy is added to the thermodynamic cycle by chemical reactions. This process must be stable and reliable for all operating points. Improving combustion addresses directly the global warming consequences of fuel consumption [73, 155]. World Meteorological Organization has been warning since 1990 of the issues of air pollution and climate change, as illustrated in Fig. 1.4. In 2001, the Advisory Council of Aeronautics Research in Europe commission

announced its prospects for 2020 [9]: a reduction of CO2 emissions by 50% and NOx emissions by 80% compared to emissions allowed by the Commission on Aviation and Environmental Protection in 2001. In general, pollutants have to be minimized to follow regulatory guidelines determined by Annex 16 Volume II of the Convention on International Civil Aviation. These rules are compulsory for all manufacturers. With the limits on pollutants decreasing drastically, none of the gas engines on todays helicopters would be certified unless manufacturers work on new combustion technologies to meet the regulation requirements.

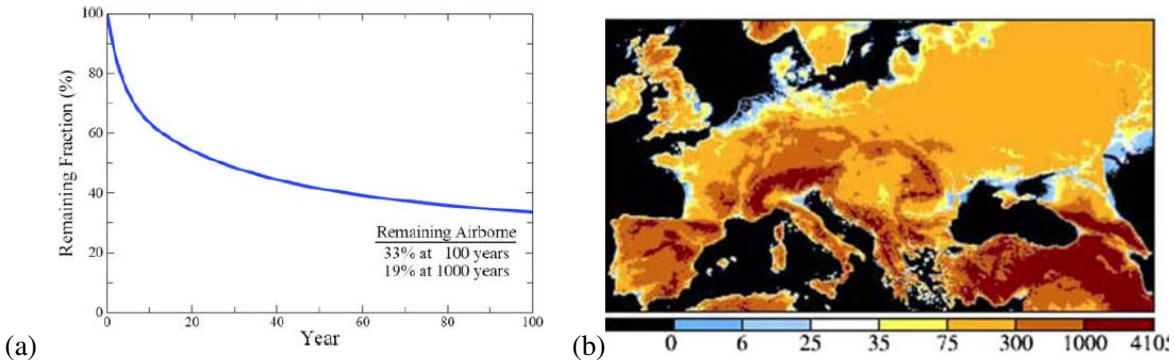

Figure 1.4: (a) Atmospheric life-time of CO_2 and (b) Areas under water for specified sea level increases in *mm*: areas between $0-25$ *mm* may be under water with a $2-3^{\circ}$ temperature rise, from Sawyer [155] .

The turbine

The second component to be considered is the turbine. Combustion chamber exit flows are non-uniform in total pressure and temperature as well as highly turbulent. Secondary flows develop from spatial gradients near the hub and shroud at the inlet of the turbine stage and are responsible for the heat transfer between the fluid and the turbine vane. The migration of different inlet radial temperature and pressure profiles through the high turbine vane of a turbine stage have been investigated profusely [15, 92]. Furthermore, technological devices, as cooling in the blades like in Fig. 1.5 or conjugate heat transfer between the blade and the fir-tree blade root, have recently demonstrated its influence on the blade temperature distribution although not normally taken into account in the design process [186, 192]. The relative importance of these parameters has been studied lately in the PhD thesis of Wlassow [191].

The current aerodynamic and thermal analysis procedures in industry for turbines rely mostly on Reynolds Averaged Navier-Stokes (RANS) flow computations, whose inflow condition are given by 1D profiles issued from a separate RANS computation of the combustion chamber. This 1D radial profile of mean temperature, called Radial Temperature Factor (RTF), is usually desired by turbine

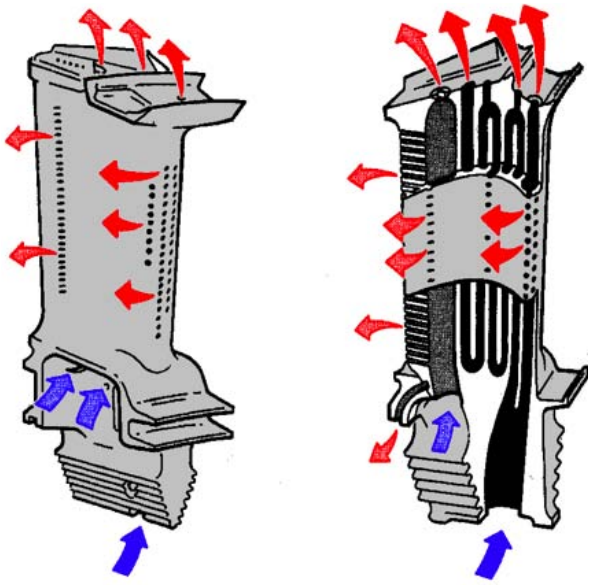

Figure 1.5: Cooling technologies in a turbine blade, from Guha [72].

engineers to be minimum on the shroud where cooling is complicated and on the hub where thermo-mechanical constraints are maximum (more information on RTF is given in Appendix A). This mainly 1D profile induces some lack of precision in the prediction of the flow field around the blades since no complex interaction effects are taken into account. For instance and among others, the influence of Free-Stream Turbulence (FST) on the local heat transfer rate in the laminar or transition regions or the actual two-dimensional temperature field to which the Nozzle Guide Vane (NGV) is exposed are clearly inaccessible in this context. Similarly, the possible effect of the turbine on the outlet of the combustion chamber is totally disregarded in this process.

The following paragraphs present a quick overview of the major steps given in the combustion chamber-turbine interaction analysis. For a more detailed study, eager readers can study the chapter dedicated to this matter in the thesis of Klapdor [92].

Combustion chamber influence on the turbine

Historically, the first interaction that cached the attention from researchers was the effect of the combustion chamber flow on the turbine stage. Experimental and numerical campaigns are plentiful for the analysis of hot streak migration, clocking effects, influence of the cooling techniques, etc [43, 44, 114].

Turbine influence on the combustion chamber

Much less investigated, the impact of the NGV on the combustion chamber flow is a very new research area, only a few publications treat this problem and this has only been investigated numerically so far [104, 151]. Up to now, the combustion community was less concerned by the effect of the turbine stage on their chamber outlet. With the generalization of Large Eddy Simulations (LES) for resolving the combustion chamber flow and the adoption of more sophisticated boundary conditions, the assumption of a constant pressure at the outlet of the combustion domain is beginning to be a rough approximation for the study of combustion instabilities [193] or noise propagation. Leyko et al. [104] investigated the effect of hot pocket conversion into acoustic while passing through the NGV. In 2008, Roux et al. [151] analyzed the influence of the NGV on the mean and unsteady velocity as well as the temperature at the outlet of the combustion chamber field. A usual simulation (i.e., only the combustion chamber was simulated) was compared to one simulation in which the stator was included into the computational domain. Strong influence on the mean quantities in the rear part of the combustor was observed. Appendix A of this thesis addresses partially this problem by investigating multi-component flow simulations of an industrial configuration.

Combustion chamber/turbine interaction

When numerical coupling strategies for the simulation of an entire engine are concerned, only Stanford researchers [4, 120, 157] have seriously attempted to develop a software framework able to execute and exchange data between the different solvers taking part in such a simulation. Previous studies from Turner *et al.* [185] had already faced the difficulties of coupling several RANS codes. In the case of Stanford's Accelerated Strategic Computing Initiative (ASCI) project, an incompressible LES solver is used to simulate the reactive flow. Unsteady RANS computations are employed for the turbine components. The major part of their study deals with the transformations needed to pass information from LES to RANS and vice versa [158, 162]. A simulation of this kind may need a computing power and time which is today available in a laboratory and less likely accessible in industry. Following this initiative, other research centers are beginning to develop coupling strategies [180].

To complement this numerical research effort going on in the multi-component analysis field, the European FACTOR (Full Aero-thermal Combustor-Turbine interactiOn Research) project was launched to study these aspects experimentally. The main objective of the FACTOR project is to optimize the combustion chamber-high pressure turbine interaction design. This will be achieved through a better understanding of the synergies between the cooling system, the secondary flows and

mixing mechanisms enabling the determination of the blade temperature with an error of +/- 5°. More information on the goals of FACTOR can be found in http://www.factor-fp7.eu/.

The main problem for experimental investigations is to build a test set-up that operates close to the real conditions. Actually, test bench temperatures remain below real temperatures in this kind of experimental configurations since such test facilities are costly to install and maintain. The major benefit from numerical simulations is that these operating conditions are not a limitation and even if CPU cost is yet high, modifications of the setup are easier to implement than in a real experimental rig. The development of a numerical approach that can take into account these combustion chamber/turbine interactions is the strategy chosen in this thesis. In the following sections, the different kind of numerical simulations available to achieve this purpose are presented.

1.2 CFD state of the art

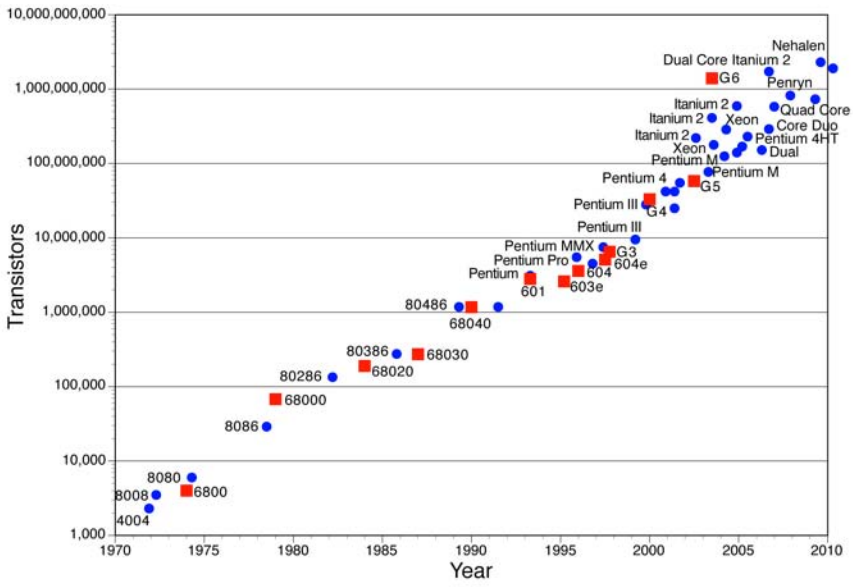

Figure 1.6: Microprocessor Transistor Counts 1971-2011& Moore's Law, from Wikipedia.

Since the 60s, CFD has inherited from the significant progress achieved in the meshing techniques as well as numerical methods, going from simple 2D configurations to todays complex 3D high Reynolds number simulations. Of course, one of the major contributions is the increasing computer capability, as shown by Fig. 1.6. All these factors have contributed to the universalization of CFD in design cycles of industry. This thesis relies on the capacity of present strategies to improve the CFD solution if used in new application fields or if coupled.

1.2.1 Physical modeling

The main modeling techniques used in the numerical simulation of turbulence are introduced here: DNS, RANS, LES and hybrid RANS-LES. Turbulence is still an open problem even if present in most of the real flows. In turbomachinery, the crucial aspects of turbulence are related to unbounded and near wall flows.

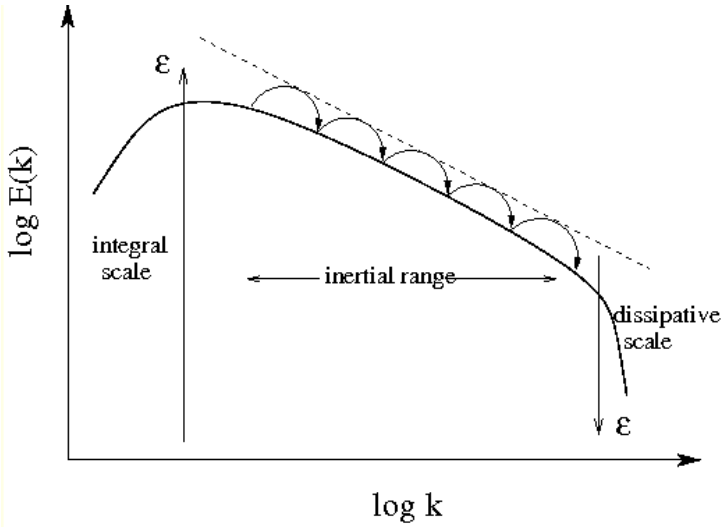

Figure 1.7: Turbulent kinetic energy cascade of Kolmogorov [82].

If the Reynolds number, defined as $Re = \frac{u.l}{\nu}$ where u and l are the characteristics velocity and length scale of the flow and ν is the kinematic viscosity of the fluid, is greater than a certain value depending of the configuration, the flow is turbulent. Turbulence causes the formation of eddies of many different length scales. A turbulent flow may be viewed as made of an entire hierarchy of eddies over a wide range of length scales. The hierarchy can be described by the energy spectrum that measures the energy of velocity fluctuations for each wave number, as seen in Fig. 1.7. Using Kolmogorov's assumptions of self-similarity, the rate of energy injection ε in the integral scales is the same as the rate of energy lost to heat at the dissipative scales. This transfer of energy occurs without any influence from dissipation and must be equal at all scales. It only depends on the size of a given scale, l, and the velocity of fluctuations, u, at that scale, so one has $\varepsilon = \frac{u^3}{l}$ [83].

The cascade creates structures that are small enough so that molecular diffusion becomes important and viscous dissipation of kinetic energy finally takes place. The scale at which this happens is the Kolmogorov length scale. In his 1941 theory [94], Kolmogorov introduced the idea that the smallest scales of turbulence are universal and that they depend only on ε and ν. The definitions of

the Kolmogorov microscales can be obtained using dimensional analysis. Since the dimension of kinematic viscosity is $\frac{[length]^2}{[time]}$, and the dimension of the energy dissipation rate per unit mass is $\frac{[length]^2}{[time]^3}$, the Kolmogorov length scale can be a function of ε and ν such that $\eta = (\frac{\nu^3}{\varepsilon})^{\frac{1}{4}}$. The ratio between the size l of the large scale eddies and the Kolmogorov length scale η defines the range of active scales in a given turbulent flow. The ratio of these two length scales follows $\frac{l}{\eta} = Re^{\frac{3}{4}}$ where Re is a turbulent Reynolds number characteristic of the large scale eddies. The small structures thus become smaller and smaller as the Reynolds number increases. If one needs to perform a 3D simulation of the flow, the number of points needed is at least equal to $Re^{\frac{9}{4}}$, if Kolmogorov scales are to be resolved [64].

Typical flows in turbomachinery have Reynolds numbers around 10^6. In these cases, the Kolmogorov scales are around 30 000 times smaller than the larger eddies in the flow. The application of Direct Numerical Simulations (DNS) which intends to solve directly all flow scales would require 3.2 10^{13} grid points. Such numbers are of course not accessible with current computing means and DNS. Practically, modeling assumptions are used to minimize the complexity of the simulation.

Before identifying the various approaches to compute/simulate turbulence, one can not forget that in a large number of engine simulations, walls are present and that turbulence does not have the same behavior near walls. Independently of the Reynolds number, the inner layer, whose length scale is δ_v, is the region close to the wall where the viscosity, ν, and the viscous shear stress at the wall, τ_w, determine the behavior of turbulence, Fig. 1.8. In the wall region, quantities are normalized by $\delta_v = \frac{\nu}{u_t}$ and $u_t = \sqrt{\frac{\tau_w}{\rho}}$, where u_t is the characteristic velocity, and are subsequently expressed in wall units. Based on the value of $y^+ = \frac{y}{\delta_v}$, where y is the distance from the wall, one can differentiate several regions near the wall. Note that y^+ plays the role of a local Reynolds number. The logarithmic law of the wall is a self similar solution for the mean tangential velocity to the wall; it is valid for flows at high Reynolds numbers and far enough from the wall for viscous effects to be neglected [156]. Here, $U^+ = \frac{1}{k} log(y^+) + A$, where k and A are well-known constants. Pope [145] validates this relation for $y^+ > 30$. Below this zone, the viscous sub-layer, Fig. 1.8, is the region where inertial effects are negligible compared to the viscous ones, i.e.: $y^+ > 0$. The profile of velocity is universal in this region and follows $U^+ = y^+$ under 5 wall units. In the buffer layer, between 5 wall units and 30 wall units, neither law is valid. It is called the overlap region where both profiles adapt to each other. One can refer to the textbook of Pope for more information [145].

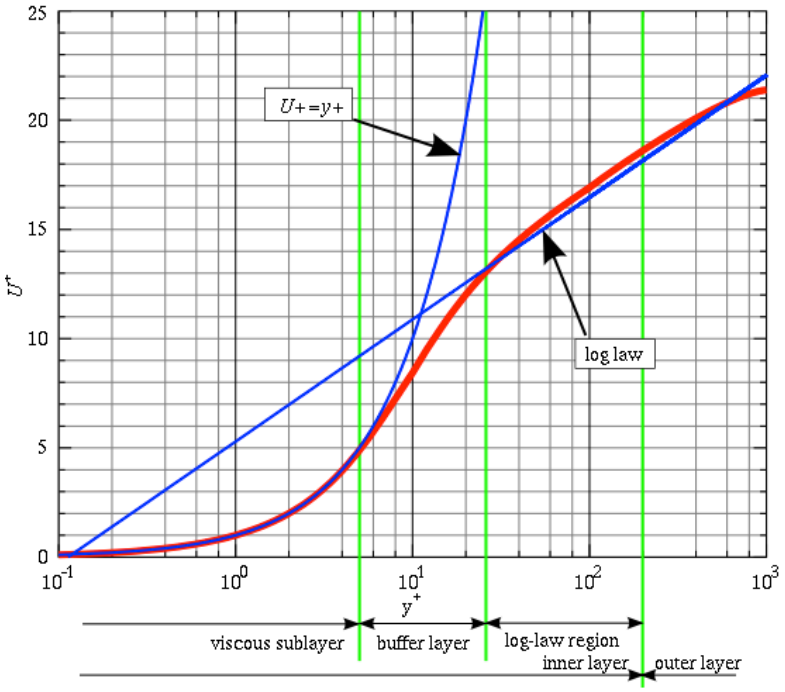

Figure 1.8: Wall law [188]

1.2.2 Current strategies for gas turbines simulations

The Navier-Stokes equations are the most widely spread model for resolving internal and external flows. The peculiarity of this system of equations is that it remains mathematically open since the well-posedness has not yet been demonstrated [93]. The Clay Mathematics Institute has called this one of the seven most important open problems in mathematics, `http://www.claymath.org/millennium/`. Simultaneously, turbulence which has a paramount importance in many flows still remains without a precise description. It is often qualified as "the most important unsolved problem of classical physics" as described by Richard Feynman, 1965 physic's nobel prize. This subsection reviews the major CFD strategies to address the resolution of numerical simulations with regard to modeling assumptions, computational cost and current applications. Figure 1.9 illustrates the 3 different existing approaches that are today available to address turbulent flows:

1. As mentioned before, DNS may enable an accurate description of all 3D scales, from the larger eddies to the smallest ones (even near wall structures would be resolved). In the turbomachinery field, the Reynolds number can be as great as 10^6. Turbulence plays a major role and the structures in the near wall region scale as $Re^{0.8}$ [83]. With current CPU means, even though this power is increasing drastically, modeling assumptions have to be taken before resolving the

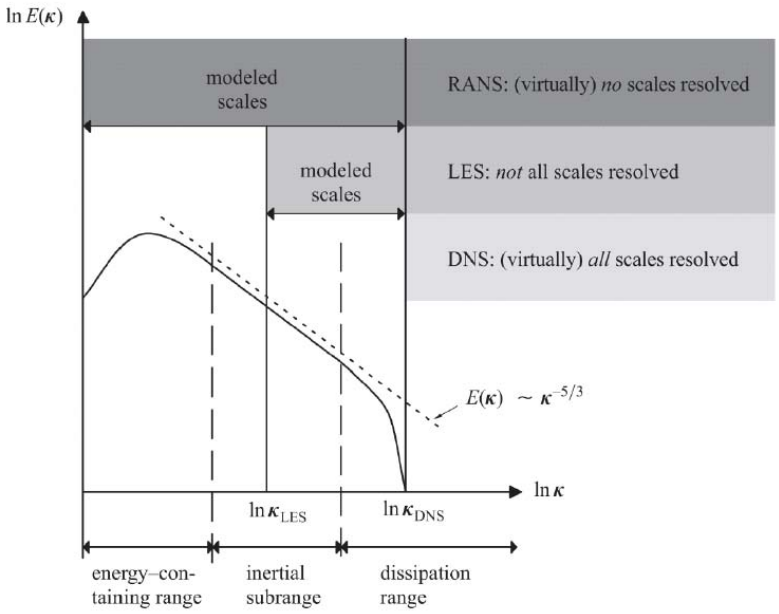

Figure 1.9: Conceptual representation of RANS, LES and DNS applied to a homogeneous isotropic turbulent field, from Gravemeier [69].

DNS of the Navier-Stokes equations. DNS is nevertheless used as a research tool for models development in more elementary configurations [129].

2. In RANS simulations, a turbulence model is used to represent the turbulence and only the mean motion is resolved. The velocity is decomposed in two parts: the average component and the fluctuating part, i.e., $u = \bar{u} + u'$. The averaging operator is defined as an ensemble average over a set of samples N, $\bar{u} = \frac{1}{N}\sum_{1}^{N} u_n$, where u_n denotes the n^{th} realization of the sample of realizations N. The RANS simulations are economical and therefore spread in industry for all kind of problems [11, 26]. The modeling of turbulent boundary layers is easy to implement in RANS codes [88], at least for canonical configurations. Up to these days, RANS models are fitted to behave in a specific way on certain classes of flows. It is indeed deemed very difficult to have a universal RANS model that will be able to predict the behavior of all turbulent flows.

3. LES introduces the differentiation between large and small scales which is done with a low-pass filter as shown in Fig. 1.9. The Navier-Stokes equations are filtered yielding an evolution equation for the velocity $\bar{u}$ that has supplementary unclosed terms. In this case, $\bar{u}$ is equal to the convolution $G * u$, where G is the filter function, so $\bar{u} = \int u(x')G_\Delta(x'-x)dx'$. This filter

has a cut-off scale associated, the filter size noted Δ. Figure 1.9 shows that LES resolve eddies larger than the filter size, the smaller ones being modeled. Therefore, the main advantage of LES is that it only has to model scales smaller than the filter size and not the entire range of turbulence [125]. Although less resource demanding than DNS, the cost of LES still exceeds by several orders of magnitude the cost of a RANS simulation. The main challenge associated with this method is the treatment of boundary layers due to the high cost of resolving these zones. The grid extension sizes $\Delta y^+ \approx 1$, $\Delta x^+ \approx 50$, $\Delta z^+ \approx 15$ are those classically retained in well-resolved LES to capture the near wall structures [85, 140]. Note that apart from potential constraints near walls, the fully unsteady resolved field issued by LES is the reason why it is widely developed in the combustion community [138, 150, 174] where flames develop far from walls. LES still faces difficulties expanding in near-wall configurations, except for limited blade or wing configurations [18, 116]. Substantial efforts have therefore been undertaken to develop wall-modeling approaches that are adapted to LES [133, 139].

More detailed aspects of the governing equations and computational techniques employed in this thesis can be found in Appendix D. Our field of interest are flows in turbomachinery, a very detailed analysis of the methods above presented (their pros and cons, their application domain, etc ...) is gathered in the study followed by Tucker [184]. In page 537 of [184], appears a summary of eddy resolving simulations with typical grid densities and Reynolds numbers for all kind of components: from compressors to turbines. As noticed in that paper, very few turbomachinery simulations make use of unstructured LES to resolve near-wall flow. Even LES simulations on high pressure turbines are not very often seen in literature [45, 67, 103]. Table 1.1 illustrates the mesh requirements that would be demanded to compute a 3D turbine stage. The use of DNS with the actual means of computation is prohibitive. Modeling assumptions (LES or RANS) have to be used in the turbomachinery context to minimize the complexity of the simulation.

Test case	**Re**	Number of points **DNS**	Number of points **LES**	Number of points **RANS**
Turbine stage	10^6	$\sim 3.2\ 10^{13}$	$\sim 1\ 10^9$	$2.2\ 10^6$

Table 1.1: Estimation of the grid requirements needed to compute a 3D turbine stage.

Not only, can one use the DNS, LES or RANS approach as standalone tool but one can also combine them, so the drawbacks of each strategy are compensated and one can benefit from the pros of each kind of simulation. Hybrid methods coupling RANS and LES have recently caught the attention of industry, since they aim to combine the accuracy of LES and the cheap computational cost of RANS

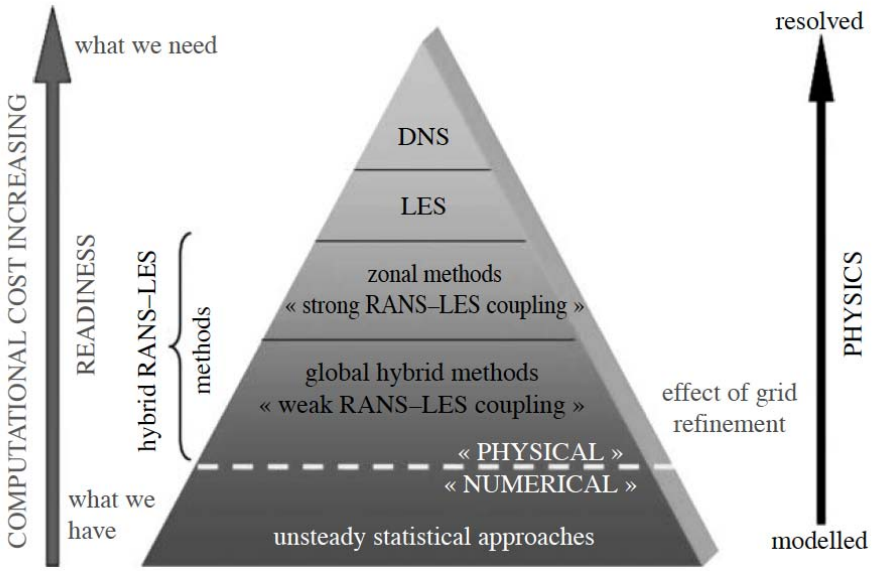

Figure 1.10: Classification of unsteady approaches according to levels of modeling and readiness from Sagaut & Deck [153].

simulations [179]. Von Terzi & Fröhlich [181] define the approach as a "quality-cost trap": i.e. a standard RANS approach is insufficient and LES is too expensive; the idea is to "perform LES only where is needed while using RANS procedures in regions where they are reliable and efficient". If using an unsteady definition of RANS simulations, the structural similarity of LES and RANS equations allows to switch from LES to RANS and vice versa (only by modifying the unresolved stress tensor τ_{ij}^t). This approach is called the unified approach as only one solver handles the simulation. There is a huge panoply of hybrid methods, for a detailed overview of hybrid LES/RANS methods one can refer to Fröhlich & Von Terzi [57]. Their division of hybrid methods is classified as unified and segregated methods. According to Sagaut & Deck [153], these two major classes of hybrid methods can be called global and zonal methods, instead of unified and segregated, respectively. This kind of global or segregated approaches will come in between standalone LES and RANS as seen in Fig. 1.10. The zonal hybrid methods refer to methods based on a decomposition of the domain before starting the simulation into regions for RANS computations and others which would be solved in LES. The connection between the distinct zones during the simulation is established via explicit coupling of the solution at the interfaces in both directions, from LES to RANS and vice versa [147, 168]. Most of the zonal hybrid applications tend to use only one solver. More recently, the segregated approach has been investigated to treat different domains with different solvers [163, 180]. Despite the increasing developments of coupled procedures, no clear mathematical justification is today provided for zonal coupling. This thesis will try to partially answer this point.

1.3 Objectives of the present work

Como no estás experimentado en las cosas del mundo,
todas las cosas que tienen algo de dificultad
te parecen imposibles–Don Quijote a Sancho–.

El Ingenioso Hidalgo Don Quijote de la Mancha,
Miguel de Cervantes.

Industrially, TURBOMECA, like all the propulsion manufacturers, seeks the improvement of the engine power as well as the larger life span of the propulsive components. The augmentation of the temperature at the inlet of the turbine stage is directly related to the rise of the net power. Unfortunately, the thermal constraints that such temperature elevations impose to the blade put a limit to this increase. Indeed, the turbine blades are placed in a hostile environment, especially the rotor blade, which also has to support the circumferential mechanical constraints. In consequence, TURBOMECA needs:

- ◇ to improve the efficiency and the design process of the propulsion system,
- ◇ to increase the life span of the turbine blades,
- ◇ to ameliorate the prevision of the flow field around the turbine blades,
- ◇ to predict correctly the temperature on the turbine blades walls.

Therefore, instead of using a monolithic approach, i.e., one code-one domain; one can split the region of interest (combustion chamber+ turbine) in two. The ideal and industrially friendly solution would be to solve the combustor chamber and turbine stage all together. However, LES is a very efficient method for predicting reactive flows in combustion chambers [24], while RANS approaches are more convenient for turbomachines [67]. This LES/RANS coupling strategy is thus targeted.

For this work and contrarily to Stanford, only compressible flow solvers are considered (a structured multi-block solver -*elsA*- and an unstructured solver -AVBP-). A zone of overlap is computed by both codes, in the industrial application it may correspond with the NGV component. This stator will thus be calculated in RANS, as usual in an industrial configuration, but also with LES.

Two steps have to be investigated before facing the industrial application. First, unstructured LES has to demonstrate its ability to accurately predict the heat flux on a high-pressure turbine blade. Second, a coupled approach has to be developed and validated to ensure the exchange of information between separate LES and RANS codes in an intelligent way. Ultimately a mathematical rigorous demonstration of this coupling should also be provided. These aims are illustrated in Table 1.2 in comparison with usual strategies used in industry. In summary, the two ideas which vertebrate this thesis and constitute the two main parts of this dissertation are:

- ◇ the set-up of an unstructured LES approach for the prediction of the wall heat transfer in a fixed blade configuration,
- ◇ the development of a zonal LES/RANS coupling strategy which would enable to do a coupled simulation with todays computing means in industrial configurations.

	Combustion chamber	**Non-rotating blade**	**Turbine stage**
RANS	✓ Used in industry	✓ Used in industry	✓ Used in industry
LES	✓ Used in industry	**PART I Unstructured mesh LES approach**	✗ CPU limit
COUPLING Combustor with	-	-	**PART II compressible LES/ compressible RANS**

Table 1.2: The contributions targeted for the present thesis should allow to compute a coupled combustion chamber and turbine stage.

1.4 Thesis outline

The work carried out during the course of this thesis is presented as follows:

- ◇ Part I presents the validation of an unstructured LES tool to determine the correct aerodynamical and thermal quantities in a high-pressure turbine configuration. This approach is compared to both structured RANS and LES.
- ◇ A new zonal hybrid LES/RANS approach dedicated to the coupling between two compressible flow codes is presented in Part II. A mathematical study of the domain decomposition method used is explained here. The possibilities of this coupling are studied thoroughly and illustrative examples of the capabilities of the method are provided. The aim of this section is to illustrate the potential of fluid/fluid coupling for industry like problems.
- ◇ Finally, conclusions come together with recommendations for future work.
- ◇ In the Appendices A and B, the reader can find a part dedicated to the applications of multi-component and multi-physics simulations of an industrial configuration analyzed during this thesis. An extension of the domain decomposition method presented in Part II is developed in Appendix C for fluid/solid conjugate heat transfer. Appendix D gives some details of the existing solvers to compute flows using RANS simulations and LES in nowadays numerical simulations of gas turbines. OpenPALM, the coupling tool is presented at the end of this Appendix.

Part I

LES and heat transfer

Introduction

A large range of numerical methods is nowadays available in the literature as pointed out in the introduction, all of which are more or less suited to near wall flows [76, 145, 152, 178]. RANS simulations require all the turbulent scales of the flow to be modeled putting stringent modeling effort on the turbulent closures near walls [2, 172]. It however inherits from years of research and developments. The limits and advantages of RANS simulations are known and it is routinely used in the design phase of most industrial applications. Fully unsteady numerical methods where all turbulent scales (DNS) or parts of the scales (LES) are solved for are also available. Although the former is clearly out of reach for real applications, the latter still requires to prove its efficiency. Recent contributions based on LES [152, 153] provide promising results especially for the prediction of heat transfer in fundamental test cases [16] or in complex geometry [19, 45].

The aim of this part of the dissertation is to demonstrate the potential of LES, especially unstructured LES, for the prediction of heat transfer for high pressure turbine in turbulent flows. One critical aspect that complexifies the use of LES for blade heat transfer predictions, is the sensitivity of the procedure to modeling which is usually linked to the local grid resolution, numerics and cell topology. Theoretically well defined isotropic and uniform meshes are better suited for LES. Near walls structured meshes comply to the preferred directions of such flows and ease the use and development of high order numerical schemes with low dispersion and dissipation properties which ensure that the Sub-Grid Scale (SGS) model works adequately and as designed [134] (to retrieve more information about SGS models, one can refer to Appendix D). Many turbine CFD investigations hence consider structured grids [27]. This method suffers, however, a major drawback: the difficulty to refine localized regions that also need to comply with the meshing of technological devices. A potential answer is the use of unstructured grids that represent a promising way for local mesh refinements necessary to take into account very complex geometries (cooling holes, etc.) [45, 99]. Very few contributions directly discuss the use of structured or unstructured LES solvers for blade flows [103] and one intent of this thesis is to address this issue. To do so, the comparison of LES and RANS predictions is first proposed to emphasize the differences of the two approaches for a test case representative of

turbine flows: the first stage of an uncooled, transonic, high-pressure turbine [10]. Comparisons of LES predictions obtained using a fully structured solver and a fully unstructured one are detailed and compared to experiments. Irrespectively of the solver used clear common features are recovered and are in good agreement with experimental data. Typically, for the investigated operating point, observations show a by-passed transition on the blade suction side, which is very difficult to predict with conventional numerical flow solvers. Experimental data [10] also indicates that the solution is largely dependent on the external turbulence level, a sensitivity which is confirmed and captured by the two LES approaches.

All the results obtained during this thesis on turbine heat transfer are gathered in Chapter 2. This part of the manuscript is arranged as follows. The experimental target configuration is first introduced in Section 2.1 along with the dependency to the upstream Free-Stream Turbulence (FST) intensity of the experiment and its length scale. Section 2.2 provides the description of the numerical methods, models, computational domains, meshes and sets of boundary conditions used for CFD. The first part of Section 2.3 is devoted to the analysis of the results with first comparisons against experimental findings of structured RANS and LES predictions. Structured versus unstructured LES is detailed for aero-thermal prediction with and without FST. The sensitivity of the calculations to geometric parameters and the potential impact it may have on heat transfer predictions is then investigated. In the last part of Section 2.3, the ability of LES to reproduce the sensitivity of the flow to FST is illustrated. For this specific analysis, different values of FST are investigated and specific flow structures are studied.

The following sections are part of a published paper in the International Journal of Heat and Mass Transfer [40]. There are here presented with additional figures to ease the reader's comprehension.

2

Turbine blade heat transfer

—No hay camino tan llano —replicó Sancho—,
que no tenga algún tropezón o barranco;
en otras casas cuecen habas, y en la mía, a calderadas.

El Ingenioso Hidalgo Don Quijote de la Mancha,
Miguel de Cervantes.

Contents

2.1 Reference experimental setup and conditions

The context of application of this study is the qualification of LES for the improvement of heat transfer predictions around distributor blades located right at the exit of the combustion chamber of aeronautical gas turbine engines. This specificity imposes having access to a high Mach number flow facility with detailed data around blades typical of turbines. To meet this purpose the Von-Karman Institute (VKI) LS 89 case [10] is retained since it is constructed to specifically address and validate CFD methods and exhibits many of the fine mechanisms often present in real applications.

2.1.1 The LS89 case

The tested configuration is a $2D$ turbine blade cascade, called LS 89 blade, largely described in Arts et al. [10] and displayed in Fig. 2.1. Only the central passage is investigated and aims at simulating a blade to correspond to periodic flow conditions. The blade chord C is of 67.647 mm with a pitch/chord ratio of 0.85 and is placed at an angle of attack of 0°.

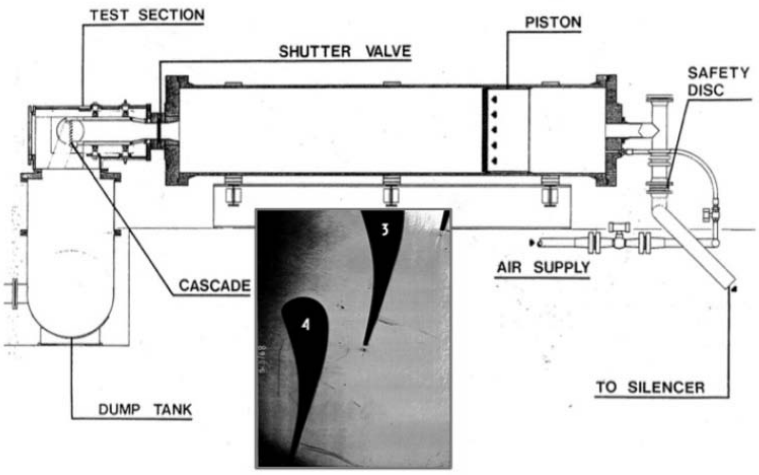

Figure 2.1: Experimental facility investigated by Arts et al. (1990) [10].

The convective heat transfer coefficient, H, measured in this experimental rig is defined as the ratio between the wall heat flux, q_{wall}, and the difference between the total free stream temperature, T_0 and the local wall temperature, T_{wall}, Eq. (2.1).

$$H = \frac{q_{wall}}{T_0 - T_{wall}} \tag{2.1}$$

Test case	Re_2	$M_{is,2}$	$P_{i,0}$	$T_{s,wall}$	Tu_0
MUR129	$1.13\,10^6$	0.840	$1.87\,10^5$ Pa	298 K	1.0%
MUR235	$1.15\,10^6$	0.927	$1.85\,10^5$ Pa	301 K	6.0%

Table 2.1: Test cases and details of the flow conditions for VKI experiment.

A large range of free stream conditions have been experimentally investigated but only two configurations are explored in this work, Table. 2.1, where the indices 0 and 2 denote quantities at the inlet and outlet, respectively. The adjustment of the position of the turbulence grid relative to the cascade controls the variation of the turbulence intensity. The considered Reynolds numbers, Re_2,

based on the chord and outlet velocity is approximately equal to 10^6 for both cases while the inlet FST intensity, Tu_0, equals 1% and 6% respectively. This two-set configuration is believed to be the more representative conditions present in a real turbine. Both cases have approximately the same inlet total pressure, $P_{i,0}$ and static mean wall temperature, $T_{s,wall}$. The isentropic Mach number at the outlet is slightly different between the cases ($M_{is,2}$ = 0.840 and 0.927).

The flow topology expected around the airfoil is represented schematically in Fig. 2.2. Several phenomena can be determined for the LS89 case: **1** is the well-know Von Karman vortex shedding in the blade's wake. This vortex shedding creates pressure waves emitted from the unsteady boundary layer detachment at the trailing edge. These pressure waves **2** then travel upstream and downstream the flow interacting with other flow regions. Part of the impacting pressure waves on the suction side wall of the underneath blade, **3**, is reflected back into the main channel. Skin vortices **4** can also be created from this impact and will then interact with the flow on the suction side. Note also that the downstream propagating pressure wave also interacts with the wake structures. With the operating conditions targeted, a shock wave, **5**, could be present with appearance of supersonic regions. The Von Karman street is well noticeable in Fig. 2.3. These complex flow phenomena have to be taken into account since they affect the aerodynamic field around the blade, and therefore, the heat transfer, which is one of the quantities of interest for turbine designers. An additional difficulty with these conditions is evidenced by the dependency of the flow patterns to the upstream turbulence as further discussed below and illustrated in Fig. 2.7.

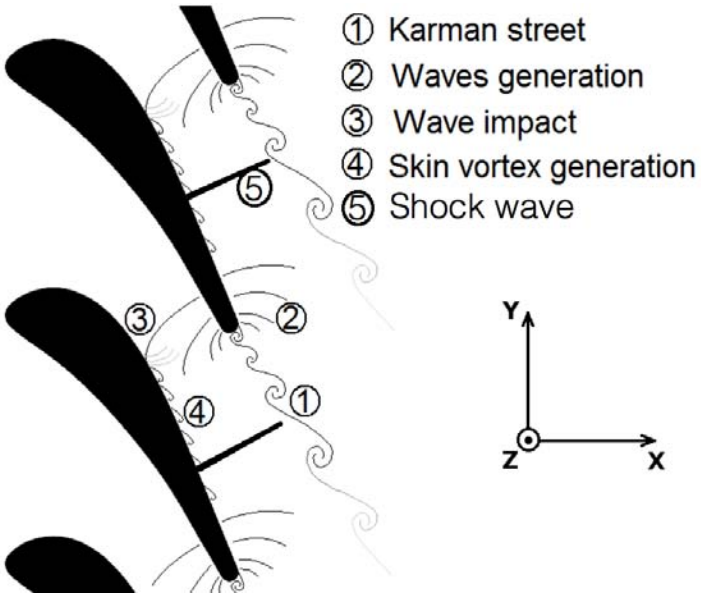

Figure 2.2: Schematic view of the flow topology around the LS89 blade (based on the MUR235 case) [103].

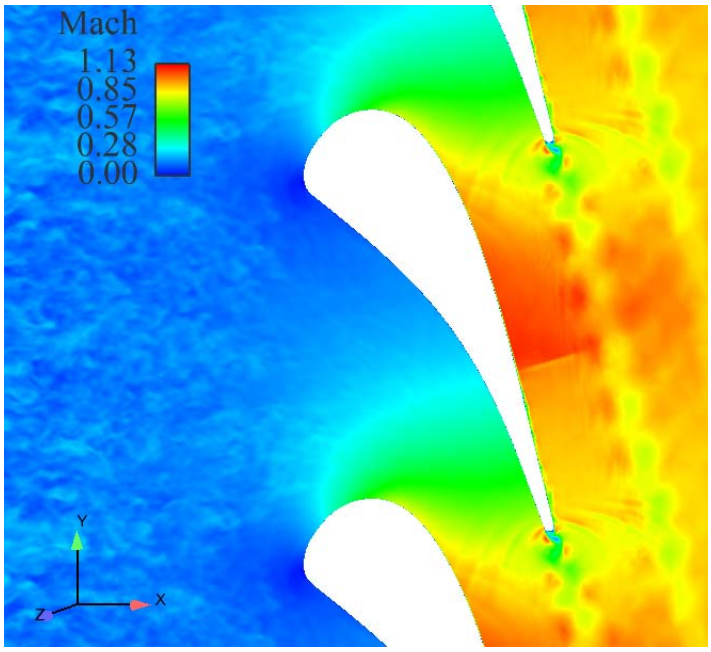

Figure 2.3: Instantaneous field of Mach number predicted by the unstructured LES.

2.1.2 Dependency to the upstream veine turbulence

In the last decades, the effect of FST and its length scale has been largely studied experimentally in high pressure turbine passages. Yardi et al. [195] analyzed those effects on the stagnation regions of a cylinder concluding that the maximum effects appear for a dimensionless length scale $L/D\sqrt{Re_D}$ between 5 and 15, where L is the integral length scale of the turbulence and D is the cylinder diameter. Dullenkopf and Mayle [50] found that fluctuations at low frequencies only impact the quasi-steady state, while those of high frequencies are damped by viscosity. As a result, only a narrow band of the turbulence intensity has an influence on heat transfer. Their major conclusion is that the augmentation of heat transfer varies linearly with the intensity weighted by the effective length scale. Ames et al. [8] analyzed the transition location with respect to the FST intensity and length scale in a C3X blade cascade. In the experiment, the decrease of the length scale increases the heat transfer and the transition location moves towards the leading edge when intensifying the turbulence intensity.

Pressure gradient and surface curvature play also a major role on the flow structure and the boundary layer response, which ultimately controls the heat transfer. As seen in Fig. 2.4, where experimental results from Table 2.1 are plotted, the heat transfer can be increased by 40% on the pressure side if turbulence is present in the main stream. Görtler observes that the boundary layer on a concave surface becomes unstable under the effect of centrifugal forces [54]. Stream-wise vortices appear along the wall, known as Görtler vortices, which are responsible of an increased local vorticity and

enhanced heat transfer to the blade. Unsteady vortical structures are detected also at the leading edge in the LES of Xiong et al. [194]. On the suction side, Fig. 2.4 underlines that the transition onset is different for the experiment with and without FST. This particular point will be largely discussed in Section 2.3.2.2.

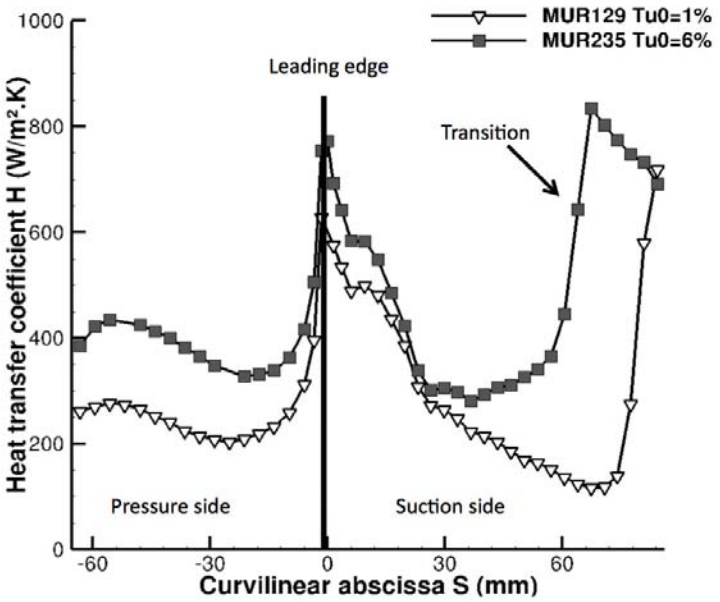

Figure 2.4: Experimental profiles of the local heat transfer coefficient, H, as a function of the blade curvilinear abscissa S (negative values for the pressure side and positive values for the suction side of the blade, the zero corresponding to the leading edge position) and Tu_0, inlet FST intensity, results from Arts et al. [10].

As the FST intensity is known in the experiment, the reader would expect a comparison of the Power Spectrum Density (PSD) between the experiment and the simulations. Results extracted at the leading edge location can serve as a validation of inlet turbulent conditions. However, there is no information in the experiments reported by Arts et al. [10] about the PSD at the considered turbulent intensities. The second point is that the length scale of inlet turbulence, L_0, is not known. To better deal with this problem, a parametric study has been added in the Section 2.3.2.2 to show the effect of the turbulent length scale on the wall heat transfer.

Numerically, the principal limits of RANS simulations are the accurate prediction of the transition onset: traditional turbulence models predict a fully turbulent flow while in reality there is a transition zone. Significant improvements have been achieved in RANS based transition models [111]. For LES, while profuse in low pressure turbine [124, 190], numerical analysis on high pressure turbine have not been addressed, except by Bhaskaran et al. [19].

2.2 Numerical simulations

Irrespectively of the turbulent modeling formalism adopted for the computation (*i.e.*, RANS or LES), the initial governing equations are the unsteady compressible Navier-Stokes equations that describe the conservation of mass, momentum and energy. In conservative form, it can be expressed in three-dimensional coordinates as:

$$\frac{\partial \mathbf{U}}{\partial t} + div\,\mathbf{F} = 0 \tag{2.2}$$

where $\mathbf{U}$ in Eq. (2.2) is the vector of primary variables themselves function of time, t, and space, $\mathbf{x}$. $\mathbf{F} = (\mathbf{f} - \mathbf{f_v}, \mathbf{g} - \mathbf{g_v}, \mathbf{h} - \mathbf{h_v})$ is the flux tensor; $\mathbf{f}, \mathbf{g}, \mathbf{h}$ are the inviscid fluxes and $\mathbf{f_v}, \mathbf{g_v}, \mathbf{h_v}$ are the viscous fluxes (including the potential contribution of models for turbulence through the addition of the so-called turbulent viscosity, ν_t). The fluid follows the ideal gas law $p = \rho\, r\, T$, where r is the mixture gas constant, T, the temperature and ρ, the density. The fluid viscosity follows Sutherland's law and the heat flux follows Fourier's law.

2.2.1 Turbulence modeling for RANS and LES

The high Reynolds number related to the studied flow implies that all the flow scales can not be efficiently represented directly with current grid sizes. Turbulence modeling is thus necessary to allow computing such flows. Different formalisms exist and the most common approach for complex configurations is still the RANS procedure which proposes to model the effect of all the turbulent scales on the mean flow in statistically stationary cases. For this formalism, the mathematical operation introduced relies on the statistical ensemble of independent realizations of the same flow problem from which only the statistical ensemble means are of interest. The initial system of equations is thus usually supplemented by additional modeled transport equations to specifically address turbulence local non-equilibrium or other turbulent flow features [110, 145, 178]. With this approach and for the specific problem of the boundary layer transition, transition criteria [2, 87, 118, 172] can be added. Note that this modeling formalism has been applied to turbine flows with moderate success [108, 113]: the transition criteria are effective to match the experiments (if the solution is known) but they usually suffer from a lack of universality.

A more comprehensive method and particularly less demanding modeling formalism is obtained with LES. In this approach the notion of separation of turbulent scales is introduced and distinguishes a separation between the resolved (large) turbulent scales and the modeled (small) scales [53, 125, 142, 145, 152]. This separation of scales is obtained by filtering out the small flow scales that can not be properly represented by the mesh, their effects on the filtered field being modeled by the so-called

SGS model. For compressible LES and RANS, the spatial Favre filtering or ensemble means are used and the operation reduces for spatially, temporally invariant and localized filter functions to:

$$\overline{\rho}\,\widetilde{f} = \begin{cases} \text{RANS:} & \dfrac{1}{N}\displaystyle\sum_{1}^{N} \rho^n(\mathbf{x},t)\, f^n(\mathbf{x},t), \\ \text{LES:} & \displaystyle\int \rho(\mathbf{x}',t)\, f(\mathbf{x}',t)\, G(\mathbf{x}'-\mathbf{x})\, d\mathbf{x}', \end{cases} \tag{2.3}$$

where G denotes the filter function while n is the n^{th} realization of a statistical ensemble composed of N of such fields. The unresolved SGS stress tensor $\overline{\tau_{ij}}^t$ and the equivalent Reynolds stress tensor appearing in RANS simulations are usually modeled using the Boussinesq assumption [171]:

$$\overline{\tau_{ij}}^t - \frac{1}{3}\overline{\tau_{kk}}^t\,\delta_{ij} = -2\,\overline{\rho}\,\nu_t\,\widetilde{S}_{ij}\,, \tag{2.4}$$

$$\text{with } \widetilde{S}_{ij} = \frac{1}{2}\left(\frac{\partial \widetilde{u}_i}{\partial x_j} + \frac{\partial \widetilde{u}_j}{\partial x_i}\right) - \frac{1}{3}\frac{\partial \widetilde{u}_k}{\partial x_k}\,\delta_{ij}. \tag{2.5}$$

In Eq. (2.4), $\widetilde{S}_{ij}$ is the resolved or ensemble mean strain rate tensor and ν_t is the SGS or RANS turbulent viscosity. The unclosed energy flux $\overline{q_i}^t$ is modeled using a turbulent heat conductivity obtained from ν_t by $\lambda_t = \overline{\rho}\,\nu_t\,\overline{c_p}/Pr_t$ where Pr_t is a constant turbulent Prandtl number,

$$\overline{q_i}^t = -\lambda_t\,\frac{\partial \widetilde{T}}{\partial x_i}. \tag{2.6}$$

In Eq. (2.6), $\widetilde{T}$ is the Favre filtered temperature which satisfies the modified filtered state equation $\overline{p} = \overline{\rho}\,r\,\widetilde{T}$ [126].

RANS closures:

For this work a two-equation type of closure is adopted. To handle transition, the standard Abu-Ghannam model [2] introduces the intermittency factor γ (parameter representing the time in which the flow is turbulent) but results [66] underline the poor predictive capability of such approach when there is an impact of FST on the heat transfer around the blade. An improvement, detailed in Section 2.3.1, is noticed when implementing Menter γ-Re_θ model [123] coupled with a two equation turbulence model k-ω using a correction on the Shear Stress Transport (SST) [122]. The novelty of this correlation-based transition model is not only to use local variables but also their gradients. Such new closure however requires additional transport equations. A transport equation for the intermittency γ model is needed to turn on the production term of the turbulent kinetic energy downstream of the transition point, Eq. (2.7), where S_γ represents the transition sources.

$$\frac{\partial(\rho\gamma)}{\partial t} + \frac{\partial(\rho U_j\gamma)}{\partial x_j} = S_\gamma + \frac{\partial[(\mu + \frac{\mu_t}{\sigma_f})\frac{\partial\gamma}{\partial x_j}]}{\partial x_j}. \tag{2.7}$$

A second transport equation is solved in terms of the transition onset momentum-thickness Reynolds number ($\widetilde{Re_{\theta t}}$) and is given by Eq. (2.8). In this equation, $S_{\theta t}$ stands for the source term which forces the transported scalar to match the local value of $Re_{\theta t}$ calculated from an empirical correlation outside the boundary layer. More information of this methodology can be found in Menter et al. [123].

$$\frac{\partial(\rho\widetilde{Re}_{\theta t})}{\partial t}+\frac{\partial(\rho U_j\widetilde{Re}_{\theta t})}{\partial x_j}=S_{\theta t}+\frac{\partial[(\mu+\mu_t)\sigma_{\theta t}\frac{\partial\widetilde{Re}_{\theta t}}{\partial x_j}]}{\partial x_j}. \tag{2.8}$$

LES closures:

The SGS model, used for both structured and unstructured meshes, is the Wall-Adapting Local Eddy-Viscosity (WALE) model [134], specially built to compute turbulence near walls. Similarly to the Smagorinsky model [171], local flow features are lost and only global quantities are represented by the SGS model. Following this closure, the SGS viscosity reads,

$$\nu_t=(C_w\Delta)^2\frac{(s^d_{ij}s^d_{ij})^{3/2}}{(\tilde{S}_{ij}\tilde{S}_{ij})^{5/2}+(s^d_{ij}s^d_{ij})^{5/4}}, \tag{2.9}$$

$$s^d_{ij}=\frac{1}{2}(\tilde{g}^2_{ij}+\tilde{g}^2_{ji})-\frac{1}{3}\tilde{g}^2_{kk}\delta_{ij}, \tag{2.10}$$

In Eq. (2.9) and Eq. (2.10) , Δ stands for the filter length ($\propto$ the cubic-root of the cell volume), C_w is the model constant equal to 0.4929 and $\tilde{g}_{ij}$ is the resolved velocity gradient. For the SGS energy flux, $\bar{q}_i{}^t$, Eq. (2.6), the turbulent Prandtl number coincides with the SGS quantity and differs from the conventional turbulent Prandtl number. The value chosen for the turbulent SGS Prandtl number is 0.6 for both solvers.

2.2.2 Numerical solvers

Two different solvers are used in this work. The first solver (*elsA*) is specialized in external and internal flow predictions using RANS, LES and Detached Eddy Simulation (DES). It is fully compressible and relies on a temporal implicit marching scheme. The second solver (AVBP) targets reactive flow predictions by use of LES and relies on an explicit temporal integration scheme of the fully compressible multi-species system of equations. Specificities about the numerics adopted for both codes are detailed below for the first code followed by the second code.

The parallel *elsA* software uses a cell centered approach on structured multi-block meshes. More information about this flow solver can be found in Cambier et al. [32]. For (steady-state) RANS simulations, convective fluxes are computed with a second order centered scheme with classical artificial dissipation parameters k^2 and k^4 [81]. Diffusive fluxes are computed with a second-order centered scheme. The pseudo time-marching is performed by use of an efficient implicit time integration approach, based on the backward Euler scheme and a scalar Lower-Upper (LU) Symmetric Successive Over-Relaxation (SSOR) method [197]. As previously indicated, for RANS, the γ-Re_θ Menter model [123] is used coupled with a two-equation k-ω turbulence model with a SST correction [122]. For LES, convective fluxes are computed with a fourth order centered scheme, considering minimal artificial dissipation [49]. The time-marching scheme is based on a second order Dual Time Stepping method [80]. Such implicit algorithms are very attractive to reduce the computational cost since the simulation is stable even with CFL numbers greater than 100 (although clear care is needed and such large values are to be avoided for LES). In the present case, $16,000$ time steps ($\Delta t = 0.12\ \mu s$) are necessary to describe one through-flow time (the time for a particle dropped at the inlet to reach the outlet, *i.e.* ≈ 2.0 ms).

The parallel LES code, AVBP [121, 164], solves the full compressible Navier-Stokes equations using a two-step time-explicit Taylor-Galerkin scheme (TTG4A) for the hyperbolic terms on a cell-vertex formulation [39], along with a second order Galerkin scheme for diffusion [42]. TTG4A provides high spectral resolution and both low numerical dissipation and dispersion, which is particularly adequate for LES [101]. Such numerics are especially designed for LES on hybrid meshes and have been extensively validated in the context of turbulent reacting flow applications [24, 174]. The scheme provides 3*rd* order space and time accuracy [39]. The major drawback of this strategy arises from the explicit nature of the solver whose time step is controlled by the low acoustic CFL number preventing from reducing characteristic cell size below the wall unit scale. Therefore, for aerodynamic applications, where the viscous sub-layer needs to be computed, mesh refinements force small time steps ($\propto 10^{-7}$s or lower, $\Delta t = 1.54\ 10^{-8}$s in this particular case) and a higher computational cost is inferred. In the present case, about $130,000$ time steps are necessary to simulate one flow-through time. Note that despite this clear constraint, the unstructured hybrid approach enables refinement of the mesh in zones of interest by using prisms in the wall region for example. Note that more information on the solvers (numerical and temporal discretization, closures, etc) can be found in Appendix D.

2.2.3 Computational setup

2.2.3.1 Computational domain and mesh generation

The computational domain examined is sketched in Fig. 2.5 (a) accompanied by a view of probe locations , Fig. 2.5 (b), used in the analysis of the unsteady features predicted by LES . For the structured mesh, the flow domain is discretized with a multi-block approach, using an O-4H meshing strategy for the guide vane passage. A partial view of the structured mesh used is presented in Fig. 2.6 (a). In order to limit the dependency of the solution to the inlet/outlet positions, the mesh extends up to $0.7C$ upstream the blade leading edge and $1.5C$ downstream the vane. Typical grid dimensions are $\sim$650 points in the stream-wise direction with $\sim$780 points around the blade, $\sim$175 points in the pitch-wise direction and $\sim$200 points in the span-wise direction. The total number of grid points for the blade passage is 29.7×10^6 points for structured LES and 35.000 points for 2D RANS. Typical cell sizes in wall units are in agreement with recommended values, suitable for LES predictions [86], Table 2.2.

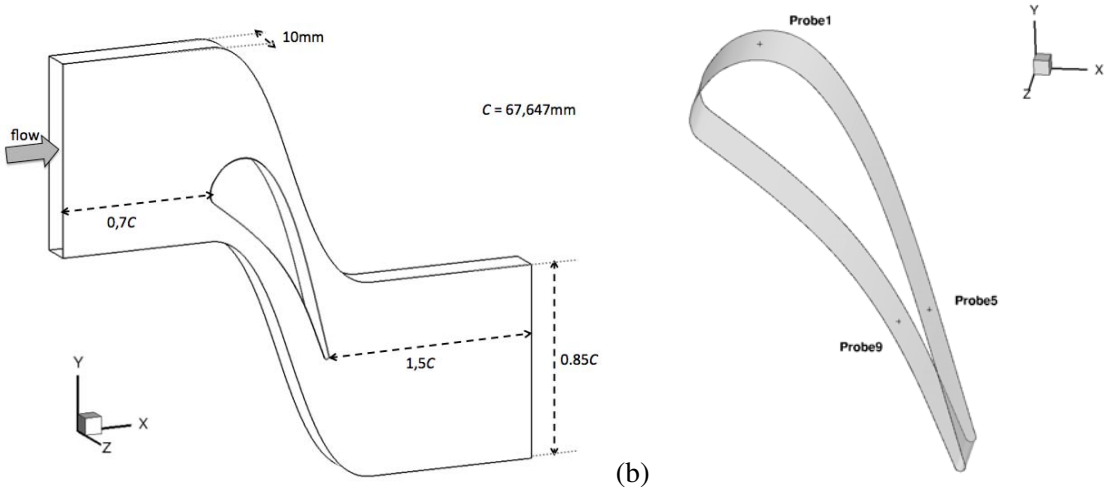

Figure 2.5: (a) Sketch of the computational domain and (b) visualization of three of numerical probes used to diagnose LES predictions.

For the unstructured simulations, a hybrid approach with prismatic layers at the wall and tetrahedra in the main duct, Fig. 2.6 (b), is adopted to reduce the number of cells in the nearby region of the wall and to meet the preferential directions of the boundary layer flow. The solution adopted has 5 layers of prisms where the vertical length of the prism Δy is smaller than the triangle base-length Δx or Δz (here, $\Delta x \sim \Delta z$) resulting in a minimum cell volume that is increased if compared to a full tetrahedral option. A limit is imposed to this mesh adaptation to avoid numerical errors in these layers,

the aspect ratio of the first and thinnest layer is set to $\Delta x^+ \sim 4\Delta y^+$, *i.e.*, $x^+ \approx 4y^+$ in agreement with known observations and boundary layer scales [31]. The last constraint to control, which is known to be critical numerically, is the stretching ratio. It can be defined as the ratio between the characteristic length of an element of a layer to the characteristic length of the neighboring cell. In this particular case, the characteristic length is equal to the prism height. The stretching ratio is here equal to 1.09. Taking into account all the constraints of this strategy, 29.3×10^6 (6.3×10^6 prisms and 23×10^6 tetrahedra) cells are required, Table 2.2. Typical grid properties are $6,000$ points around the blade, $\sim$200 points in the pitch-wise direction and $\sim$230 points in the span-wise direction.

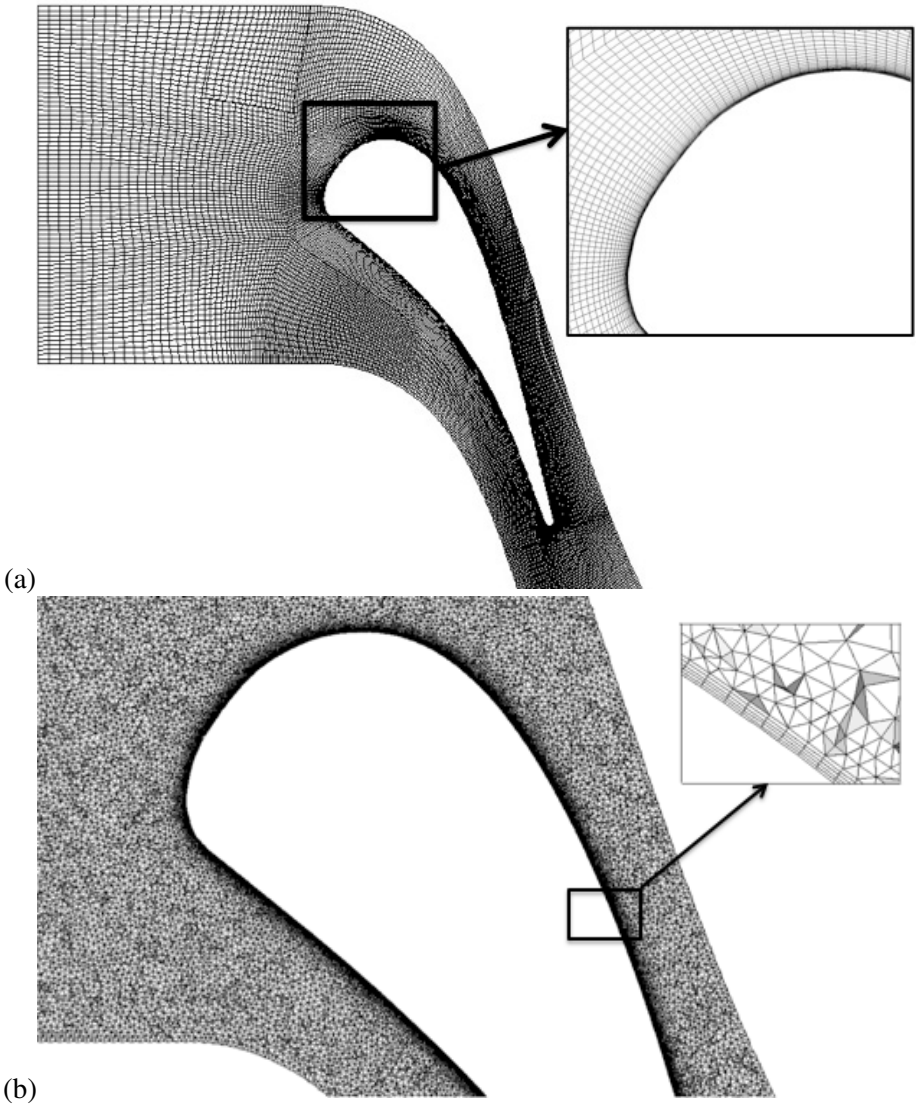

(a)

(b)

Figure 2.6: (a) Detail of the structured mesh grid and (b) unstructured mesh grid for the LS89 blade.

	RANS structured	**LES** structured	**LES** unstructured
$< y^+ >$	$\sim$1	$\sim$1	$\sim$4
1^{st} **layer size**	2μm 2D	2μm $\Delta z^+ \sim 25$ $\Delta x^+ \sim 150$	8μm $\Delta z^+ \sim 4\Delta y^+$ $\Delta x^+ \sim 4\Delta y^+$
Mesh size	0.035M cells	29.7M cells	29.3M cells

Table 2.2: Wall refinement and mesh size for RANS and LES approaches for MUR235.

2.2.3.2 Boundary conditions

Inflow and outflow mean conditions are applied for both codes based on available experimental data, Table. 2.1. Walls are treated as isothermal and the mean static pressure is applied at the downstream end to set the outlet isentropic Mach number at the desired value. Periodicities are used for lateral and radial ("top and bottom") sections of the computational domain, Fig. 2.5 (a).

Specific attention is taken for the inflow conditions, the difficulty relating to the studied flow imposes to take into account the turbulence intensity. Mean inflow information is first set for all simulations based on measured total temperature and total pressure for both solvers: *i.e.*, the mean carrying field is constant in space and time at the inflow. For RANS simulations, turbulence intensity is of critical importance along with the turbulent length-scale for the transition criterion [123]. There are set constant in time and space at a reference chosen value of the inflow condition (Tu_0 = 6% and L_0 = 1.5 mm). The main drawback of this modeling, analyzed in Section 2.3.1.2, is that it is not able to take into account the effect of turbulent structures in the suction side of the blade, which are responsible of an increase of 40% in the heat transfer when there is FST.

For LES, the notion of turbulent inflow imposes a notion of unsteadiness as well as spatial variations of the flow at the inflow condition. Different methods exist either relying on a turbulent channel precursive simulation [19], synthetic turbulence [33] or recycling methods [82]. The aim of all these methods remains common and is to mimic the effects of turbulence without relying on white noise that is not effective due to the lack of spatial and temporal coherence. The methods retained for the study are the "2D" version of the "Synthetic Eddy Method" (SEM) proposed by Jarrin et al. [82] available with the structured LES solver and the synthetic approach proposed by Guezennec et al. [71] for the unstructured solver, Fig. 2.7. These two inflow conditions require a value of Tu_0 and a most energetic turbulent length-scale, L_e. They are conceptually identical and yield similar LES results on simple turbulent flows. With both approaches, the inflow information is recast into:

Figure 2.7: Instantaneous field of $||\frac{\partial \rho}{\partial x_i}||/\rho$ as obtained by unstructured LES using synthetic turbulence [97] at the inflow boundary.

$$\widetilde{u}_i(\mathbf{x},t) = <\widetilde{u}_i>(\mathbf{x}) + \widetilde{u}'_i(\mathbf{x},t) \text{ with } \frac{\partial \widetilde{u}'_i}{\partial x_i} = 0. \tag{2.11}$$

In Eq. (2.11), $\widetilde{u}_i$, refers to a LES velocity filtered quantity and $<\widetilde{u}_i>$ refers to the RANS equivalent. Note that this correspondence supposes a statistically stationary and ergodic flow [145, 178]. $\widetilde{u}'_i$ is defined by its position and its amplitude and results from 100 to 1,000 random wave number fields whose individual amplitudes are divergence free and relate to given turbulent synthetic spectra [136, 144] of given integral length-scale that is proportional to L_e [33, 82, 97].

2.3 Results and discussions

In order to proceed and qualify both LES solvers on the LS89 problem, several computations are produced, the detail of which is provided in Table. 2.3. RANS and LES results are first compared, Section 2.3.1, to study the suitability and limits of these approaches. Case Ia & Ib are confronted to Cases IIa & IIb and IIIa & IIIb in terms of aerodynamical and thermal predictions. More detailed analyses of the two LES strategies in terms of the sensitivity of both the mesh topology and the FST parameters is carried out in Section 2.3.2.

	RANS structured	LES structured	LES unstructured
Scheme	Implicit	Implicit	Explicit
Model	k-ω, transition criteria [122]	WALE	WALE
MUR129	**Case Ia**	**Case IIa**	**Case IIIa**
MUR235	**Case Ib**	**Case IIb**	**Case IIIb**

Table 2.3: Cases analyzed in Section 2.3.

2.3.1 RANS versus LES predictions

A first point of interest of the present investigation is to quantify and qualify the contribution of LES in the context of highly loaded guide vane of turbines. In the following, Figs. 2.8 & 2.9 & 2.10, direct qualitative comparisons of the available RANS model and both LES are produced for the two operating conditions (all Cases from Table.2.3). For the MUR129 case, all solvers predict a subsonic flow around the blade, Figs. 2.8 (a) & 2.9 (a) & 2.10 (a). For MUR235, mean flow features are clearly captured by both approaches: *i.e.* the existence of the shocks (noted 1 in Figs. 2.8 (b) & 2.9 (b) & 2.10 (b)), the blade wake and the flow acceleration on the suction side issued by the profile strong curvature are present in RANS and LES. Differences essentially appear in the actual extent of the blade wake and the presence of a Von Karman street in the structured and unstructured LES (Figs. 2.9 & 2.10). The Von Karman street is however less visible in Fig. 2.10 with this scaling. Strong pressure waves generated at the trailing edge flow separation are also evidenced by both LES which is not the case in RANS simulations. When FST is imposed at the inlet, MUR235, LES indicate that turbulent flow patterns impact the vane leading edge, resulting in the development of vortices on the pressure side, noted 2 in Fig. 2.9 (b) and also noticeable in Fig. 2.10 (b).

More quantitative comparisons are provided in Fig. 2.11. Aerodynamic fields are first judged through the evolution of the isentropic Mach number along the curvilinear abscissa of the blade, S (set equal to zero for the blade leading edge and negative/positive for the pressure side/suction side, respectively). In agreement with the observations from the flow field views given in Figs. 2.8 - 2.10, no major distinctions between RANS and LES are noted around the blade for the two cases. Only the curves for MUR129 are showed in Fig. 2.11. Note that experimental measurements of the isentropic Mach number are not available for the conditions of Table 2.1, the comparison presented serves only to gauge the magnitude of the parameter, $M_{is,2} \sim 0.84$ for all the numerical approaches vs $M_{is,2} \sim 0.88$ for the experimental data. As seen in Figs. 2.8 (a) & 2.9 (a) & 2.10 (a), the flow is subsonic all around the blade in MUR129. A more detailed investigation of the flow boundary layer behavior

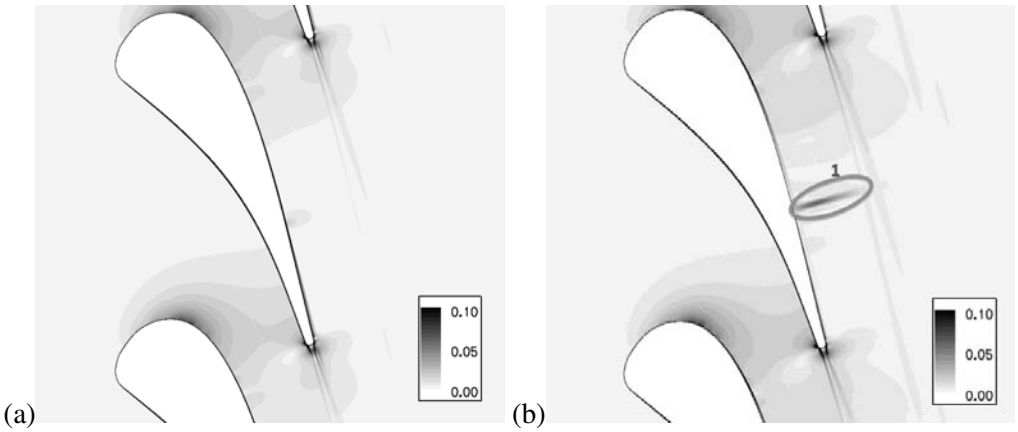

Figure 2.8: Mean RANS predictions of $||\frac{\partial \rho}{\partial x_i}||/\rho$ for (a) Case Ia and (b) Case Ib of Table 2.3.

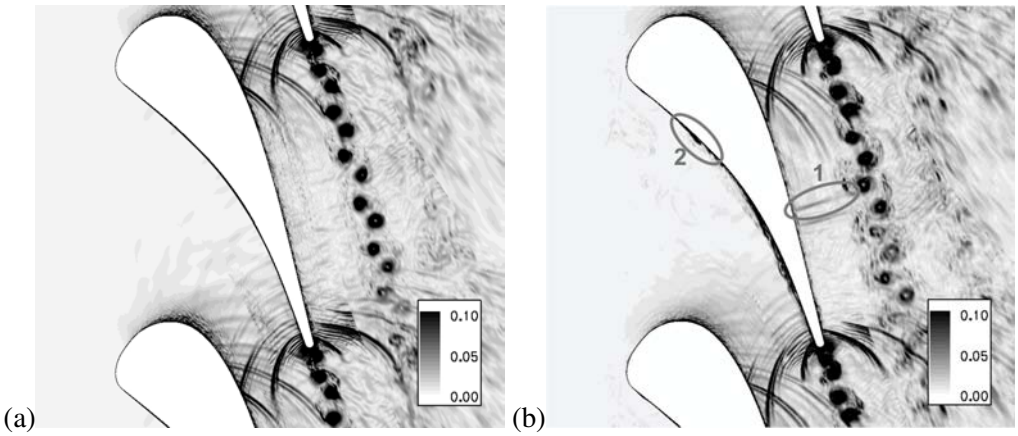

Figure 2.9: Instantaneous LES predictions of $||\frac{\partial \rho}{\partial x_i}||/\rho$ for (a) Case IIa and (b) Case IIb of Table 2.3.

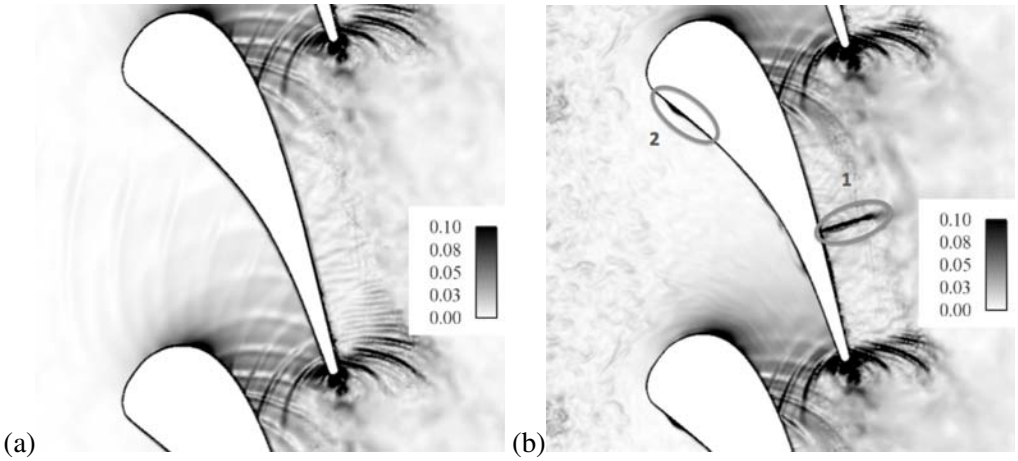

Figure 2.10: Instantaneous LES predictions of $||\frac{\partial \rho}{\partial x_i}||/\rho$ for (a) Case IIIa and (b) Case IIIb of Table 2.3.

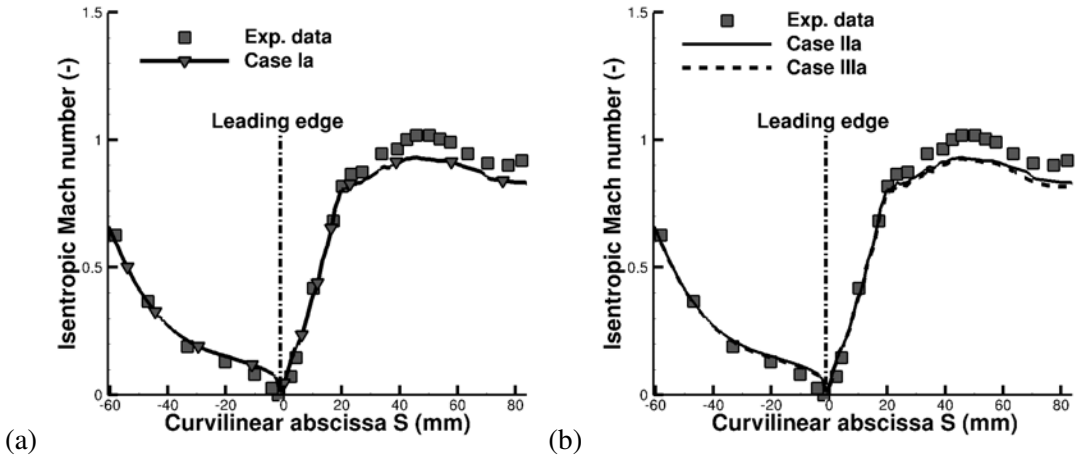

Figure 2.11: Isentropic Mach number distribution along the blade wall for (a) RANS and (b) LES computations of MUR129. The experimental conditions are slightly different from the ones of Table 2.1.

of these two predictions is then carried out by looking at the heat transfer flux at the blade wall in Figs. 2.12 & 2.15.

2.3.1.1 Test case wihout FST:

In MUR129, Fig. 2.12, the boundary layers remain mainly laminar on both suction and pressure sides. The heat transfer coefficient H obtained by RANS and LES is correctly estimated on the pressure side and on most of the suction side. The common behavior of H for RANS and LES in the near leading edge region corresponds to the development of the laminar boundary layer on both sides of the profile. RANS and LES anticipate the boundary layer transition seen on the experimental curve at $S = 75$ mm. This difference is common to RANS and LES in the estimation of heat transfer with respect to the experimental results, RANS and LES having nearly the same transition abscissa ($S \approx 61$mm). The disparity between experimental and numerical results is possibly due to the pressure gradient, whose value for the solvers becomes negative at this specific location, as shown in Fig. 2.11, and eases transition at this spot of the numerical predictions. The major difference between RANS simulation and both LES is the level of heat transfer coefficient they reach after the transition, $H \approx 850$ W/m^2.K for RANS and $H \approx 500$ W/m^2.K for LES.

Based on this test case and although both approaches are theoretically very different, the flow is adequately captured by the steady and unsteady solvers confirming the proper behavior of the LES and RANS models for this operating condition which at the wall remains laminar and stationary. Views of the flow activity near the wall region and as captured by LES are shown in Fig. 2.13. For identification, the Q-criterion (colored by the velocity field) is employed to discriminate flow structures from pure

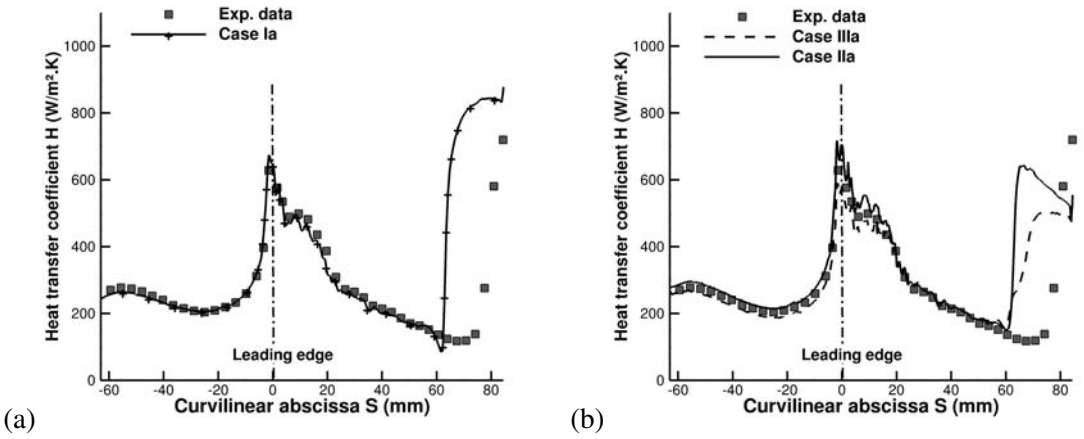

Figure 2.12: Heat transfer coefficient, H, predicted by (a) RANS and (b) structured and unstructured LES at MUR129.

shear at the wall. As evidenced by these results, limited flow activity is present on the pressure side, Fig. 2.13 (b), and almost no activity appears on the suction side. Very small vortices appear past the coordinates $S \approx 20$ mm where acoustic waves generated at the trailing edge upper blade impact the suction side of the blade placed below (Fig. 2.13 (a)). These structures however remain aligned and do not seem to initiate transition to a turbulent boundary layer.

Similar observations hold for the pressure side of the blade where the activity is further delayed and only appears near the trailing edge. These observations are confirmed by the time/frequency maps, Fig. 2.14, constructed based on the temporal signal recorded for the three probes identified in Fig. 2.5 (b). Note that in this case, a Strouhal number (based on the boundary layer height and section bulk velocity) is used and time is adimensionalized accordingly. For all three points probed, low frequency and low intensity activity is visible confirming the pseudo stationary flow in these regions also explaining the low level of the heat transfer coefficient around the blade.

2.3.1.2 Test case with FST:

Results of Fig. 2.15 (a) for MUR235, Table. 2.1, point to the difficulty for this flow and the importance of the main vein turbulence intensity on the boundary layer behavior. For this specific case and with the model adopted, RANS simulations fail to accurately predict the wall heat transfer on the pressure side. The heat transfer enhancement issued by the main flow turbulence is underestimated by about 30%; no influence of the FST is noticed on the pressure side: the heat transfer coefficient H is nearly identical to the MUR129 test case. In the leading edge zone, on the contrary, the γ-Re_θ model of Menter [123] is able to take into account the turbulence intensity effect. Further downstream on the

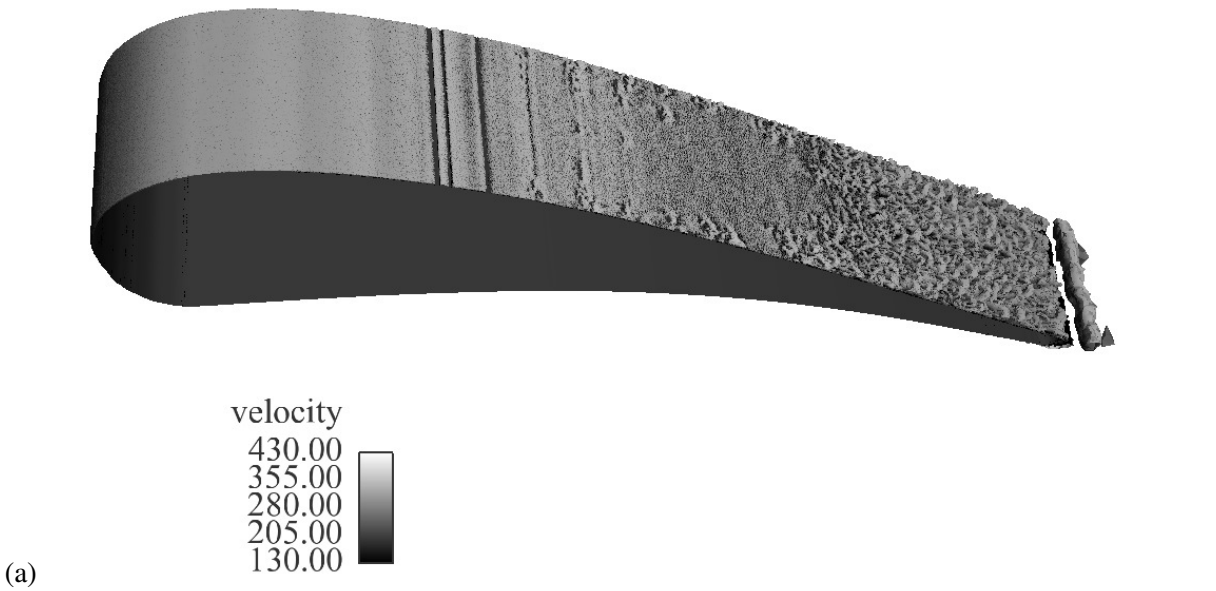

(a)

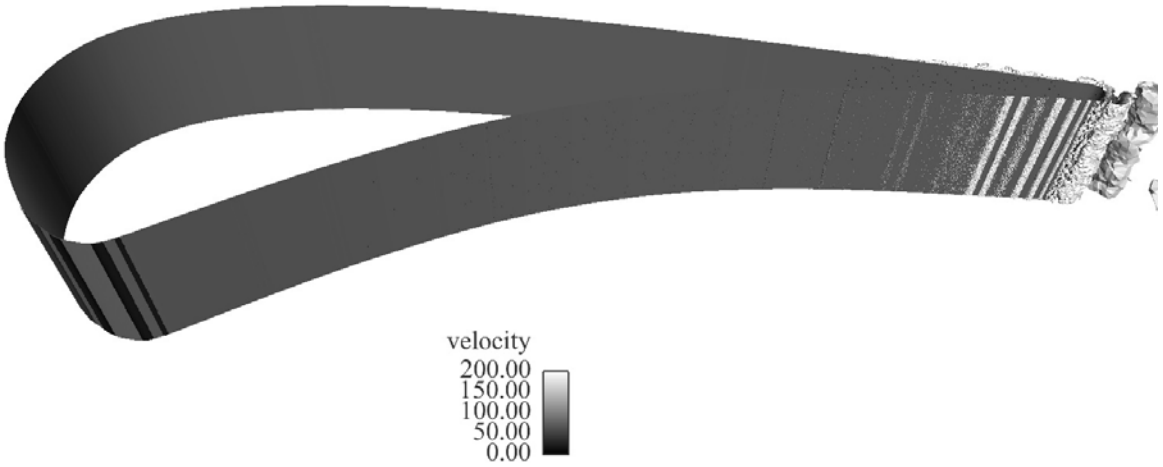

(b)

Figure 2.13: Instantaneous view of the LES flow activity on the (a) suction side and (b) pressure side of the MUR129 test case (Case IIIa of Table 2.3).

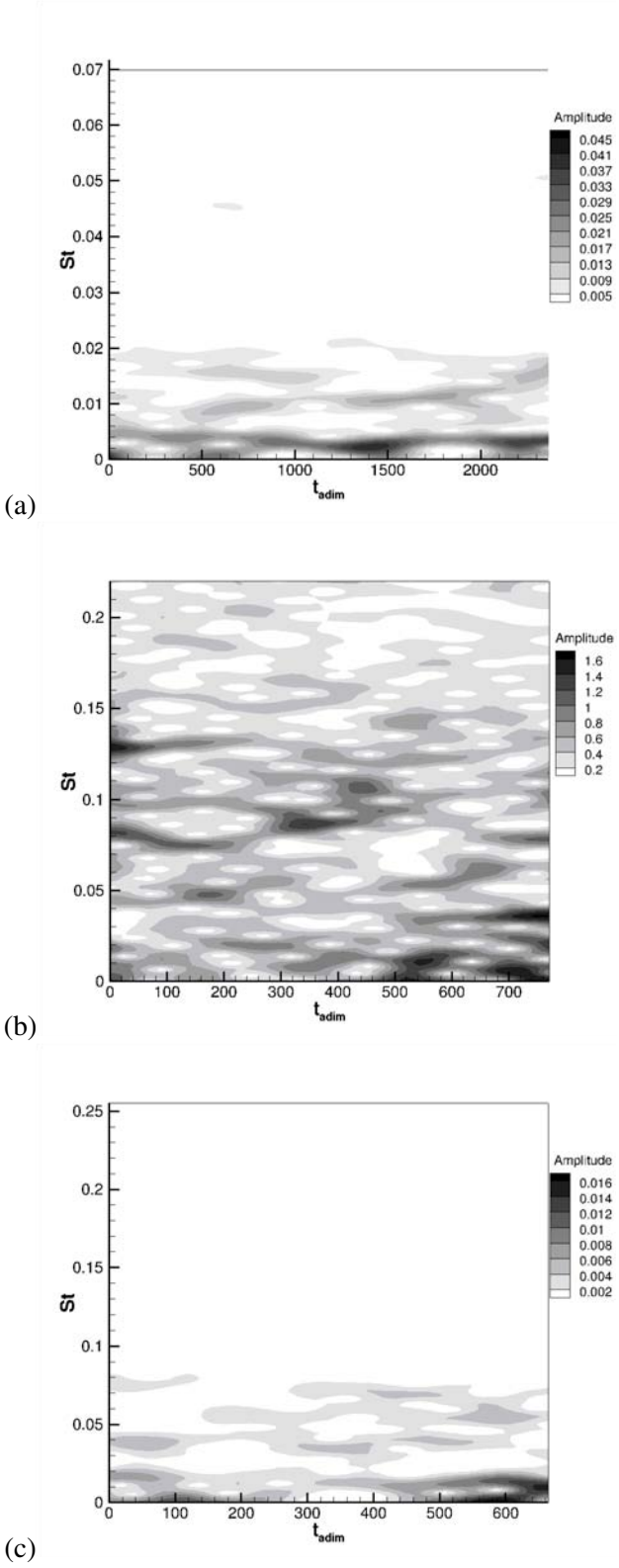

Figure 2.14: Temporal evolution of the frequency content recorded at the three probes identified in Fig. 2.5 (b): (a) Probe 1, (b) Probe 5 for the suction side of the blade and (c) Probe 9 for the pressure side (Case IIa of Table 2.3).

suction side, RANS model does not correctly locate the experimental onset of pre-transition ($S \approx 20$ mm), which is triggered in the RANS simulation by the shock wave at $S \approx 62$ mm. At this location, the error reaches up to 70%. Indeed, RANS model predicts a decreasing evolution from $S \approx 20$ mm to $S \approx 62$ mm, whereas there is a plateau in the experimental heat transfer curve. For $S > 65$ mm, the MUR235 boundary layer is fully turbulent and RANS simulation predicts the correct order of magnitude for the guide vane heating with a discrepancy of 30% if compared to the experimental results. For this case, the model seems better calibrated compared to the results obtained with the Abu-Ghannam approach and shown in Gourdain et al. [66].

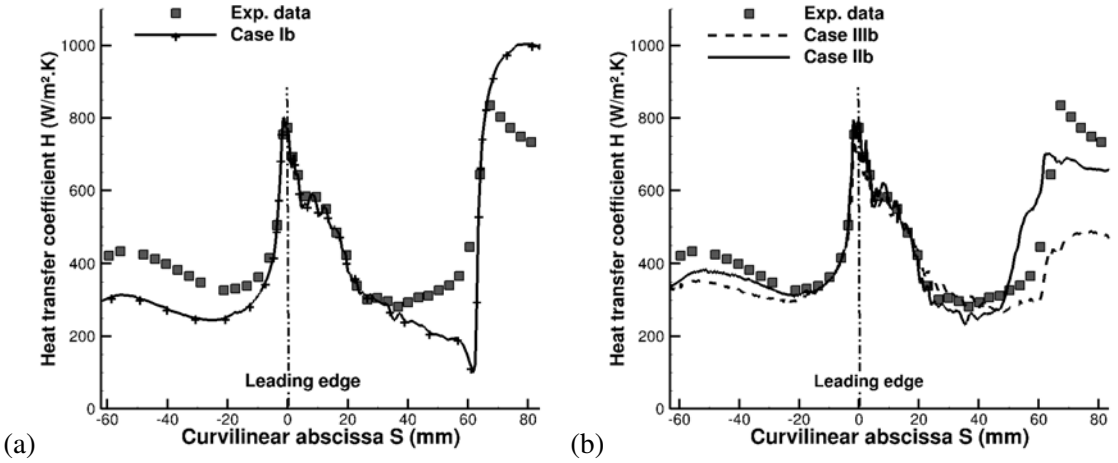

Figure 2.15: Heat transfer coefficient, H, predicted by (a) RANS and (b) structured and unstructured LES at MUR235.

Structured and unstructured LES predictions are also able to reproduce adequately the boundary layer heat transfer coefficient in the near leading edge region, Fig. 2.15 (b). In this zone, for both approaches the error is under the experimental uncertainty reported at 5%. The pressure side development improves if compared to RANS simulations. That is the heat transfer enhancement is captured by both solvers but the level of improvement is not sufficient to recover the experimental findings (18% error at most in Case IIIb and 10% in Case IIb). On the suction side, both LES strategies provide an improvement of the prediction when compared to RANS simulations especially for the prediction of the location and length of the onset of transition. Shock strengths are not equal indicating that both strategy differ and room for improvement still exists.

The main contribution of LES for this highly loaded blade profile naturally arises from the formalism ability to reproduce the proper boundary layer transition on the pressure side with increasing FST [19]. Although LES still underestimates the overall heat transfer on the pressure side, as noticed before, the difference with experimental data is reduced to 10% for the structured LES and 18% for

the unstructured approach. The effect of FST is also clearly captured in the suction side, Fig. 2.15 (b). The main gain appears in the prediction of the pre-transition region: *i.e.* from $S = 20$ mm to $S = 62$ mm. On this side of the blade and all around the leading edge, the heat transfer coefficient is estimated with an error less than 5% (*i.e.* within the experimental uncertainty) until $S = 50$ mm. The maximum error appears close to the trailing edge where structured and unstructured LES locally underestimate the wall heat transfer by approximately 25% and 40%, respectively.

Visualizations of the flow instantaneous activity captured by LES are provided in Fig. 2.17. Compared to Fig. 2.13, flow structures are much stronger, much less aligned and initiated much earlier on the suction side, Fig. 2.17 (a), confirming the importance of such turbulence in the heat transfer enhancement in this region of the flow. A detail of the physics on the suction side with FST is pictured in Fig. 2.16 (a). Fig.2.16 (b) shows the location of the plot. The long stream-wise streaky structures are responsible for the augmentation of the heat transfer and lead to the transition on the suction side boundary layer. On the pressure side, Fig. 2.17 (b), high disrupted flow structures are evidenced; they are not present in the MUR129 case explaining the differences observed experimentally on the heat transfer coefficient. If investigating the time/frequency maps, Fig. 2.18, most of the differences between MUR129 and MUR235 occur at Probe 5, Fig. 2.18 (b), where a lot of intense activity appears. No clear pattern is however noted pointing to the turbulent nature of the activity present in this region of the flow. More information illustrative of the blade boundary layer state along the blade can be found in Gourdain et al. [66].

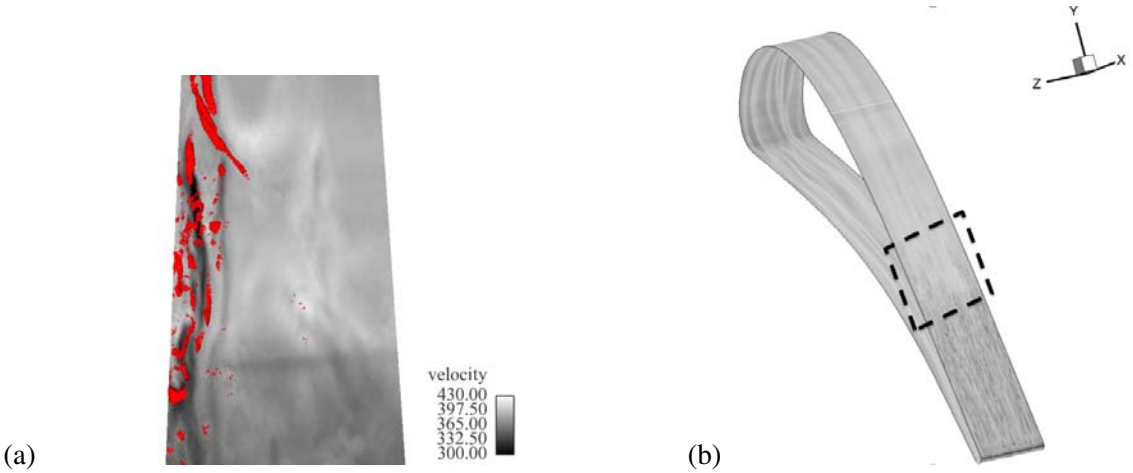

Figure 2.16: For unstructured MUR235, (a) iso-surfaces of second invariant of velocity gradient tensor overlaid with the plan view of velocity contours show the vortex at the location of the spot precursor and (b) location of the view in the whole domain.

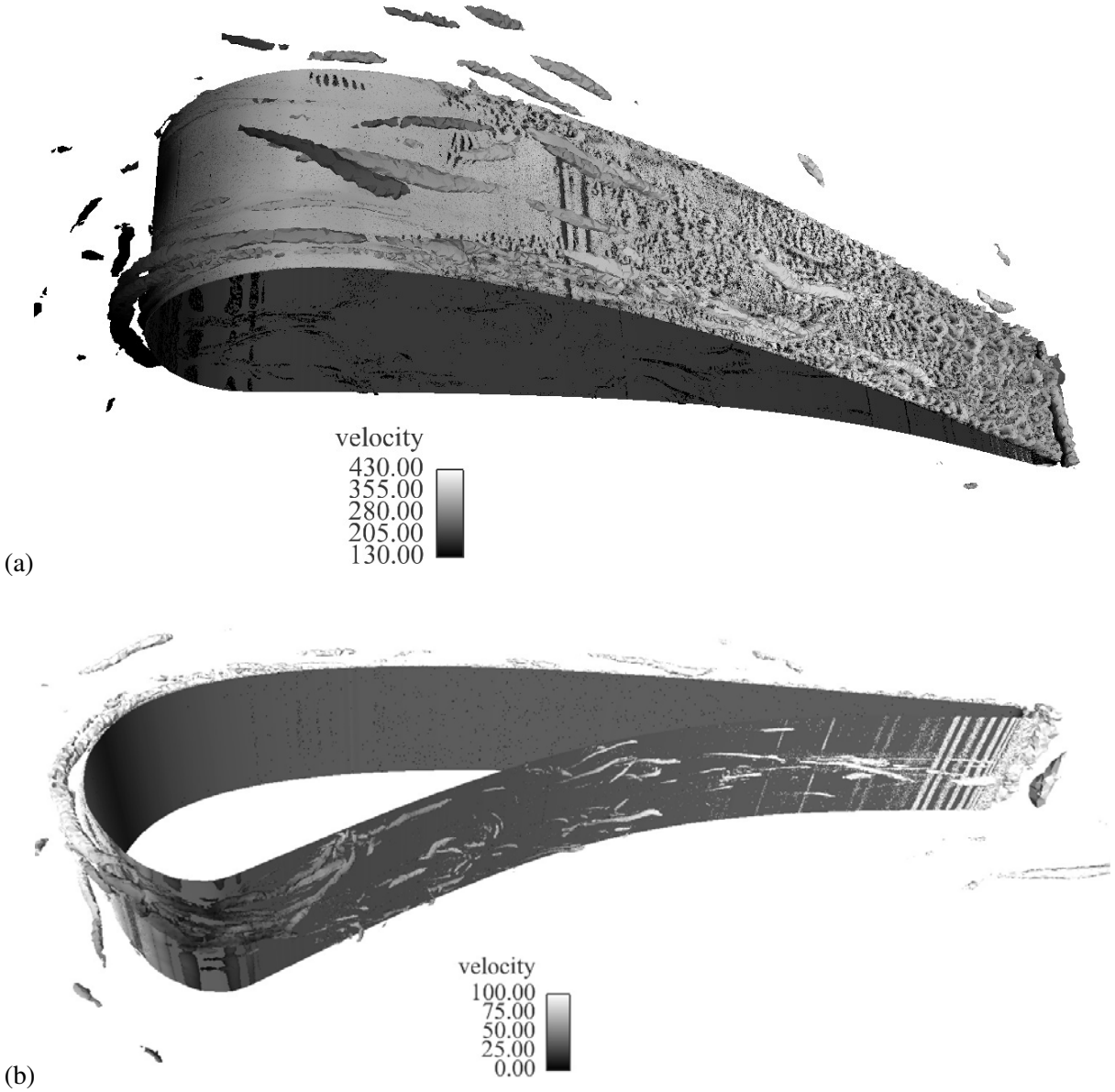

Figure 2.17: Instantaneous view of the LES flow activity on the (a) suction side and (b) pressure side of the MUR235 test case (Case IIIb of Table 2.3).

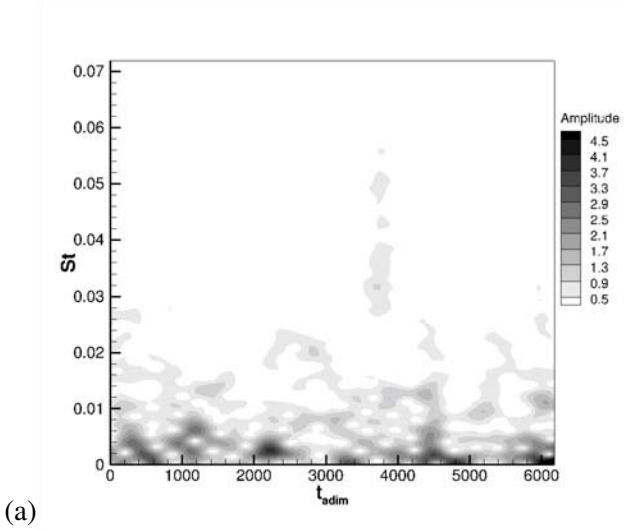

(a)

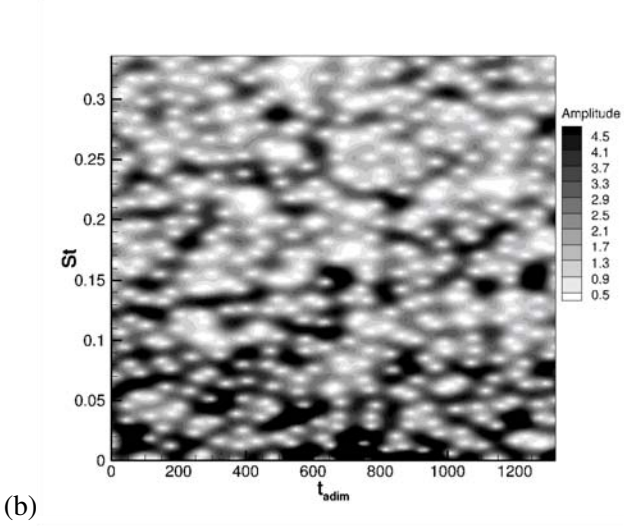

(b)

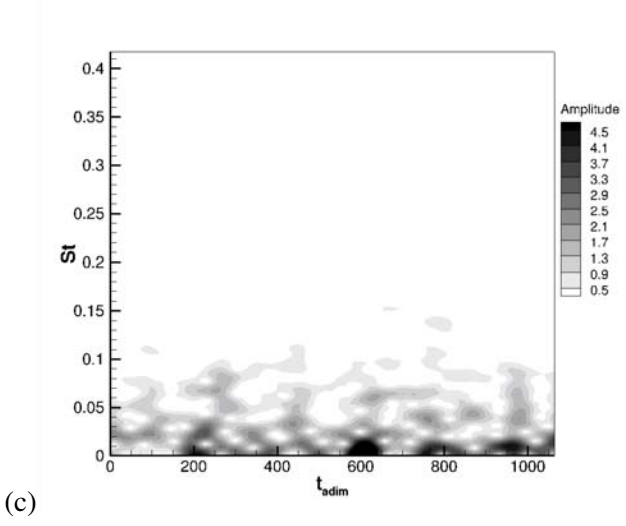

(c)

Figure 2.18: Temporal evolution of the frequency content recorded at the three probes identified in Fig. 2.5 (b): (a) Probe 1, (b) Probe 5 for the suction side of the blade and (c) Probe 9 for the pressure side (Case IIb of Table 2.3).

2.3.2 LES sensitivity analysis and impact on the flow predictions

Although of interest and very promising, the previous LES set of predictions underline few aspects and difficulties specific to this approach. Both LES strategies used here clearly improve the flow predictions when compared to RANS simulations (at least over the set of modeling options retained for this work). In particular and with proper mesh design, structured or unstructured LES are able to correctly reproduce the FST sensitivity of this highly loaded turbine blade thereby improving heat transfer predictions along the blade wall. Details on the actual sensitivity of the approach seem therefore recommended in order to fully identify the potential sources of errors added by the multiple parameters introduced in a LES of such flows. Specific aspects of such a list are discussed below to highlight the potential of the two proposed approaches and the importance of known characteristic flow to resolved/grid scales.

2.3.2.1 Sensitivity of LES to mesh extent, topology and grid resolution

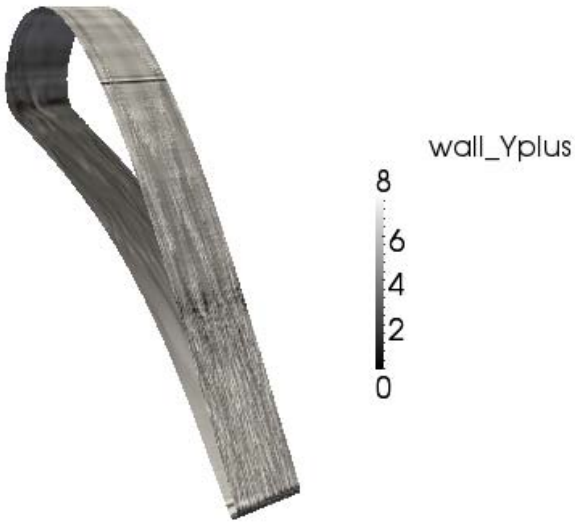

Figure 2.19: y^+ at the surface of the blade computed with unstructured LES.

For the structured approach, the minimum cell size is less than 2 μm all around the blade and in the wall normal direction (corresponding to a mean wall distance $y^+ \approx 1$). The wall normal expansion ratio used in this case is close to 1.05. Note that experimentally the $2D$ nature of the flow is confirmed and the number of points in the span-wise direction needed for RANS simulation is found not to be a critical parameter and can be reduced to only 2 points. For structured LES such procedures are clearly not applicable due to the unsteady and $3D$ nature of the resolved turbulence needed for this approach. Figure 2.20 (a) presents the evolution of the normalized wall distances $\Delta x^+, \Delta y^+$ and Δz^+

around the blade: the maximum value of y^+ being always below 2. In other directions, normalized wall distances are kept under acceptable values ($< \Delta z^+ >= 25$ and $< \Delta x^+ >= 150$).

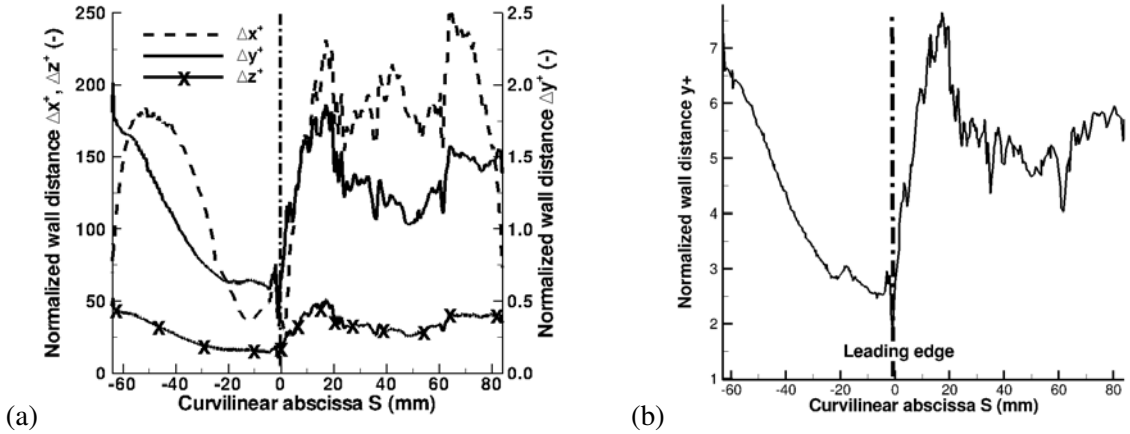

(a) (b)

Figure 2.20: (a) Normalized wall distances Δx^+, Δy^+ and Δz^+ for the structured *elsA* code (Case IIb) and (b) normalized wall distances Δy^+ for the unstructured AVBP code (Case IIIb).

To achieve a mean wall distance of $y^+ \approx 4$ with the unstructured solver without impairing on the simulation time step (explicit solver), the minimum wall cell size needed is approximately $8\,\mu$m yielding $\Delta t \sim 1.54\ 10^{-8}$s for an acoustic CFL condition of 0.7, as plotted in Fig. 2.19. In the case of the structured solver, the scheme is implicit and the used acoustic CFL is much less drastic. For the current structured solver LES simulations, a CFL of 25 is used yielding a time step of $1.2\ 10^{-7}$s. The unstructured meshes rely on 5 layers of prismatic wall cells described in Section 2.2.3.1. The aspect ratio of the prisms is at maximum equal to 4 in the x and z directions resulting in $< \Delta z^+ >= 16$ and $< \Delta x^+ >= 16$ (Table. 2.2 recapitulates all these constraints). Figure 2.20 (b) presents the wall resolution issued by the unstructured mesh. As expected and by construction, the overall shape of y^+ obtained on the unstructured mesh is in agreement with results of the structured mesh, Fig. 2.20 (a). Only the absolute value reached differs although they remain in agreement with the imposed characteristic scales of the different cell topologies. This comforts the ability of LES to produce the proper gross behavior of the boundary layer of the MUR235 case with the proposed schemes and mesh constraints.

In the previous validation, only the cell characteristic size is addressed and this irrespectively of the extent in the span-wise direction of the computational domain. The computational domain dimensions are chosen to limit the dependency of the solution to the inlet/outlet positions as detailed in Section 2.2.3.1 and the span-wise extent of the computational domain covers 10% of the vane span (*i.e.* 10 mm in the span-wise direction) in the previous set of results. Tests are introduced to better

evaluate the dependency of the MUR235 results to this parameter: they include a 20% vane span simulation keeping the same set of numerical parameters: *i.e.* twice the total number of points for the structured solver and twice the number of cells for the unstructured solver as well as a 5% vane span simulation. Both test (20% and 5%) are compared to the baseline 10% vane span simulation for the structured and unstructured simulations (references Cases II & III) whose meshes are detailed in the first part of this subsection and in Table 2.2 .

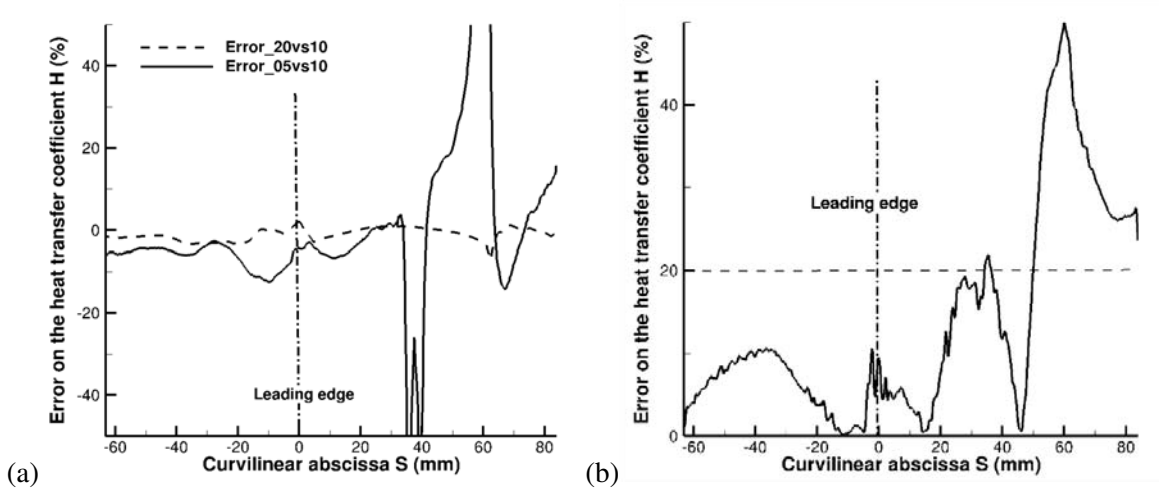

Figure 2.21: (a) Error on heat transfer coefficient, H when comparing a computation with 20% of the span to the baseline computation (10% of the span) and a computation with 5% to the baseline computation, for the structured solver and (b) Difference on the H coefficient when confronting results from Case IIIb to Case IIb, both taking 10% of the span.

Results obtained with the fully structured meshes are provided in Fig. 2.21 (a) for the mean wall heat transfer and confirm that considering a 10% or 20% span-wise extent does not affect the predictions. The error remains below 5% for all curvilinear abscissae. The same conclusion is reached with the unstructured solver underlying that the numerics of both solvers (implicit versus explicit) with the dedicated resolutions are efficient for this test case. It also emphasizes the fact that flow structures and the turbulence developing from these two sets of simulations are not constrained by the span-wise extent of the computational domain. The same conclusion is not validated when comparing the case with the span-wise computational domain of 5 mm (Fig. 2.21 (a)). This span-wise extent is clearly insufficient to achieve a correct simulation. Turbulence is too constrained and errors on the heat transfer coefficient reach locally values above 100% (near the transition point). Note that a 10% span-wise length corroborates preliminary results obtained by LES on a fully structured solver by Bhaskaran et al. [19] using a 11 mm thick domain.

In Fig. 2.21 (b) a direct comparison is done between the results of the unstructured approach (Case IIIb) and the structured analysis (Case IIb) for MUR235. On the pressure side, the differences, taking as a reference the structured solver, remain under 10% corroborating the analysis from Fig. 2.15 (b). The major discrepancy between the approaches is noticed after the pre-transition region, at $S = 62$ mm, where the transition is triggered. This difference could be explained by the shock capturing ability of the solvers and the SGS models behavior after the transition.

2.3.2.2 Sensitivity of LES predictions to FST

Figure 2.22: (a) Instantaneous wall flux at the blade surface.

Figures 2.23 & 2.25 show the instantaneous heat flux contours at the blade surface as in Fig. 2.22 but cutting the blade at its trailing edge and performing an auxiliary view of the plane. The MUR129 test case ($Tu_0 = 1\%, Re_2 = 10^6$ and $M_{is,2} = 0.84$) is the simplest test case to simulate since the boundary layers remain mainly laminar on both suction and pressure sides. No turbulence is imposed at the inlet when comparing with experimental data at $Tu = 1\%$. As illustrated in Fig. 2.12, the heat transfer coefficient H is well captured by both solvers on the appropriate meshes. In experiments, the leading mechanism in this configuration is the natural boundary layer transition triggered by Tollmien-Schlichting waves. As seen in Figs. 2.23 (a) & (b), the instantaneous boundary layer visualizations of heat transfer show the uniformity of the flow in the span-wise direction and on both sides of the leading edge. At S = 40 mm, acoustic waves impact the blade suction side, Fig.2.9 (a) or Fig.2.10 (a), as a consequence, local perturbations are visible at this position in Fig 2.23. These disturbances are, however, damped and it is the adverse pressure gradient at S = 62 mm which is responsible for the transition of the boundary layer. The two solvers show the same behavior for the MUR129 case.

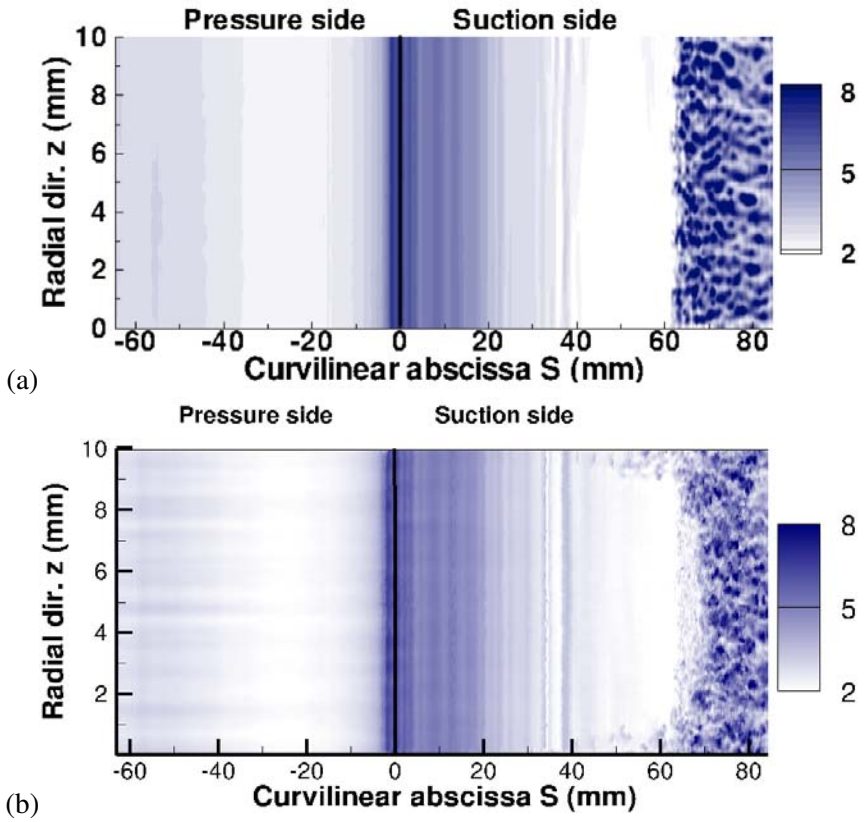

Figure 2.23: Instantaneous wall heat fluxes $q(W/cm^2)$ (a) Case IIa and (b) Case IIIa.

The MUR235 ($Tu_0 = 6\%, Re_2 = 10^6$ and $M_{is,2} = 0.927$) test case although very close to MUR129 is much more complicated especially because of the near wall dynamics that are greatly affected by FST. The triggering mechanisms are here twofold: (a) FST which interacts with the local boundary layer state and (b) the shock-boundary layer interaction on the suction side of the blade. Two parameters are needed to specify the turbulence injected at the inlet of the computation: Tu_0 and L_0. The data related to the FST intensity at the inlet has been measured in the experiments. However, no information on the turbulence length scale at the inlet is available. An exhaustive compilation of studies on the influence of Tu_0 and L_0 on the LS89 test case can be found in Liu [108].

In this particular analysis, to measure the influence of L_0, several simulations have been performed with both solvers for MUR235. Results obtained with the LES structured code are shown in Fig. 2.24 for L_0 = 1.5 mm, 3.5 mm and 8 mm for a 10% baseline vane span. On the pressure side, the increase of L_0 is responsible for a decrease of 30% of the heat transfer coefficient. On the suction side, turbulence modifies the transition point position, S_{trans} = 55 mm for L_0 = 1.5 mm and S_{trans} = 60 mm for L_0 = 8 mm (out of Fig. 2.24). No influence is noted after the transition point.

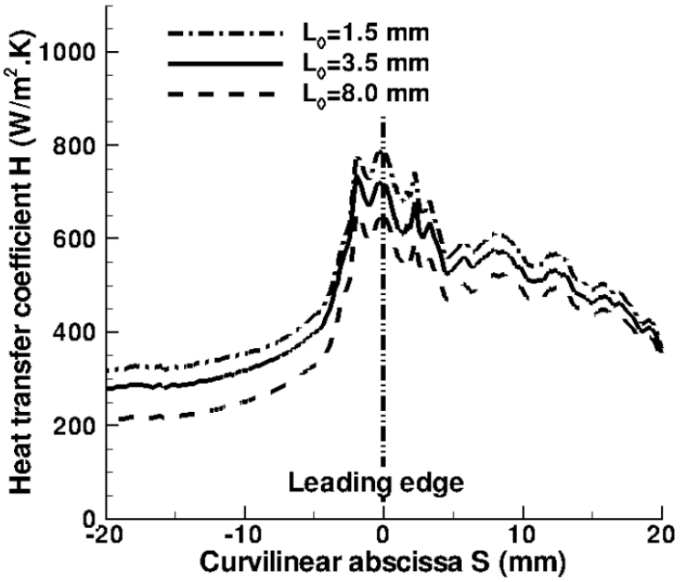

Figure 2.24: Effect of the inlet turbulent length scale L_0 on the wall heat transfer coefficient H on the leading edge area predicted with structured LES (Case IIb).

In the MUR235 case, the flow topology has the same behavior for both solvers leading to the results of Fig. 2.15 (b) and as shown in Fig. 2.25, which presents similar views as in Fig. 2.23 but for Cases IIb & IIIb (MUR235). The turbulent eddies coming from the main upstream flow and imposed in the simulation by use of the synthetic turbulent injection model, Fig. 2.7, and Eq. (2.11), impact the leading edge of the blade, $S = 0$ mm. The future of these vortices from the leading edge around the blade involves first stretching of the initially isotropic structures and interactions with the local boundary layer flow. These complex interactions yield streaky structures originating from the stagnation flow region present at the leading edge and clearly visible in Fig. 2.25 in both LES's. This flow response explains the local heat transfer increase noticed previously for MUR235, differentiating it from MUR129. Note that the relative size of the incoming turbulent structures to the local boundary layer thickness is probably of critical importance for a proper evaluation of the heat transfer rate along the blade (as already pointed out in Fig. 2.24).

On the suction side, $S > 0$, for both the structured and unstructured strategies, the vortices are rapidly distorted and eventually damped out by the accelerating flow issued by the strong curvature of the blade. At $S = 20$ mm, only elongated structures of span-wise size proportional to the incoming turbulent scales are present in both the structured and unstructured predictions. After this point, vortical stream-wise vortices eventually break-down and turbulent spots develop in the boundary layer (20 mm $< S <$ 50 mm) of the structured and unstructured solutions and as seen in White [189]. This wall behavior combined with the local adverse pressure gradient yields a slower decrease of the heat

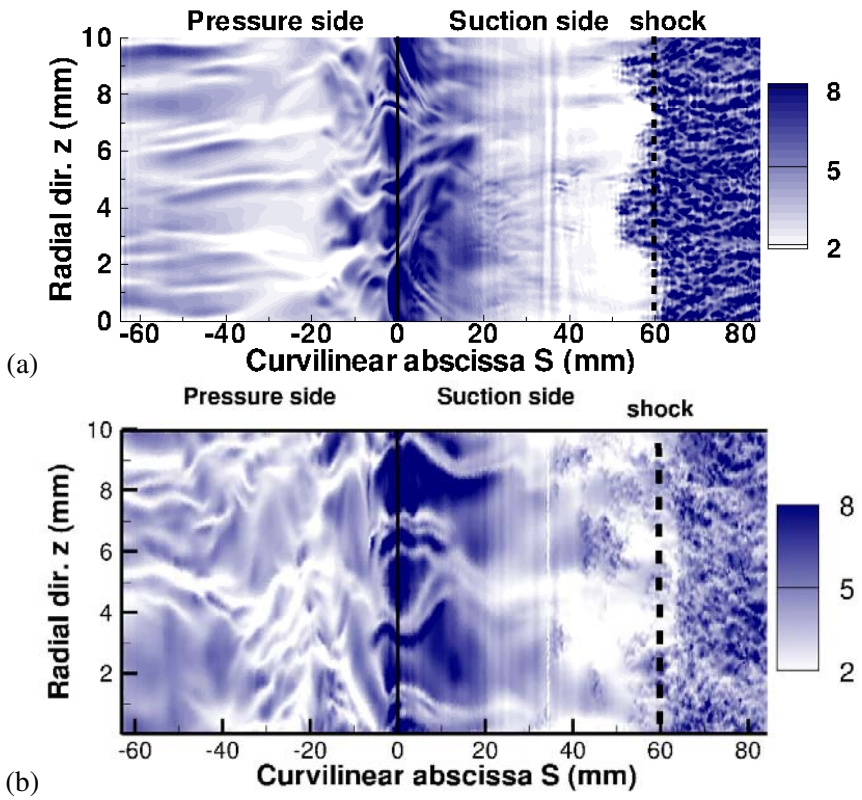

Figure 2.25: Instantaneous wall heat fluxes $q(W/cm^2)$ computed with LES for MUR235 with (a) structured and (b) unstructured LES solvers.

flux at the wall compared to MUR129 and it is only slightly prior to $S = 62$ mm (shock location) that a massively turbulent boundary layer appears. Although the overall dynamics is equivalent in the two LES's, subtle differences appear between the two predictions resulting in a slightly delayed transition point with the unstructured LES solver: the wall flow becomes fully turbulent slightly before the shock at $S = 55$ mm for the structured LES and at the shock for the unstructured LES method. A critical point underlined by such differences (aside from the proposed numerical approaches) is the dependency of such flow predictions to the characteristic length scale of FST as already anticipated by Fig. 2.24.

On the pressure side, the initially generated flow structures appearing at the leading edge orient with the main flow stream-wise direction, mainly because of the favorable pressure gradient in this zone. Further downstream, $S = -20$ mm, the local blade curvature may be at the origin of Görtler like vortices [154] and a clear rise of the wall heat transfer is observed because of the perturbation of the thermal boundary layer in agreement with experimental findings. Observations apply for both the structured and unstructured LES's with similar conclusions as for the suction side.

Conclusion

This part of the thesis describes the investigations made about the prediction of wall heat transfer in a highly loaded turbine guide vane with RANS and two LES approaches (structured and unstructured). The effect of inlet turbulence on heat transfer and boundary layer development has been studied at two different flow operating conditions ($M_{is,2} = 0.840/0.927$, $Re_2 = 10^6$, $Tu_0 = 1/6\%$).

First, the results analyzed show that the RANS approach (coupled with a transition criterion) is effective in predicting wall heat transfer when the boundary layer transition does not play a major role and it remains efficient in terms of computational resources. However, when the wall flow patterns depend on the main vein turbulence or from the inflow specification, RANS methods lack predictive capability. The adoption of a transport equation for the transition criteria helps to partially overcome this problem although RANS procedures are still not capable of predicting the significant effect of turbulent structures when no transition of the boundary layer is present.

Second, the study has revealed that LES can take into account the effects of FST in the wall region. Both structured and unstructured approaches are very promising methods, especially when an accurate description of the boundary layer transition is necessary. The simulated blade isentropic Mach number distribution and heat transfer coefficient show a very good agreement with the experiments of Arts et al. [10]. While LES still requires a very large computational power (a 30M points grid is necessary to represent only 10% of the vane span), this method is able to describe natural as well as by-passed transitions. Not only regarding mesh size, but also for CPU needs is LES much more costly than RANS simulations: by a factor of approximately 6,000 for the meshes of Table 2.2. The main reasons are of course mesh requirements and formalisms: RANS simulation only costs 0.3 CPU hours ($\sim$15 CPUh for a full 3D simulation) to reach convergence. The simulation of 10 through-flow times for the structured LES solver requires $90,000$ CPU hours for the same state, Table 2.4. Note also that 10 through-flow times is the time necessary to converge statistical quantities of the flow. The equivalent cost with the fully unstructured approach yields $140,000$ CPU hours.[1]

[1] All numerical simulations are performed on a SGI Altix computing platform.

	RANS structured	**LES** structured	**LES** unstructured
CFL	20	25	0.9
Time step	NA	$1.2\ 10^{-7}$s	$1.54\ 10^{-8}$s
CPU cost	t_{RANS}	$\sim$6000 t_{RANS}	$\sim$1.5*6000 t_{RANS}

Table 2.4: Temporal parameters and CPU cost comparison for all the approaches for MUR235.

This work has also detected by use of two different solvers the presence of streaky structures on both blade sides. These structures are responsible for the intensification of heat transfer on the blade surface. Stretching of vortices from the inlet turbulence around the leading edge and the following transport of these vortices into the blade passage produce these boundary layer streaks. Around the leading edge, these streaks cause an increase of the laminar heat transfer. This phenomenon can also be observed on the pressure side. Note however that the suction side is less sensitive to inlet turbulence. The present analysis also unveils the influence of the FST energetic length scale on the heat transfer coefficient, issues that have since then been more deeply investigated in the context of quantification of uncertainties [64].

Furthermore, it has recently been illustrated by Wlassow [191] that the FST has also a major impact on the heat transfer of RANS simulations in real industrial engines (pages 133-135 of his dissertation). In his manuscript, FST is classified among the most important factors to take into account when predicting the blade temperature. Surprisingly, in todays industrial procedures, the FST level is set at the inlet of the turbine stage arbitrarily without taking into account the FST coming from the upstream combustion chamber.

Heat predictions with LES are not currently feasible in a whole turbine stage principally because of the colossal number of points needed and CPU cost, as pointed out before, but also because no clear method emerges in LES to treat the stator/rotor interface. Nevertheless, an alternative solution must be found to get the maximum information from the upstream LES computation of the combustion chamber to feed the downstream RANS computation, since the final goal pursued in industry is to improve the physics the rotor sees.

The first step is to succeed in the LES resolution of the combustion chamber with the turbine Nozzle Guide Vane (NGV). The feasibility of the LES simulation of a fixed blade has just been demonstrated in this part by both structured and unstructured context. The combustion chamber + NGV computation and the conclusions drawn from it are presented in Appendix A. The main findings are that the flow prediction in the NGV is improved compared to RANS simulations if the mesh is

sufficiently fine since the FST level is taken into account implicitly in the NGV sector, but also that the inclusion of the NGV has a notable influence on the combustion chamber exit profiles because of its potential effects.

The second step is the implementation of a coupling strategy between LES and RANS codes. *In fine*, this PhD proposes to develop a method that could be applied in industrial problems to achieve a coupled computation of

- ◇ a LES resolution of the combustion chamber + NGV,
- ◇ a structured usual RANS computation of the turbine stage (NGV + rotor).
- ◇ with the NGV present in both computations.

The second part of this manuscript deals with the development of this zonal LES/RANS coupling strategy.

Part II

Towards multi-component simulations

Introduction

As mentioned in the conclusions of the first part of this manuscript, the industrial community is longing for a CFD solution that can treat the multi-component aspect in their simulations. Before beginning the next chapter, let's remind briefly some of the reasons why we do need to couple LES and RANS codes to simulate the combustion chamber and the turbine stage. The answer is of twofolds.

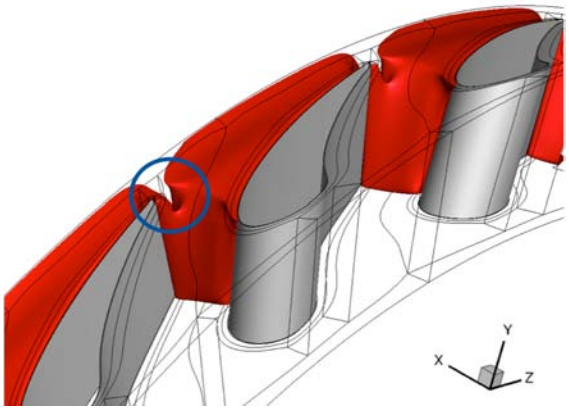

Figure 2.26: Mach=1 iso-surface in the NGV vein passage. The vein is not totally blocked.

First, performing a multi-component simulation is compulsory as there is an interaction between the combustion chamber and the turbine stage. Indeed, if an iso-surface of Mach equal to one is plotted in the high-pressure Nozzle Guide Vane (NGV) of a aeronautical engine, a zone near the shroud where the flow is subsonic can be identified in Fig. 2.26. Thus, a multi-component simulation between the combustion chamber and the turbine is needed since information will travel both ways and two separate calculations will never be able to capture those synergies without interacting. This means that the information exchange has to go in both, downstream and upstream directions.

Second, one could ideally think of doing all the computation with only one solver. The solver that is usually employed for TURBOMECA applications in combustion chambers is AVBP [164] and the one used for turbine applications is *elsA* [32]. However, *elsA* is not capable of taking into account the species reactions and can not be used in the combustion chamber. AVBP, suited for combustion problems, is not prepared to evolve in a turbine stage as the unstructured solver lacks of a methodology

to treat the stator-rotor interface. Even so, the wall refinements needed to resolve properly the wall behavior are scarce and no clear answer emerges to retain LES as a solution in the turbine realistic industrial applications, at least not in the rotor. Each solver being suited for a specific component, the zonal coupling dawns as the solution for the multi-component simulations we need to perform.

Interest in zonal LES/RANS code coupling for industrial applications for GT engines began with the ASCI project within which Stanford started to search a zonal coupling in the 2000s. After some years of developments of the coupling platform and test cases validation [162], Stanford researchers did in 2007 the first and, until now, the sole unsteady simulation of an entire engine with LES/RANS coupling. Their simulation relies on unsteady RANS simulations for compressor/turbine and incompressible LES for the combustion chamber [120]. A simple time-average of the velocity provides a mean velocity at the inlet of the RANS domain. This velocity distribution is highly non-uniform which allows to describe turbulence at the inlet with the local turbulence generation from the mean velocity. They propose to use an auxiliary duct in which the RANS turbulence model equations are solved for the transferred mean velocity. In an industrial case, the mean velocity from the combustor outlet is passed to the duct and the equations for k and ω are iterated until convergence for a frozen mean flow. Finally, the mean velocity from the combustor and k and ω from the duct are passed to the turbine inlet. This produces an inflow boundary condition for the RANS domain that is consistent with the RANS turbulence model used. However, this method, retained by Stanford to compute combustion chamber/turbine interactions, does neither have any feedback from RANS to LES nor physical consistency of pressures between the compressible and incompressible solvers. The body force applied in their test cases is not used in the full engine application [161]. Furthermore, no mathematical justification is given for the methodology employed by the authors to assure the convergence of the solution. In this thesis, both these points will be addressed but will clearly need more analyses.

This part of the dissertation is arranged as follows:

- ◇ Chapter 3 presents the philosophy of the methodology proposed, that is a domain decomposition method. Inflow and outflow conditions and solvers synchronization, as well as other coupling aspects treated in this thesis are also detailed in this Chapter.
- ◇ Chapter 4 deals with the mathematical justification of the coupled procedure in a 1D simplified scheme giving some insights of the way one should couple to reach convergence, among other things. A numerical 1D toy illustrates some of the findings of this Chapter.
- ◇ The different test cases used to validate the methodology are detailed in Chapter 5. They are representative of the physics that can be found in real turbomachinery and serve to evaluate the coupling approach proposed.
- ◇ The last chapter gathers the major conclusions drawn from this study.

3

Coupling methodology

Contents

In 1870, Schwarz published an iterative method to solve simple problems relying on Partial Differential Equations (PDE) [165]. He proposed to divide the initial problem in subdomains. The global solution is obtained by solving iteratively the subproblems in each subdomain and exchanging the solution obtained by the neighbor subdomains. It was not until the 80s that P. L. Lions [107] promoted the use of the overlapping Schwarz methodology in the numerical resolution of PDE problems by using the increasing computing power and parallelization of tasks as can be seen in Fig. 3.1. A complete overview of the different decomposition methods is proposed in Balin [12]. To simplify, only the two major trends in Domain Decomposition Methods (DDM) are presented here. There are of two types:

- ◇ subdomains without overlap: the intersection between the subdomains is only at the boundaries, Fig. 3.2 (a), where $\Omega_1 \cap \Omega_2 = \partial\Omega_1 \cap \partial\Omega_2$.
- ◇ subdomains with overlap: each subdomain covers a part of the neighboring subdomain as plotted in Fig. 3.2 (b), where $\Omega_3 = \Omega_1 \cap \Omega_2$.

In this thesis, only the overlap technique is considered, although it could be of interest to have Ω_3 go to zero so one obtains the non-overlapping contact.

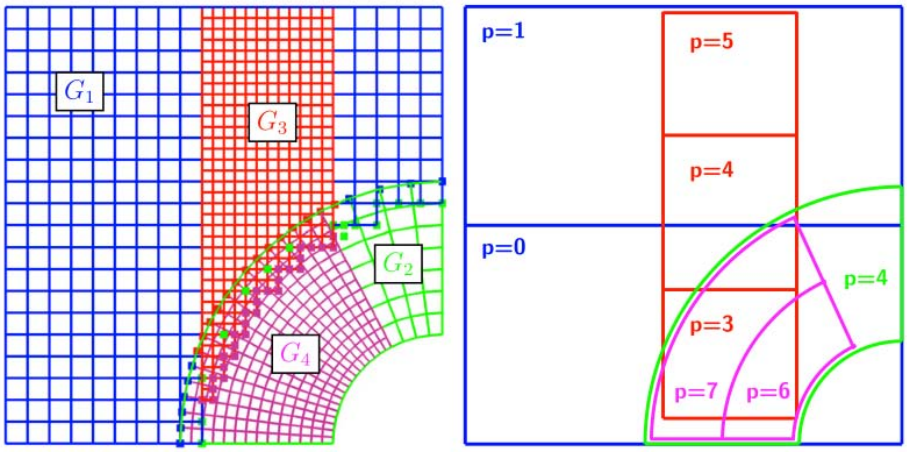

Figure 3.1: Each base grid can be distributed over a contiguous range of processors. In this example the base grid G1 is distributed over processors [0, 1], the base grid G2 over processor [4], the refinement grid G3 over processors [3, 4, 5] and the refinement grid G4 over processors [6,7] from Henshaw & Schwendeman [74].

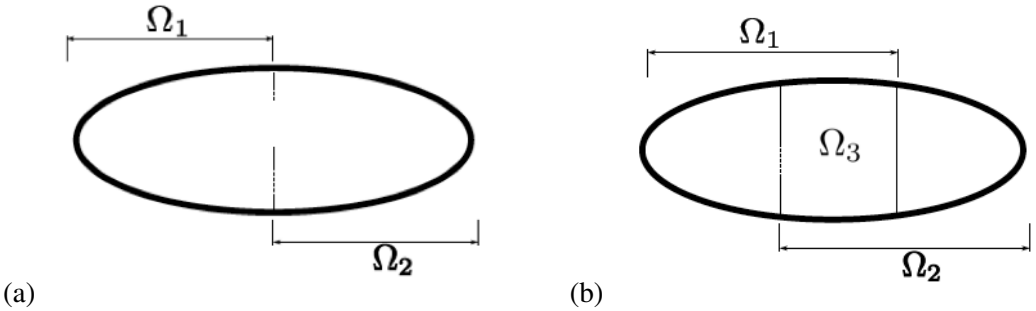

Figure 3.2: (a) DDM without overlap and (b) DDM with overlap.

Simultaneously to the development of DDM in the mathematical field, another procedure upraised in the fluids mechanics community, the Chimera method, also called the overset grid method in the literature [17]. Historically, the fluids mechanics field went from non overlapped domains (parallel computations) to overlapped domains, as in the Chimera technique. Overset grid methods were born originally to diminish the mesh generation difficulties in structured grids. Chimera is a variant of the Schwarz algorithm used in CFD to ease the meshing of complicated objects as in Fig. 3.3. The mathematical formulation of Chimera is presented for a 2D Laplace problem in Brezzi *et al.* [28].

Numerically, the method transfers the solution from overlapping grids through interpolation. The Chimera method is implemented in the *elsA* solver and has widely been applied to industrial configurations. An exhaustive synopsis on Chimera technique, its origins and applications with *elsA* solver

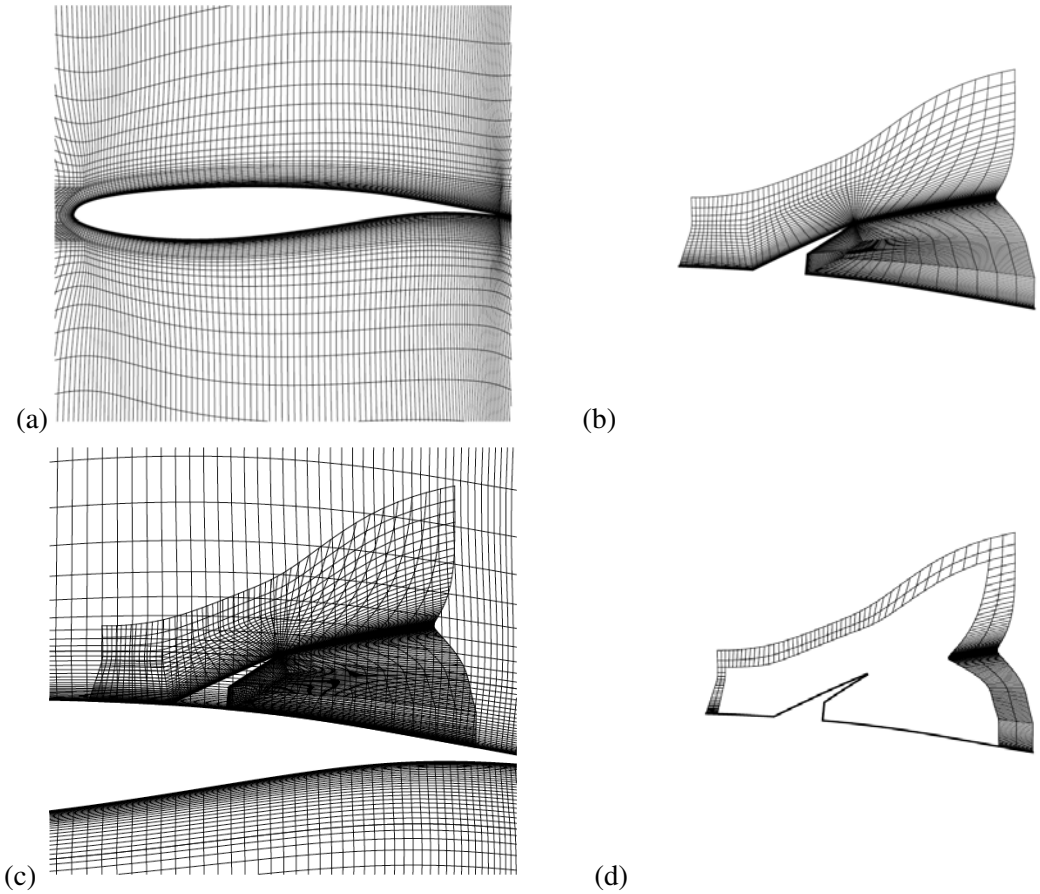

Figure 3.3: Illustration of the use of Chimera for aerodynamic computations [22]: (a) mesh of the wing, (b) mesh of the flap, (c) cells of the wing mesh inside the flap mesh and (d) cells whose values are calculated by interpolation in the flap mesh.

is available in Blanc [21]. The fact that the Chimera scheme does not satisfy a global discrete conservation property has been labeled as the source of anomalies observed in some utilizations. Keeling *et al.* [89] introduce a new mathematical framework within which Chimera schemes can be properly analyzed to study such loss phenomena. Particularly, it can be noticed that dissipation problems can occur if a mesh is drastically de-refined in a single domain computation and does not come exclusively from domain decomposition.

The current chapter describes the framework for the DDM/Chimera based execution of RANS and LES flow solvers. The portray of the RANS and LES flow solvers has already been done in Chapter 2 and Appendix D, the first question to answer in this chapter is what makes the coupling presented in this thesis different from other LES/RANS coupling strategies:

◇ Two different codes are used, an unstructured LES solver and a structured RANS solver.

◇ Not only is the RANS solver compressible but so is the LES code.

◇ There is a feedback from the RANS computation to the LES computation.

This two-way exchange avoids reducing the problem to standard LES computation, where the RANS solution is computed *a priori* and only serves to provide a boundary condition to LES. The implementation of our two-way coupling technique needs also to define:

◇ the spatial coupling, where the information is exchanged,

◇ the nature of the physical quantities transmitted,

◇ the synchronization of the coupling system.

Each of these points will be treated hereafter.

3.1 Domain decomposition targeted

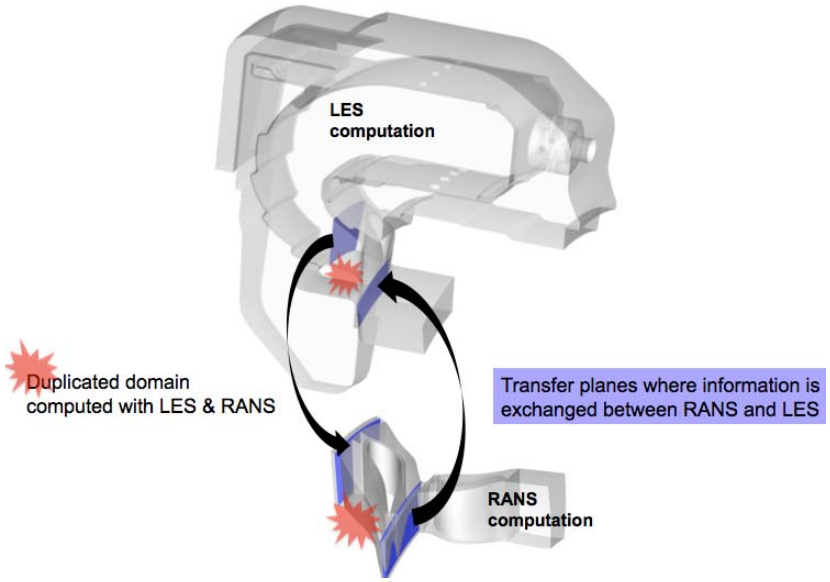

Figure 3.4: LES and RANS coupled computation of the combustion chamber/turbine in a real engine: the solvers run simultaneously and exchange only the necessary information at the interfaces: the nozzle guide vane is computed in both LES and RANS.

In this thesis, the LES domain is always upstream of the RANS domain because of the specific application. The RANS domain receives flow data from the LES solver to define its inflow boundary conditions. In return, the upstream LES solver has to receive flow information from the downstream RANS flow solver. This last step is necessary in order to take into account the influence of the

downstream flow development on the flow in the LES domain. The strategy chosen after the study of the state of the art is to couple LES and RANS exchanging information at specific planes. An overlap region will be computed by each solver, i.e, in the final industrial application, the nozzle guide vane (NGV), could be simulated by both AVBP and *elsA*, in LES and RANS, respectively as shown in Fig. 3.4. With such a decomposition, mean values of the flow computed by AVBP before the NGV should take into account the potential effects of the downstream stator computed by *elsA*. For more information on the computation of a combustion chamber + NGV in LES, one can refer to Appendix A. Note that no longer will there be an average in the azimuthal direction in the plane that will serve as inlet condition for the *elsA* computation. In addition, the outlet of the AVBP combustion chamber + high pressure NGV computation will be set by the information extracted from the middle of the *elsA* computational domain, in a plane between the stator and rotor. The potential effects from the NGV and rotor would be taken into account by the AVBP flow, whereas in todays computations the pressure is constant at the outlet plane. In this thesis, the aim is to implement a DDM to be used on non-conforming overlapping grids that can serve, when validated, to solve highly complex configurations. In a generic form, this DDM can be pictured as in Fig. 3.5.

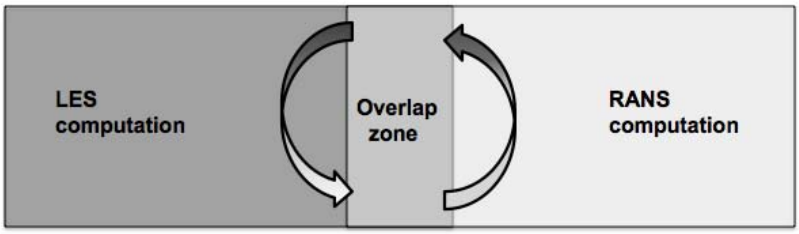

Figure 3.5: Schematic DDM proposed in this thesis, an identical illustration of this method is plotted in Fig. 3.2 (b) .

The goal of such a zonal coupling is to compute all models in their own regime of validity: steady RANS for flows with stationary statistics and unsteady LES where it is needed. Even though one can choose the best suited method for each subdomain without considering their compatibility, inappropriate coupling conditions can lead to contamination of the results in the LES or RANS subdomains. As a consequence, an effort is needed for implementing complex coupling conditions. Depending on the type of the interface illustrated in Fig. 3.5, the requirements on the coupling conditions differ. Indeed, a domain decomposition method is defined not only by the geometric criteria by which the global domain is partitioned, but also by the information which is transferred between subdomains. Since the LES will be always placed before the RANS domain, as pictured in Fig. 3.5, the definition of the the nature of the physical quantities transmitted is equivalent to establish the RANS inflow and LES outflow conditions.

3.2 Physical quantities transmitted

3.2.1 RANS inflow data specification

The construction of boundary conditions for RANS from LES data is quite straightforward and has been used on multiple occasions [57, 161, 191]. The LES data can be averaged over time and used as boundary conditions for the RANS solver (at least for the first moments). A temporal classical average can be performed in the LES computation, at each time step the flow field from LES participates to the average field computation. This method needs an adaptation time linked to the average statistics convergence of the LES fields. For turbulent flows, the average statistics of LES results can also be used as inlet conditions for the turbulent model variables (higher order moments) although care is necessary [120]. In this thesis, a sliding average is performed when needed. More details about the time averaging technique can be found in Sections 3.3 and 5.4.

A general method for downstream coupling with a sharp interface was devised by Von Terzi & Fröhlich [180]. For the velocity coupling, the explicitly Reynolds-averaged velocity field of the LES domain is imposed as a Dirichlet condition for the RANS inflow boundary. In this thesis, the choice has been to interpolate onto the first two rows of the downstream subdomain mesh all the conservative variables plus the two turbulent variables, when needed. The downstream solver uses this information to update its residuals computation in the nearby row. This method can be understood as a one-way Chimera, since the feedback is done at the other end of the overlap zone. The extension of the two rows to be interpolated from the upstream region is set for reasons of compatibility with the numerical scheme, as shown in Fig. 3.6, and the need to impose information in a weak form (i.e. fluxes and not hard conditions).

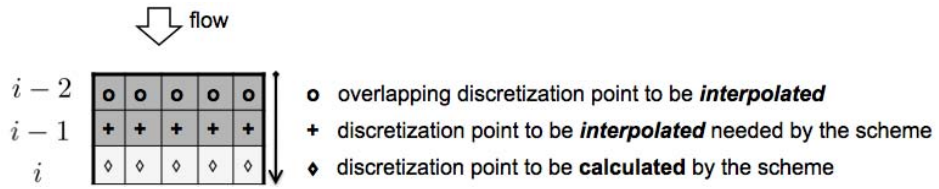

Figure 3.6: Two rows to be interpolated from the upstream subdomain to the downstream subdomain for a 5 points scheme in the downstream domain.

In agreement with the Chimera technique implemented within *elsA*, the zone of transfer in the vicinity of an overlapping boundary must be extended so that the numerical stencil of the discretization applied to the boundary interface is complete. For a simple numerical stencil, the extension must take place in the direction perpendicular to the boundary and to a discretization point layer count deduced from the number of points of the numerical stencil in one direction. For example, no extension

for a scheme with 3 points in a topological direction whereas an extension to 1 layer is needed for a scheme with 5 points in a topological direction. Since a 5 points scheme is used in all the applications of this thesis, deduction of the points to be interpolated in the vicinity of an overlapping boundary in a direction is pictured in Fig. 3.6: two rows ($i-2$ and $i-1$) should be interpolated, the third (i) being calculated by the downstream scheme. In this case, the downstream code uses the variables in the first two rows to advance its scheme. The information in these two rows has been interpolated from the cells of the upstream domain. Fig. 3.3 (b) also shows the two rows of cells which are receiving the interpolated values. It goes without saying that the conservativity of this approach directly relies on the interpolation method [84, 175]. We use a linear interpolation. According to Henshaw [75], for the resolution of a time-dependent and elliptic equation with a second order numerical method, a linear interpolation is sufficient between the subdomains for the errors to go to zero.

3.2.2 LES outflow data specification

LES delivers a time-dependent solution but RANS simulation can only provide mean values. Therefore, the role of the outflow interface is to allow for mean flow information to propagate upstream and for the fluctuations to leave the LES domain without too much reflection. As stated by Schlüter *et al.* [163], a natural choice to ensure the transfer of information from the downstream domain to the upstream domain would be to prescribe the outflow pressure distribution. However, the ASCI researchers could not adopt this method as in their project the LES solver was a low-Mach number incompressible code. As a consequence, the pressure evolution is determined by a Poisson equation where its magnitude adjusts to the velocity field. This formulation makes it impossible to prescribe the pressure of a compressible code at the outlet of the LES domain directly, since it is not coherent with a divergent free velocity field. Instead, only the velocities or their derivatives can be specified as boundary conditions in the LES flow solver, the pressure adjusts accordingly. In their approach, the mean velocity profiles are enforced by adding a virtual body force to the right-hand side of the momentum equations inside the overlap region of the computational domains of the LES and the RANS flow solvers [159]. More information and mathematical analysis on full convective outflow conditions for LES can be found in Fröhlich & Von Terzi [57].

For any RANS zone downstream of a LES zone, the desired task from a hybrid LES/RANS coupling at an outflow type interface is to propagate mean flow information upstream. In this thesis and contrarily to the ASCI project, two compressible codes are used so the choice is done to give an information on pressure through the LES outlet boundary condition as will be detailed below. Boundary conditions are of paramount importance in a compressible LES computation because the concept is unsteady by nature and includes also acoustic waves. For this reason, characteristic boundary conditions were proposed by Poinsot & Lele [141] (NSCBC approach). This method is an extension of the

characteristic decomposition of the Euler equations to viscous flows and allows to define waves that can directly be acted upon by the boundary condition. There are several ways to impose boundary conditions in the discretized equations. Considering a simplified form with a single step time advancement, where $\mathbf{U}_j^n$ is the vector of conservative variables on the node j at the time step n, the hard way to impose Dirichlet boundary conditions is to replace the flow variables predicted by the scheme for the time step $n+1$ by the imposed value at the nodes located on the domain boundary $\partial\Omega$:

$$\mathbf{U}_j^{n+1} = \mathbf{U}_j^n - \frac{\Delta t}{V_j}\left(d\mathbf{U}_j^n\right)_{\text{scheme}} \qquad \forall j \in \{\Omega \setminus \partial\Omega\} \tag{3.1}$$

$$\mathbf{U}_j^{n+1} = \left(\mathbf{U}_j^{n+1}\right)_{\text{BC}} \qquad \forall j \in \{\partial\Omega\} \tag{3.2}$$

For Neumann boundary conditions, the correction is applied after the calculation of the fluxes. The boundary condition is used to determine a corrected nodal residual $d\mathbf{U}_j^n$ that replaces the residual predicted by the scheme before advancing the equations in time to obtain a new vector of flow variables $\mathbf{U}_j^n$:

$$\mathbf{U}_j^{n+1} = \mathbf{U}_j^n - \frac{\Delta t}{V_j}\left(d\mathbf{U}_j^n\right)_{\text{scheme}} \qquad \forall j \in \{\Omega \setminus \partial\Omega\} \tag{3.3}$$

$$\mathbf{U}_j^{n+1} = \mathbf{U}_j^n - \frac{\Delta t}{V_j}\left(d\mathbf{U}_j^n\right)_{\text{BC}} \qquad \forall j \in \{\partial\Omega\} \tag{3.4}$$

This last method is used in AVBP for the non-characteristic application of Neumann boundary conditions directly on conservative variables but also for the characteristic boundary conditions (Dirichlet and Neumann type) that modify the residual at the boundary nodes. The concept of characteristic boundary conditions is the following: waves that are leaving the domain are well computed by the numerical scheme, they only contain upwind information, and must be left unchanged, while waves entering the domain cannot be computed by the numerical scheme, they transport downwind information, and must therefore be replaced by user-defined values. These values are given in AVBP by the physics of the boundary conditions [141]. The number of waves imposed for an inlet or an outlet is justified by Table 3.1 (Chapter 9 of [142]) and coincides with the number of waves traveling in the exiting or entering directions at the considered domain boundary.

Implementing boundary conditions directly from waves corresponding to the full Navier-Stokes equations is far too difficult. The aim of this section is to show theoretical developments on the well known conservative form of Euler equations, which are treated using the characteristic theory in AVBP. The extension to Navier-Stokes equations is then done according to the NSCBC principles leaving viscous terms apart. To look in more detailed to the passage from Navier-Stokes equations to characteristic form, one can refer to Nicoud [132]. To summarize,

$$\partial W = L_U \partial U \tag{3.5}$$

Boundary type	Euler	Navier-Stokes
Supersonic Inflow	5	5
Subsonic Inflow	4	5
Supersonic Outflow	0	4
Subsonic Outflow	1	4

Table 3.1: Number of physical boundary conditions required for well-posedness (3D flow) [142].

where L_U is the matrix to pass from conservative variables to characteristic variables (U stands for the conservative variables and W for the characteristic variables). The associated propagation velocities are:

$$\begin{pmatrix} \lambda_1 \\ \lambda_2 \\ \lambda_3 \\ \lambda_4 \\ \lambda_5 \end{pmatrix} = \begin{pmatrix} u_n + c \\ u_n - c \\ u_n \\ u_n \\ u_n \end{pmatrix} \tag{3.6}$$

where u_n and c are the normal velocity and the speed of sound, respectively. For an acoustic wave traveling upstream of a subsonic outflow boundary condition, ∂W^2 (superscript ^{2} because it is the second component) is the acoustic wave of interest.

To build the boundary condition, the explicit time advancement scheme of AVBP leads to the predicted value U^{n+1}_{pred} :

$$\partial U = U^{n+1}_{pred} - U^n = -\mathcal{R}^P \Delta t \tag{3.7}$$

The total residual $\mathcal{R}^P$ can be split into two parts :

$$\partial U = -\Delta t(\mathcal{R}^P_{BC} + \mathcal{R}^P_U) \tag{3.8}$$

$\mathcal{R}^P_{BC}$ which will be modified by the BC treatment and $\mathcal{R}^P_U$ will be left unchanged. The objective of the BC treatment is to construct the final value of U at time $n+1$: U^{n+1}

$$U^{n+1} = U^n - \Delta t(\mathcal{R}^C_{BC} + \mathcal{R}^P_U) \tag{3.9}$$

where $\mathcal{R}^C_{BC}$ is the part of the residual which has been corrected using $\mathcal{R}^P_U$, U^n, the type of boundary condition and the target values. More details about all the methods to determine $\mathcal{R}^P_U$ can be found in Nicoud [132]. The follow-on question lies in the evaluation of the different waves in the spatial formulation, which is the initial form of the NSCBC method [141]. The ∂W are obtained from spatial gradients:

$$\partial W = -\lambda \frac{\partial W}{\partial n} \Delta t \tag{3.10}$$

where λ is the vector containing the eigenvalues, i.e. the propagation speed of the waves as previously defined in Eq. (3.6). This means that the variations of characteristic variables in the spatial formulation are proportional to normal gradients of variables (true for a 1D problem). Following the development of Poinsot & Lele [141] we can introduce the $\mathcal{L}$ notation:

$$\mathcal{L} = \lambda \frac{\partial W}{\partial n} \tag{3.11}$$

As a consequence, defining $\mathcal{L}$ through the boundary condition allows to retrieve ∂U with the combination of Eqs. (3.5), (3.8) and (3.10). The acoustic behavior of a subsonic outlet is easy to study as only one wave is imposed in the characteristic formalism employed in AVBP. Three main behaviors are possible at the outlet:

- ◇ If the amplitude of the wave going upstream is zero, which is the same that imposing $\mathcal{L}_2 = (u_n - c)\frac{\partial W^2}{\partial n} = 0$, the boundary is fully non reflecting. A downside of this method is that pressure drifts may occur.
- ◇ To elude this drawback, a relaxation can be added whose function is to drive the pressure towards a user defined target value, P^t. In this case:

$$\mathcal{L}_2 = \theta(P - P^t) \qquad \text{where } P \text{ is the state pressure.} \tag{3.12}$$

  Non zero values of the relaxation parameter, θ, lead to partially reflecting boundaries. θ may be chosen as small as possible when wanting to avoid acoustic reflections by the boundary since the relaxation acts as a low-pass filter [167].
- ◇ The last solution is to impose directly the pressure outlet in a totally reflecting way. The incoming wave will be determined both by a pressure difference as previously, but also by the outgoing wave.

In this thesis, the choice is done to use the second type for our LES solver, a relaxed type of outlet boundary condition. However, by this definition, the incoming wave is independent of the outgoing wave, which is the definition of a non-reflecting boundary condition. As both solvers are compressible, the nearby downstream computation can be used to determine the amplitude of the wave reflected at each point of the LES boundary condition. As it has been coded for this particular coupling process, one has $P^t = P_{elsA}$, where P_{elsA} is the *elsA* local time averaged (in a RANS sense) pressure.

3.3 Synchronization of the coupled solvers

Two strategies can be imagined for a coupled application depending on the necessity or not to make both solvers coincide in physical time. Let's call T_1 the time the Solver 1 advances in time between two updates of the boundary values and T_2, the same quantity for Solver 2. Two cases are of interest:

- $T_1 \neq T_2$, the two solvers are not synchronized in physical time,
- $T_1 = T_2$, the two solvers are synchronized in physical time.

f_{cpl} is called the coupling synchronization frequency. It is how often the boundary conditions are updated. Another aspect to take into account is that in a parallel machine, codes may run together or sequentially. Fig. 3.7 shows how the transmission conditions previously defined in Section 3.2 are exchanged in a sequential procedure, also called staggered coupling. At synchronization step k_{cpl} of the solvers, after a physical time T_1, Solver 1 provides $\mathbf{U}_1^{k_{cpl}}$ (corresponding to two rows of conservative variables) to Solver 2, which then starts and runs for T_2 and sends back pressure $P_2^{k_{cpl}}$.

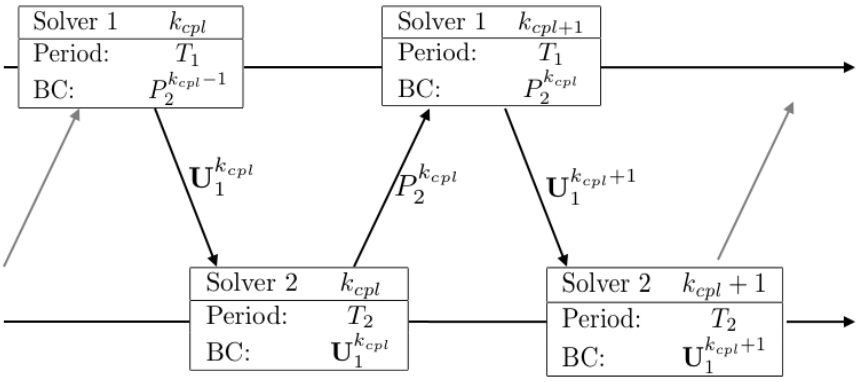

Figure 3.7: Sequential coupling strategy.

On the contrary, in the parallel approach, both solvers run simultaneously and exchange information at the user-defined frequency. The information given from one code to the other at the step k_{cpl} is used to run each solver during a common period of time until next *rendez-vous*. The parallel approach is pictured in Fig. 3.8.

Most existing applications that use the sequential procedure are based on steady state in one side of the coupled problem [187]. On the contrary, as explained by Duchaine *et al.* [46], the use of the parallel approach is usually devoted to the analysis of transient or fully unsteady phenomena. Even if this particular aspect of the coupled LES/RANS is not the main aim of this thesis, the development (from a computing point of view) of a parallel procedure has been included to allow further studies in this direction.

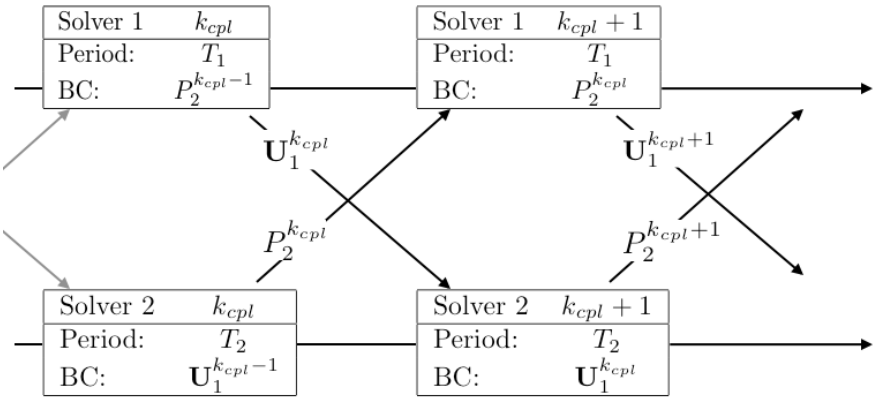

Figure 3.8: Parallel coupling strategy.

3.3.1 LES/RANS coupling

In our particular LES/RANS coupling, the aim is to preserve the specificities and resolution methods of each solver in the LES and RANS sides, separately. For the RANS simulation, the coupling instants essentially coincide with an alteration of the boundary condition while converging to the steady state solution. Since LES resolves large-scale turbulence in space and time, the time step between two consecutive times of the partial differential equation integration scheme is relatively small. RANS flow solver, on the contrary, averages all turbulent motions over time and predicts ensemble average solutions of the steady mean (i.e., independent of time) flow. Even when an unsteady RANS approach is used, the time step employed by the RANS flow solver is still much larger than the one used for a LES flow solver. In such cases, to provide the RANS computation with statistically average values, a sufficient number of integration steps should be achieved in the LES subdomain.

To be coherent with RANS, a sliding average is done to the LES quantities over the time period corresponding to (*d*) in Fig. 3.9, before transmitting them to the RANS computation (steps *a*). In practice, in such a staggered approach, a sub-cycling strategy can be implemented so that both subdomains are advanced using different time steps. On the RANS side, step (*b*) in Fig. 3.9 stands for the run towards a converged state. Such schemes in fact reproduce a fixed point iteration process to ensure coherent coupled steady state solutions (mean fields) of a given problem solved on one side by use of an unsteady model.

The coupling algorithm goes like this for each cycle:

- ◇ Step *a*): A sliding average is performed (in the time window corresponding to *d*) on the information sent to the Solver 2. In our coupling staggered procedure, it corresponds to the average

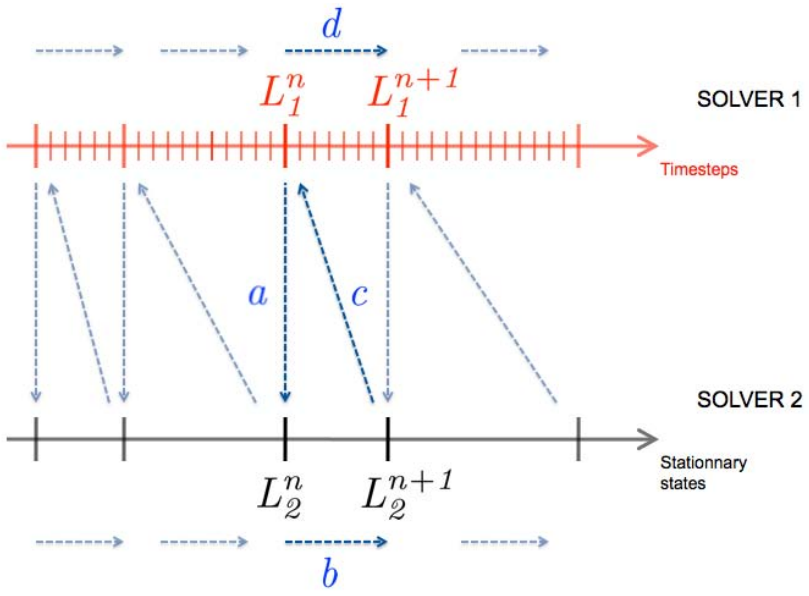

Figure 3.9: Coupling strategy for LES/RANS procedure.

conservative variables which are interpolated on the first two rows of Solver 2.

- ◇ Step *b*): Solver 2 runs until convergence. Solver 1 waits.
- ◇ Step *c*): Solver 2 sends its information to Solver 1. In our case, pressure to advance the Neumann boundary condition of the upstream solver.
- ◇ Step *d*): Solver 1 runs for a determined number of time steps. Solver 2 waits. No time coherence is compulsory between the subdomains physics. The coupling procedure starts again.

3.4 Other coupling strategies

Even if this thesis is centered around the LES/RANS approach to answer the industry needs, other coupling procedures have been investigated during this research activity. The justification being that zonal fluid coupling between two different compressible solvers has barely been confronted. Therefore, before introducing the complexity of coupling two different compressible techniques such as LES and RANS, a coupling between the same compressible code is a step that has been addressed to test the coupling background (CWIPI, interpolations, ... presented in Appendix D.2). For this test case, AVBP comes as a natural candidate: it has proven its capability in solving combustion problems [174] as well as providing good results even if expensive in blade context, cf Part I. The analysis of the AVBP/AVBP coupling is not showed in this dissertation. This embryo of coupling between two

instances of the same AVBP code has been much further developed by Dr. Wang to take into account the rotation of one of the AVBP parts, among other additions. The results of such a study should be available shortly.

			Consistency
DNS/DNS	low Re low Re	Steady Unsteady	Space Time and Space
LES/LES (not presented here)	high Re	Unsteady	Time and Space
LES/RANS	high Re	Unsteady/Steady	Of averaged fields in Space

Table 3.2: Coupling strategies tested during this thesis.

To be coherent with this philosophy, before confronting LES/RANS coupling, the AVBP/*elsA* platform has been declined in the different kinds of solutions that can appear when solving compressible flows: steady laminar or unsteady laminar. For example, as shown in Table 3.2, if the flow has a low Reynolds number and the solution is steady, the consistency between the two subdomains has only to be ensured in space at the interfaces. If there is an unsteady behavior in the solution such as vortex shedding, the coupling will have to assure the consistency both in time and space. These aspects are not directly related to the LES/RANS coupling but seemed interesting to treat in order to set the basis for LES/LES coupling for example (Table 3.2). The reader will find in the two following chapters a differentiation between the problems where a time coherence is needed and those, like LES/RANS, where it is not.

Before applying some of these ideas to more realistic problems, the convergence of the coupling methods is studied thanks to a simplified 1D model in Chapter 4. Resolving a 1D Euler characteristic system of equations allows to study only one equation at a time as the 3 equations resulting from this problem are uncoupled. It also enables to maintain the transmission aspect (downstream/upstream) in the analysis of the convergence even if not resolving the full viscous problem. The resolution of such systems should enable the identification of the different coefficients present in the coupling process (relaxation parameters, coupling iteration ...). Chapter 4 is thus fully dedicated to well-posedness of the coupling process of two compressible fluid subdomains.

4

Mathematical analysis for zonal coupling

Contents

After having presented the coupling methodology in the previous chapter, the coupling procedure is here treated by Domain Decomposition Method (DDM) of a one-dimensional problem. The fundamental question we want to address is whether the solution coming from the coupling of two overlapping subdomains through their interfaces is the same solution we would have if we had faced the same equations in a sole domain.

A generic form of DDM is proposed to analyze different strategies of transmissions (Dirichlet, Neumann, Robin) between the subdomains. The transmission conditions are applied at the boundaries of the subdomains. This approach does not exactly correspond to the method retained for our

coupling, in the sense that the coupling procedure explained in the previous chapter is based on the interpolation of the conservative variables at the inlet of the downstream domain. Nevertheless, in a 1D approach, our procedure is equivalent to imposing a Dirichlet condition.

The first section of this chapter presents the DDM problem in the Euler context. To be more representative of the physics and bounded domains we use, the second section introduces the diffusion term in the equations. The Euler equations are then retrieved by taking the hyperbolic limit. In the third section, the influence of the time step on the convergence rate is briefly described. The last section introduces a panel of numerical tests to analyze the DDM parameters influence with a 1D simple tool.

4.1 Analysis of the 1D coupled Euler equations

The aim of this section is to perform the convergence analysis on the continuous coupled problem. To do so, we solve the Euler hyperbolic time dependent problem using a Schwarz domain decomposition technique. An overview of the different decomposition methods is proposed in Balin [12]. Contrary to the classical approach where one discretizes time to obtain a sequence of steady problems to which the domain decomposition algorithms is applied [3, 41], the algorithm is directly formulated for the original problem without discretization. The advantage of this approach lies in the avoidance of the algebraic equivalent of our coupling in overlapping non conforming grids. The continuous procedure allows us to treat the coupling from a simpler pure geometric level. The spatial domain is decomposed into subdomains and solves iteratively time dependent problems on subdomains exchanging information at the boundaries. The algorithm is defined as in the classical Schwarz case [107] but with time dependent subproblems. The idea of this section is to merge two existing techniques in the mathematical literature: the passage to the Laplace space to express the time dependency [58] and the methodology of DDM as considered by Houzeaux & Codina [78]. Let's remind the definition of the Laplace unilateral transform. The Laplace transform of a function $\widetilde{F}(t)$ is the function $F(s)$ defined by:

$$F(s) = L(\widetilde{F}(t)) = \int_0^\infty e^{-st}\widetilde{F}(t)dt \qquad \forall t \in \mathbb{R}^+$$

with parameter $s \in \mathbb{C}$, $\Re(s) > 0$.

Starting with a 1D system of the hyperbolic advection equation:

$$\widetilde{F}u = \frac{\partial u}{\partial t} + a\frac{\partial u}{\partial x} = 0 \qquad \forall x \in \Omega \tag{4.1}$$

where advection is constant and such that

$$a > 0. \tag{4.2}$$

The Euler equations in one dimension are 3 scalar independent equations. The case with $a < 0$ will be treated after in this section.

Applying the Laplace transform with parameter $s \in \mathbb{C}$, $\Re(s) > 0$, one finds Eq. (4.1) to be of the form:

$$Fu : us + a\frac{\partial u}{\partial x} = 0 \qquad \forall x \in \Omega \tag{4.3}$$

We obtain an Ordinary Differential Equation (ODE) for a given s. The spatial domain is decomposed in two overlapping subdomains $\Omega_1 = (-\infty, \delta)$ and $\Omega_2 = (-\delta, \infty)$. For our analysis, k stands for the iteration index of the coupling process. At $k = 0$, no exchange between the subdomains has been done. $k = 1$, one transmission occurs. What we want to study is the convergence with respect to the number of coupling iterations. Given two initial guesses u_1^0 and u_2^0 for the two domains, the aim is to find u_1^{k+1} and u_2^{k+1} and prove that $u_1 \cup u_2 \to u$ for $k \to \infty$, u being the solution of the non partitioned problem. The general iteration by subdomain decomposition algorithm of overlap 2δ to solve the system associated to Eq. (4.3) reads:

$$\begin{cases} Fu_1^{k+1} = 0 & \forall x \in \Omega_1, \\ \Phi_1(u_1^{k+1}) = \theta_1 \Phi_1(u_2^k) + (1-\theta_1)\Phi_1(u_1^k) & \text{at } x = \delta, \end{cases} \tag{4.4}$$

$$\begin{cases} Fu_2^{k+1} = 0 & \forall x \in \Omega_2, \\ \Phi_2(u_2^{k+1}) = \theta_2 \Phi_2(u_1^{k'}) + (1-\theta_2)\Phi_2(u_2^k) & \text{at } x = -\delta, \end{cases} \tag{4.5}$$

where Φ_1 and Φ_2 are the linear functionals representing the transmission conditions at δ and $-\delta$, respectively, and θ_1 and θ_2 are positive constants, called relaxation parameters. Finally, k' is the iteration index which can be:

$$k' = \begin{cases} k+1 & \text{for the sequential version,} \\ k & \text{for the parallel version.} \end{cases}$$

The reader should note that the terms *parallel* and *sequential* have been already used in this manuscript to refer to the synchronization of the coupled solvers in time in Section 3.3. In this chapter, sequential and parallel indicate the coupling process and do not designate the time synchronization. Even though for stationary flow solution, a connexion between both approaches can be done, as will be seen later in Chapter 5. The DDM presented previously is illustrated for $\theta_1 = \theta_2 = 1$ and $k' = k+1$ in Fig. 4.1. In agreement with the scheme illustrated, the problem on subdomain Ω_1 is solved for the coupling iteration $k+1$ thanks to the transmission conditions on u_1^{k+1}, function of u_2^k, value given

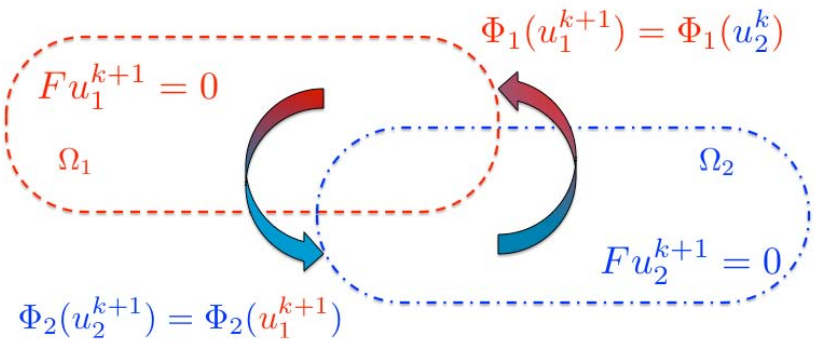

Figure 4.1: DDM with two overlapping subdomains for the Euler equation in a unrelaxed sequential case.

by subdomain Ω_2 at the k^{th} step. The resolution of the problem in subdomain Ω_1 gives u_1^{k+1}, whose value is used in the transmission condition of subdomain Ω_2. The system of subdomain Ω_2 can now be solved. The process is sequential as the resolution of one subdomain depends explicitly (through the transmission condition) on the resolution of the other subdomain. On the contrary, if the coupling is parallel, the resolution of the subdomains depends implicitly on the solution of the other subdomain.

If it is assumed that the solution noted $u(x,s)$ of the problem expressed by Eq. (4.3) satisfies the transmission conditions, then the error $e_i^{k+1} = u_i^{k+1} - u(x,s)$ verifies the following homogeneous system of equations for $k \geq 0$:

$$\begin{cases} Fe_1^{k+1} = 0 & \forall x \in \Omega_1, \\ \Phi_1(e_1^{k+1}) = \theta_1 \Phi_1(e_2^k) + (1-\theta_1)\Phi_1(e_1^k) & \text{at } x = \delta, \end{cases} \tag{4.6}$$

$$\begin{cases} Fe_2^{k+1} = 0 & \forall x \in \Omega_2, \\ \Phi_2(e_2^{k+1}) = \theta_2 \Phi_2(e_1^{k'}) + (1-\theta_2)\Phi_2(e_2^k) & \text{at } x = -\delta, \end{cases} \tag{4.7}$$

Three transmission conditions are of particular interest here:

$$\text{Dirichlet:} \quad \Phi_D(u) = u,$$

$$\text{Neumann:} \quad \Phi_N(u) = \frac{a^2}{s}\frac{\partial u}{\partial x} n_x,$$

$$\text{Robin:} \quad \Phi_R(u) = \frac{a^2}{s}\frac{\partial u}{\partial x} n_x - (a n_x) u,$$

n_x is the exterior normal which can take the values $n_x = 1$ and $n_x = -1$, for $x = \delta$ and $x = -\delta$, respectively. Note that with these forms, $\frac{a^2}{s}$ has the dimension of a viscosity.

Solving Eqs. $(4.6)_1$ and $(4.7)_1$ (the index here stands for the equation number of the system between parentheses), the general solution is of the form:

$$e_i^{k+1}(x,s) = C_i^{k+1} exp(-\frac{s}{a}x),$$

where C_i^{k+1} is a constant dependent on the transmission conditions given by Eqs. $(4.6)_2$ and $(4.7)_2$.

Before going into more details, a generic matrix formulation is introduced. It will help us in the study of convergence. Let's note the $\bar{C}^{k+1}$ vector as

$$\bar{C}^{k+1} = \begin{bmatrix} C_1^{k+1} \\ C_2^{k+1} \end{bmatrix}, \tag{4.8}$$

all the decomposition domain algorithms lead to an algebraic system of the form:

$$\bar{C}^{k+1} = \mathbf{T}\,\bar{C}^{k},$$

where $\mathbf{T}$ is called the iteration matrix. The errors $e_1^{k+1}(x,s)$ and $e_2^{k+1}(x,s)$ will converge to zero as the iteration proceeds if and only if

$$\lim_{k\to\infty} \bar{C}^{k+1} = 0.$$

It can be shown that a necessary and sufficient condition is that the spectral radius $\rho(\mathbf{T})$ of $\mathbf{T}$, also called convergence rate, satisfies

$$\rho(\mathbf{T}) = \sup_{\lambda_i \in Sup(\mathbf{T})} |\lambda_i| < 1. \tag{4.9}$$

where λ_i are the eigenvalues of the iteration matrix. The Laplace transform being a continuous linear application, if e_i^{k+1} converges to zero, so does $L^{-1}(e_i^{k+1})$.

To sum up, three separated problems have to be treated and will affect convergence towards the solution of the whole domain problem:

- sequentiality vs parallelism of the iterations,
- the kind of boundary condition imposed at the coupling interfaces,
- the relaxation introduced at the boundary conditions.

Every aspect is treated hereafter.

4.1.1 Sequential system

Let's study the convergence of the continuous problem for the unrelaxed sequential version: $k' = k+1$ and $\theta_1 = \theta_2 = 1$. The effects of relaxation will be studied later. One can re-write the error coefficients expression from Eq. $(4.6)_2$ and Eq. $(4.7)_2$, for $k \geq 0$, in a simplified form valid for every transmission condition (Dirichlet, Neumann or Robin):

$$\begin{aligned} C_1^{k+1} &= \rho_1 C_2^k \\ C_2^{k+1} &= \rho_2 C_1^{k+1} \end{aligned} \tag{4.10}$$

where ρ_1 and ρ_2 do not depend on the iteration number k. For $k \geq 1$, using the fact that $C_2^k = \rho_2 C_1^k$, we can write:

$$\begin{aligned} C_1^{k+1} &= \rho_1 \rho_2 C_1^k \\ C_2^{k+1} &= \rho_1 \rho_2 C_2^k \end{aligned} \tag{4.11}$$

and the iteration matrix becomes

$$\mathbf{T} = \begin{bmatrix} \rho_1\rho_2 & 0 \\ 0 & \rho_1\rho_2 \end{bmatrix} \tag{4.12}$$

whose double multiplicity eigenvalue is $\lambda = \rho_1\rho_2$, so that $\rho(\mathbf{T}) = \rho = |\rho_1\rho_2|$.

The expressions of ρ are going to be determined for each decomposition method. In our case, a Dirichlet condition is imposed for Φ_2 at $x = -\delta$. The combination of this condition with any of the three conditions at $x = \delta$ will lead to three families of overlapping domain decomposition methods, Dirichlet/Dirichlet (Schwarz method), Dirichlet/Neumann and Dirichlet/Robin.

Dirichlet/Dirichlet Dirichlet conditions are imposed at both $x = -\delta$ and $x = \delta$. The transmission conditions give:

$$\begin{aligned} &x = \delta \\ &\begin{cases} \Phi_1(e_1^{k+1}(\delta, s)) = C_1^{k+1} exp(-\frac{s}{a}\delta) \\ \Phi_2(e_2^{k+1}(\delta, s)) = C_2^{k+1} exp(-\frac{s}{a}\delta) \end{cases} \\ &x = -\delta \\ &\begin{cases} \Phi_1(e_1^{k+1}(-\delta, s)) = C_1^{k+1} exp(\frac{s}{a}\delta) \\ \Phi_2(e_2^{k+1}(-\delta, s)) = C_2^{k+1} exp(\frac{s}{a}\delta) \end{cases} \end{aligned}$$

Substituting these expressions into the equations for the error transmission Eq. $(4.6)_2$ and Eq. $(4.7)_2$, one can conclude that $\rho_1 = 1$ and $\rho_2 = 1$ yielding therefore $|\rho| = 1$. The error at $k+1$ remains and is the initial error since the expression of the error at the coupling iteration $k+1$ is directly related to the initial error by:

$$e_i^{k+1}(x, s) = \rho^{k+1} e_i^0(x, s).$$

An alternative view on the problem granting the same conclusion can be of interest. Let's combine the two following expressions:

$$e_1^{k+1}(x,s) = C_1^{k+1} exp(-\tfrac{s}{a}x),$$

$$e_2^{k+1}(x,s) = C_2^{k+1} exp(-\tfrac{s}{a}x),$$

with the transmission relation at $x=-\delta$: $\left[e_2^{k+1}(-\delta,s) = e_1^k(-\delta,s)\right]$

$$e_2^{k+1}(-\delta,s) \quad = C_2^{k+1} exp(\tfrac{s}{a}\delta) = e_1^k(-\delta,s),$$

and thus substituting C_2^{k+1} in the expression of $e_2^{k+1}(x,s)$:

$$\begin{aligned} e_2^{k+1}(x,s) \quad &= e_1^k(-\delta,s) exp(-\tfrac{s}{a}\delta) exp(-\tfrac{s}{a}x), \\ &= e_1^k(-\delta,s) exp(-\tfrac{s}{a}(x+\delta)), \end{aligned}$$

Since at $x=\delta$, the transmission condition applies, one also has:

$$e_1^{k+1}(\delta,s) \quad = C_1^{k+1} exp(-\tfrac{s}{a}\delta) = e_2^k(\delta,s).$$

Substituting the value of C_1^{k+1} (some expressions appear in bold or underlined to ease the reader comprehension, for instance, the following expression in bold will be used below):

$$\begin{aligned} e_1^{k+1}(x,s) \quad &= e_2^k(\delta,s) exp(\tfrac{s}{a}\delta) exp(-\tfrac{s}{a}x), \\ \mathbf{e_1^{k+1}(x,s)} \quad &= \underline{e_2^k(\delta,s)} exp(-\tfrac{s}{a}(x-\delta)), \end{aligned}$$

so at the end,

$$\begin{aligned} e_2^k(x,s) \quad &= e_1^{k-1}(-\delta,s) exp(-\tfrac{s}{a}(x+\delta)), \\ \underline{e_2^k(\delta,s)} \quad &= e_1^{k-1}(-\delta,s) exp(-\tfrac{s}{a}(2\delta)), \end{aligned}$$

and thus substituting in the expression of $\mathbf{e_1^{k+1}(x,s)}$

$$e_1^{k+1}(x,s) = e_1^{k-1}(-\delta,s) exp(-\tfrac{s}{a}(x-\delta)) exp(-\tfrac{s}{a}(2\delta)),$$

$$e_1^{2k}(x,s) = e_1^0(-\delta,s) exp(-\tfrac{ks}{a}(x+\delta)).$$

To obtain the convergence result for bounded time intervals, the back-transformation is performed. Since

$$e^{-\alpha s} = \int_0^\infty e^{-st}\delta(t-\alpha)dt$$

and using the convolution result on Laplace transform, $L(f*g) = L(f)L(g)$, and Laplace transform with $\alpha = \frac{k}{a}(x+\delta)$:

$$e_1^{2k}(x,t) = e_1^0(-\delta,t) *_t \delta(t - \frac{k}{a}(x+\delta)) = \int_0^\infty e_1^0(-\delta,\tau)\ \delta(t - \frac{k}{a}(x+\delta) - \tau)d\tau$$

$$e_1^{2k}(x,t) = e_1^0(-\delta, t - \frac{k}{a}(\delta + x))$$

$$e_1^{2k}(\delta,t) = e_1^0(-\delta, t - \frac{k}{a}(2\delta)) \qquad \text{at } x = \delta$$

In the time space, there has been a translation (depending on the overlap region 2δ) of the initial error but no amplification. It is the same conclusion as retrieved in the Laplace space. In the following, the study will be limited to the latter space.

Dirichlet/Neumann A Neumann condition is imposed now at $x = \delta$ where $n_x = 1$. The transmission conditions hence read:

$$\Phi_1(e_1^{k+1}(\delta,s)) = -a\ C_1^{k+1} exp(-\tfrac{s}{a}\delta)$$
$$\Phi_1(e_2^{k+1}(\delta,s)) = -a\ C_2^{k+1} exp(-\tfrac{s}{a}\delta)$$

$$\Phi_2(e_1^{k+1}(-\delta,s)) = C_1^{k+1} exp(\tfrac{s}{a}\delta)$$
$$\Phi_2(e_2^{k+1}(-\delta,s)) = C_2^{k+1} exp(\tfrac{s}{a}\delta)$$

Substituting these equations into the equations for the error transmission Eq. $(4.6)_2$ and Eq. $(4.7)_2$, one can conclude that $\rho_1 = 1$ and $\rho_2 = 1$ and similarly to the previous case $|\rho| = 1$. The error at $k+1$ retains the initial error.

Dirichlet/Robin A Robin condition is imposed now at $x = \delta$. The transmission conditions thus give:

$$\Phi_1(e_1^{k+1}(\delta,s)) = [-2a]\ C_1^{k+1} exp(-\tfrac{s}{a}\delta)$$
$$\Phi_1(e_2^{k+1}(\delta,s)) = [-2a]\ C_2^{k+1} exp(-\tfrac{s}{a}\delta)$$

$$\Phi_2(e_1^{k+1}(-\delta,s)) = C_1^{k+1} exp(\tfrac{s}{a}\delta)$$
$$\Phi_2(e_2^{k+1}(-\delta,s)) = C_2^{k+1} exp(\tfrac{s}{a}\delta)$$

Substituting these equations into the equations for the error transmission Eq. $(4.6)_2$ and Eq. $(4.7)_2$, one can conclude that $\rho_1 = 1$ and $\rho_2 = 1$ and therefore $|\rho| = 1$. The error at $k+1$ also retains the initial error.

For each of the three transmission conditions, in the case of the unrelaxed sequential approach, the convergence rate is equal to 1. Another important observation out of this analysis is that the overlap length has no influence in the convergence rate in all three cases.

4.1.1.1 Waves traveling upstream

Let's consider a 1D advection problem that becomes an advection-reaction problem after the Laplace transform:

$$\begin{cases} Fu = su + a\dfrac{\partial u}{\partial x} = 0 & \forall x \in \Omega \end{cases} \tag{4.13}$$

where advection is constant and such that $a < 0$. Let's remind that $k' = k+1$ and $\theta_1 = \theta_2 = 1$ in this case. Introducing the transmission coefficients suitable for each case in the unrelaxed sequential version, one can deduce the expressions for ρ_1 and ρ_2. For this particular study, we concentrate on the Dirichlet/Neumann transmission condition since it is the one we are employing in the application cases. A legitimate question may arise for the convergence of the Neumann/Dirichlet method for $a > 0$, conceptual symmetric of the Dirichlet/Neumann with $a < 0$ as shown by Fig. 4.2.

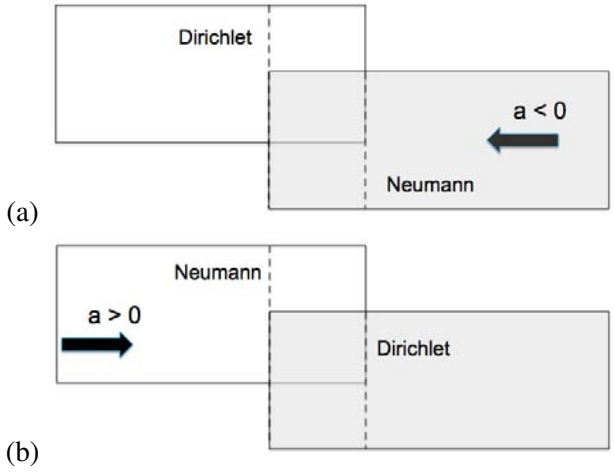

Figure 4.2: (a) Dirichlet/Neumann with $a < 0$, conceptual symmetric of the (b) Neumann/Dirichlet method for $a > 0$.

Neumann/Dirichlet For a Dirichlet condition at $x = \delta$ and a Neumann condition imposed at $x = -\delta$,

$$\begin{aligned} \Phi_1(e_1^{k+1}(\delta, s)) &= C_1^{k+1} exp(-\tfrac{s}{a}\delta) \\ \Phi_1(e_2^{k+1}(\delta, s)) &= C_2^{k+1} exp(-\tfrac{s}{a}\delta) \end{aligned}$$

$$\begin{aligned} \Phi_2(e_1^{k+1}(-\delta, s)) &= a\, C_1^{k+1} exp(\tfrac{s}{a}\delta) \\ \Phi_2(e_2^{k+1}(-\delta, s)) &= a\, C_2^{k+1} exp(\tfrac{s}{a}\delta) \end{aligned}$$

Substituting these equations for the errors transmission conditions in Eq. $(4.6)_2$ and Eq. $(4.7)_2$, one obtains: $\rho_1 = 1$ and $\rho_2 = 1$. The rate of convergence is equal to 1. The Neumann/Dirichlet method with $a < 0$ has the same behavior as the Dirichlet/Neumann method with $a > 0$.

4.1.1.2 Relaxed sequential system

In order to compare the results of the relaxed version to unrelaxed ones, ρ_1 and ρ_2 from the unrelaxed sequential approach are used in the following sections. The relaxed version of the sequential domain decomposition methods can be obtained from Eqs. $(4.6)_2$ and $(4.7)_2$ for $k \geq 0$:

$$\begin{aligned} C_1^{k+1} &= \theta_1\rho_1 C_2^k + (1-\theta_1)C_1^k \\ C_2^{k+1} &= \theta_2\rho_2 C_1^k + (1-\theta_2)C_2^k \end{aligned} \tag{4.14}$$

where ρ_1 and ρ_2 are the unrelaxed rates of convergence calculated in the last subsection. The iteration matrix $\mathbf{T}$ is for $k \geq 0$:

$$\mathbf{T} = \begin{bmatrix} 1-\theta_1 & \theta_1\rho_1 \\ \theta_2(1-\theta_1)\rho_2 & \theta_1\theta_2\rho_1\rho_2 + (1-\theta_2) \end{bmatrix} \tag{4.15}$$

Making the simplification (θ_1, θ_2)=$(\theta, 1)$, since in our methodology only the feedback from RANS to LES has a relaxation, and calculating the characteristic polynomial, one finds a double eigenvalue λ, which is given by $\lambda = 1 + \theta(\rho_1\rho_2 - 1)$. Therefore, for all the transmission conditions earlier given, since $\rho_1\rho_2 = 1$, one has $\lambda = 1$ so that $|\rho| = 1$ meaning that relaxation at the interface has not influence in this case.

4.1.2 Parallel system

The convergence analysis on the continuous problem can also be studied for the unrelaxed parallel version. In this case, $k' = k$ and $\theta_1 = \theta_2 = 1$. One can re-write the error coefficient expressions from Eq.$(4.6)_2$ and Eq.$(4.7)_2$, for k≥0, as it has been done before for the unrelaxed sequential system:

$$\begin{aligned} C_1^{k+1} &= \rho_1 C_2^k \\ C_2^{k+1} &= \rho_2 C_1^k \end{aligned} \tag{4.16}$$

which leads to the iteration matrix:

$$\mathbf{T} = \begin{bmatrix} 0 & \rho_1 \\ \rho_2 & 0 \end{bmatrix} \tag{4.17}$$

whose eigenvalue is $\lambda = \sqrt{|\rho_1\rho_2|}$, so that $\rho = \sqrt{|\rho_1\rho_2|}$. Convergence criteria for the parallel system is the same as the one for the sequential version (for all the transmission conditions studied). The rate of convergence is the square root of the one in the sequential method. For the cases of interest, it remains equal to 1.

4.1.2.1 Relaxed parallel system

The iteration matrix for the relaxed parallel version reads

$$\mathbf{T} = \begin{bmatrix} 1-\theta_1 & \theta_1\rho_1 \\ \theta_2\rho_2 & 1-\theta_2 \end{bmatrix} \tag{4.18}$$

whose characteristic equation is equal to $\lambda^2+(\theta_1+\theta_2-2)\lambda+1-\theta_1-\theta_2+\theta_1\theta_2(1-\rho_1\rho_2)=0$ and whose discriminant is $\Delta=(\theta_1-\theta_2)^2+4\theta_1\theta_2\rho_1\rho_2$. Making again the simplification (θ_1,θ_2)=$(\theta,1)$, the discriminant becomes $\Delta=(\theta-1)^2+4\theta\rho_1\rho_2$. For each type of transmission coefficient, $\rho_1\rho_2=1$, as a consequence Δ becomes equal to $(\theta+1)^2$. The two eigenvalues are 1 and $-\theta$. To have convergence, one must assure that $|\theta|\leq 1$.

4.1.3 Concluding remarks

In this section, a justification of the mathematical foundation of our coupling procedure has been presented through a simple example on the Euler equations. The main conclusions are that the initial error is retained for all the procedures proposed. The initial guesses will be of paramount importance since they will affect the subsequent coupled computation. Moreover, the overlap length has no influence in the convergence rate. Table 4.1 gathers the convergence rates. Furthermore, for the relaxed parallel approach, one has to assure that the relaxation parameter is smaller than 1.

	Rate of convergence	**Conditions for convergence**
Unrelaxed sequential	1	–
Relaxed sequential	1	–
Unrelaxed parallel	1	–
Relaxed parallel	1	$\|\theta\|\leq 1$

Table 4.1: Summary of the mathematical analysis for the Euler scalar equations.

The convergence rates obtained with the proposed algorithm in this section have been compared for the unrelaxed parallel case with the methodology developed by Dolean *et al.* [41] to study the convergence rate from a quantitative point of view in 2 and 3D cases for overlapping decompositions. Their method relies on the formulation of an additive Schwarz algorithm involving transmission conditions that are derived naturally from a weak formulation. These interface conditions are Dirichlet conditions for the characteristic variables. They correspond to incoming waves also called natural interface conditions which take into account the hyperbolic nature of the Euler equations. Only the negative eigenvalues are applied at the boundary condition for subdomain 1 and only the positive ones are applied at the boundary condition of subdomain 2. Similar formulations were previously studied for the semi-discrete Euler equations by Bjørhus [20] and for more complicated models as Navier-Stokes equations by Quarteroni *et al.* [146]. The main difference is that we treat the scalar equation and they do the matrix approach. We have applied their analysis [41] to the 1D problem and the same results have been retrieved for the unrelaxed parallel approach: $\rho=1$.

The resolution of the scalar Euler 1D equation does not take into account the bounded boundary layers present in real configurations. Indeed, the usual domains do not extend from $(-\infty,\infty)$ but are bounded $(-l_1,l_2)$. The first remark is that the initial errors may interact with this supplementary boundary conditions and behave differently: they may be amplified or reduced. This is the reason why we propose an additional section, where we will be treating a one-dimensional advection-diffusion scalar equation (well-posed with 2 boundary conditions). In the hyperbolic limit, we will recover the Euler scalar equation.

4.2 The advection-diffusion general problem statement

It has been seen in the previous section that no convergence rate inferior to 1 can be achieved if using the DDM proposed for the advection system. The aim of the present section is to consider also the diffusion for the problem definition and then take the hyperbolic limit to retrieve the linearized Euler equations.

Instead of the pure advection system of Eq. (4.3), the advection-diffusion problem for 1D becomes an advection-diffusion-reaction problem after the Laplace transform:

$$\begin{cases} Fu = -\nu\dfrac{\partial^2 u}{\partial x^2} + su + a\dfrac{\partial u}{\partial x} = 0 & \forall x \in \Omega = (-l_1,l_2) \\ u = 0 & \text{at } x = -l_1, l_2 \end{cases} \tag{4.19}$$

where l_1 and l_2 are positive. ν and s are constant such that $s > 0$ and $\nu > 0$. The advection is supposed constant and such that $a > 0$. $l = l_1 + l_2$ is the total length of the domain.

Two non-dimensional parameters can be defined, the Reynolds number, Re, and the reaction number, R, as:

$$Re = \frac{a\,l}{\nu} \qquad \text{and} \qquad R = \frac{s\,l}{a}$$

Performing the same process as previously, the iteration by subdomain decomposition algorithm of overlap 2δ to solve (4.19) is:

$$\begin{cases} Fe_1^{k+1} = 0 & \forall x \in \Omega_1, \\ e_1^{k+1} = 0 & \text{at } x = -l_1, \\ \Phi_1(e_1^{k+1}) = \theta_1\Phi_1(e_2^k) + (1-\theta_1)\Phi_1(e_1^k) & \text{at } x = \delta, \end{cases} \tag{4.20}$$

$$\begin{cases} Fe_2^{k+1} = 0 & \forall x \in \Omega_2, \\ e_2^{k+1} = 0 & \text{at } x = l_2, \\ \Phi_2(e_2^{k+1}) = \theta_2 \Phi_2(e_1^{k'}) + (1-\theta_2)\Phi_2(e_2^k) & \text{at } x = -\delta, \end{cases} \tag{4.21}$$

The three transmission conditions are defined as:

$$\text{Dirichlet:} \quad \Phi_D(u) = u,$$

$$\text{Neumann:} \quad \Phi_N(u) = \nu \frac{\partial u}{\partial x} n_x,$$

$$\text{Robin:} \quad \Phi_R(u) = \nu \frac{\partial u}{\partial x} n_x - (a n_x) u.$$

Solving Eqs. $(4.20)_1$ and $(4.21)_1$, the solution is of the form:

$$e_i^{k+1} = A_i^{k+1} exp((\omega + \tau)x) + B_i^{k+1} exp((\omega - \tau)x)$$

where A_i^{k+1} and B_i^{k+1} are constants depending on the boundary conditions given by $(4.20)_2$ and $(4.21)_2$. Taking into account these boundary conditions, the errors can be expressed as:

$$e_1^{k+1} = C_1^{k+1} exp(\omega x)\ sinh(\tau(l_1 + x)),$$

$$e_2^{k+1} = C_2^{k+1} exp(\omega x)\ sinh(\tau(l_2 - x)).$$

ω and τ are given by:

$$\omega = \frac{Re}{2l} \qquad \text{and} \qquad \tau = \frac{1}{l}\sqrt{(Re/2)^2 + ReR}$$

4.2.1 Sequential system

Introducing the transmission coefficients suitable for each case in the unrelaxed sequential system, one can deduce the following expressions for ρ_1 and ρ_2, as done in the previous section. Let's remind that $k' = k+1$ and $\theta_1 = \theta_2 = 1$ in this case.

Dirichlet/Dirichlet

$$\rho_1 = \frac{sinh(\tau(l_2 - \delta))}{sinh(\tau(l_1 + \delta))} \qquad \text{and} \qquad \rho_2 = \frac{sinh(\tau(l_1 - \delta))}{sinh(\tau(l_2 + \delta))} \tag{4.22}$$

Therefore,

$$\rho = \frac{sinh(\tau(l_2-\delta))}{sinh(\tau(l_2+\delta))}\frac{sinh(\tau(l_1-\delta))}{sinh(\tau(l_1+\delta))} \tag{4.23}$$

Since $l_2 > \delta$ and $l_1 > \delta$, ρ_1 and ρ_2 are positive, and so is their product $\rho_1\rho_2$. We will use this property in Section 4.2.3.1 to determine the validity regime for the relaxation parameter.

Dirichlet/Neumann For a Neumann condition imposed at $x = \delta$,

$$\Phi_1(e_1^{k+1}(\delta,s)) = C_1^{k+1} exp(\omega\delta)[\nu\omega\ sinh(\tau(l_1+\delta)) + \nu\tau\ cosh(\tau(l_1+\delta))]$$

$$\Phi_1(e_2^{k+1}(\delta,s)) = C_2^{k+1} exp(\omega\delta)[\nu\omega\ sinh(\tau(l_2-\delta)) - \nu\tau\ cosh(\tau(l_2-\delta))]$$

Substituting these equations and the ones for the Dirichlet condition for the error transmission conditions in $(4.20)_3$ and $(4.21)_3$, one obtains:

$$\rho_1 = \frac{\omega\ sinh(\tau(l_2-\delta)) - \tau\ cosh(\tau(l_2-\delta))}{\omega\ sinh(\tau(l_1+\delta)) + \tau\ cosh(\tau(l_1+\delta))} \quad \text{and} \quad \rho_2 = \frac{sinh(\tau(l_1-\delta))}{sinh(\tau(l_2+\delta))} \tag{4.24}$$

and ρ is given by:

$$\rho = \left| \frac{\omega\ sinh(\tau(l_2-\delta)) - \tau\ cosh(\tau(l_2-\delta))}{\omega\ sinh(\tau(l_1+\delta)) + \tau\ cosh(\tau(l_1+\delta))} \frac{sinh(\tau(l_1-\delta))}{sinh(\tau(l_2+\delta))} \right| \tag{4.25}$$

To determine the sign of the product $\rho_1\rho_2$, ρ_1 can be expressed as:

$$\rho_1 = \frac{\omega\ tanh(\tau(l_2-\delta)) - \tau}{\omega\ tanh(\tau(l_1+\delta)) + \tau} \frac{cosh(\tau(l_1+\delta))}{cosh(\tau(l_2-\delta))} \tag{4.26}$$

It is easy to prove that ρ_1 is always negative since the norm of the hyperbolic tangent function is always smaller than one and τ is always bigger than ω. Furthermore, as ρ_2 is always positive, the product $\rho_1\rho_2$ is negative. As said before, we will use the sign of $\rho_1\rho_2$ in Section 4.2.3.1 to determine the validity regime for the relaxation parameter.

Dirichlet/Robin For the Robin condition imposed at $x = \delta$,

$$\Phi_1(e_1^{k+1}(\delta,s)) = C_1^{k+1} exp(\omega\delta)[\nu\tau\ cosh(\tau(l_1+\delta))]$$

$$\Phi_1(e_2^{k+1}(\delta,s)) = C_2^{k+1} exp(\omega\delta)[-\nu\tau\ cosh(\tau(l_2-\delta))]$$

So that

$$\rho_1 = \frac{-cosh(\tau(l_2-\delta))}{cosh(\tau(l_1+\delta))} \qquad \text{and} \qquad \rho_2 = \frac{sinh(\tau(l_1-\delta))}{sinh(\tau(l_2+\delta))} \tag{4.27}$$

and finally,

$$\rho = \left| \frac{sinh(\tau(l_1-\delta))}{sinh(\tau(l_2+\delta))} \frac{cosh(\tau(l_2-\delta))}{cosh(\tau(l_1+\delta))} \right| \tag{4.28}$$

The product $\rho_1\rho_2$ is always negative. We will use this in Section 4.2.3.1.

The important observation is now the fact that the extent of the overlap will impact the convergence rate for all three types of transmission coefficients.

4.2.2 The hyperbolic limit

To consider the hyperbolic limit of the advection-diffusion-reaction equation is to take $\nu \to 0$, i.e., $Re \gg 1$ and as a consequence, $\tau \gg 1$. Sinh and cosh can be simplified as $\sinh(\xi) \approx \cosh(\xi) \approx exp(\xi)/2$ when $\xi \gg 1$. s is considered non-zero and since Re $\gg 1$, $\tau > \omega$.

Equations (4.23), (4.25) and (4.28) give the following rates of convergence in the hyperbolic limit:

$$\begin{cases} Dirichlet/Dirichlet & \rho_1\rho_2 \approx exp(-4\tau\delta), \\ Dirichlet/Neumann & \rho_1\rho_2 \approx exp(-4\tau\delta)\dfrac{-R/Re}{1+R/Re}, \\ Dirichlet/Robin & \rho_1\rho_2 \approx -exp(-4\tau\delta) \end{cases} \tag{4.29}$$

Since the reaction term R is bounded, the following stability conditions can be announced:

$$\begin{cases} Dirichlet/Dirichlet & \delta > 0, \\ Dirichlet/Neumann & \delta \geq 0, \\ Dirichlet/Robin & \delta > 0. \end{cases} \tag{4.30}$$

In this case, writing the full advection-diffusion-reaction equations and taking the hyperbolic limit shows that unlike in the latter section, when only the Euler system was considered, one can prove that

all these three transmission conditions are unconditionally stable in a sequential overlapped approach, highlighting the importance of δ and its potential impact on convergence.

4.2.2.1 Relaxed sequential system

The approach presented in the previous Euler section is generic. We can apply the same equations to the actual scalar advection-diffusion equation. ρ_1 and ρ_2 refer to the unrelaxed sequential values deduced from transmission conditions. As explained in Section 4.1.1.2, the eigenvalue λ of multiplicity two is given by $\lambda = 1+\theta(\rho_1\rho_2-1)$. Therefore, the rate of convergence is $\rho = |1+\theta(\rho_1\rho_2-1)|$. The convergence condition $\rho < 1$ gives $|1+\theta(\rho_1\rho_2-1)| < 1$ which is equivalent to $-2 < \theta(\rho_1\rho_2-1) < 0$. As $|\rho_1\rho_2| < 1$ for each of the three approaches studied, the condition of convergence on the relaxation parameter becomes

$$0 < \theta < \frac{2}{1-\rho_1\rho_2} \tag{4.31}$$

In the hyperbolic limit, aside from the previous limitation on δ, θ is bounded between 0 and 2 ($\rho_1\rho_2$ tending to zero as formerly proved).

4.2.3 Parallel system

For $k' = k$ and $\theta_1 = \theta_2 = 1$, the convergence conditions $|\rho| < 1$ for the parallel version are the same as the ones from the sequential version since $\rho = \sqrt{|\rho_1\rho_2|}$.

4.2.3.1 Relaxed parallel system

The characteristic equation is equal to $\lambda^2 + (\theta_1+\theta_2-2)\lambda + 1 - \theta_1 - \theta_2 + \theta_1\theta_2(1-\rho_1\rho_2) = 0$ and its discriminant is $\Delta = (\theta_1-\theta_2)^2 + 4\theta_1\theta_2\rho_1\rho_2$. Making again the simplification (θ_1,θ_2)=$(\theta,1)$, the discriminant becomes $\Delta = (\theta-1)^2 + 4\theta\rho_1\rho_2$. Owing to Eq. (4.29), the product $\rho_1\rho_2$ is always positive in the hyperbolic limit for Dirichlet/Dirichlet transmission conditions. The eigenvalues of the characteristic equation are then real and equal to:

$$\lambda_i = \frac{1}{2}\left((1-\theta) \pm \sqrt{(\theta-1)^2 + 4\theta\rho_1\rho_2}\right)$$

The convergence can not be improved by relaxing the Dirichlet/Dirichlet approach. The optimal relaxation couple found is (θ_1,θ_2)=(0,0). On the contrary, the mixed transmission conditions (Neumann/Dirichlet or Robin/Dirichlet) have a negative product $\rho_1\rho_2$ and thus, an interval for the couple (θ_1,θ_2) exists in which one can choose an optimal value for each of these relaxation parameters to increase the convergence of the method [79]. In our case, $\theta_1 = \theta$ and $\theta_2 = 1$, the discriminant becomes:

$$\Delta = (\theta-1)^2 + 4\theta\rho_1\rho_2 = (\theta-1)^2\left[1+4\frac{\theta\rho_1\rho_2}{(\theta-1)^2}\right]$$

In the hyperbolic limit, a Taylor expansion of this discriminant can be performed as $\rho_1\rho_2$ tends to zero for all transmission conditions. One finds the value for both eigenvalues to be:

$$\begin{cases} \lambda_1 = -\dfrac{\theta\rho_1\rho_2}{(\theta-1)} \\ \lambda_2 = (\theta-1) + \dfrac{\theta\rho_1\rho_2}{(\theta-1)} \end{cases} \tag{4.32}$$

As a consequence, to reach convergence, one must assure that $\theta < 2$ in the hyperbolic limit.

4.2.4 Waves traveling upstream

Let's consider a 1D advection-diffusion problem that becomes an advection-diffusion-reaction problem after the Laplace transform:

$$\begin{cases} Fu := -\nu\dfrac{\partial^2 u}{\partial x^2} + su + a\dfrac{\partial u}{\partial x} = 0 & \forall x \in \Omega = (-l_1, l_2) \\ u = 0 & \text{at } x = -l_1, l_2 \end{cases} \tag{4.33}$$

where advection is constant and such that

$$a < 0. \tag{4.34}$$

Let's remind that $k' = k+1$ and $\theta_1 = \theta_2 = 1$ in this case. The definition for ω and τ remains unchanged. Introducing the transmission coefficients suitable for each case in the unrelaxed sequential version with $a > 0$, one can deduce the expressions for ρ_1 and ρ_2 in (4.23), (4.25) and (4.28). From the symmetry of Eqs. (4.23) and (4.28), one can conclude that the Dirichlet and Robin conditions can be located independently of the direction of the flow. This is not the case of the Dirichlet/Neumann transmission conditions, Eq.(4.25). A question may arise for the convergence of the Neumann/Dirichlet method for $a > 0$, conceptual symmetric of the Dirichlet/Neumann with $a < 0$.

Neumann/Dirichlet For a Neumann condition imposed at $x = -\delta$,

$$\Phi_1(e_1^{k+1}(\delta,s)) = C_1^{k+1} exp(\omega\delta)[\nu\omega\ sinh(\tau(l_1-\delta)) + \nu\tau\ cosh(\tau(l_1-\delta))]$$

$$\Phi_1(e_2^{k+1}(\delta,s)) = C_2^{k+1} exp(\omega\delta)[\nu\omega\ sinh(\tau(l_2+\delta)) - \nu\tau\ cosh(\tau(l_2+\delta))]$$

Substituting these equations and the ones for the Dirichlet condition for the errors transmission conditions in $(4.20)_3$ and $(4.21)_3$, one obtains:

$$\rho_1 = \frac{\omega\ sinh(\tau(l_1-\delta)) + \tau\ cosh(\tau(l_1-\delta))}{\omega\ sinh(\tau(l_2+\delta)) - \tau\ cosh(\tau(l_2+\delta))} \quad \text{and} \quad \rho_2 = \frac{sinh(\tau(l_2-\delta))}{sinh(\tau(l_1+\delta))} \tag{4.35}$$

and ρ is given by:

$$\rho = \left| \frac{\omega\ sinh(\tau(l_1-\delta)) + \tau\ cosh(\tau(l_1-\delta))}{\omega\ sinh(\tau(l_2+\delta)) - \tau\ cosh(\tau(l_2+\delta))} \frac{sinh(\tau(l_2-\delta))}{sinh(\tau(l_1+\delta))} \right| \tag{4.36}$$

Equation (4.36) gives the following rate of convergence in the hyperbolic limit:

$$\left\{ Neumann/Dirichlet \quad \rho_1\rho_2 \approx exp(-4\tau\delta)\frac{1+R/Re}{-R/Re}, \right. \tag{4.37}$$

An additional term in the expression is needed to increase the precision of the expansion. Conserving a term function of δ gives:

$$\left\{ Neumann/Dirichlet \quad \rho_1\rho_2 \approx exp(-4\tau\delta)\frac{1+R/Re}{-R/Re - exp(-2\tau(l_2+\delta))/2}, \right. \tag{4.38}$$

Since the reaction term R is bounded, solving a second order equation gives the following stability condition:

$$\left\{ Neumann/Dirichlet \quad exp(Re\frac{\delta}{l}) > \frac{-exp(-Re\frac{l_2}{l}) + \sqrt{exp(-2Re\frac{l_2}{l}) + 4R/Re(R/Re+1)}}{2R/Re}, \right. \tag{4.39}$$

Simplifying for $Re \gg 1$,

$$\left\{ Neumann/Dirichlet \quad \delta > \frac{l}{Re} ln(\sqrt{\frac{Re}{R}}) \right. \tag{4.40}$$

which expression as a function of a reads:

$$\left\{ Neumann/Dirichlet \quad \delta > \frac{\nu}{a} ln(\frac{|a|}{\sqrt{\nu s}}) \right. \tag{4.41}$$

In Section 4.2.2, we concluded that the Dirichlet/Neumann method is *unconditionally* stable with $a > 0$ (cf Eq. (4.29)). The transmission conditions are consistent with the subdomains boundary conditions in the hyperbolic limit, i.e. Neumann condition at outflow and Dirichlet condition at inflow. In this section, the Dirichlet/Neumann coupling is deduced to be *conditionally* stable with $a < 0$, cf Eq. (4.40). That means that an overlap length must exist if imposing this couple of transmission conditions and will help stabilizing the problem as proven by Eq. (4.40).

4.2.5 Concluding remarks

Table 4.2 below summarizes the behaviors detailed in this section:

		Rate of convergence	Conditions for convergence
Unrelaxed sequential	Dirichlet/Dirichlet	$\rho_1\rho_2 \approx exp(-4\tau\delta)$	$\delta > 0$
	Dirichlet/Neumann	$\rho_1\rho_2 \approx exp(-4\tau\delta)\frac{-R/Re}{1+R/Re}$	$\delta \geq 0$
	Dirichlet/Robin	$\rho_1\rho_2 \approx -exp(-4\tau\delta)$	$\delta > 0$
Relaxed sequential with (θ_1,θ_2)=$(\theta,1)$	Dirichlet/Dirichlet Dirichlet/Neumann Dirichlet/Robin	$\rho = \lvert 1+\theta(\rho_1\rho_2-1)\rvert$	$0 < \theta < \frac{2}{1-\rho_1\rho_2}$
Unrelaxed parallel	Dirichlet/Dirichlet	$\rho = \sqrt{\lvert\rho_1\rho_2\rvert}$	$\delta > 0$
	Dirichlet/Neumann		$\delta \geq 0$
	Dirichlet/Robin		$\delta > 0$
Relaxed parallel with (θ_1,θ_2)=$(\theta,1)$	Dirichlet/Dirichlet	no possible improvement	–
	Dirichlet/Neumann	Eq. (4.32)	$\lvert\theta\rvert < 2$
	Dirichlet/Robin	Eq. (4.32)	$\lvert\theta\rvert < 2$

Table 4.2: Summary of the mathematical analysis in the hyperbolic limit of the advection-diffusion-reaction equations ($a > 0$).

Some of these conclusions will be tested in an application case in Section 4.4.2. The Dirichlet and Robin transmission conditions can be located indifferently of the flow direction because their convergence rate exhibits an interesting symmetric behavior with respect to the subdomains lengths l_1 and l_2 in Eq. (4.23) and Eq. (4.28). As previously seen, the Dirichlet/Neumann can not be positioned independently of the flow direction. Dirichlet/Neumann can achieve convergence with no overlapping domain for $a > 0$, whereas an overlap length (function of the Reynolds number but not on the subdomain lengths) has to be present if $a < 0$.

To understand physically the reason of this dissymmetry, one can think of the boundary layer we are imposing when given a Dirichlet condition at the outflow of the domain Ω_1 (with $a > 0$). Let y be the thickness of this boundary layer, when the diffusion term is equivalent to the advection term, $\nu u/y^2 \sim au/y$. As a consequence, $y/l \sim Re^{-1}$. The condition given by Eq. (4.40) means that to avoid divergence, δ must be bigger than the boundary layer y created by imposing the Dirichlet condition at $x = \delta$ as shown in Fig. 4.3. Here, the overlap zone is necessary to have a convergent approach. This could explain the necessity for Stanford researchers to impose a body force in their coupling strategy. Precisely, for high Reynolds simulations, the RANS approach has effectively a lower Reynolds number than the LES approach so that the downstream RANS zone of influence would be even bigger as stated by the relation of y and Re.

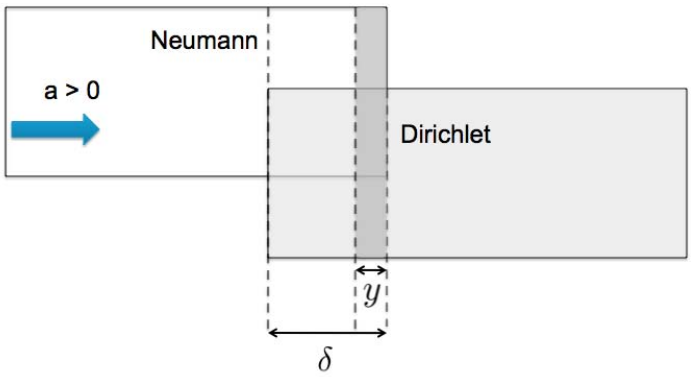

Figure 4.3: Neumann/Dirichlet method for $a > 0$: y and δ.

The goal of this section was to propose a general method to analyze the convergence of the DDM in a 1D problem. Of course a lot of researchers have already tried to answer the questions we have here raised. Among the most important, one can cite Lions [107] that was not only the first to study the Schwarz additive problem in two domains but has also developed the method for N domains. The

convergence for higher space dimensions has been investigated profusely by Dolean *et al.* [41], Gander *et al.* [59], Quarteroni *et al.* [146]. We refer the reader to Lui [109] for the study of the DDM applied to the Navier-Stokes equations. This section is only a preview of what can happen in multidimensional and complex problems, it however confirms the suitability of the proposed coupling strategy.

In the previous continuous analysis, the reaction term comes from the Laplace transform. This term will come from the time discretization in the real computations, where s will be related to the time step. Note that when this term is not present, the Dirichlet/Neumann method with $a < 0$ can not converge for high Reynolds numbers (cf Eq. (4.40)). The reaction term is thus favorable to the convergence of the Dirichlet/Neumann method.

4.3 Time step influence

In this section, we will no longer perform a Laplace transform since the goal is to establish a relation between the convergence rate and the temporal evolution. The usual approach is to combine the Schwarz procedure with the semi-discretization in time of the equations [107]. A simple implicit backward Euler scheme can be used to build an approximation of $\frac{\partial u_1}{\partial t}$ and $\frac{\partial u_2}{\partial t}$. We analyze the space and time decomposition iteration for an advection-diffusion equation in one dimension:

$$\begin{cases} \widetilde{F}u = -\nu\dfrac{\partial^2 u}{\partial x^2} + \dfrac{\partial u}{\partial t} + a\dfrac{\partial u}{\partial x} = 0 & \forall x \in \Omega = (-l_1, l_2) \\ u = g(x) & \text{at } t = 0 \\ u = 0 & \text{at } x = -l_1, l_2 \end{cases} \tag{4.42}$$

where l_1 and l_2 are positive. The aim is to determine a relaxation between k, Δt and possibly the other coupling parameters. In Fig. 4.4, one can see a coupling for which the convergence is achieved with 3 sequential coupling iterations inside each time step.

The recursive system of equations to study this problem is the one we called unrelaxed sequential with Dirichlet/Dirichlet conditions in the two previous sections. Additionally the initial conditions are here defined.

$$\begin{cases} \widetilde{F}e_1^{k+1} = 0 & \forall x \in \Omega_1, \\ e_1^{k+1} = 0 & \text{at } x = -l_1, \\ e_1^{k+1} = e_2^k & \text{at } x = \delta, \\ e_1^{k+1}(x,0) = 0 & \text{for } t = 0. \end{cases} \tag{4.43}$$

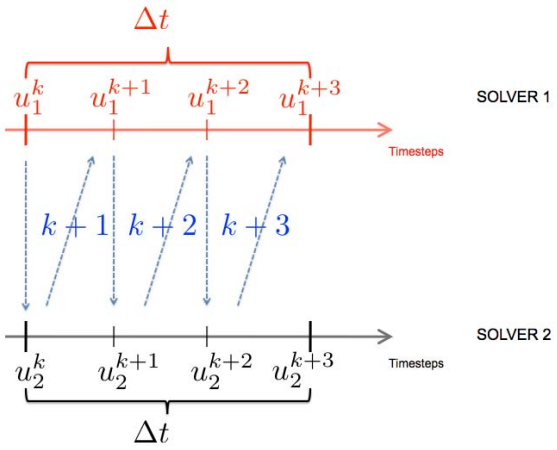

Figure 4.4: Example of coupling: in each time step, 3 sequential coupling iterations are performed.

$$\begin{cases} \widetilde{F} e_2^{k+1} = 0 & \forall x \in \Omega_2, \\ e_2^{k+1} = 0 & \text{at } x = l_2, \\ e_2^{k+1} = e_1^{k+1} & \text{at } x = -\delta, \\ e_2^{k+1}(x,0) = 0 & \text{for } t = 0. \end{cases} \tag{4.44}$$

Giladi & Keller [61] prove that such a system of equations determines the evolution of the error at a fixed time level Δt as a function of the iteration number k such that:

$$\frac{||e_i^{k+1}||_{\Delta t}}{||e_i^0||_{\Delta t}} \leq exp\left(\frac{Re}{2}\right) exp\left(-\frac{(2\,(k-1)\,\delta)^2}{\nu\,\Delta t}\right) \qquad \text{with} \qquad k \to \infty \tag{4.45}$$

We are not including the details of the demonstration. All necessary lemmas and proofs can be found in [61]. The bound condition for the iteration depends on the overlap length δ, the size of the time window Δt (or temporal integration time step) and the diffusion coefficient ν. The asymptotic convergence rate is governed by the diffusion of the error across the overlap between the subdomains and appears through the dimensionless factor $\dfrac{\delta^2}{\nu\Delta t}$. The use of a high time window or a small overlap length does not affect convergence rate if a small diffusion coefficient is used (high Reynolds flow). Gander *et al.* [58] arrive to the same conclusion on the convergence rate dependency for such an algorithm with a Laplace transform method, similarly to the procedure employed in the two previous sections, taking the supremum in time on a bounded time interval (each coupling state can be seen as a steady state, the temporal term in $\dfrac{1}{\Delta t}$ playing the role of our reaction term).

4.3.1 The hyperbolic limit

If Eq. (4.45) is analyzed when Re is high:

$$\frac{||e_i^{k+1}||_{\Delta t}}{||e_i^0||_{\Delta t}} \leq \left[exp\left(-\frac{a\,\delta}{\nu}\right) + exp\left(-\frac{a\,l}{2\nu}\right)\right]^2 \tag{4.46}$$

which is valid for all $t > 0$ and $k \geq 1 + \frac{1}{2\pi}\frac{\nu}{a\,\delta}$ [61]. In the hyperbolic limit, the exponential decay is governed by the two Reynolds numbers respectively based on δ and l but is independent of Δt! When ν tends to zero, the asymptotic convergence rate tends to zero.

In the DDM proposed, we have considered the coupling algorithm directly without discretization. The spatial domain has been divided in two subdomains with an overlap. We have solved iteratively time dependent problems on each subdomain through exchange information at boundaries. The interest of this procedure was to analyze the dependency of ρ with all the domain decomposition parameters so as to define which decomposition yields the minimum coupling iteration number for solving the problem for a certain precision. Then, in this section, the goal was to find a relation between ρ and the time discretization Δt.

4.4 Coupling parameters influence

Aside from the influence of k or Δt, the impact of the other coupling parameters (relax coefficient, overlap length, etc) can be analyzed. In this section, only the sequential approach with Dirichlet/Neumann transmission conditions is studied for the problem expressed in Eq. (4.42) since they will be the ones implemented in the real test cases.

4.4.1 Theoretical approach

Some ideas of additional test cases come from the conclusions of Section 4.2. As can be deduced from the following Table 4.3, Dirichlet/Neumann transmission conditions allow to have an overlap length null, i.e, $\delta = 0$ with $a > 0$, and still are able to achieve convergence when no relaxation is introduced. If the overlap length is not null, the bigger the overlap is, the faster the convergence is achieved.

		Rate of convergence ρ	Conditions for convergence
Unrelaxed sequential	Dirichlet/Neumann	$\rho_1\rho_2 \approx exp(-4\tau\delta)\dfrac{-R/Re}{1+R/Re}$	$\delta \geq 0$
Relaxed sequential	Dirichlet/Neumann	$\lvert 1+\theta(\rho_1\rho_2-1)\rvert$	$0<\theta<\dfrac{2}{1-\rho_1\rho_2}$

Table 4.3: Extract from Table 4.2 for Dirichlet/Neumann sequential approach with (θ_1,θ_2)=$(\theta,1)$ and $a>0$.

In this thesis, the procedure used is the relaxed sequential strategy with (θ_1,θ_2)=$(\theta,1)$. Therefore, the problem of interest here is:

$$\begin{cases} Fu_1^{k+1}=0 & \forall x\in\Omega_1,\\ u_1^{k+1}=0 & \text{at } x=-l_1,\\ \Phi_1(u_1^{k+1})=\theta\Phi_1(u_2^k)+(1-\theta)\Phi_1(u_1^k) & \text{at } x=\delta,\\ & \\ Fu_2^{k+1}=0 & \forall x\in\Omega_2,\\ u_2^{k+1}=0 & \text{at } x=l_2,\\ \Phi_2(u_2^{k+1})=\Phi_2(u_1^{k+1}) & \text{at } x=-\delta. \end{cases} \tag{4.47}$$

with $\Phi_1(u)=u$ and $\Phi_2(u)=\nu\dfrac{\partial u}{\partial x}n_x$.

We know that $\delta\nearrow$ implies $\rho_1\rho_2\searrow$ according to the expression in Table 4.3. But how does ρ evolve as a function of $\rho_1\rho_2$ in the sequential approach? As a function of θ? The relaxed convergence rate ρ can be seen as a surface in a 3D space (θ, $\rho_1\rho_2$, ρ) like in Fig. 4.5. It is however difficult to apprehend the possible behaviors of the convergence rate as a function of (θ, $\rho_1\rho_2$) by only looking at that figure. Transverse cuts of the surface are taken to simplify the analysis. First of all, one can study the evolution of the relaxed convergence rate as a function of the unrelaxed convergence rate in Fig. 4.6 but no conclusion can be drawn directly. The behavior of ρ towards $\rho_1\rho_2$ is not unique. ρ can as well increase or decreased with $\rho_1\rho_2$ depending on the value of the relaxation parameter. Note that $\rho_1\rho_2$ is always negative as predicted before (look at the sign of ρ_1 in Eq. (4.26)).

When $\rho_1\rho_2\searrow$, Fig. 4.6 becomes Fig. 4.7 (a) and (b) for $\theta\searrow$ and $\theta\nearrow$ within its limits. In the hyperbolic limit, $\theta\in(0,2)$ is the range of validity for θ as can be seen in Table 4.3.

It also has to be taken into account that $\rho_1\rho_2\ll 1$, so that Fig. 4.5 really becomes in the hyperbolic limit a line with a slope of an inverse triangle like in Fig. 4.8 (a). Some behaviors can be inferred from this study:

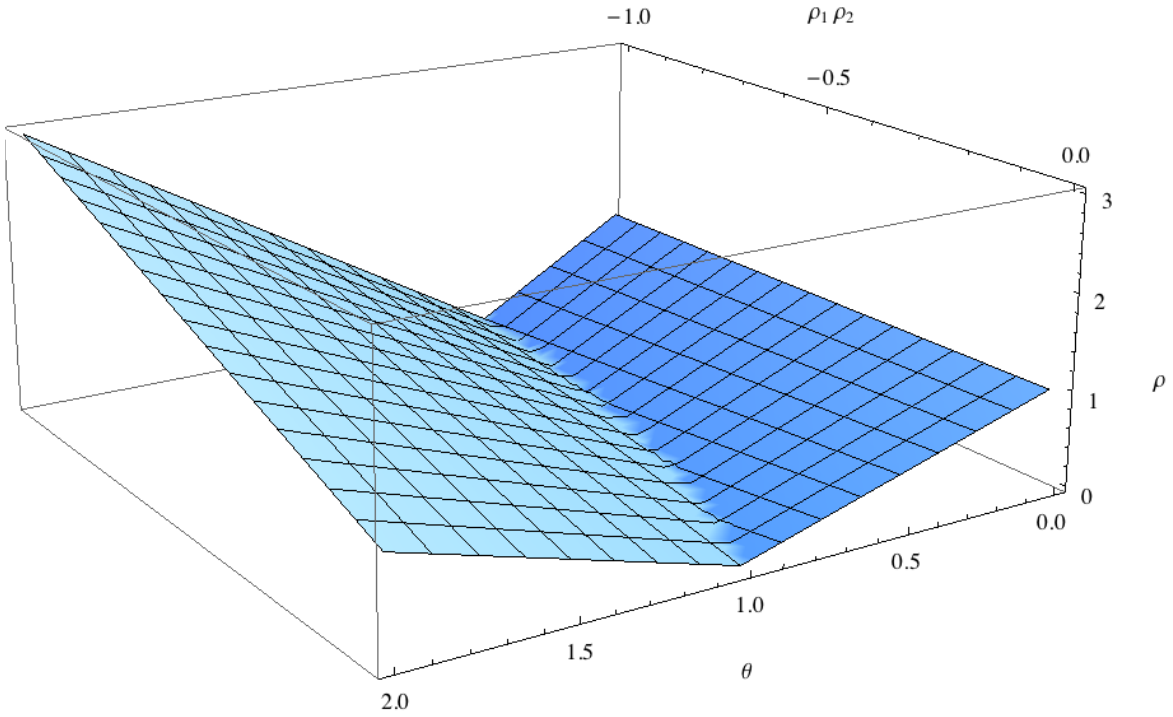

Figure 4.5: Surface of the relaxed convergence rate, ρ, as a function of ($\rho_1\rho_2$, θ), the unrelaxed convergence rate and relaxation parameter, respectively.

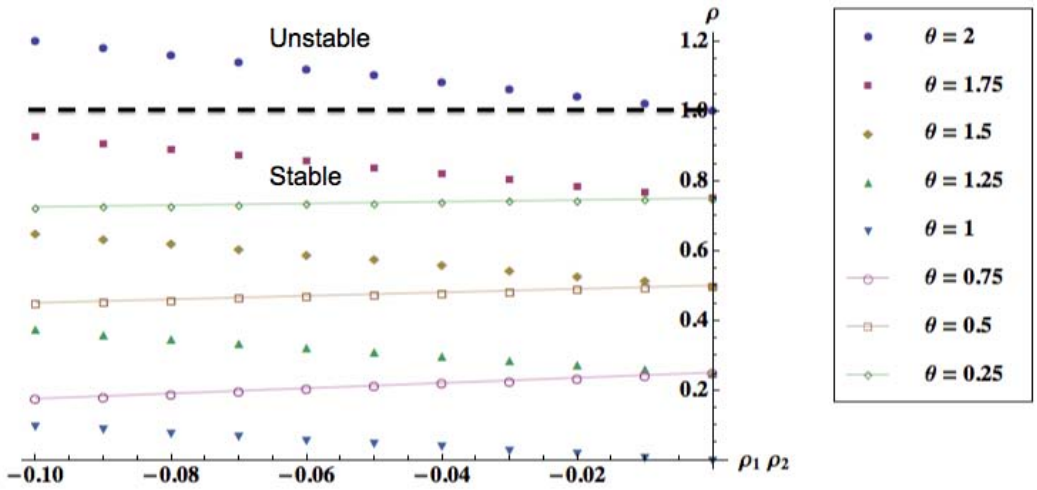

Figure 4.6: ρ as a function of $\rho_1\rho_2$ for several values of θ ∈ (0,2).

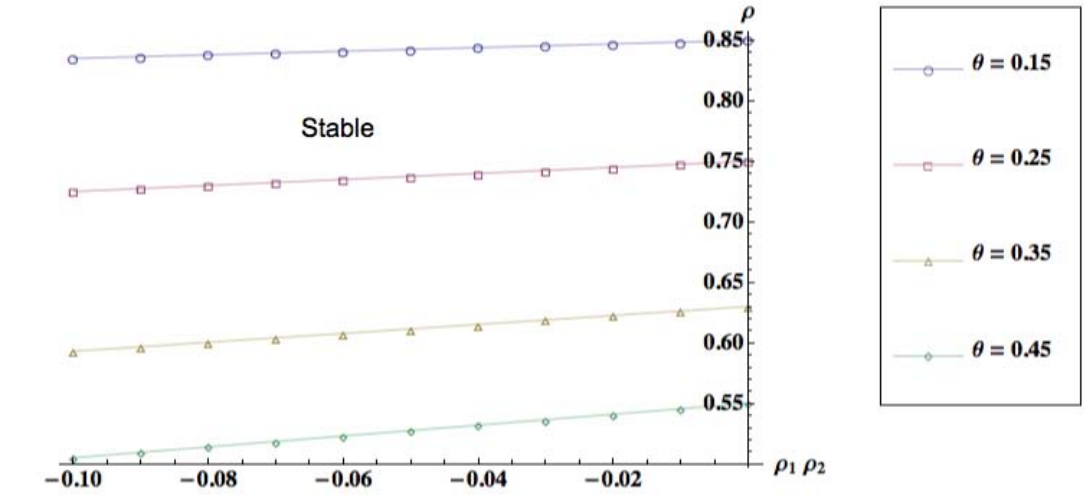

(a)

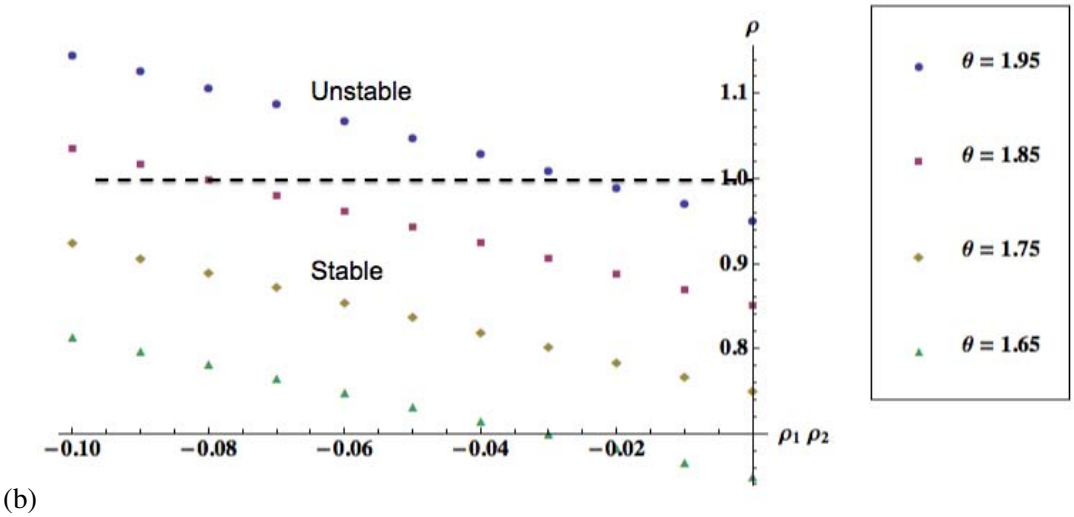

(b)

Figure 4.7: Two zooms of Fig. 4.6: ρ as a function of $\rho_1\rho_2$ for several values of θ: (a) for $\theta \to 0$ and (b) for $\theta \to 2$.

- ◇ for θ ∈ (0, ∼1): if θ ↗, ρ ↘.
- ◇ for θ ∈ (∼1, 2): if θ ↗, ρ ↗.

Figure 4.8 (b) also points out that beyond a limit for θ, the rate of convergence is not longer smaller than one confirming that θ must be chosen carefully.

Another way to study the global parameters influence is by means of a 1D numerical program. In the first part of next section, the convergence as a function of k will be analyzed. In a second part, we will study a time-dependent DDM problem with $k = 1$ at each time step.

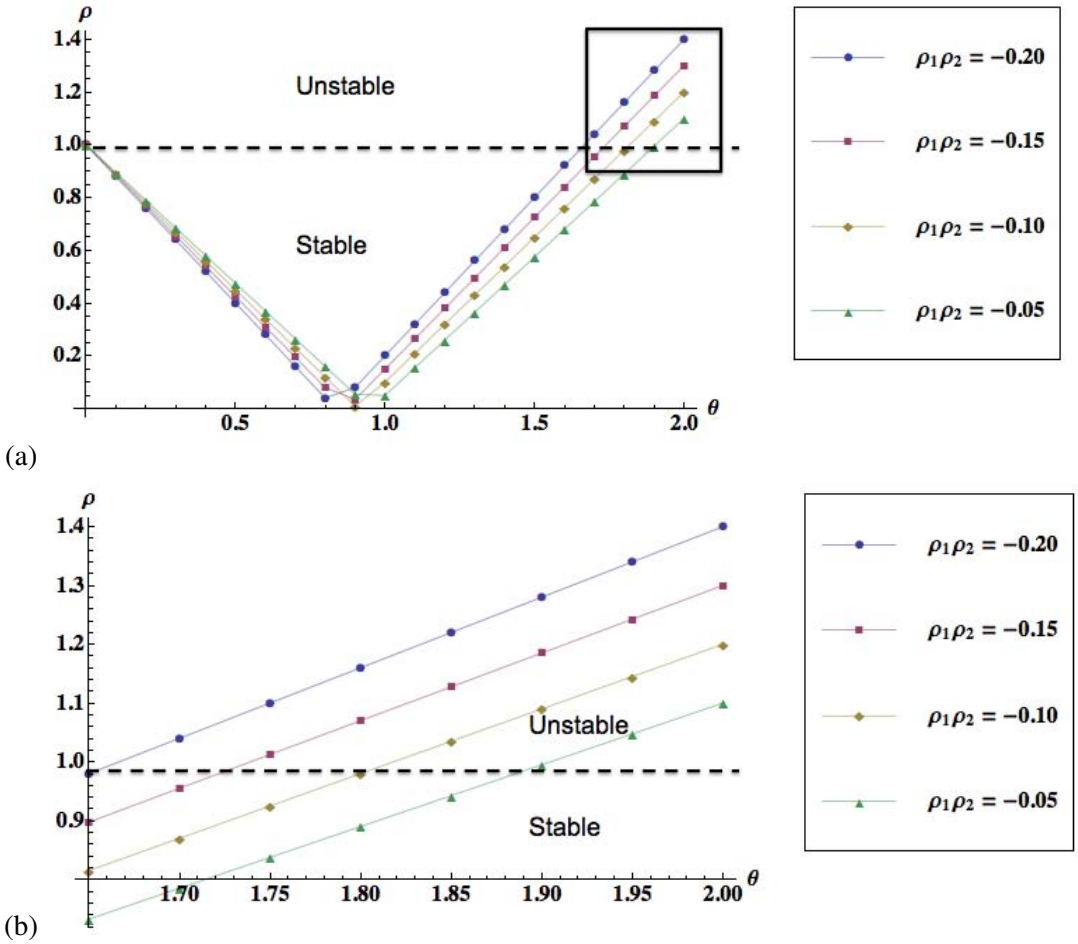

Figure 4.8: (a) ρ as a function of θ for several values of $\rho_1\rho_2$ tending to zero and (b) zoom of Fig. 4.8 (a) in the region of $\theta \sim 2$.

4.4.2 1D numerical calculations

4.4.2.1 Pseudo-steady state problem

Let's solve numerically the advection diffusion equation written in Eq. (4.19) by the DDM adopted: that is a sequential fashion and by use of the Dirichlet/Neumann conditions for -δ and δ respectively. At each time step, the equation can be seen as an ordinary differential equation depending solely on x and no longer as a partial differential equation (depend on x and t). The system to solve described by Eqs. (4.20) & (4.21) becomes a pseudo steady system with $s \sim \frac{1}{\Delta t}$ as written in Eq. (4.48) for the global problem and for the DDM problem in Eqs. (4.49) & (4.50). The computational domain goes from $-5 < x < 5$.

$$\begin{cases} -\nu\dfrac{\partial^2 u}{\partial x^2}+\dfrac{u}{\Delta t}+a\dfrac{\partial u}{\partial x}=0 & -5<x<5, \\ u(x)=0 & \text{at } x=-5, \\ \dfrac{\partial u}{\partial x}(x,t)=0 & \text{at } x=5. \end{cases} \tag{4.48}$$

The term in $\dfrac{1}{\Delta t}$ comes from the discretization in time. For a fixed time step, the term in $\dfrac{\partial u}{\partial t}$ can be seen as $\dfrac{u}{\Delta t}$. u here represents the current u in the time iteration. After the pseudo-discretization in time, we iterate in k. Indeed, the coupled system solves -with the simplification $(\theta_1,\theta_2)=(\theta,1)$- the following equations:

$$\begin{cases} -\nu\dfrac{\partial^2 u_1^{k+1}}{\partial x^2}+\dfrac{u_1^{k+1}}{\Delta t}+a\dfrac{\partial u_1^{k+1}}{\partial x}=0 & -5<x<\delta, \\ u_1^{k+1}(x)=0 & \text{at } x=-5, \\ \dfrac{\partial(u_1^{k+1})}{\partial x}=\theta\dfrac{\partial(u_2^{k})}{\partial x}+(1-\theta)\dfrac{\partial(u_1^{k})}{\partial x} & \text{at } x=\delta, \end{cases} \tag{4.49}$$

and

$$\begin{cases} -\nu\dfrac{\partial^2 u_2^{k+1}}{\partial x^2}+\dfrac{u_2^{k+1}}{\Delta t}+a\dfrac{\partial u_2^{k+1}}{\partial x}=0 & -\delta<x<5, \\ \dfrac{\partial(u_2^{k+1})}{\partial x}(x)=0 & \text{at } x=5, \\ u_2^{k+1}=u_1^{k+1} & \text{at } x=-\delta. \end{cases} \tag{4.50}$$

The numerical investigation is limited to the resolution of the linear system with constant coefficients. $\Delta x=\dfrac{L}{N}$ is the space discretization, where $L=10\,m$ is the total length and N, the number of uniform segments in which the domain is discretized. The nodes are $x_j=(j-1)\Delta x$ for $j=1,...,N+1$. A centered second order discretization in space reads:

$$a\frac{u_{j+1}-u_{j-1}}{2\Delta x}-\nu\frac{u_{j+1}-2u_j+u_{j-1}}{\Delta x^2}$$

This very simple scheme works fine only if the speeds a remains below a critical limit given by $|a_{crit}|=\dfrac{2\nu}{\Delta x}$. This comes from writing that the Pèclet number based on the mesh discretization equals 1.

$$Pe_{\Delta x}=\frac{|a|\Delta x}{2\nu}=1$$

If the space discretization is sufficiently refined, the scheme is stable since $Pe_{\Delta x}$ will be smaller than 1 and the $O(\Delta x^2)$ convergence is recovered.

The parameters values for the coupled baseline computation are given in Table 4.4. The reader should note that δ corresponds to half of the total overlap length. An enormous amount of different simulations can be done with such a DDM. Here are presented only the main results, focusing especially on the ones that confirm the trends deduced from the mathematical continuous analysis.

Δx	Δt	a	ν	ν_{num}	Re	L	δ	θ
1/100	1/100	1	0.005	0.005	2000	10	1	1

Table 4.4: Numerical parameters for the baseline computation.

With this set of numerical parameters the convergence is then measured based on a residual definition. This latter follows:

$$E = \int_{-\delta}^{\delta} ||u_1(x) - u_2(x)||dx.$$

We are calculating the estimated number of coupling iterations for a threshold $\varepsilon = 10^{-2}$ in the norm of this error. As can be seen in Fig. 4.9 (a), the problem is convergent in this case. In this figure is plotted the base-10 logarithm of the norm of the error between u_1 and u_2 in the overlap zone. The initial residual is reduced by a huge factor in one coupling step.

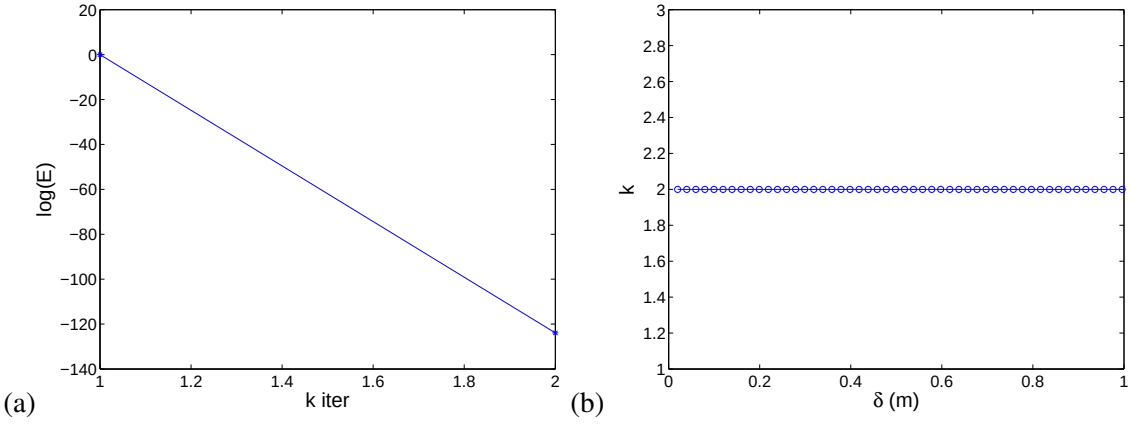

Figure 4.9: (a) Number of coupling iterations k needed for the relative error in the overlap to be under the threshold $\varepsilon = 10^{-2}$ with the numerical parameters of Table 4.5 and (b) number of coupling iterations k as a function of the overlap length.

Many other calculations have been performed (varying δ, the Reynolds number, ...). The main conclusions of these numerical 1D tests are that:

- ◇ The number of coupling steps is independent of δ (Fig. 4.9 (b)) and also of the Reynolds number. The relative error goes to zero whatever their values (even for $\delta = 0$), but the values of δ and Re (from 1 to 200.000) play a role in the rate of convergence as already noticed in Table 4.3 in the case of the hyperbolic limit. For all cases tested, the term coming from the discretization in time is the one driving the convergence. The smaller Δt, the bigger s (and R) and the better for achieving convergence and diminishing k.
- ◇ If Re is high, ρ tends to zero independently of Δt as proved in Section 4.3.1.
- ◇ Another interesting result is that when the term from temporal discretization is not present ($s = 0$), the Dirichlet/Neumann method converges in 1 step even though $s = 0$. On the contrary, for low Reynolds numbers, the DDM does not converge.
- ◇ For $s = 0$, the Dirichlet/Neumann method can not converge in the hyperbolic limit with $a < 0$, as previously shown mathematically. The solutions never get to agree in the overlap zone meaning that the gap between them never disappears with the advancement of k. To achieve convergence in the hyperbolic limit, the length of the overlap has to be of the same order of magnitude than the size of the Neumann subdomain. This solution has no interest for industrial applications. Hopefully, in our case, a time discretization term is always present and allows convergence (if one ensures that the overlap length is superior to $\frac{l}{Re}$).

In this section, we have pointed out the dominant role played by Δt. However, no particular novel aspects are introduced by this exercise with respect to the role played by the relax parameter or the overlap length in the convergence rate. Additional illustrations of their impact will be provided in the following paragraphs in a time-dependent problem. Gander *et al.* [58], Giladi & Keller [61] have shown that the error can be divided by a factor of 10^{-2} with $k = 1$. This level of accuracy seems sufficient for our purposes. In the following, $k = 1$ for each Δt. This choice is done not to penalize the coupling applications in process time.

4.4.2.2 Time dependent domain decomposition

Some questions of interest remain unanswered. For example, what happens if the initial guesses for the two domains are different? Can the coupled solution still converge? This kind of investigation needs to define initial conditions and thus, a dependency with time.

A very visual way to analyze the coupling approach if a time evolution appears is by means of a numerical toy. The reference solution is no longer the analytical solution but the one deriving from the sole domain computation. As said before, $k = 1$. This means that for each time step, only one coupling iteration is performed. The sequential coupling procedure follows the scheme plotted in Fig. 4.10.

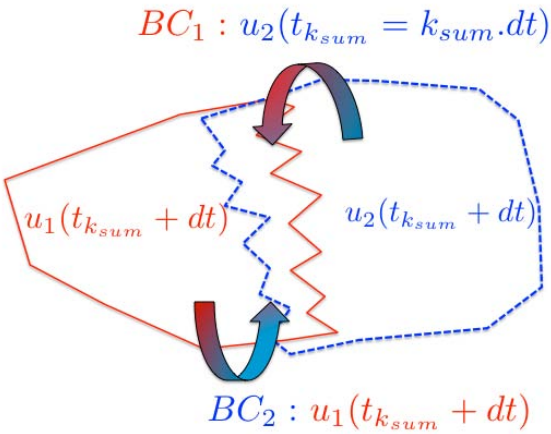

Figure 4.10: Sequential coupling strategy for $k = 1$.

It is equivalent to Fig. 4.4 with only one coupling iteration instead of 3. For iteration $k_{sum}+1$ (k_{sum} stands for the sum of all the iterations made, 1 coupling iteration corresponding to 1 time step), Solver 1 receives at its boundary condition (BC) the information of the previous time step from Solver 2. The solution of subdomain 1 is computed for $t_{k_{sum}} + dt$ and this information is given to Solver 2 to advance its scheme during the time step $t_{k_{sum}} + dt$.

The space-time domain decomposition of the advection-diffusion unsteady scalar equation is studied with a small diffusion coefficient. We consider the problem in the computational domain $(-5 < x < 5)$ defined by:

$$\begin{cases} -\nu\dfrac{\partial^2 u}{\partial x^2} + \dfrac{\partial u}{\partial t} + a\dfrac{\partial u}{\partial x} = 0 & -5 < x < 5, \quad 0 < t < T = 10, \\ u(x,t) = 0 & \text{at } x = -5, \\ \dfrac{\partial u}{\partial x}(x,t) = 0 & \text{at } x = 5, \\ u(x,0) = -exp(2.(x+3))^2 & -5 < x < 5. \end{cases} \tag{4.51}$$

The coupled system solves -with the simplification $(\theta_1, \theta_2) = (\theta, 1)$- the following equations:

$$\begin{cases} -\nu\dfrac{\partial^2 u_1^{k_{sum}+1}}{\partial x^2} + \dfrac{\partial u_1^{k_{sum}+1}}{\partial t} + a\dfrac{\partial u_1^{k_{sum}+1}}{\partial x} = 0 & -5 < x < \delta, \quad 0 < t < T = 10, \\ u_1^{k_{sum}+1}(x,t) = 0 & \text{at } x = -5, \\ \dfrac{\partial (u_1^{k_{sum}+1})}{\partial x} = \theta\dfrac{\partial (u_2^{k_{sum}})}{\partial x} + (1-\theta)\dfrac{\partial (u_1^{k_{sum}})}{\partial x} & \text{at } x = \delta, \\ u_1^0(x,0) = -exp(2.(x+3))^2 & -5 < x < \delta, \end{cases} \tag{4.52}$$

and

$$\begin{cases} -\nu\dfrac{\partial^2 u_2^{k_{sum}+1}}{\partial x^2}+\dfrac{\partial u_2^{k_{sum}+1}}{\partial t}+a\dfrac{\partial u_2^{k_{sum}+1}}{\partial x}=0 \qquad -\delta<x<5, \qquad 0<t<T=10, \\ \dfrac{\partial u_2^{k_{sum}+1}}{\partial x}(x,t)=0 \qquad \text{at } x=5, \\ u_2^{k_{sum}+1}=u_1^{k_{sum}+1} \qquad \text{at } x=-\delta, \\ u_2^0(x,0)=-exp(2.(x+3))^2 \qquad -\delta<x<5. \end{cases} \tag{4.53}$$

The initial solution as well the conditions at the boundaries are given by these two systems of equations which are based on the mathematical procedure analyzed in Section 4.2. The numerical investigation is limited to the resolution of the linear system with constant coefficients. The term $\dfrac{\partial u_i}{\partial t}$ is discretized with a first order explicit scheme, so one has to assure that the CFL = $a\,\dfrac{\Delta t}{\Delta x}\leq 1$ (to retrieve more information on the CFL number, the reader can refer to Appendix D). This complemented by the previous spatial stability condition (the same space discretization than in the pseudo-steady state is used) ensures numerical stability of the proposed solution.

We are working in the hyperbolic limit of the equations, when $\nu\to 0$ and $Re\gg 1$. The parameters values for the baseline coupled computation are given in Table 4.5, they are the same as when the pseudo-steady system was studied. The reader should note that δ corresponds to half of the total overlap length.

Δx	Δt	a	ν	ν_{num}	CFL	Re	L	δ	θ
1/100	1/100	1	0.005	0.005	1	2000	10	1	1

Table 4.5: Numerical parameters for the baseline computation.

We solve the problem with two subdomains with an initial overlap set to 20% of L. As can be seen in Fig. 4.11, the transmissions condition grants the information to be convected and very weakly diffused. Indeed, we have chosen the limit of stability CFL = 1 and $\nu_{num}=\nu$. This set of numerical parameters allows to have precise results so that we can better discern the origin and influence of the errors when varying the coupling parameters.

The snapshots of Fig. 4.11, in which the overlap is displayed, show that the coupling algorithm works even when $k=1$. The solutions from subdomain 1 and 2 overlay for almost each x and t. However differences subsist. It is not simple to distinguish the errors between the subdomain solutions in the overlap zone and between the subdomains solutions and the reference solution u in

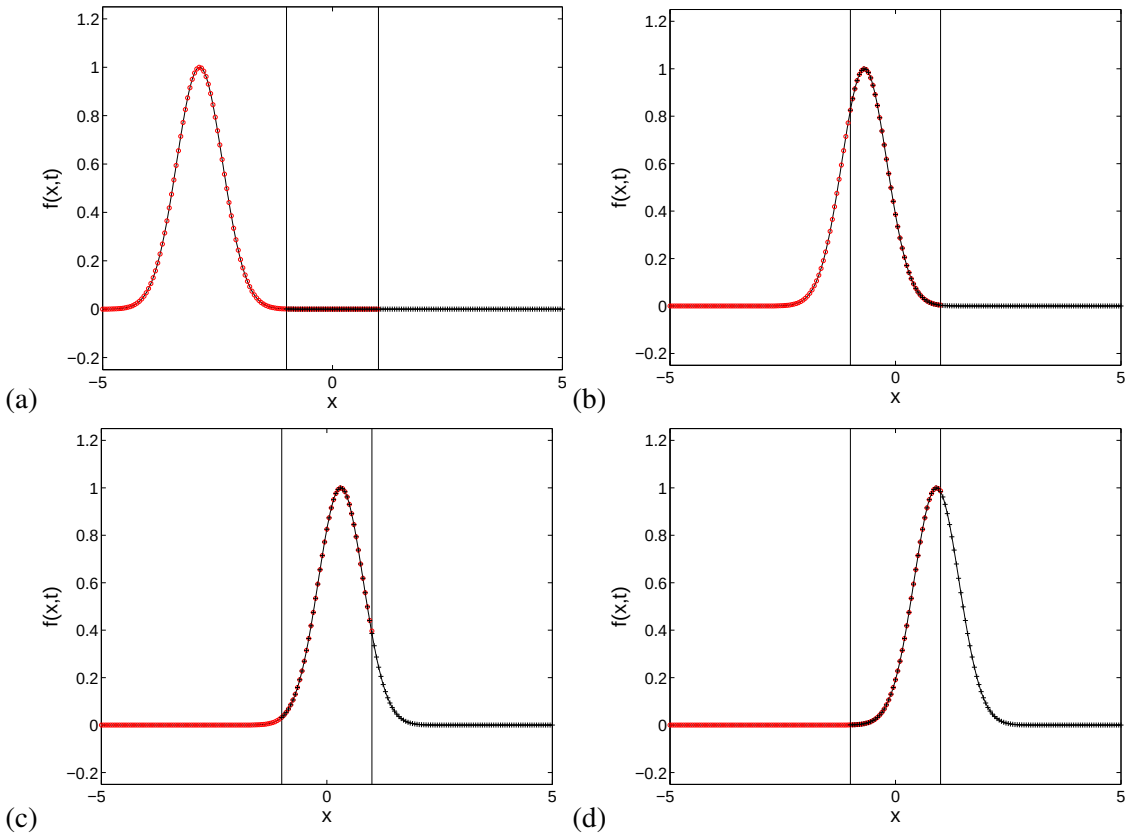

Figure 4.11: Evolution with time of the solution of the entire domain u (solid line), u_1 (red circles) and u_2 (black crosses).

such figures. In the following, the relative errors will be analyzed instead. They depend on time and space. The three interesting quantities to study are:

- $E_i(t)$, which corresponds to the integrated subdomain error with respect to the numerical "exact" solution for each time step. The expression of such an error is

$$E_i(t) = \int_x ||u_i(x,t) - u(x,t)||dx = \int_{-5}^{\delta} ||u_1(x,t) - u(x,t)||dx + \int_{-\delta}^{5} ||u_2(x,t) - u(x,t)||dx$$

  It underlines when the error is generated and how it evolves in time.

- $E_{12}(t)$ stands for the relative error between the solutions:

$$E_{12}(t) = \int_x ||u_1(x,t) - u_2(x,t)||dx$$

- E_i stands for the overall integrated error:

$$E_i = \int_t \int_x ||u_i(x,t) - u(x,t)||dx\, dt$$

In the next paragraphs, the influence of different aspects of the coupling on these errors is analyzed. In this section are only presented the most significative behaviors encountered when studying:

Influence of the initial solution

Let's modify the initial state of the subdomain 1 such that

$$\left\{ u_1(x,0) = u(x,0) + 0.05 = -exp(2.(x+3))^2 + \mathbf{0.05} \qquad -5 < x < \delta. \right. \tag{4.54}$$

The other parameters of the computation remain unchanged and $u_2(x,0) = u(x,0)$ for $-\delta < x < 5$. In Fig. 4.12 (a), we study the evolution of $E_i(t)$ for each subdomain. The coupled computation seems unable to forget the initial state of the problem (this behavior was already pointed out in Section 4.1). It is interesting to notice that even though the initial error remains with respect to the "exact" solution u at the end of the simulation, the relative error between u_1 and u_2 disappears as plotted in Fig. 4.12 (b).

Other simulations have been performed varying the relax parameter value and δ with this set of initial solutions. No major influence of the relax or the overlap length values (several have been tested) is noted on the trends here deduced when respecting the mathematical limits previously found for these parameters.

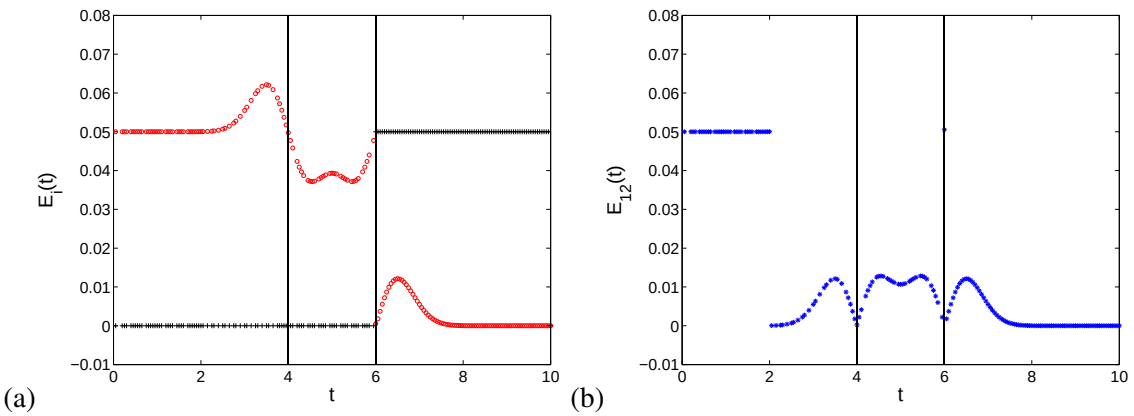

Figure 4.12: Influence of the initial condition: (a) $E_1(t)$ and $E_2(t)$ (red circles correspond to subdomain 1 and black crosses to subdomain 2) and (b) the evolution with time of the relative error between u_1 and u_2. Overlap appears here in time.

In the following, note that the initial solution has been chosen not to have any interaction with the overlap zone at $t = 0$ like in Fig. 4.11(a) and $u_1(x,0) = u(x,0)$ and $u_2(x,0) = u(x,0)$.

Influence of the overlap region

We analyze the influence of δ in the resolution of the system defined in Eqs. (4.52) & (4.53) with the parameters gathered in Table 4.5. Only the value of δ varies. The ρ calculated by resolving such a system is equal to zero at each time step for all δ, which means that having this set of numerical parameters and $k = 1$ is sufficient to achieve convergence at each time step. The time step reaction term is the one that drives convergence. As seen in Eq. (4.45), the coefficient directing the convergence rate is $\frac{\delta^2}{\nu \Delta t}$. In this particular case, Δt is so little that no major influence of δ can be appreciated.

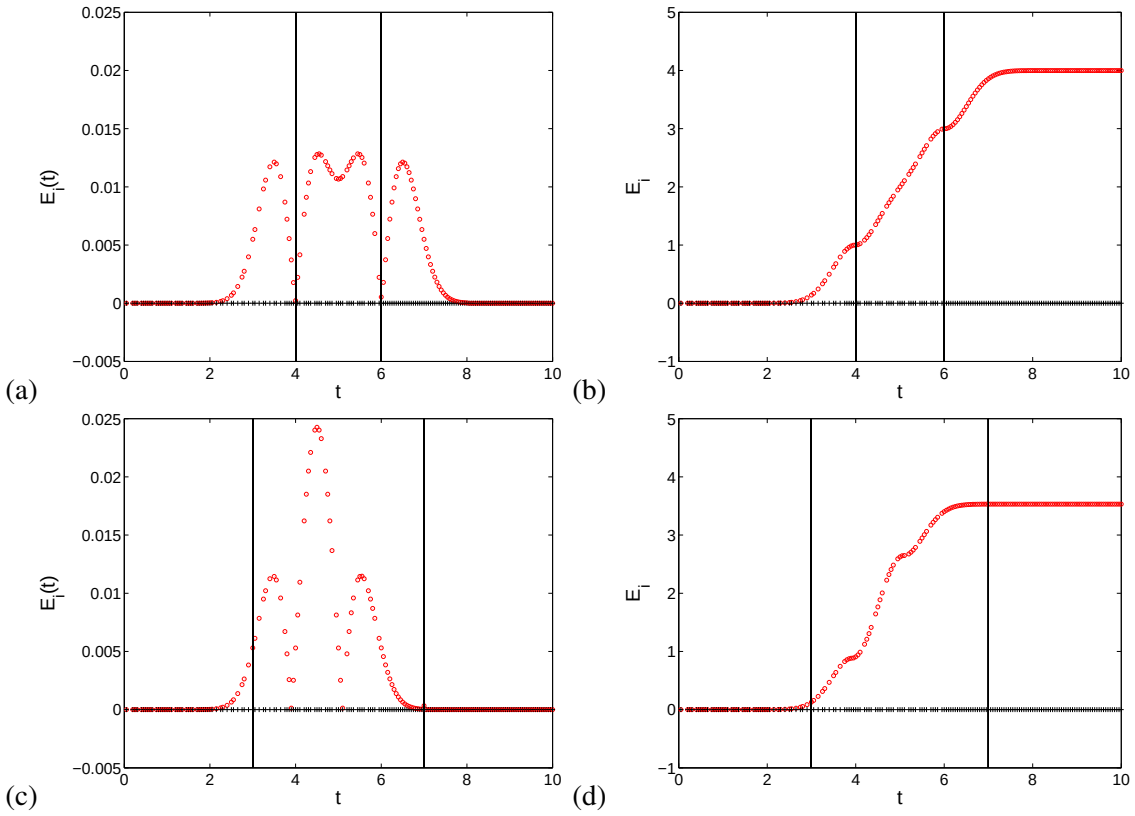

Figure 4.13: Influence of the overlap extent: $E_i(t)$ and E_i for $\delta = 1$ ((a) & (b), respectively) and $\delta = 2$ ((b) & (c), respectively). Red circles correspond to subdomain 1 and black crosses to subdomain 2.

One can however study in detail the errors induced by the change of δ and draw some conclusions. Figure 4.13 (a) and 4.13 (c) emphasize the impact of the overlap length on the coupling procedure. The error (concentrated only in the subdomain receiving the Neumann condition) evolves completely differently depending on the overlap extent (plotted also in the figures). The cumulated error, whose value is the one corresponding to $t = 10$ in Figs. 4.13 (b) and 4.13 (d), is however very similar although its temporal evolutions progress disparately. Note that $E_i(t)$ is at most equal to 0.025 which

represents 2.5% of the maximum in the Gaussian propagation curve. The error E_i is smaller for $\delta = 2$. Henceforth, the overlap extent used in all the following simulations will be equal to 2.

Influence of the relax parameter

When analyzing the behavior of the errors previously defined for the baseline coupled computation but now with $\delta = 2$ and $\theta = 2$, differences in the behavior appear after $t = 6$ in Fig. 4.14 (a) with respect to Fig. 4.13 (c). Fig. 4.14 (b) gives a better insight to what is happening. The error is no longer bounded at the end ($t = 10$). It continues to increase. If $\theta > 2$ is employed, the error goes to infinity. This results coincide with the limit predicted with the mathematical analysis in the hyperbolic limit in Table 4.3: θ can not be equal or superior to 2.

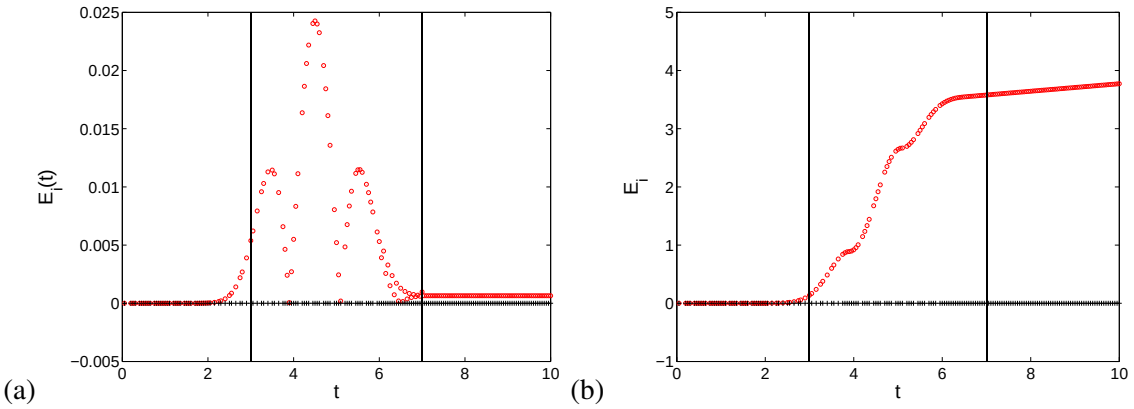

Figure 4.14: Influence of the relax parameter: $E_i(t)$ and E_i, (a) and (b) respectively, for $\theta = 2$. Red circles correspond to subdomain 1 and black crosses to subdomain 2.

Waves traveling upstream

For $a < 0$, the behavior has been analyzed in depth in previous sections. With this toy, the same main conclusions about the considerable impact of δ are recovered. For little values of δ, the computation does not provide acceptable results. For certain values of δ, the results show good agreement like in Fig. 4.15 (a).

The main conclusion is that the choice of δ may have a repercussion on the quantities transmitted. δ acts like a filter inducing a dispersion of the signal transmitted to the neighboring subdomain. Great care has to be taken when treating problems where there is coherence in time at the interfaces between the subdomains so as to avoid situations like the one plotted in Fig. 4.15 (b), where reflections in the Dirichlet boundary create a wave that propagates upstream with a phase-shift.

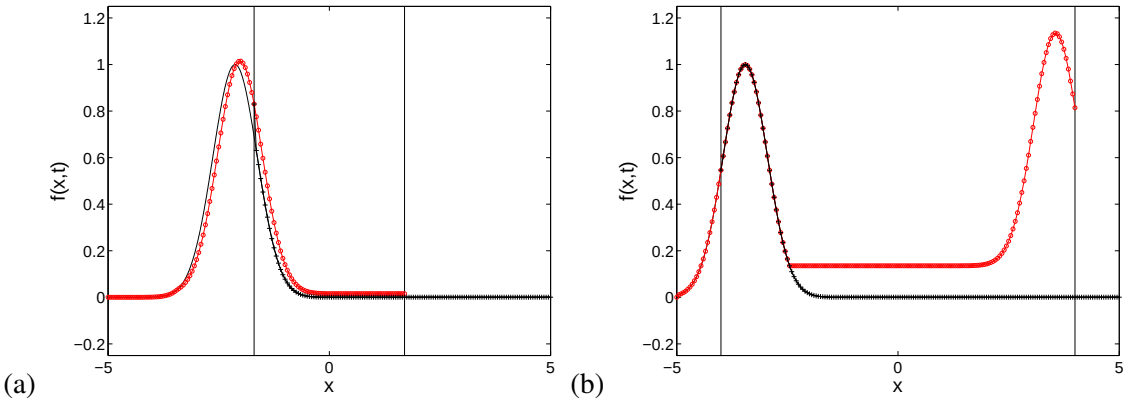

Figure 4.15: Evolution with time of the solution of the entire domain u (solid line), u_1 (red circles) and u_2 (black crosses) for a wave traveling upstream with (a) $\delta = 1.7$ and (b) $\delta = 4$.

Apart from the influences already studied, some other interesting tests can be done which are not directly related to our coupling methodology.

Aliasing

If coherence in time has to be ensured at the boundaries, it is peremptory to iterate between the subdomains at each time step to avoid aliasing of the quantities transmitted, as can be seen in Fig. 4.16 (a) & (b). Here, the solvers do not exchange at each iteration but at multiple of each iteration. The boundary conditions are no longer updated at each iteration. Aliasing could be another full-fledged dissertation, we will not confront to this topic in this manuscript. For more information, the reader can look up in Moreau [127], Schlüter *et al.* [160].

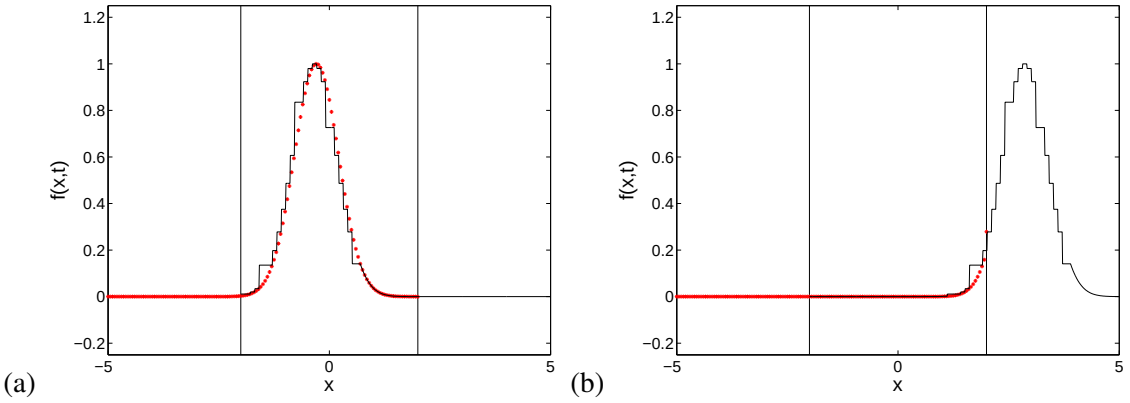

Figure 4.16: Evolution with time of the solutions of both subdomains if information is not exchanged at each time step (u_1 in red starts and u_2 in solid line).

Low Reynolds simulation

The toy enables the use of low Reynolds numbers coupled computations. When the Reynolds number goes from 2000 to 200, ρ is no longer zero but 0.9. The decrease of the Reynolds number lowers the convergence rate, as pointed out in the mathematical developments. The difference with previous computations is only that ν has been increased by a factor of 10, so that Δx is now $\frac{1}{\Delta x} = 0.1$ to guarantee numerical stability.

4.4.3 Concluding remarks

This last section has served to illustrate the earlier theoretical parts. The same major conclusions are drawn from these simulations of the coupled 1D problem. This simple 1D coupled computation enables the analysis of the coupling parameters influence before going to more difficult configurations. It has emphasized the interconnection between all the parameters intervening in the coupling process. The tool has turned out to be very powerful and unfortunately, only a little percentage of its capacity has been exploited. The last two paragraphs (aliasing and low Reynolds influence) underline the potential of this tool. Moreover, numerical stability has not been studied in depth in this chapter and should be considered before further developments.

More generally, we have designed a domain decomposition inspired by the work of mathematicians in the field of DDM. We have reduced the system to scalar equations and analyzed the influence of positive and negative eigenvalues of the uncoupled Euler system of equations. The resulting algorithm behaves well for advection dominated equations. A more comprehensive 1D numerical test has been performed to assess the applicability of the proposed procedure to large scale computations even at high Reynolds number. This work can also be seen as a first step for deriving domain decomposition methods for coupling the 2D or 3D compressible Navier-Stokes equations.

As pointed out before, the numerical toy allows to compare all the types of equations (pure diffusion, advection, equation without reaction term, etc) in the DDM procedure. For most of them, an analytical expression is available in the pseudo-steady state. A good exercise for future students or researchers could be to further develop the embryo here presented on such different types of equations. It could be interesting to run the tool for two types of equations in each subdomain (different ν_i or even different Δt_i) so as to test a 1D LES/RANS coupling.

Another aspect of the coupling regarding pure diffusion has also been analyzed in the context of fluid/solid conjugate heat transfer, cf Appendix C.

5

Coupled test cases

Contents

¿Qué te parece desto, Sancho?–dijo Don Quijote–
Bien podrán los encantadores quitarme la ventura,
pero el esfuerzo y el ánimo será imposible.

El Ingenioso Caballero Don Quijote de la Mancha,
Miguel de Cervantes

5.1 Memento on the strategy to validate the coupling approach

In the previous two chapters, the question that has been treated is how to determine consistent boundary conditions for coupled simulations that would require an exchange of information at the interfaces of the computational domains. To sum up what has been explained in previous sections, one can plot the approach implemented in Fig. 5.1:

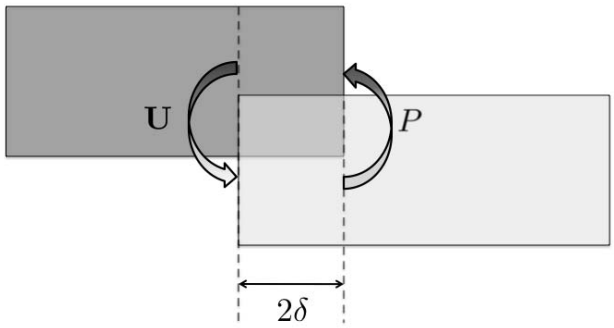

Figure 5.1: Diagram of the coupling procedure.

- ◇ The vector of conservatives variables, $\mathbf{U} = (\rho, \rho u, \rho v, \rho w, \rho E)+(\rho k, \rho l)$ when needed, is interpolated in the first two rows of cells of the downstream subdomain. The downstream solver uses this information to advance its scheme.
- ◇ The pressure from the downstream domain is imposed via the boundary formulation of the upstream subdomain.

2δ is the overlap length. The first point corresponds to imposing a Dirichlet condition for what is ought to become the inflow of the RANS subdomain. The second point is equivalent to applying a Neumann condition to characteristic variables. In AVBP, to go from the characteristic variables to the conservatives ones, an inversion of a matrix is sufficient as stated by Eq. (3.5). Our coupling follows a sequential approach as pictured in Fig. 3.9. The Dirichlet/Neumann transmission conditions are the most appropriated method for advection dominated flows, as the Neumann and Dirichlet conditions are imposed according to the hyperbolic character of the equation, as deduced in Chapter 4. The Neumann condition is relaxed but the Dirichlet condition is not. The couple (θ_1, θ_2) becomes $(\theta, 1)$, which was the simplification made in Chapter 4.

The strategy followed in this thesis to validate the coupling procedure is to perform the first steps detailed in Table 5.1. This table gathers the applications of increasing difficulty, some of which are detailed in the coming sections.

DNS/DNS			**Consistency of coupling**	**Test case**
	Re $\sim$ 500	Steady	Space	Laminar tube
	Re $\sim$ 100	Unsteady	Time and Space	Cylinder tandem
LES/RANS				
	Re $\sim$ 20 000	Unsteady/Steady	Of averaged fields in Space	Turbulent tube
	Re$\sim$ 100 000	Unsteady/Steady	”	To be defined
	$\downarrow\downarrow\downarrow$	$\downarrow\downarrow\downarrow$	$\downarrow\downarrow\downarrow$	$\downarrow\downarrow\downarrow$
	Re $\sim [1e^4\text{-}1e^6]$	Unsteady/Steady	”	Combustion chamber + turbine

Table 5.1: Table of increasingly difficult test cases, some of which are employed in this thesis to validate the coupling strategy.

- ◇ The first application to be faced is the Poiseuille tube whose analysis will serve to validate the methodology. This case is fully laminar and steady so the problem reduces to the resolution of a DNS/DNS coupled simulation spatially consistent at the interface. Temporal iterations are only required to eliminate errors introduced by the initial solutions.
- ◇ Secondly, the outflow LES condition is inspected in a configuration where a recirculation zone is present: the arrangement of a tandem of cylinders. This case is laminar but unsteady. There should be consistency in time and space at the interface between the two subdomains for the solution to be fully equivalent to a single domain CFD solution.
- ◇ Thirdly, to investigate the turbulent variables transfer, a high Reynolds number tube is studied with a fully developed LES/RANS coupling strategy. In this test case, the sliding average influence on the turbulent variables is going to be analyzed.
- ◇ At last, before applying the coupling procedure to an industrial case, the methodology should be tested on an academic configuration with a high Reynolds number: cylinder tandem [106] or rod + profile [25] are good candidates for such a simulation as experimental and numerical data is available for both simulations. This computation would stand for a very simplified combustion chamber/turbine simulation and will show the improvements available with such a coupling in those kinds of computations and if compared to a mere chaining between AVBP and *elsA* (respectively used in their LES and RANS modes).

To retrieve more details of the computing background behind the AVBP/*elsA* coupling, the reader can refer to Appendix D.2.

5.2 Poiseuille tube

The reasons to choose a laminar tube as a first application case have been three-folds:

- ◇ the simplicity of the geometry and implementation,
- ◇ the pure advective problem and turbulence free context,
- ◇ the analytical solution available, which can serve to gauge the coupled results directly.

Despite its low difficulty, the resolution of a Poiseuille flow is not trivial. Its simplicity may pitilessly bring to light any default of the methodology. For example any inconsistency in the initial guesses supplied to AVBP and *elsA* will exhibit issues as discussed in Chapter 4. Table 5.2 below gathers the general features of the flow in this laminar tube.

Governing Equations:	**3D Navier-Stokes**
Flow regime:	**laminar**
Turbulence:	**no turbulence**
Chemistry model:	**no chemistry**
Number of species:	**1 (air)**
Number of reactions:	**0**
Reynolds number:	$\approx$ **500** (Based on diameter and mean axial velocity)
Mach number:	$\approx$ **0.02**

Table 5.2: General flow characteristics

5.2.1 Computational domain

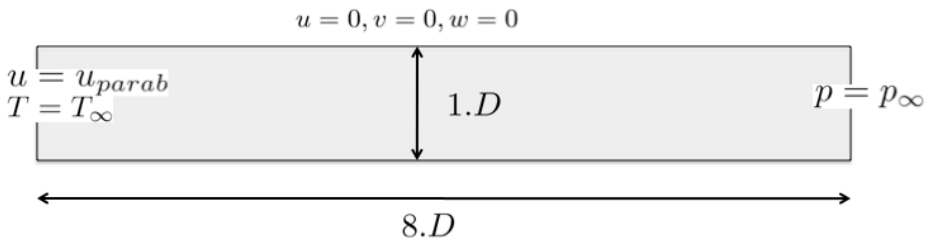

Figure 5.2: Transverse sketch of the global computational domain.

The computation domain is illustrated in Fig. 5.2. It is a circular section tube whose length is set to 8 diameters. The diameter D is 1mm. The boundary conditions can be written as:

- ◇ For the inlet, $u_{parab} = 2.u_{mean}(1 - \frac{r^2}{R^2})$, $v = 0$, $w = 0$ and $T = T_\infty$,
- ◇ For the outlet, $p = p_\infty$,
- ◇ For the walls of the tube, $u = 0$, $v = 0$, $w = 0$,

where r is the radial cylindrical coordinate and u_{mean} the mean axial velocity. At the inlet, a parabolic profile is imposed in agreement with the analytical solution of such flow. The profile has a mean axial velocity of $7.5m/s$, which corresponds to a Reynolds number based on the diameter of approximately 500, resulting in a fully laminar flow. T_∞ is the free-stream temperature and p_∞, the atmospheric pressure.

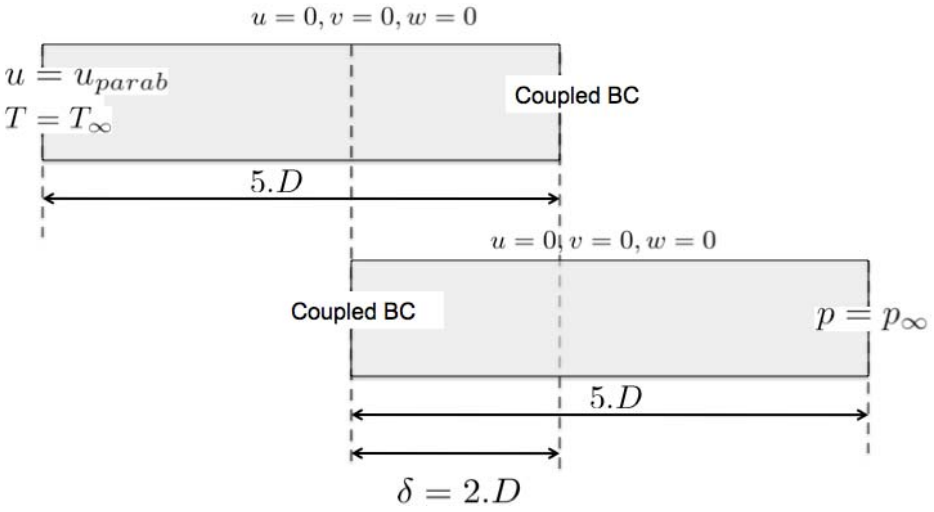

Figure 5.3: Sketch of the computational domain for the AVBP solver (left) and the *elsA* code (right).

Taking a transverse cut of the Poiseuille tube, the two subdomains for the coupled resolution are illustrated in Fig. 5.3. Note that the tubes are positioned at the same vertical abscissa but for clarity the second one has been translated in the vertical direction in the figure. The overlap zone is equal to $2D$. As explained in Chapter 3, the idea is to interpolate the information from the interior of the grid of the source solver to the boundary condition of the target solver. The AVBP computational domain is meshed with an O-grid arrangement using hexahedral elements. The *elsA* domain has also been meshed with this same philosophy and is divided in 5 structured blocks. Figure 5.4 gives an illustration of the meshes in this application and Table 5.3 gathers the mesh refinements for the AVBP and *elsA* computations.

The mesh density is quite similar for both subdomains but nodes have been deliberately chosen not to be coincident to test the interpolation effect on this simple application test case. This influence

	Δx	Δy	Δz	n° cells	n° points
AVBP	D/5	D/20	D/20	8500	11833
elsA	D/5	D/20	D/20	8500	11154

Table 5.3: Mesh refinements for the coupled AVBP and *elsA* domain.

was already studied in the AVBP/AVBP coupling methodology, whose results are not presented in this thesis. It is visible that the nodes are neither coincident in the axial (Fig. 5.4 (a)) nor in the radial direction (Fig. 5.4 (b)).

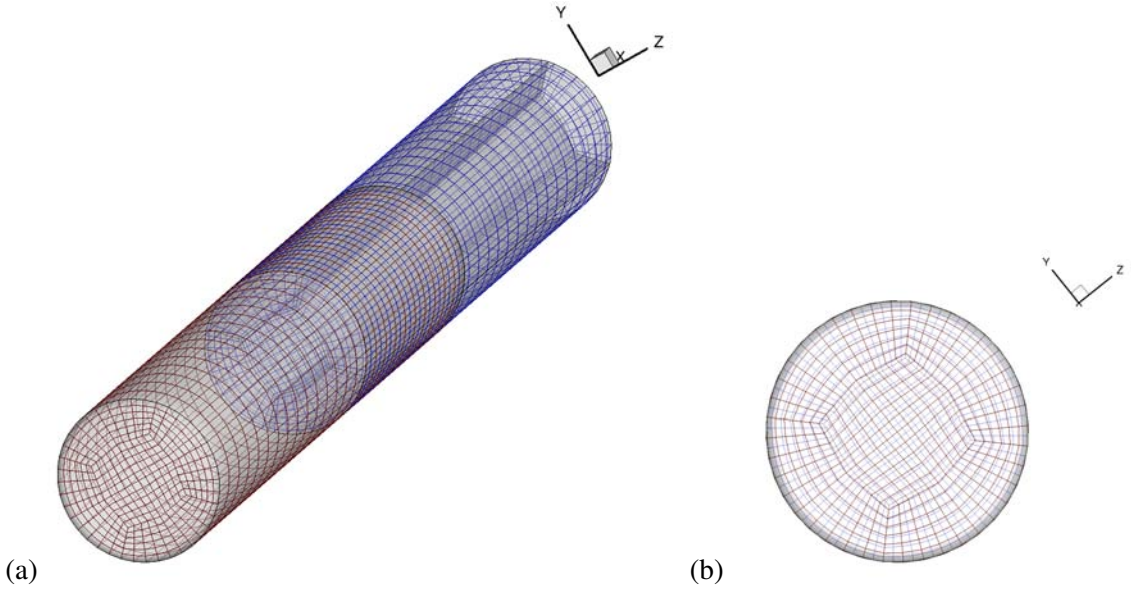

(a) (b)

Figure 5.4: (a) AVBP and *elsA* meshes and (b) transverse view of both meshes.

5.2.2 Numerical parameters

Neither LES nor RANS model is employed for the computation of the AVBP or *elsA* domain since the solution is laminar. Specificities about the numerics adopted for both codes are detailed below. The convective time of the global computation is approximatively:

$$t_{conv} = \frac{8.10^{-3}\ m}{7.5\ m/s} = 1.0677\ 10^{-3}\ s \tag{5.1}$$

In the present case, the time step from the AVBP computation has been fixed to $\Delta t = 1\ 10^{-8}\ ms$. AVBP solves the full compressible Navier-Stokes equations using TTGC scheme. TTGC is a version of the two-step Taylor-Galerkin (TG) schemes. This family of schemes is based on the finding that

finite-volume methods in a cell-vertex framework can be interpreted as a finite-element approach, allowing the development of Taylor-Galerkin type schemes. TTGC is of third order in time and space [39].

The parallel *elsA* software uses a cell centered approach on the 5 structured multi-block mesh. Convective fluxes are computed with a Roe scheme, third order limiter [76]. Diffusive fluxes are computed with a second-order centered scheme. The global time-marching is performed by the use of an implicit time integration approach with the same time step as AVBP but based on the backward Euler scheme and a scalar Lower-Upper (LU) Symmetric Successive Over-Relaxation (SSOR) method [197].

To compute a through-flow ≈100 000 iterations are needed. Each subdomain is calculated separately until the variables have reached the stationary state. Then, the codes are coupled sequentially after each time step to obtain the results shown here. In a second coupled simulation, the introduction of a coupling frequency in the coupling loop has also been evaluated. The coupling frequency defines how often the coupling transmissions are performed. Although, the solution is steady for this application and each subdomain has already reached the steady state separately, the speed at which the final coupled results are reached depends on the coupling frequencies. They have been chosen arbitrarily in this test case. The solution being steady, iterating in t or k is analogous. The coupling frequency parameter will be re-introduced and further investigated in the cases where the turbulent variables play a predominant role.

5.2.3 Results and discussions

5.2.3.1 Operating point

Analytical equations are not detailed in this section. Only the main results of the operating point, to which the numerical solutions will be compared, are gathered in Table 5.4.

μ	ν	u_{mean}	Q	$\dot{m}$	$-dp/dx$
$1.717 \cdot 10^{-5}\ kg/m/s$	$1.48 \cdot 10^{-5}\ m^2/s$	$7.5\ m/s$	$5.89 \cdot 10^{-6}\ m^3/s$	$6.89 \cdot 10^{-6}\ kg/s$	$4120.8\ Pa/m$

Table 5.4: Poiseuille analytical flow properties.

It stands to reason that both AVBP and *elsA* computations follow the same Sutherland's law. Additionally, since the sole specie is air, no difference exists between the thermodynamical reference quantities (γ, R, c_p, etc) of the two subdomains.

The converged flow is checked for conservation of the velocities and compared to the analytical results for the axial pressure loss. Before that, a comparison on the mass flow rate of both computations is imperative. First of all, the kind of inflow interface in this coupled procedure guarantees a mass conservation across the interface if there is no interpolation error, since among the variables exchanged there are ρ and ρu. In the coupled application, the analytical result is $6.89 \cdot 10^{-6} kg/s$. The error on the mass flow rate in the first tube is 0.29% compared to the analytical solution.

The error performed on the mass flux rate is directly related to the wall shear computation in the solver: $\tau_w = -\frac{R}{2} \cdot \frac{dp}{dx}$ and from the integration of u across the tube section $\frac{dp}{dx} = -\frac{8\mu}{\pi R^4} \cdot Q$, where Q is the volumetric flow rate. This relation comes from the balance between the shear stress force ($\tau_w \cdot 2\pi RL$) and the pressure difference acting on the tube which produces the force ($-dp/dx \cdot L\pi R^2$). In the second tube, the relative error with respect to the analytical solution is much less: 0.04%. Between the two tubes, the relative difference of mass flow rate is of 0.1%. This difference is due to the numerical errors resulting from the linear interpolation used for data communication and the difference of the spatial scheme accuracy between the two tubes. Nevertheless, the error is still within the same order of magnitude of the ones tolerable in engineering applications.

5.2.3.2 Variables exchanged via CWIPI

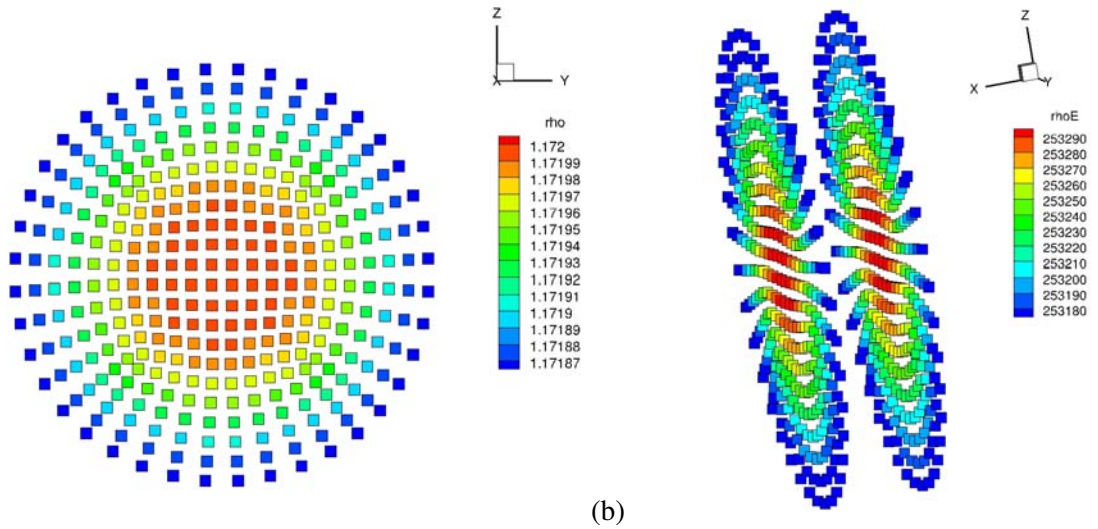

(a) (b)

Figure 5.5: (a) Field of the first conservative variable sent from AVBP to *elsA* and (b) in a traversal view, the two rows of ρE transmitted by the coupler.

An amusing visualization to do is the one of the exchanged variables. On the upstream/downstream direction, AVBP "gives" to *elsA* the whole vector of conservatives variables $\mathbf{U} = (\rho, \rho u, \rho v, \rho w, \rho E)$ in two rows at each exchange performed so *elsA* can advance its residuals computation. One can then plot these fields. Only the ρ and ρE are displayed in Figs. 5.5 (a) & (b), respectively. Qualitatively, one can affirm that the exchanged variables actually follow a parabolic profile, as predicted by the analytical solution. To certify more quantitatively this behavior, a comparative analysis has been performed beneath for velocity and pressure evolutions .

5.2.3.3 Velocities and pressure drop

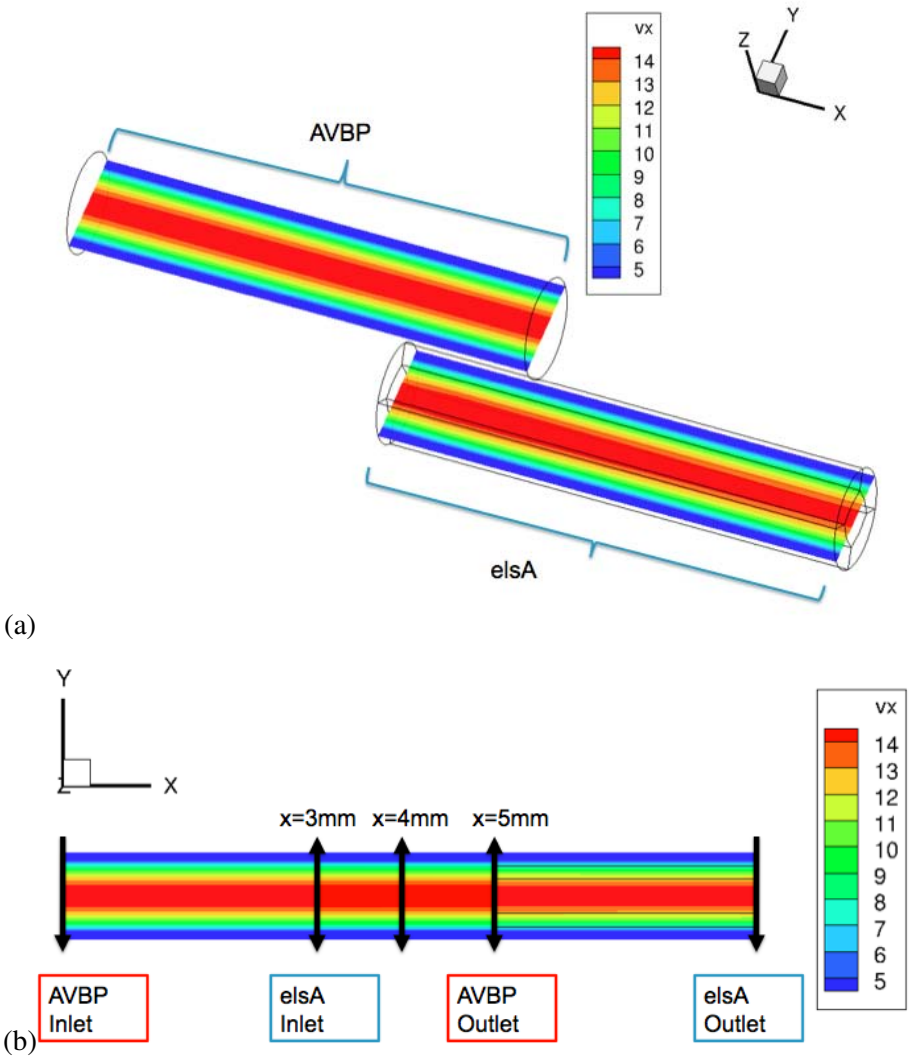

Figure 5.6: (a) Axial velocity fields of the coupled computation and (b) location of the axial velocity profiles in the following figures.

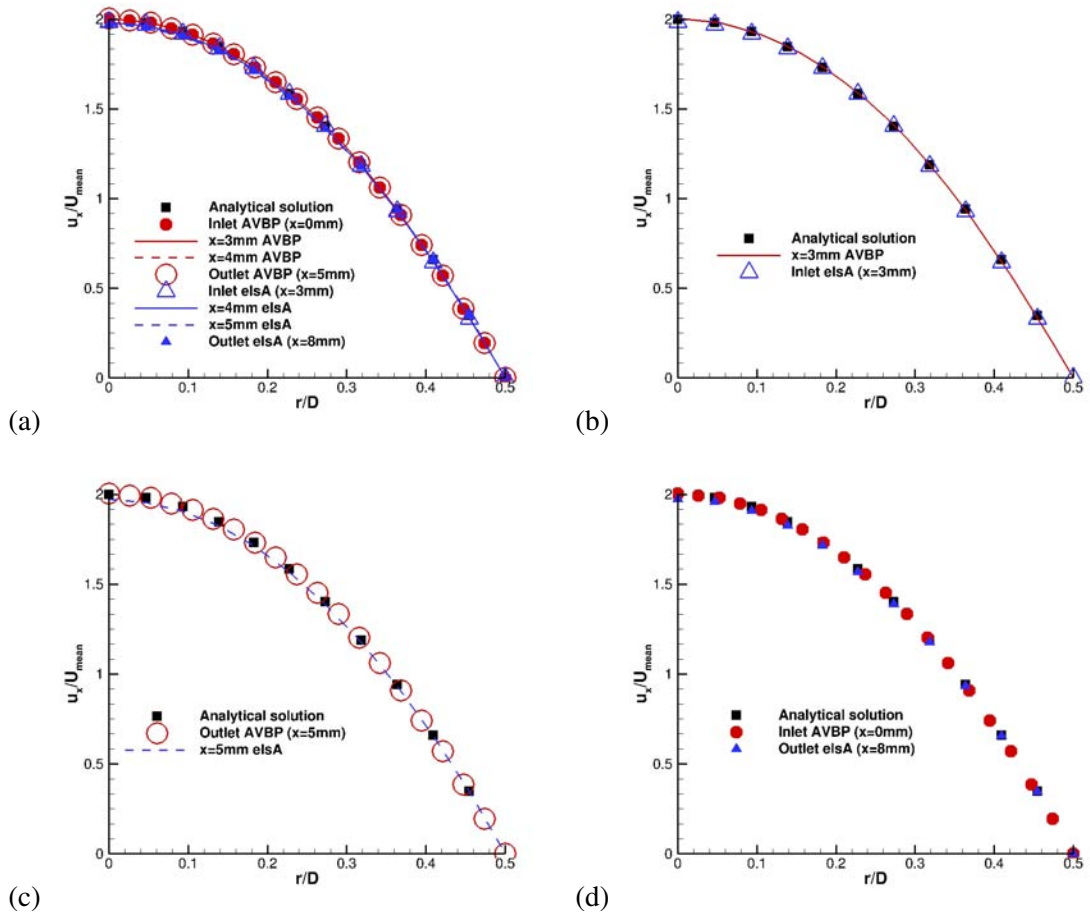

Figure 5.7: Profiles of axial velocity at different stages of the coupled simulation.

Figures 5.6 (a) & (b) show the resulting velocity fields for both subdomains for such a coupled computation. This figure does neither provide a quantitative analysis but allows to visualize the whole domain results. We rely on the 4 next figures (Fig. 5.7 (a)-(d)) to study the evolution of the axial velocity through the tube. The black rectangles denote the analytical solution, i.e, the parabolic profile corresponding to the solution of a fully-developed Poiseuille tube. This should be the solution at any downstream location in the tube. Figure 5.7 (a) shows the dimensionless axial velocity profiles at different locations of the AVBP and *elsA* computations.

Separating the profiles may give a better insight of the quality of the results. Figure 5.7 (b) presents the profiles of AVBP and *elsA* at $x = 3mm$, the plane at which the information is given to *elsA*. The slight error on the mass flow rate is noticeable also at this abscissa, especially at the center of the section, i.e, $r = 0$. Figure 5.7 (c) exhibits the profiles at $x = 5mm$. This location corresponds to the AVBP outlet condition. It is seen that the flow is also perfectly axisymmetric. The whole coupled

domain inlet and outlet profiles are plotted in Fig. 5.7 (d). Considering the inlet velocity profile as the initial and targeted velocity, the outlet of the *elsA* computation follows a parabolic profile with an error of at most 1%. This difference comes from the deviation on the mass flow rate but also from the interpolation of the conservative variables $(\rho, \rho U)$. Let's remind that Schlüter *et al.* [161] also targeted an accuracy of 1% for velocity profiles in a very similar test case.

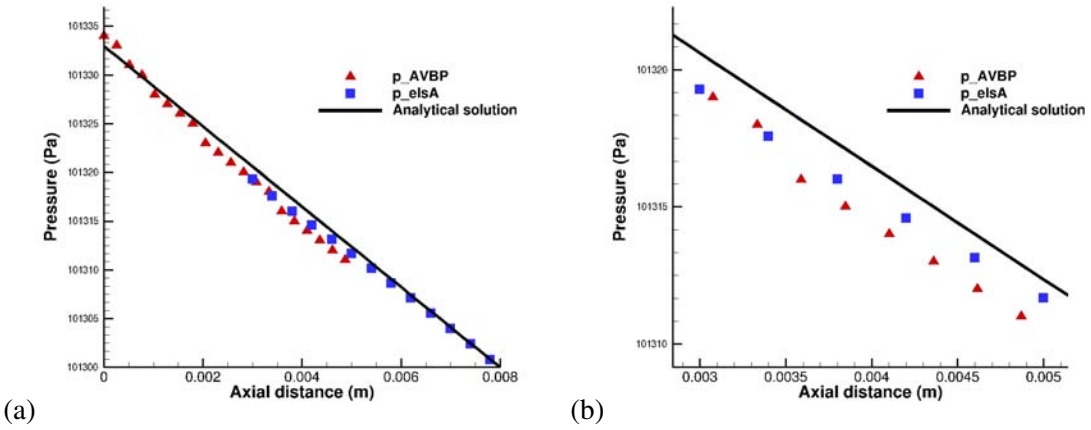

Figure 5.8: (a) Pressure drop in the tubes and (b) zoom in the overlap zone.

Figure 5.8 (a) shows the pressure drop for both tubes of the coupled simulation compared to the theoretical ramp. The coupled simulation exhibits a slightly stronger gradient (dp/dx = -4250 Pa/m compared to dp/dx = -4120.8 Pa/m for the analytical solution). The error on the pressure gradient is of 3.1%. As a comparison, the error on the pressure gradient is of 4.8% for a computation of the whole tube (from $x = 0$ mm to $x = 8$ mm) in AVBP. AVBP is indeed corrected by the *elsA*'s feedback pressure at the AVBP outflow condition. The increased spatial accuracy of *elsA* counteracts the lower order estimates of AVBP that act over a shorter distance. It is however still not sure that this trend is retrieved in all kind of flows. Figure 5.8 (b) displays a zoom of the Fig. 5.8 (a) in the overlap zone. The maximum difference with respect to the analytical solution is of 2 Pa, which represents 0.05% of dp/dx.

5.2.4 Concluding remarks

To conclude, the coupled simulations results in quite good representation of the 3D Poiseuille flow. However, the coupled simulation introduces slightly more viscous losses than predicted by the analytical solution, but this cannot be imputed to the coupling process but instead comes from the CFD

solvers. This simple application case also allows to emphasize the difficulty of the coupling process between two different codes, even more between two compressible solvers where multiple sources of errors can now combine rendering a potentially unstable solution or erroneous predictions.

Even if no direct relation can be established between the relax value in the AVBP/*elsA* coupled simulation (typical values of the relax for a laminar tube are of 500 at the outlet) and the θ parameter used in the mathematical analysis, an influence on this parameter is noticed in the convergence rate towards the results. An influence of the type of the boundary condition used at the outlet of AVBP has also been observed. The use of the condition OUTLET_RELAX_P_3D instead of OUTLET_RELAX_P improves the results for both AVBP/AVBP and AVBP/*elsA* coupling procedures. The difference between these two types of boundaries is the implementation of the transverse terms in the expression of the incoming wave's amplitude in the OUTLET_RELAX_P_3D condition so as to reduce spurious acoustic wave reflections. Based on the work of Yoo & Im [196], a damping coefficient β is needed while using these transverse terms. The correction is based on the local Mach number at each node on the boundary patch [68]. More work needs to be done in the future to determine the exact influence of the relaxation parameter and the boundary condition on the convergence rate.

Two major steps have still to be faced: a strong dependence between the upstream domain and the downstream domain as well as the introduction of the turbulent variables in the coupling process. These two aspects are independent and will be treated in two separate sections.

5.3 Tandem of two cylinders

The channel flow is a sensitive but uncritical test case, no downstream information is really needed for the upstream tube. This is different in the flow past a tandem of cylinders. The flow around the first cylinder depends strongly on the flow around the second cylinder.

Forced convection heat transfer around circular cylinders has numerous application in engineering practice. The studies involving flow over two cylinders have been the subject of numerous experimental and numerical works in the last two decades. Both the flow field and force coefficients depend highly on the configuration and the spacing of the cylinder pair due to both the wake and proximity-induced interference effects. Some of the earliest experimental studies on cylinder pairs in a tandem orientation that were carried out by King & Johns [91], Kostic & Oka [95], Tanida *et al.* [177] demonstrated the presence of two major flow regimes with a complex transition region between them. For closely spaced cylinders, the flow separates behind the first cylinder and reattaches to the second one while, for larger spacing, vortex shedding occurs behind the tandem.

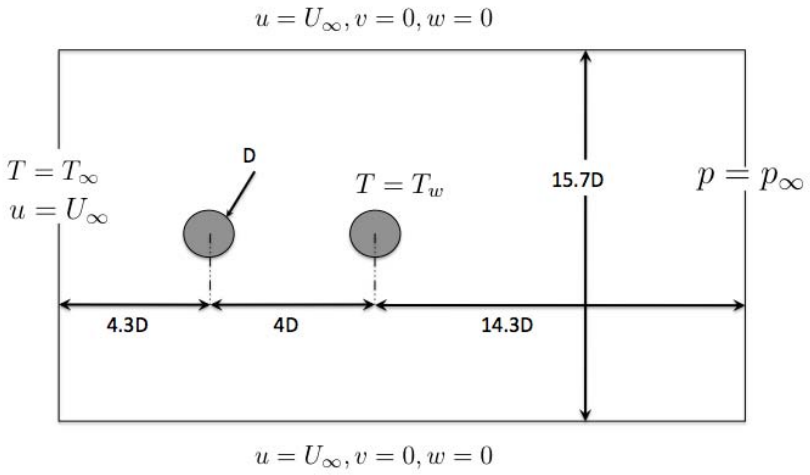

Figure 5.9: Global computation domain.

Extensive reviews of numerical results in tandem can be found in the published works of Blevins [23], Zdravkovich [198]. Critical spacing, which is defined as the minimum gap between the walls of the cylinders, has a substantial influence on the flow regimes established for a particular tandem arrangement. The numerical studies confirm the experimental findings: if the gap is greater than the critical spacing ($\sim 3.5D$ - $3.8D$), the upstream cylinder sheds vortices onto the downstream cylinder. In our case, the cylinder spacing is of $3D$, what Zdravkovich [198] called the in-between regime.

In this work, the unsteady laminar convective flow from two isothermal cylinders of a tandem arrangement is numerically investigated. The numerical analysis is carried out by the coupled AVBP and *elsA*. The working fluid is air. The analysis is done for the Reynolds number of 100 and for center-to-center distance ratio, L/D, of 4. The temperature field is generated to interpret the flow and heat transport visualization. Flow parameters as the pressure coefficient and Strouhal number are also obtained and compared with those available in literature. Finally, the coupled results are compared to a full AVBP computation.

5.3.1 Computational domain

The computational domain and the configuration of the cylinders are illustrated in Fig. 5.9. It is a rectangular domain of height $15.7D$ and length $18.6D + L$. Even if the flow remains 2D, the computational domain is slightly 3D, for coupling reasons, with a characteristic length in the transversal direction of $0.7D$ (D is the cylinder diameter).

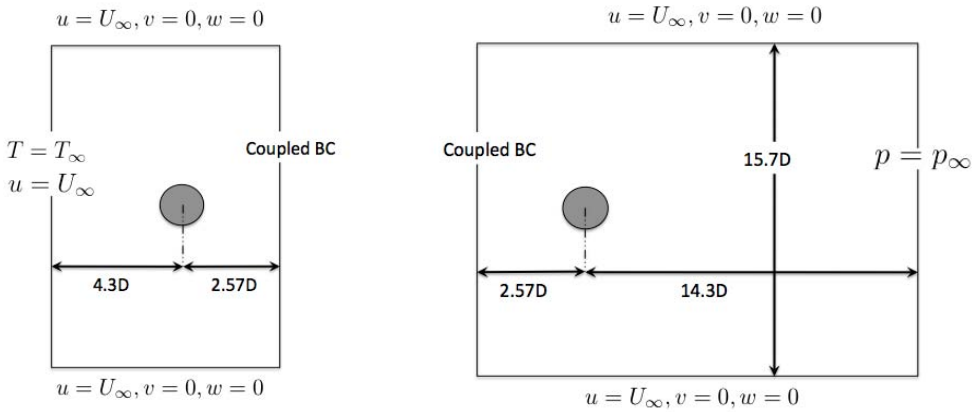

Figure 5.10: Computational domain for (a) the AVBP solver and (b) the *elsA* code.

The boundary conditions are imposed according to:

- ◇ For the AVBP inlet, $u = U_\infty$, $v = 0$, $w = 0$ and $T = T_\infty$,
- ◇ For the *elsA* outlet, $p = p_\infty$,
- ◇ For the top and bottom, $u = U_\infty$, $v = 0$, $w = 0$,
- ◇ For the cylinders wall, $u = 0$, $v = 0$, $w = 0$ and $T = T_w$,
- ◇ Periodicity in the transversal direction,

where T_w is the cylinder wall constant temperature and U_∞, T_∞ are the free-stream velocity and temperature, respectively. The Reynolds number is defined as $Re = U_\infty D/\nu$ and is equal to 100. The

two computational domains solved are illustrated in Fig. 5.10. The overlap zone is plotted in Fig. 5.11, its length is equal to 1.14D in this case. Figure 5.11 also shows where information goes from AVBP to *elsA* on BC_1 and vice versa on BC_2.

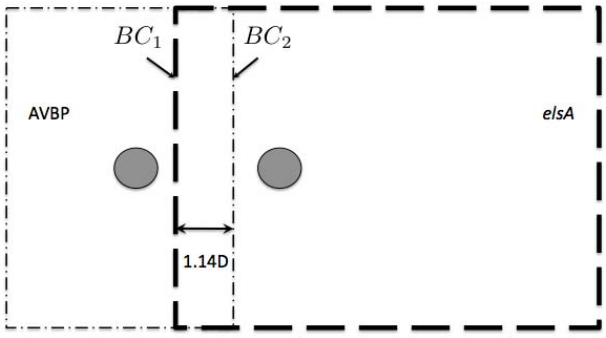

Figure 5.11: Coupled domains with overlap zone.

The number of grid points is an important matter in such unsteady laminar flow over cylinders because of the complex phenomena existing in this type of flow (separation and vortex shedding). The AVBP computational domain is meshed using triangular elements. A non-uniform grid distribution was employed with more refinement around the cylinder wall and in the wake region as can be seen in Fig. 5.12. For the AVBP problem, the total number of nodes are around 150.000. For *elsA*, the mesh is composed of 8 structured blocks and an overall number of points of 100.000. No more refinement was included in the *elsA* mesh out of concern for CPU time. Besides, the disparity of refinement in the overlap zone is highly likely to appear in the industrial application and should be tested.

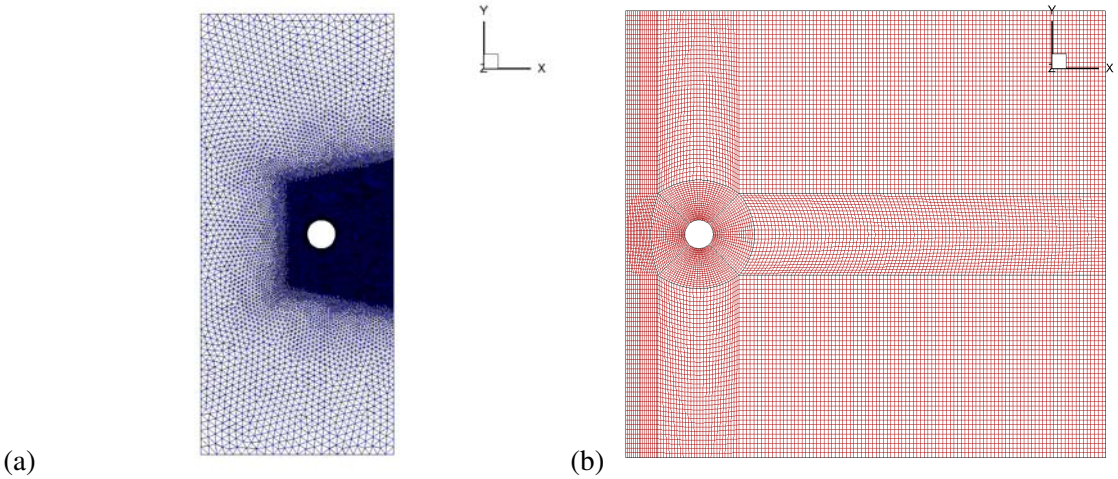

(a) (b)

Figure 5.12: (a) AVBP and (b) *elsA* mesh.

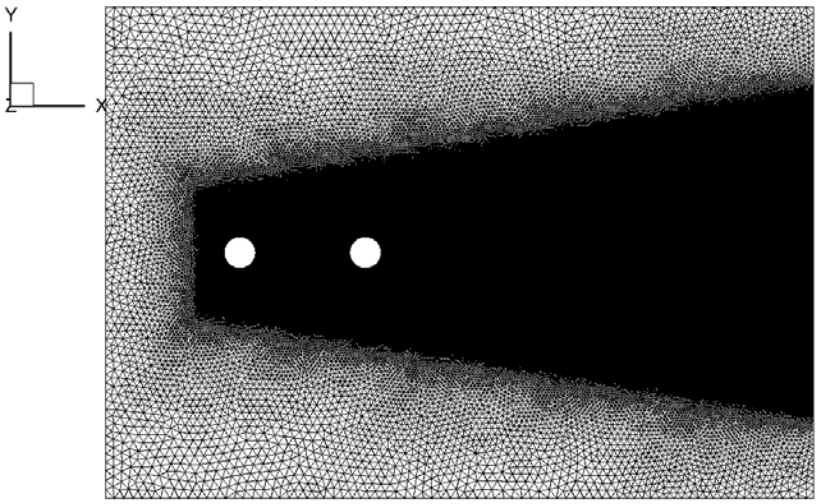

Figure 5.13: AVBP full domain mesh.

5.3.2 Numerical parameters

With this refinements, two separate DNS are performed in the AVBP domain and the *elsA* domain. Indeed, both codes solve the same unsteady equations, no LES nor RANS models are employed.

Specificities about the numerics adopted for both codes are detailed below. The parallel *elsA* software uses a cell centered approach on structured multi-block meshes. Convective fluxes are computed with a Roe scheme with a minmod limiter [76]. Diffusive fluxes are computed with a second-order centered scheme. The global time-marching is performed by use of an implicit time integration approach, based on the backward Euler scheme and a scalar Lower-Upper (LU) Symmetric Successive Over-Relaxation (SSOR) method [197].

AVBP solves the full compressible Navier-Stokes equations using a time-explicit Taylor-Galerkin scheme (TTG4A) for the hyperbolic terms on a cell-vertex formulation, along with a second order Galerkin scheme for diffusion [42]. The scheme provides $3rd$ order space and time accuracy [39].

In the present case, both time steps have been fixed to $\Delta t = 6\ 10^{-8}\ ms$. Around 34 000 time steps are necessary to describe one vortex-shedding period, i.e., $T \approx 2.05\ ms$. The solvers are coupled sequentially and do 1 time step each before exchanging information.

5.3.3 Results and discussions

The full AVBP computation, to which the coupled simulation is compared, has the exact same computation domain as in Fig. 5.9. Its mesh (1 018 776 nodes) is plotted in Fig. 5.13. The numerical parameters are the same that the ones used for the coupled AVBP subdomain. In the following, AVBP full will refer to the full AVBP simulation, AVBP to the coupled AVBP simulation and *elsA* to the coupled *elsA* simulation.

5.3.3.1 Axial and transverse profiles

Figure 5.14 shows the evolution of the mass flow rate of both the coupled AVBP and *elsA*. Even though the mass flow rate deviation becomes slightly bigger that in the Poiseuille tube, the difference is of at most 0.12%. It still remains acceptable for an engineering purpose.

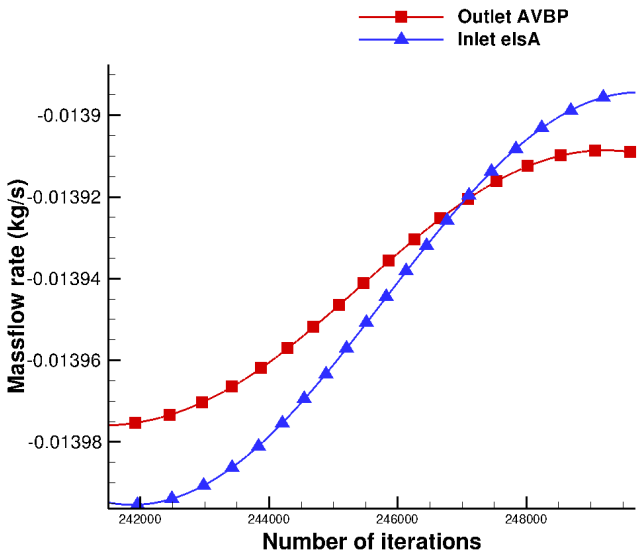

Figure 5.14: Mass flow rate in the AVBP outlet and *elsA* inlet during a fraction of the vortex shedding time.

One can analyze the influence of the downstream domain on the upstream domain comparing the longitudinal profiles of pressure on the cylinders axis (for $x \in$ [-4.3D, 18.6D]), like in Fig. 5.15. The difference in the pressure profiles is at most of 100 Pa in Fig. 5.15 (b) , in other words, 0.09% of the operating mean pressure. The slope of both simulations in the overlap is quite similar, even though in Fig. 5.15 (b), one can notice the effect of the boundary condition on the pressure evolution for the

AVBP solver. It is also interesting to look at the transversal profiles of velocity in the overlap zone in Fig. 5.16.

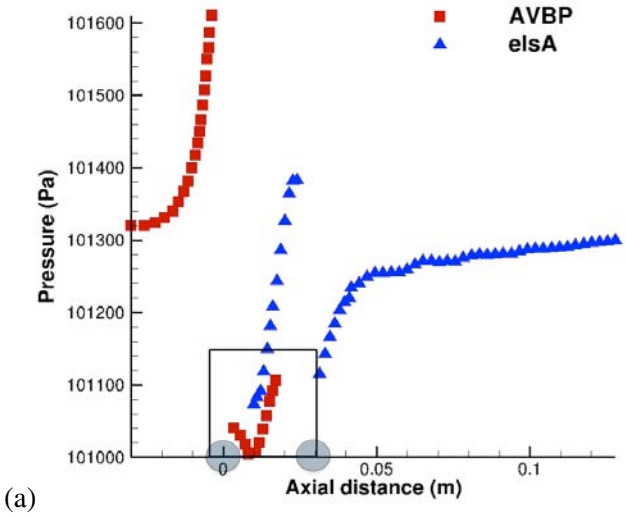

(a)

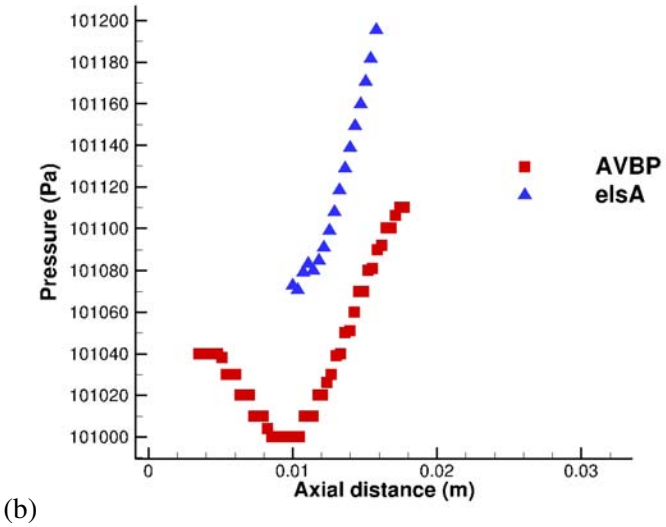

(b)

Figure 5.15: (a) Evolution of the pressure in the axial direction and (b) zoom in the overlap zone.

As done for the Poiseuille tube, one can visualize the velocity at the same axial location in the overlap zone with the two different codes. In Fig. 5.16, the cut is done in the exact middle of the overlap zone. The extent and strength of the recirculation zone is well captured by both solvers. The proposed outflow boundary condition adjusts the pressure directly, and indirectly, the velocity components.

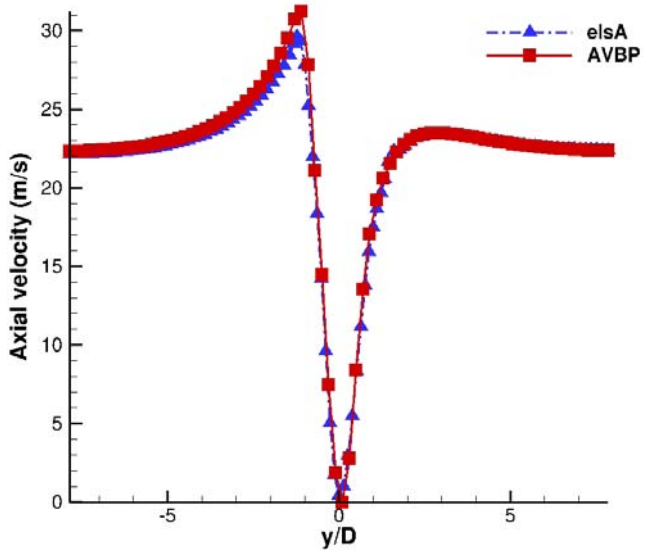

Figure 5.16: Instantaneous value of the axial velocity in the middle of the overlap zone ($x = 14mm$) for AVBP and *elsA* simulations.

5.3.3.2 Isotherms and vorticity contours

According to Zdravkovich [198] with a spacing L/D of 4, one should be in between the reattachment regime and the co-shedding regime. A vortex street is formed due to separated shear layers from both the upstream cylinder and downstream cylinder. Figure 5.17 depicts the vortex structures visible in a temperature field and the isotherms between the two cylinders and downstream region during a complete vortex shedding cycle. Both the flow field from the coupled computation as well as the isotherms from Mahir & Altaç [112] present very similar features.

5.3.3.3 Pressure coefficient

An additional comparison that can been performed between the full AVBP and the coupled simulation is the one on the pressure coefficient, c_p. It is interesting to predict c_p accurately since the aerodynamic performance, drag coefficient and lift coefficient, depends directly on its value.

Figure 5.18 (a) shows time-averaged pressure coefficient distributions on the surface of the first cylinder for the full AVBP computation and the coupled AVBP. The front stagnation corresponds to $\alpha = 0°$. The values are consistent with the observations of earlier researches on isolated elements (page 36 of [170]). The results for the second cylinder are plotted in Fig. 5.18 (b). The predictions

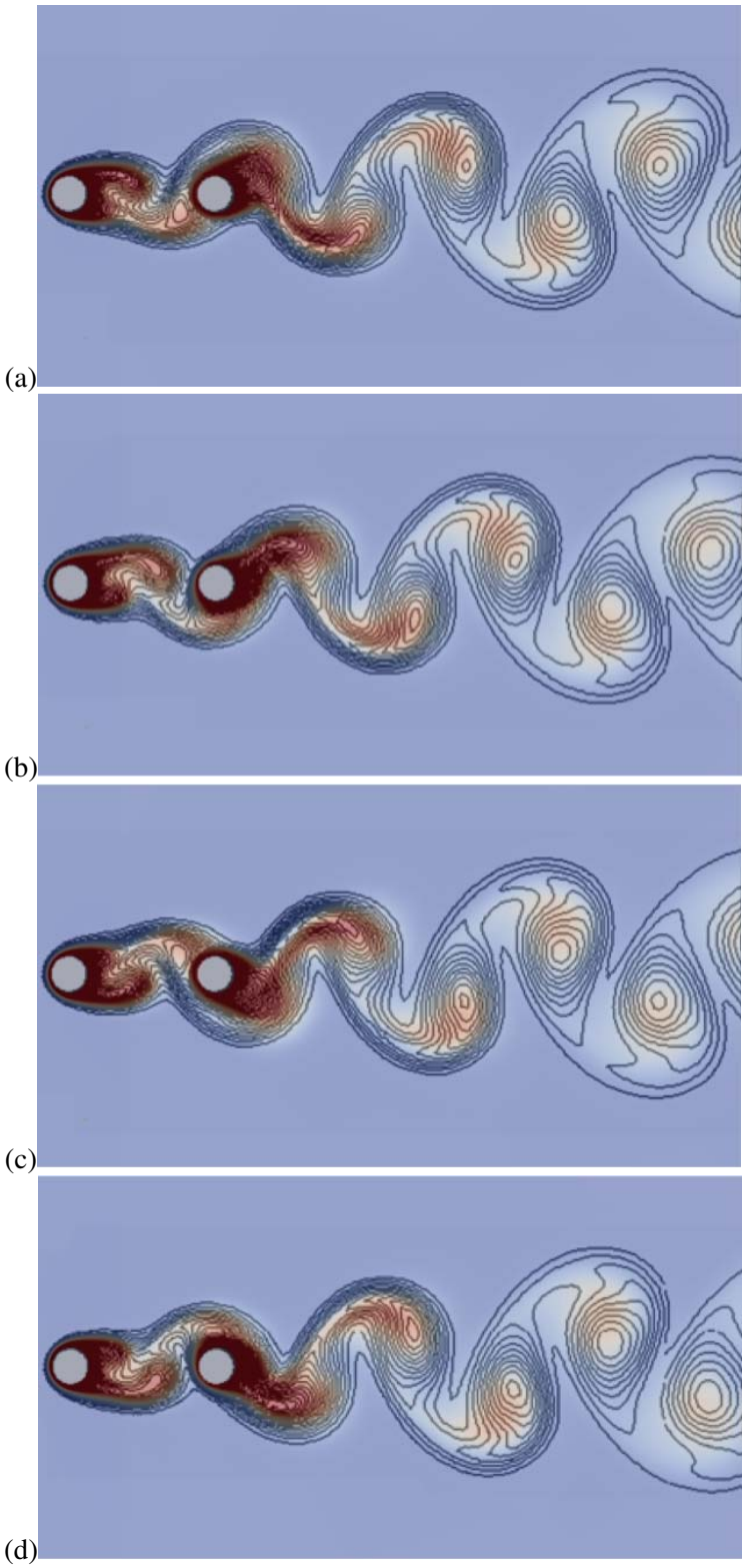

Figure 5.17: Fields of temperature for the tandem arrangement of two cylinders during a complete vortex shedding cycle. Superposition with isotherms results from Mahir & Altaç [112]: (a) $T/4$, (b) $2T/4$, (c) $3T/4$, (d) T.

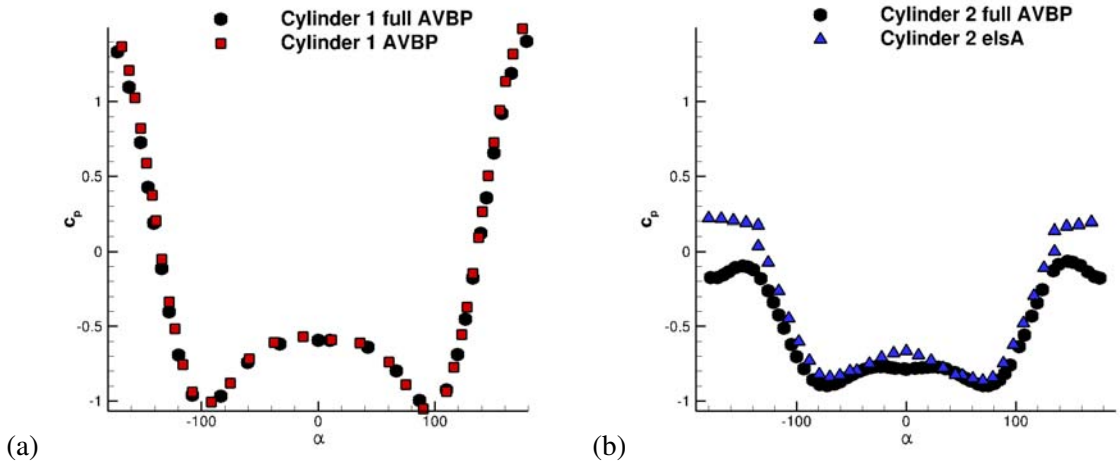

Figure 5.18: Pressure distribution on the surface of (a) the first cylinder and (b) the second cylinder for the time average flow field.

from the coupled simulation are very similar to the ones of the standalone AVBP solver. Obviously, the prediction on the second cylinder differ as can be seen in Fig. 5.18 (b). This discrepancy is due to the distinct numerical set-up between the AVBP and *elsA* solvers and the very different mesh discretization (Fig. 5.12 (b) vs Fig. 5.13).

5.3.3.4 Strouhal number

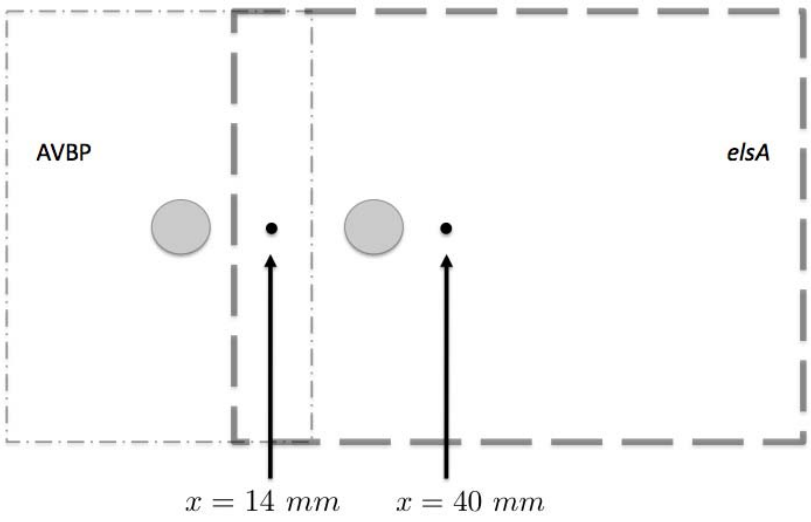

Figure 5.19: Visualization of the two numerical probes used to diagnose the coupled predictions in comparison to standalone AVBP results.

The vortex shedding frequency f is obtained from the Fast Fourier Transform (FFT) of the time history of the vertical velocity data in order to compute the Strouhal number, $f \cdot D/U_\infty$, which is the measure of oscillating fluid (here $U_\infty = 21.9\ m/s$). The results on this frequency analysis are gathered in Table 5.5 for the full AVBP computation and the coupled simulation for the probes shown in Fig. 5.19. In the full AVBP computation, the Strouhal number of both cylinders is the same. The same conclusion is found in the literature [112]. The dominant frequency is found to be 490.6 Hz. This frequency gives a Strouhal which is really close to the experimental data of 0.156 [112]. For the sake of simplicity, only frequencies are displayed in Table 5.5, a Strouhal of 0.156 corresponding to a frequency of 488 Hz.

	Experimental data [112]	Full AVBP	Coupled AVBP	Coupled *elsA*
$x = 14\ mm$	488 Hz	490.6 Hz	490.2 Hz	490.2 Hz
$x = 40\ mm$	488 Hz	490.6 Hz	–	490.2 Hz

Table 5.5: Dominant frequencies of the coupled computation for a probe at $x = 14\ mm$ in the overlap zone and another probe at $x = 40\ mm$, behind the second cylinder, and comparison to the results from a full AVBP simulation and to the data available in literature.

The same study is performed for the coupled results. Conclusions are similar. The dominant frequency is the same for both cylinders; results are identical in the region between the cylinders ($x = 14\ mm$) and behind the second cylinder ($x = 40\ mm$). Since $x = 14\ mm$ is the abscissa just in the middle of the overlap zone, the values in this spot can be compared for the coupled *elsA* and AVBP. The dominant frequency seen by both codes is the same. The overall error with respect to the experimental data is of 0.45%.

5.3.4 Concluding remarks

The purpose of this study was to numerically investigate the coupling on a configuration of two cylinders of equal diameter in tandem arrangements subject to a cross flow of air yielding $Re = 100$. This test case is pertinent to study the outflow conditions implemented in the coupling process since there is a flow interaction between the two cylinders. The combined wake is different from that of a single cylinder. The flow parameters, such as pressure and velocity profiles, have been obtained and compared to a full AVBP computation and with literature, when available, to verify the coupling approach. The isotherms were also obtained to interpret the flow around the tandem. The comparison with others studies show very good agreement. Furthermore, both the pressure coefficients and the

Strouhal numbers have demonstrated that the methodology is able to give good results on such a type of configuration.

As in the previous laminar case, the relaxation parameter influence has been investigated. The convergence rate towards the coupled solution is increased when enhancing the outlet relax value in AVBP. Additionally, the inflow for the downstream domain introduced by this coupling methodology allows to have a negative velocity inlet profile at the *elsA* inlet as in Fig. 5.20, even though the ordinary inlet boundary conditions for the *elsA* solver does not permit a negative axial velocity at this location. This could be quite important in industrial configurations, where it has been shown that recirculation can appear in the region between the combustion chamber and the turbine, a region where the coupling overlap zone is meant to be used (cf Fig. A.10 in Annexe A).

The introduction of the turbulence variables is the next major step to face in the coupling process. This point will be treated in the last section of this chapter.

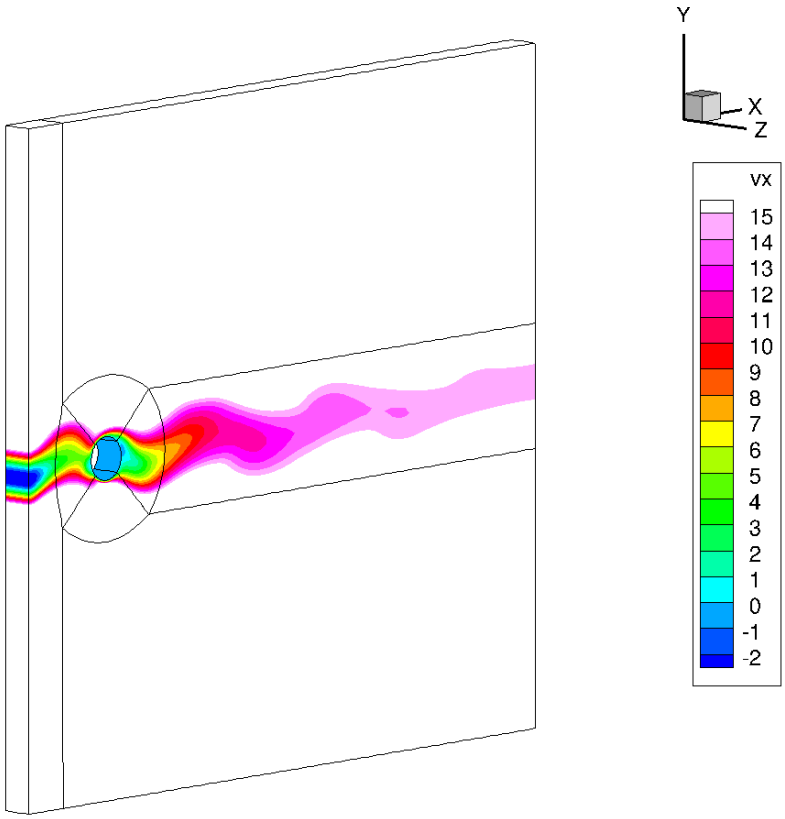

Figure 5.20: Negative axial velocity at the inlet of *elsA*.

5.4 Turbulent tube

The goal of this section is to achieve a computation between two different compressible LES and RANS solvers including the transmission of the turbulent variables. To do so we study a simple case in comparison with a turbomachinery: a turbulent pipe flow. Table 5.6 below gathers the general features of the flow in this turbulent tube.

Governing Equations:	**3D Navier-Stokes**
Flow regime:	**turbulent**
Turbulence:	**LES/RANS**
Chemistry model:	**no chemistry**
Number of species:	**1 (air)**
Number of reactions:	**0**
Reynolds number:	$\approx$ **20 000**
Mach number:	$\approx$ **0.28**

Table 5.6: General flow characteristics

5.4.1 Computational domain

The computation domain is illustrated in Fig. 5.21. It is a circular section tube whose length is set to 6 diameters. The diameter D is 3mm and the bulk velocity is $U_b = 100 m/s$. The fluid is air at $300 K$ with a kinematic viscosity $\nu = 1.51\ 10^{-5} m^2/s$. Thus, the Reynolds number based on these parameters is:

$$Re = \frac{U_b D}{\nu} \sim 20\,000. \tag{5.2}$$

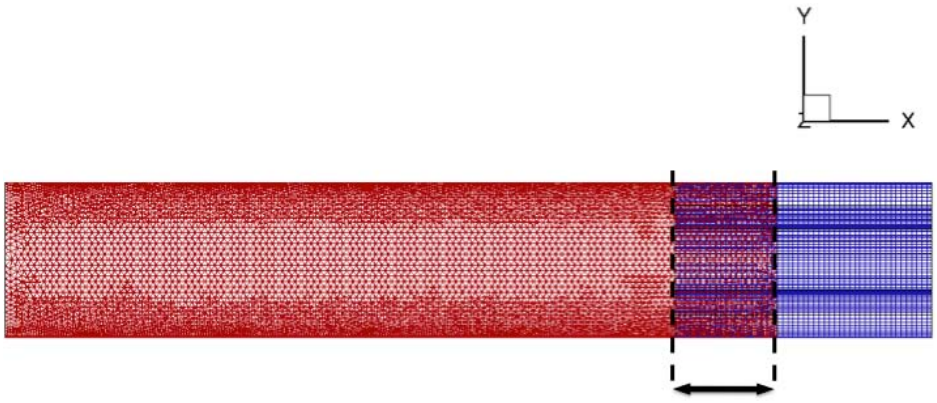

Figure 5.21: Transverse sketch and meshes of the turbulent pipe test case.

Instead of developing turbulence spatially, one can use the turbulence injection at the inlet of the domain, as done in Part I of the manuscript at the blade inlet. More references on turbulence injection in tubes can be obtained in Guezennec [70], Jarrin *et al.* [83]. The mean velocity radial profile at the inlet patch is given by the empiric power law:

$$\bar{u}(r) = \frac{U_b}{2}(n+2)(n+1)\left(1-\frac{r}{R}\right)^n \tag{5.3}$$

where R is the radius of the tube and $n = 1/7$. The modelization of the velocity fluctuations $\sqrt{\overline{u_i'^2}}(r)$ is also requested at the inlet. The Kraichnan/Celik method [96] is used for the fluctuations in this test case.

An axial view for the AVBP mesh and the *elsA* mesh is given in Fig. 5.21. The AVBP domain goes from 0 to 15 *mm*. The *elsA* domain extends from 13 to 18 *mm*. The overlap zone is equal to 2 *mm*. As explained in Chapter 3, the idea is to interpolate the information from the interior of the grid of the source solver to the boundary condition of the target solver. This is valid in both ways, from AVBP to *elsA*, and vice versa. The AVBP computational domain is meshed using 308 000 tetrahedral elements. The *elsA* domain is meshed following a O-grid arrangement and is divided in 5 structured blocks (the number of nodes is doubled in each direction with respect to the laminar case). This refinement is sufficient for this section purpose which is to analyze the turbulent variables transmission. Meshes have been deliberately chosen to be unstructured and structured, respectively for AVBP and *elsA*, to represent the real industrial conditions, where each approach is usually used for each code. Table 5.7 gives the mesh refinements. The turbulent rate at the inlet is equal to 10% and wall laws are used in both subdomains for modeling the behavior at the tube walls ($y^+ \sim 45$ for AVBP and $y^+ \sim 30$ for *elsA*).

	Δx	Δy	Δz	n° cells	n° points
AVBP	D/30	D/30	D/30	308 000	58 250
elsA	D/20	D/40	D/40	68 000	78 183

Table 5.7: Mesh refinements for the coupled AVBP and *elsA* domain.

The mesh density is quite similar for both subdomains but nodes have been deliberately chosen not to be coincident. It is visible that the nodes are neither coincident in the axial (Fig. 5.21) nor in the radial direction (Fig. 5.22). More references on the interpolation method are given in Appendix D.2.

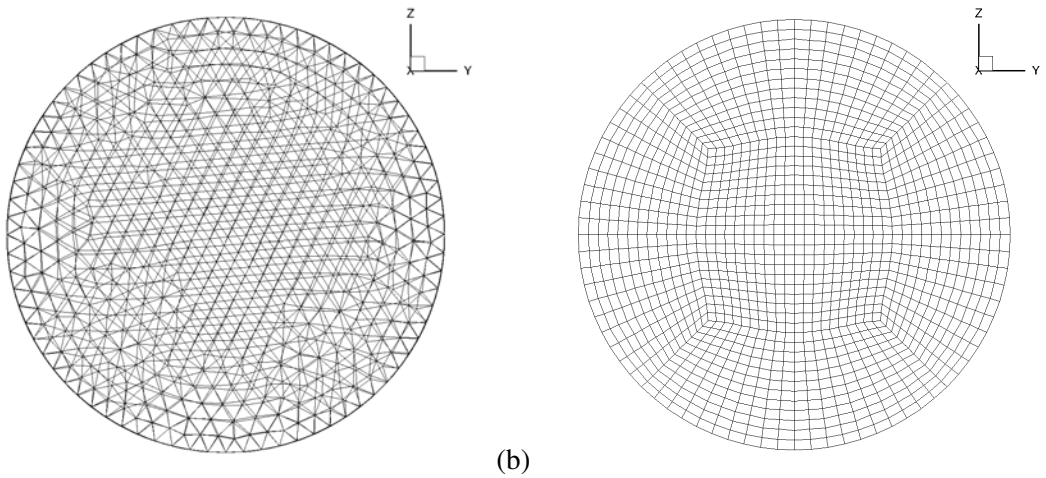

(a) (b)

Figure 5.22: Traversal view of the mesh for: (a) the AVBP solver and (b) the *elsA* code.

5.4.2 Numerical parameters

LES and RANS models are employed for the computation of the AVBP and *elsA* domain, respectively, since the solution is no longer laminar. Specificities about the numerics adopted for both codes are detailed below. The convective time of the global computation is approximatively:

$$t_{conv} = \frac{18\ 10^{-3}\ m}{100\ m/s} = 1.8\ 10^{-4}\ s, \tag{5.4}$$

where 100 $m.s^{-1}$ is the bulk velocity and 18 mm, the tube total length. In the present case, the time step from the AVBP computation has been fixed to $\Delta t = 5\ 10^{-8}\ ms$. AVBP solves the full compressible unsteady Navier-Stokes equations using Law-Wendroff scheme [102]. This scheme uses an explicit time integration with a single Runge-Kutta step. Its accuracy in both space and time is of second order. The scheme is quite robust due to a diffusive term that stabilizes it very effectively even if it is a centered scheme in space. Furthermore, it is characterized by low computational cost. The Smagorinsky model [171] is used to predict SGS behavior in the computation.

The parallel *elsA* software uses a cell centered approach on the 5 structured multi-block mesh. For steady-state RANS simulations, convective fluxes are computed with a second order centered scheme with classical artificial dissipation parameters k^2 and k^4 [81]. Diffusive fluxes are computed with a second-order centered scheme. The pseudo time-marching is performed by using an implicit time integration scheme, based on the backward Euler scheme and a scalar Lower-Upper (LU) Symmetric Successive Over-Relaxation (SSOR) method as proposed in Yoon & Jameson [197]. The turbulent viscosity is computed with the two equations model of Smith [173] based on a $k-l$ formulation.

Before coupling, each subdomain is calculated separately until the variables have converged statistically for the AVBP solver and until convergence of the residuals and mass flow rates for the *elsA* solver. Then, the codes are coupled sequentially as explained in Fig. 3.9. To be coherent with RANS, a sliding average is done to the LES quantities over the time period defined by the user.

5.4.3 Prescribing RANS inflow conditions

How to define the mean value of the vector of conservative variables $\overline{\mathbf{U}}$ transmitted to the RANS computation? The approach chosen can be defined as a sliding average over a trailing time window T:

$$\overline{\mathbf{U}} = \frac{1}{T}\int_{t-T}^{t} \mathbf{U}$$

The difficulty comes from the choice of T. T has to be taken so as to average the turbulent fluctuations but still short enough to allow the unsteadiness of the mean profile to pass through the interface. T would act as a filter and should therefore be carefully designated depending on what information wants to be transmitted.

Definition of the higher momentum terms

The RANS model from *elsA* needs an information on the couple (k,l). An obvious suggestion is to compute k as:

$$k = \sum_{1}^{n_{dim}} (\overline{u_i^2} - \overline{u}_i{}^2)$$

both quantities ($\overline{u}_i{}^2$ and $\overline{u_i^2}$) are easily accessible as $\overline{\mathbf{U}}$ is already computed in our method. The calculation of turbulent length scale l is however less direct. A rough approximation could be used so to impose $l(x,y,z) = 0.33D$. Since this is the length scale enforced for the AVBP inlet. Or we could calculate the exact expression of $l = \dfrac{C_\mu\, k^{3/2}}{\varepsilon}$, where C_μ is the model constant. Neither solution seems pertinent. The first is oversimplified, the last too complicated for this first step towards LES/RANS coupling as it requires the exact computation of ε.

Our choice of expression for l comes from a Solomonic decision: an equilibrium between physical representativity and CPU cost. The Prandtl algebraic expression (page 448 of Chassaing [35]) allows to express the mixing length in a pipe flow as:

$$\frac{l_m}{R} = 0.14 - 0.08\left(1-\frac{r}{R}\right)^2 - 0.06\left(1-\frac{r}{R}\right)^4. \tag{5.5}$$

The flow at $x = 13$ *mm* has a high Reynolds number and can be supposed at equilibrium for a simple given shear $\left|\dfrac{\partial U}{\partial y}\right|$. Therefore, the supposition that a zone exists where production equals dissipation can be done. This hypothesis is also performed by Stanford researchers [120]. Introducing k in

the mixing Prandtl model equation (like in page 463 of Chassaing [35]), the expression of turbulent viscosity gives:

$$C_1\sqrt{k}l = {l_m}^2\left|\frac{\partial U}{\partial y}\right|. \tag{5.6}$$

This last expression implies that l and l_m are related by:

$$l = l_m\left(\frac{C_1^3}{C_2}\right)^{-1/4} \tag{5.7}$$

where C_1 and C_2 are respectively equal to 0.002 and 0.09. This last relationship allows to estimate l through a simple algebraic expression in this application test.

5.4.4 Results and discussions

The mass flow rate error between the two domains is equal to 0.14%. Slightly higher than in previous test cases, this error is again tolerable in engineering applications. In this case, it can be easily diminished if refining the meshes in both subdomains and improving the interpolation method [84, 135].

5.4.4.1 Velocity profiles

Figure 5.23 presents the fields of axial velocity in the plane $z = 0$ for both simulations. The flow is turbulent in the AVBP domain and characteristic turbulent structures are visible. Their sizes are typically from $0.2D$ to $0.4D$ which is in good agreement with the value of $l = 0.33D$ imposed on the inlet patch. The growth of the boundary layer along the wall is also noticeable on this figure. This phenomenon highlights a relaminarization in the vicinity of the wall owing to the low mesh refinement compared to the turbulence scales in this part of the flow. In the visible part of the *elsA* subdomain, the axial velocity field does not present any structure. The flow is completely steady. More information about the flow can be reached by the analysis of the mean axial velocity profiles.

Figure 5.24 shows radial profiles for the axial velocity. On the inlet patch, $x = 0$ *mm*, there is a very good agreement between the simulation and the target profile. Profiles at $x = 13$ *mm* (beginning of the overlap), 15 *mm* (end of the overlap) and at the outlet patch show how the flow tends to a laminar form close to the wall for both codes. In particular, the peak of turbulent velocity tends to vanish. At every stage, the radial profiles show a good agreement between the solvers.

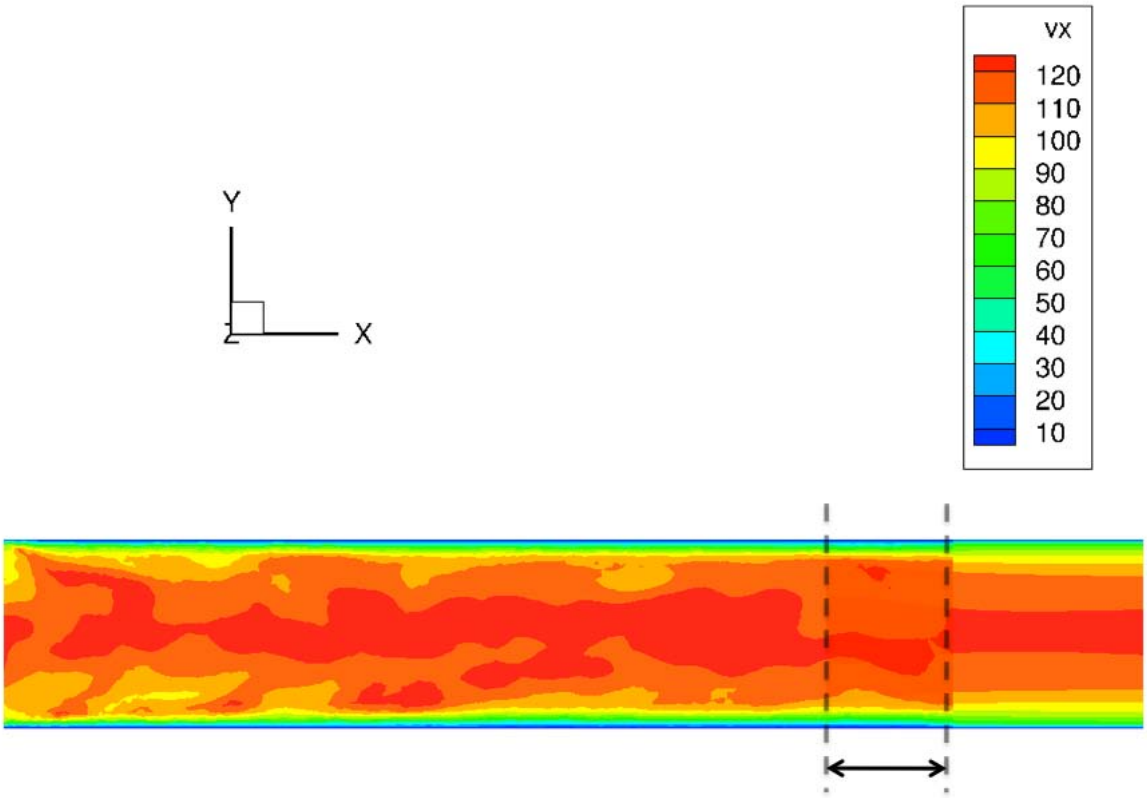

Figure 5.23: LES instantaneous and RANS flow field of axial velocity for AVBP (left) and *elsA* (right) coupled computations. In the overlap zone, only AVBP is visible.

5.4.4.2 Pressure drop

The pressure drop ΔP for turbulent flow in a pipe of length L and diameter D is given by:

$$\Delta P = \frac{\lambda \rho U_b^2 L}{2D} \tag{5.8}$$

where λ is the friction factor [182]. The experimental law of Blasius gives an evaluation of λ for $2000 < Re < 10^5$ [145]:

$$\lambda = 0.3164 Re^{-\frac{1}{4}} \tag{5.9}$$

For this study, the theoretical pressure drop is $\Delta P = 894\ Pa$. The coupled simulation exhibits a slightly stronger pressure drop ($\Delta P = 937\ Pa$) equivalent to 4.8% error. Again, as in the laminar case, the *elsA* computation improves the whole coupled solution behavior.

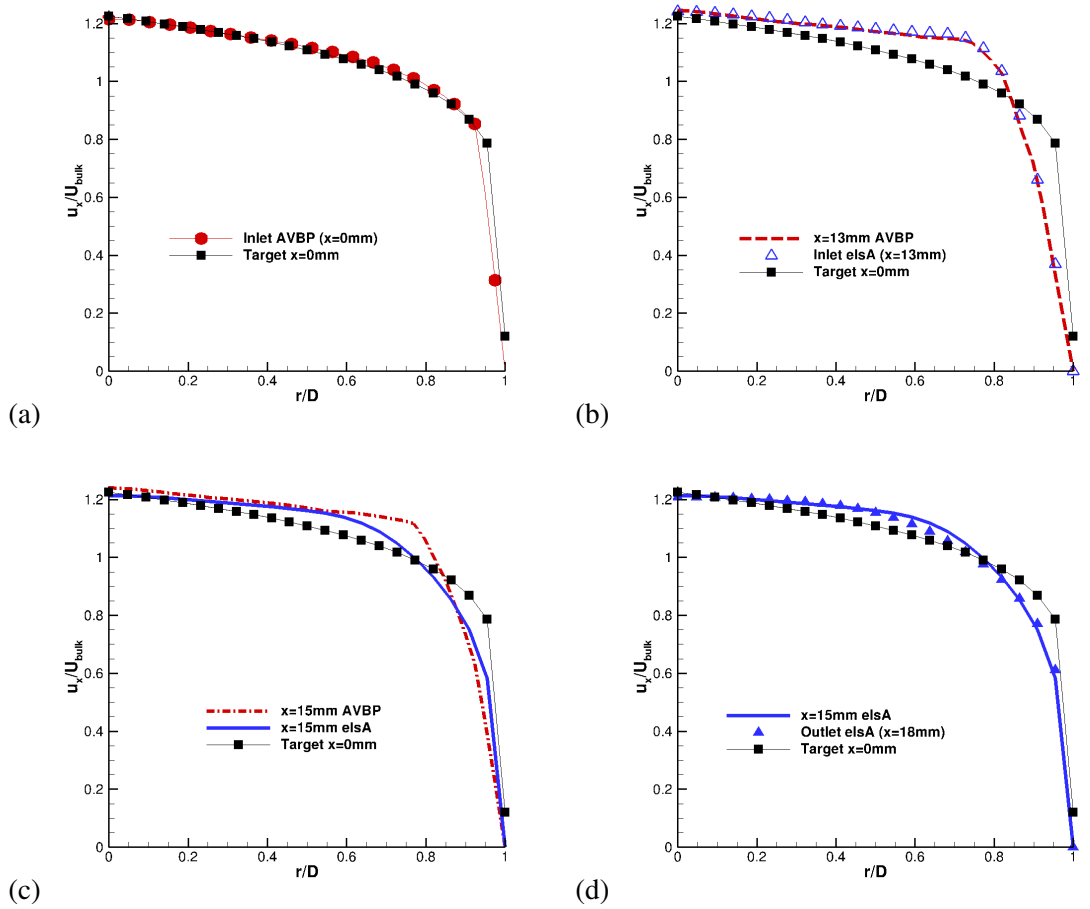

Figure 5.24: Radial profiles of axial velocity component for AVBP and *elsA* coupled computations at different stages of the pipe with respect to the theoretical profile.

5.4.4.3 Turbulent variables

Figure 5.25 presents the typical shape of the kinetic energy K for a turbulent pipe flow. The quantity y^+ is the dimensionless distance to the wall:

$$y^+ = \frac{(R-r)U^*}{\nu} \tag{5.10}$$

Where U^* is the wall friction velocity. Tournier [182] proposes an evaluation of U^* for turbulent pipe flows at Reynolds numbers between 2000 and 10^5:

$$U^{*2} = 0.03955 U_b^{\left(\frac{7}{4}\right)} \left(\frac{\nu}{2R}\right)^{\frac{1}{4}} = 0.03955 \frac{U_b^2}{Re^{\frac{1}{4}}} \tag{5.11}$$

Therefore the value of the wall friction velocity for this test case is $U^* = 5.7m/s$. The maximum value simulated by both solvers is very close. The overall slope is also very similar. The peak is located at a slight different y^+ since the *elsA* mesh is a little more refined in this direction than the AVBP mesh.

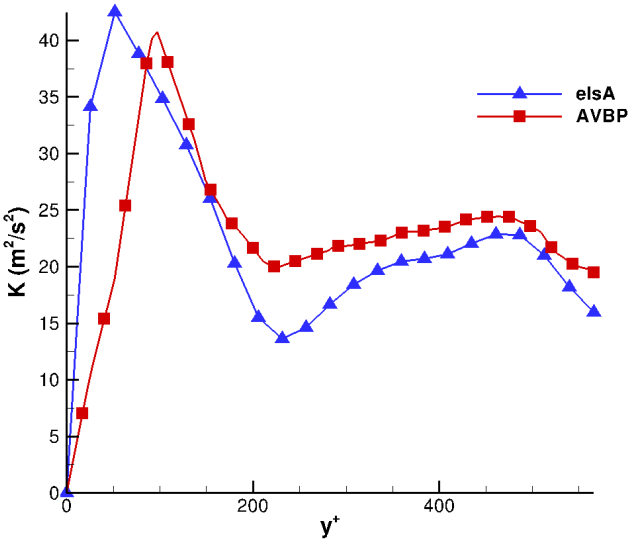

Figure 5.25: Radial profile of the turbulent kinetic energy K for AVBP and *elsA* coupled computations in the overlap zone.

The averaging time span influence

To provide the RANS computation with statistically average values, a sufficient number of integration steps should be achieved in the LES subdomain. All the previous results have been obtained with an averaging time span equal to one flow-through time ($T_{adim} = 1$ expressed in a dimensionless way where the flow-through time is the reference). In order to determine the influence of the choice of the averaging time-span, two supplementary computations are performed varying the length of the trailing average ($T_{adim} = 2$ and $T_{adim} = 0.5$). As can be seen in Fig. 5.26, there are remarkable discrepancies depending on the trailing time window in the turbulent kinetic energy received by *elsA*. This turbulent kinetic energy represents the turbulent fluctuations transmitted. Similar conclusions were drawn by Schlüter *et al.* [161] (page 18).

In this case, averaging over one time unit, given the ratio of tube diameter and bulk velocity, is found to be sufficient for this coupling. This criteria requires the averaging time to be of the order of the integral time scale of the turbulence, which for a turbulent tube flow in proportional to the ratio

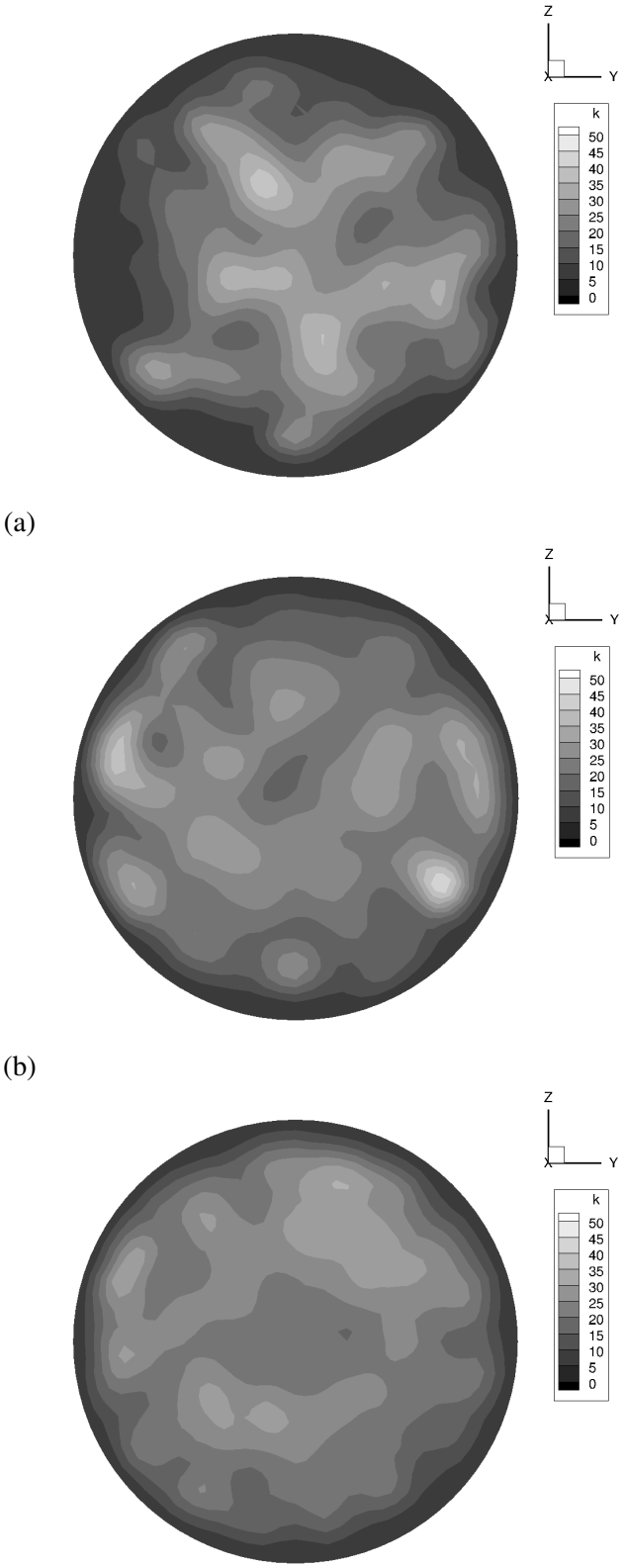

(a)

(b)

(c)

Figure 5.26: Transversal cuts of turbulent kinetic energy of the *elsA* coupled computation with a trailing time window of: (a) $T_{adim} = 0.5$, (b) $T_{adim} = 1$ and (c) $T_{adim} = 2$.

of the tube diameter to bulk velocity (T_{adim} = 1.5 was chosen by Zhang *et al.* [199] in their turbulent channel).

To accelerate the coupling in a real applications, the Stanford researchers concluded that the turbulent variables should instead be computed from the mean flow velocity field [119]. Indeed, the mean velocity is a first order moment which converges significantly faster than the RMS velocities (second order moments) and thus, a smaller averaging window can be employed. The proposed solution is the use of an auxiliary duct in which the RANS turbulence model equations are solved for the mean velocity field transferred from the mean solution obtained from the LES simulation as inlet. Actually, with the methodology they use, the body force relaminarizes the LES velocity field so they fell back on the auxiliary duct to generate the inlet turbulent variables for their RANS pipe.

5.4.5 Concluding remarks

A turbulent pipe has been here simulated by means of a LES/RANS coupling tool. Velocity and pressure drop analysis show good agreement between the solvers and the theoretical predictions. The aim of this section was not centered around the exhaustive description of the flow in a turbulent pipe flow, but more around the impact of the coupling on the physics predicted. Obviously, to achieve a better description of the flow, better depiction of the wall gradients or finer meshes would be needed. Besides some shortfalls of the employed numerical schemes, grid structure, etc, this test case allow us to illustrate the impact of the coupling on the transmitted values.

The preeminent factor to take into account in the LES/RANS coupling is the trailing time window on which the LES fields are averaged before going to the RANS solver. In Section 5.2 which describes the laminar tube, this parameter was also tested but no influence was noticed on a steady application. Here, it is the dominant criterion. *In fine*, the choice of T will depend on what wants to be simulated. In the future, if the coupling tends to LES/URANS or LES/LES simulations, the definition of T should be revisited to be coherent with the physics modeled.

Conclusion

A coupling methodology has been developed to exchange information between a LES solver and a RANS solver. The coupling tool performs:

- ◇ An interpolation of the vector of conservatives variables, $\mathbf{U} = (\rho, \rho u, \rho v, \rho w, \rho E) + (\rho k, \rho l)$ in the first two rows of cells of the downstream *elsA* subdomain.
- ◇ An imposition of the pressure from the downstream *elsA* domain via the boundary formulation of the upstream AVBP subdomain.

A domain decomposition inspired by the work of mathematicians in the field of DDM has also been proposed to study the convergence of the coupled problem. The influence of positive and negative eigenvalues of the uncoupled Euler linearized system of equations has been studied. Additionally, a 1D numerical tool test has been performed to assess the applicability of the proposed procedure to large scale computations even at high Reynolds number. Finally, three representative and simple test cases have been implemented to validate the methodology.

Due to its relevance for industrial applications, coupling of LES and RANS solvers is a very active field of research. This thesis is only a first step towards a coupling tool that could be employed in industrial configurations. The main contributions of this coupling methodology are:

1. its operability. It has been validated in different test cases, from laminar to turbulent, with recirculation zones, ...
2. its mathematical basis. The analysis for convergence here proposed has a big potential and can be declined for other types of coupling, cf appendix C.

Many additional computations can be performed to further evaluate the coupling process. Some of them have already been tested during this thesis, but need a more detailed study. Among the most interesting aspects that can be analyzed are:

- ◇ test one-way: does the outflow condition have any influence in the Poiseuille tube?
- ◇ robustness against mass-conservation, like already done by Schlüter *et al.* [161]
- ◇ influence of the relax parameter/the overlap length like done in Section 4.4.2.
- ◇ acoustic tests: waves traveling downstream/upstream of the domain and transmission considerations.

As far as the LES/RANS coupling is concerned, the influence of the choice of the averaging timespan has been revealed. In the following developments, the contribution of the modeled part of the turbulent kinetic energy should be taken into account in the contribution given to the downstream solver. The estimation of l can be additionally ameliorated [120].

Another interesting point to treat is the one related to the different Reynolds number seen by the LES and RANS solver since ν_t in the RANS solver is greater and can have an influence on the minimum overlap length chosen, as pointed out in the mathematical analysis.

To further develop this promising methodology for industrial applications, the following steps are to be treated in priority:

1. AVBP works with a multi-species philosophy whereas *elsA* only considers mono-species computation (more information is given in Appendix D). A consistent transition between the solvers should be investigated. Moreover, the implementation of a variable γ in *elsA* could improve the results drastically. Indeed, the downsize of the coupling is that it inherits the weakest point from the solvers. Wlassow [191] has evaluated the errors attributable to the limitation coming from a constant γ and they are not negligible.
2. The study on numerical stability [135] and the analysis of aliasing [157] have to be pursued.
3. The implementation of others coupling strategies based on mathematical or physical analysis as suggested by the work of Gander *et al.* [59], Kim *et al.* [90] could be interesting.
4. The development of a LES/URANS or LES/LES approach and determining the benefits from such strategies appears as the natural outcome of the work here presented.

General conclusion and Outlooks

In the context of gas turbine applications, thermal management becomes critical for the high pressure turbine located directly after the combustion chamber and which experiences high temperature gradients at walls. Typical engine life duration today directly relies on the capacity of designers to correctly estimate the wall heat transfer at the blade wall. Unfortunately, such flow phenomena are extremely difficult to predict in such aggressive environments where technological small scale devices (such as cooling holes, tip gap, etc.) impact the turbine flows and clearly increase geometrical complexity. Turbulence also plays a major role on heat transfer and a laminar to turbulent transition is often observed on the turbine blade walls. Despite such long-lived difficulties, classical steady state CFD simulations are the only alternative to correlations for most gas turbine configurations. These CFD solutions are indeed very attractive as they induce relatively short response time in comparison to more costly experimental campaigns. Unstructured LES and zonal LES/RANS coupling procedure have not still proven their value in this context.

The work presented in this manuscript was motivated by two main objectives: the assessment of unstructured LES in high turbine background for heat transfer quantification and the development of a coupling methodology between LES and RANS compressible solvers. Conclusions are presented with respect to each of these objectives:

- ◇ LES and heat transfer:

  Few studies directly address the use of fully structured versus unstructured, implicit versus explicit flow solvers and their respective impact for LES modeling of complex wall bounded flows. To partly answer these important issues, an unstructured computational solver is applied and assessed by comparing the predictions of the heat transfer around the experimental high pressure turbine blade profile cascade of Arts *et al.* [10] to the results from structured LES and RANS simulations. First, both LES predictions are compared to RANS modeling with a particular interest for the accuracy/cost ratio and improvement of the physical phenomena around

the blade. LES are then detailed and further investigated to assess their ability to reproduce the inlet turbulence effect on heat transfer and the development of the transitional boundary layer around the blade. Quantitative comparisons against experimental findings show excellent agreement especially on the pressure side of the profile. Detailed analysis of the flow predictions provided by both the structured and unstructured solvers underline the importance of long stream-wise streaky structures responsible for the augmentation of the heat transfer and leading to the transition of the suction-side boundary layer.

Finally, the study presented demonstrates that LES is ready to help the understanding of complex flow phenomena that are observed in high-pressure turbines (including at high Reynolds numbers). Maybe not yet in an established design process but punctually could LES be used to help engineers on a particular aspect of the conception progression.

◇ Coupling compressible solvers:

During the past years, coupling is taking increasingly place in the CFD community, not only because of a trend movement but because it is an intelligent solution to sum the pros from long trajectories of standalone solvers and intend the resolution of unattainable problems otherwise. In the specific problem of the turbine/combustion chamber interaction, the coupling could provide both a more complete inlet condition for the downstream RANS computation and a more predictive LES outflow condition.

A house should be built by its basis, that why the demonstration of the final industrial configuration has not been the priority of this research, even though all steps are ready (LES computation of the combustion chamber + NGV (Appendix A), coupling methodology (Part II) and RANS turbine stage computations current in industry). More emphasis has been given to fundamental aspects as the mathematical groundwork for such coupling procedures. The 1D theoretical study provides the identification of the coupling parameters which have an impact on the coupling process, before facing more complex applications. The resulting approach has been successfully tested in three different cases. Each case aims at accentuating a characteristic that could be relevant in the engine final application. Recirculating zones at both inlet/outlet of the domains, for instance, can be treated by the procedure implemented in this PhD.

With respect to the objectives requested by TM, we have partially achieved to answer their demands by implementing:

- ◇ the set-up of a hybrid mesh approach in LES for the prediction of the wall heat transfer in a fixed blade configuration,
- ◇ the development of a zonal LES/RANS coupling strategy which makes possible the coupled computation of industrial configurations with todays computing means.

However and since our study is one among the firsts to analyze the response of unstructured LES around blades and the coupling between two compressible solvers, many discoveries are still to be accomplished. The major aspects that should be further tested or investigated are gathered below for each goal of the thesis:

- ◇ LES and heat transfer:

  Throughout this thesis work, we have seen that flow physics at walls is a still an open problem that covers laminar to turbulent, natural and forced transitions, compressibility effects such as shocks, wall curvature or roughness, FST intensity, external pressure gradient effects, etc. In industrial applications, such issues and difficulties also point to massively separated flows, reattachment points, rotational forces, relaminarization, etc.

  Recent developments and demonstrations for the prediction of turbulent flows around blades point to LES as a very promising tool. Theoretical limits and scales of wall bounded flows are now well mastered in simple cases but complex industrial applications usually introduce unknowns and mechanisms that are difficult to apprehend beforehand especially with LES which is usually computationally intensive and bounded to code scalability, mesh quality, modeling performances and computer power.

  To completely validate this formulation in such configurations, more adapted sub-grid modeling model to take into account the spatial distribution of the streaks near the wall [133] should be analyzed. Wall laws including Mach number evolution could also be a solution to improve the efficiency of LES in such configurations. Despite the fact that this numerical method still requires modeling and intense computing effort compared to RANS simulations, this fully unsteady simulation technique provides valuable information on the turbulent flow otherwise inaccessible. An effort is nonetheless necessary to use LES in an industrial context (full 3D, stage configurations, etc.).

◇ Coupling compressible solvers:

One of the main advantages of the coupling procedure is that each solver can be ameliorated individually and follow its own development. For example, AVBP kinetic scheme could be improved or *elsA* could benefit from a new version with variable γ. These separate revisions would enhance the overall computation without impinging the structure of the current coupling methodology. The coupling procedure itself could be improved, for example, with the inclusion of a more accurate description of k which would take into account the SGS contribution in the LES/RANS coupling. Moreover, the coupling implementation has been thought so as to adapt to further developments towards parallel synchronization or LES/URANS and even LES/LES coupling without much effort. Another aspect that could also be revised without touching the coupling platform is the interpolation precision.

The domain decomposition community is very animated. A more in depth look on the methodologies adopted by mathematicians could give some ideas on the most optimized conditions to apply at the interfaces [58]. Notably, to reduce the probability of undesired reflections, a method to discern which waves are traveling upstream or downstream could be performed and a symmetric differentiate treatment (Neumann/Dirichlet and Dirichlet/Neumann, respectively) could be imposed in the coupling between two compressible solvers. Moreover, some literature exists in the mathematic field that studies the domain decomposition for two aspects that could be interesting for our particular problem:

- the first comes when heterogeneities exist between the subdomains [13]. These analyses can be further developed to apply them to our particular case where AVBP is multi-species and *elsA* only models a specie,
- the second heterogeneity that it could be interesting to treat is the one between equations. One could imagine a shock wave to appear in between the subdomains and treat the problem with a coupling procedure [149]. The nature of the equations changes at this spot. Mathematical analyses have already been performed on such problems [146] and could be additionally explored with a simple 1D tool. This study could also serve research on the wave transmission across the turbine [105].

Another interesting experience could be to use a 1D numerical tool similar to the one developed here to proceed to a coupled simulation with a high Reynolds number on one side and a lower Reynolds number on the other side. Another important aspect to which no attention has been

given in the CPU consumption, future developers should take great care of this parameter, especially when the coupling procedure will be applied to industrial configurations.

In the true geometry of the propulsion system, additional cooling devices are present, in particular at the trailing edge of the NGV. These systems were not included in this study for simplicity. The first step in the further analysis is going to be the inclusion of these cooling devices present in the trailing edge of the stator as well as the addition of a more realistic internal cooling system [55]. Some experimental results will be available soon for the NGV blade temperature. A comparison should be driven to determine the accuracy of the LES computation or, instead, the modifications which should be done to improve the simulation.

The following step will be for the geometry to take into account the re-injection in the vein between stator and rotor, the tip squealer and the fir-tree root in the high pressure rotor. Moreover, conjugate heat transfer will be computed in both stator and rotor, which implies, respectively, the coupling between LES code AVBP and thermal code AVTP and the coupling between RANS code *elsA* and thermal code AVTP, both already available [45, 192]. In the future, computations will take into account different phenomena like conjugate transfer but also radiation when solving the fluid motion. A glance of such an analysis on a combustion chamber + NGV domain can be viewed in Appendix B.

The final aim is to determine how many geometrical details in both stator and rotor are compulsory to obtain a good prediction of the high pressure rotor temperature. Also, to determine if a LES calculation, thermal coupling and code coupling are necessary to accurately predict the high pressure rotor temperature. All the results from the approach anteriorly detailed could be then compared with the RANS approach followed by F. Wlassow [191].

References

[1] A. PIACENTINI, T. MOREL, A. THEVENIN & DUCHAINE, F. 2011 OpenPALM: an open source dynamic parallel coupler. In *In IV International Conference on Computational Methods for Coupled Problems in Science and Engineering*. 210

[2] ABU-GHANNAM, B. & SHAW, R. 1980 Natural transition of boundary layers - the effects of turbulence, pressure gradient, and flow history. *J. of Mechanical Engineering Science* **22** (5), 213–228. 27, 34, 35

[3] ACHDOU, Y., LE TALLEC, P., NATAF, F. & VIDRASCU, M. 2000 A domain decomposition preconditioner for an advection–diffusion problem. *Computer methods in applied mechanics and engineering* **184** (2), 145–170. 82

[4] ALONSO, J. J., HAHN, S., HAM, F., HERRMANN, M., IACCARINO, G., KALITZIN, G., LEGRESLEY, P., MATTSSON, K., MEDIC, G., MOIN, P., PITSCH, H., SCHLÜTER, J., SVARD, M., VAN DER WEIDE, E., YOU, D. & WU, X. 2006 CHIMPS: a high-performance scalable module for multi-physics simulation. In *42nd AIAA/ASME/SAE/ASEE Joint Propulsion Conference & Exhibit*. 14

[5] AMAYA, J. 2010 Unsteady coupled convection, conduction and radiation simulations on parallel architectures for combustion applications. PhD thesis, Université de Toulouse, France - MeGeP Dynamique des Fluides. 211

[6] AMAYA, J., CABRIT, O., POITOU, D., CUENOT, B. & ELHAFI, M. 2009 Unsteady coupling of Navier-Stokes and radiative heat transfer solvers applied to an anisothermal multicomponent turbulent channel flow. In *Press IST, editor, Eurotherm83 - Computational Thermal Radiation in Participating Media III*, pp. 185–196. Lisbon, Portugal. 211

[7] AMAYA, J., COLLADO, E., CUENOT, B. & POINSOT, T. 2010 Coupling LES, radiation and structure in a gas turbine simulations. In *Proceedings of the Summer Program*, pp. 239–249. 187, 188, 211

[8] AMES, F. E. 1997 The influence of large-scale high-intensity turbulence on vane heat transfer. *J. Turbomachinery* **119**, 23–30. 32

[9] ARGUELLES, P., BISCHOFF, M., BUSQUIN, P., DROSTE, BAC, EVANS, R., KROLL, W., LAGARDERE, JL, LINA, A., LUMSDEN, J., RANQUE, D. *et al.* 2001 European aeronautics: A vision for 2020. *Report of the Group of Personalities, The European Commission, January 2001* . 12

[10] ARTS, T., DE ROUVROIT, M. LAMBERT & RUTHERFORD, A. W. 1990 Aero-thermal investigation of a highly loaded transonic turbine guide vane cascade. Technical Note 174. Von Karman Institute for Fluid Dynamics. 28, 29, 30, 33, 59, 155

[11] AZZI, A. & LAKEHAL, D. 2002 Perspectives in modeling film cooling of turbines blades by transcending conventional two-equation turbulence models. *J. Turbomachinery* **124**, 472–484. 19

[12] BALIN, N. 2005 Etude des méthodes de couplage pour la résolution des équations de Maxwell. PhD thesis, INSA de Toulouse. 67, 82

[13] BAMBERGER, A., GLOWINSKI, R. & TRAN, Q.H. 1997 A domain decomposition method for the acoustic wave equation with discontinuous coefficients and grid change. *SIAM Journal on Numerical Analysis* pp. 603–639. 158

[14] BAQUÉ, B., ERRERA, M.P., ROOS, A. & FEYEL, F. 2010 Etude numérique de la thermique par une approche globale multiphysique. In *Congrès Français de Thermique Energies et Transports durables.*. Le Touquet, France. 212

[15] BARRINGER, MD, THOLE, KA, POLANKA, MD, CLARK, JP & KOCH, PJ 2009 Migration of combustor exit profiles through high pressure turbine vanes. *J. Turbomachinery* **131**, 021010. 12

[16] BENARAFA, Y., CIONI, O., DUCROS, F. & SAGAUT, P. 2007 Temperature wall modelling for large-eddy simulation in a heated turbulent plane channel flow. *Int. J. Heat and Mass Transfer* **50** (21-22), 4360–4370. 27

[17] BENEK, JA, STEGER, JL, DOUGHERTY, FC & BUNING, PG 1986 Chimera. A Grid-Embedding Technique. *Tech. Rep.*. DTIC Document. 68, 206

[18] BHASKARAN, R. 2010 Large eddy simulation of a high pressure turbine cascade. PhD thesis, Stanford University. 20, 205

[19] BHASKARAN., R. & LELE, S. 2010 Large eddy simulation of free-stream turbulence effects on heat transfer to a high-pressure turbine cascade. *J. Turbulence* **11** (6), 1–15. 27, 33, 40, 48, 54

[20] BJØRHUS, M. 1995 Semi-discrete subdomain iteration for hyperbolic systems. *Tech. Rep.*. Technical Report 4, NTNU. 91

[21] BLANC, F. 2009 Aéroélasticité des surfaces de contrôle. PhD thesis, CERFACS. 69

[22] BLANC, F. 2010 Patch assembly: An automated overlapping grid assembly strategy. *J. of aircraft* **47** (1), 110–119. 69

[23] BLEVINS, RD 1985 The effect of sound on vortex shedding from cylinders. *J. Fluid Mechanics* **161** (1), 217–237. 131

[24] BOILEAU, M., STAFFELBACH, G., CUENOT, B., POINSOT, T. & BÉRAT, C. 2008 LES of an ignition sequence in a gas turbine engine. *Combust. Flame* **154** (1-2), 2–22. 22, 37

[25] BOUDET, J., GROSJEAN, N. & JACOB, M.C. 2005 Wake-airfoil interaction as broadband noise source: a large-eddy simulation study. *Int. J. of Aeroacoustics* **4** (1), 93–116. 121

[26] BOUDIER, G., GICQUEL, L. Y. M., POINSOT, T., BISSIÈRES, D. & BÉRAT, C. 2007 Comparison of LES, RANS and experiments in an aeronautical gas turbine combustion chamber. *Proc. Combust. Inst.* **31**, 3075–3082. 19

[27] BOYLE, R. J. & AMERI, A.A. 1997 Grid orhogonality effects on turbine midspan heat transfer and performance. *J. Turbomachinery* **119** (1), 31–38. 27

[28] BREZZI, F., LIONS, J.L. & PIRONNEAU, O. 2001 Analysis of a Chimera method. *Comptes Rendus de l'Académie des Sciences-Series I-Mathematics* **332** (7), 655–660. 68

[29] BUIS, S., PIACENTINI, A., DÉCLAT, D. & THE PALM GROUP 2006 PALM: a computational framework for assembling high-performance computing applications. *Concurrency and Computation: Practice and Experience* **18** (2), 231–245. 211

[30] CABRIT, O. 2009 Modélisation des flux pariétaux sur les tuyères des moteurs à propergol solide. PhD thesis, Université Montpellier II - DOCTORALE ISS - Spécialité Mathématiques et Modélisation. 205

[31] CABRIT, O. & NICOUD, F. 2008 DNS of a periodic channel flow with isothermal ablative wall. In *ERCOFTAC workshop - DLES 7*. Trieste, Italy. 39

[32] CAMBIER, L. & VEUILLOT, J.P. 2008 Status of the elsA CFD software for flow simulation and multidisciplinary applications. *46th AIAA Aerospace Science Meeting and Exhibit* (664). 37, 65, 204, 210

[33] CELIK, I., SMIRNOV, A. & SMITH, J. 1999 Appropriate initial and boundary conditions for LES of a ship wake. In *Proceedings of the 3rd ASME/JSME Joint Fluids Engineering Conference*, , vol. FEDSM99-7851. San Francisco, California, USA. 40, 41

[34] CHASSAING, P. 2000 *Mécanique des fluides, Éléments d'un premier parcours*. Cépaduès-Éditions. 193

[35] CHASSAING, PATRICK 2000 *Turbulence en mécanique des fluides. Analyse du phénomène dans une perspective de modélisation à l'usage de l'ingénieur*. Institut National Polytechnique de Toulouse. 145, 146

[36] CHATELAIN, A. 2004 Simulation des grandes echelles d'ecoulements turbulents avec transferts de chaleur. Phd thesis, INP Grenoble. 189

[37] CHEMIN, S. 2006 Étude des interactions thermiques fluides-structure par un couplage de codes de calcul. PhD thesis, Université de Reims Champagne-Ardenne. 189, 195, 196

[38] COLIN, O., DUCROS, F., VEYNANTE, D. & POINSOT, T. 2000 A thickened flame model for large eddy simulations of turbulent premixed combustion. *Phys. Fluids* **12** (7), 1843–1863. 180

[39] COLIN, O. & RUDGYARD, M. 2000 Development of high-order Taylor-Galerkin schemes for unsteady calculations. *J. Comput. Phys.* **162** (2), 338–371. 37, 125, 134, 208

[40] COLLADO-MORATA, E., GOURDAIN, N., DUCHAINE, F. & GICQUEL, L.Y.M. 2012 Effects of free-stream turbulence on high pressure turbine blade heat transfer predicted by structured and unstructured LES. *Int. J. Heat and Mass Transfer* **55**, 5754 – 5768. 28

[41] DOLEAN, V., LANTERI, S. & NATAF, F. 2004 Convergence analysis of additive Schwarz for the Euler equations. *Applied numerical mathematics* **49** (2), 153–186. 82, 91, 101

[42] DONÉA, J., ROIG, B. & HUERTA, A. 2000 High-order accurate time-stepping schemes for convection-diffusion problems. *Comput. Methods Appl. Mech. Eng.* **182**, 249–275. 37, 134

[43] DORNEY, D.J., GUNDY-BURLET, K.L. & SONDAK, D.L. 1999 A survey of hot streak experiments and simulations. *Int. J. of Turbo and Jet Engines* **16** (1), 1–16. 13

[44] DORNEY, D.J. & SONDAK, D.L. 2000 Effects of tip clearance on hot streak migration in a high-subsonic single-stage turbine. *J. Turbomachinery* **122**, 613. 13

[45] DUCHAINE, F., CORPRON, A., PONS, L., MOUREAU, V., NICOUD, F. & POINSOT, T. 2009 Development and assessment of a coupled strategy for conjugate heat transfer with Large Eddy Simulation. Application to a cooled turbine blade. *Int. J. Heat Fluid Flow* **30** (6), Pages 1129–1141. 20, 27, 159, 189, 191, 196, 211

[46] DUCHAINE, F., MENDEZ, S., NICOUD, F., CORPRON, A., MOUREAU, V. & POINSOT, T. 2008 Coupling heat transfer solvers and large eddy simulations for combustion applications. In *Proceedings of the Summer Program Center for Turbulence Reseach, NASA AMES - Stanford University* (ed. NASA Ames/Stanford Univ. Center for Turbulence Research). 77, 193

[47] DUCHAINE F., MOREL T. & A., PIACENTINI 2011 On a first use of CWIPI at CERFACS. Contract report TR-CMGC-11-3. CERFACS. 213

[48] DUCHAINE F., MOREL T. & E., QUÉMERAIS 2011 OpenPALM tutorial: a first toy with NSC2KE. Contract report TR/GMGC-11-45. CERFACS. 213

[49] DUCROS, F., FERRAND, V., NICOUD, F., WEBER, C., DARRACQ, D., GACHERRIEU, C. & POINSOT, T. 1999 Large-eddy simulation of shock-turbulence interaction. *J. Comput. Phys.* **152**, 517–549. 37

[50] DULLENKOPF, K., SCHULZ, A. & WITTING, S. 1991 The effect of incident wake conditions on the mean heat transfer of an airfoil. *J. Turbomachinery* **113**, 412–418. 32

[51] ERIKSSON, K. 1996 *Computational differential equations*, , vol. 1. Cambridge Univ Pr. 206

[52] ESTEP, D., TAVENER, S. & WILDEY, T. 2008 A posteriori analysis and improved accuracy for an operator decomposition solution of a conjugate heat transfer problem. *SIAM J. Numer. Anal* **46** (4), 2068–2089. 189

[53] FERZIGER, J. H. 1977 Large eddy simulations of turbulent flows. *AIAA J.* **15** (9), 1261–1267. 34

[54] FLORYAN, J. M. 1991 On the Görtler instability of boundary layers. *Progress in Aerospace Sciences* **28**, 235–271. 32

[55] FRANSEN, R., GOURDAIN, N. & GICQUEL, L. Y. M. 2012 Steady and unsteady modeling for heat transfer predictions of high pressure turbine blade internal cooling. In *ASME Turbo Expo 2012* (ed. ASME GT2012-69482). Copenhagen. 159

[56] FRANZELLI, B., RIBER, E., SANJOSÉ, M. & POINSOT, T. 2010 A two-step chemical scheme for large-eddy simulation of kerosene-air flames. *Combust. Flame* **157** (7), 1364–1373. 177

[57] FRÖHLICH, J. & VON TERZI, D. 2008 Hybrid LES/RANS methods for the simulation of turbulent flows. *Progress in Aerospace Sciences* **44** (5), 349–377. 21, 72, 73

[58] GANDER, M.J., HALPERN, L., NATAF, F. *et al.* 1999 Optimal convergence for overlapping and non-overlapping Schwarz waveform relaxation. In *the Eleventh International Conference on Domain Decomposition Methods, CH. Lai, P. Bjørstad, M. Cross, and O. Widlund, eds*, pp. 27–36. Citeseer. 82, 102, 110, 158

[59] GANDER, M.J., HALPERN, L., NATAF, F. *et al.* 2000 Optimized Schwarz methods. pp. 15–27. In the 12th International Conference on Domain Decomposition Methods. 101, 154

[60] GICQUEL, L.Y.M., CUENOT, B., STAFFELBACH, G., VERMOREL, O., RIBER, E., DAUPTAIN, A. & POINSOT, T. 2011 Panel session 4-34 - LES modeling of combustors: CERFACS perspective - invited conference. In *ASME Turbo-Expo*. Vancouver, Canada. 209

[61] GILADI, E. & KELLER, H.B. 2002 Space-time domain decomposition for parabolic problems. *Numerische Mathematik* **93** (2), 279–313. 102, 103, 110

[62] GILES, M. B. 1997 Stability analysis of numerical interface conditions in fluid-structure thermal analysis. *Int. J. Numer. Meth. Fluids* **25** (4), 421–436. 189, 196

[63] GOMAR, A., GOURDAIN, N. & DUFOUR, G. 2011 High fidelity simulation of the turbulent flow in a transonic axial compressor. In *European Turbomachinery Conference*. Istanbul, Turkey. 205

[64] GOURDAIN, N. 2011 High-performance computing of gas turbine flows: current and future trends. Habilitation à diriger des recherches. 17, 60, 208

[65] GOURDAIN, N., GICQUEL, L.Y.M. & COLLADO, E. 2011 Comparison of RANS simulation and LES for the prediction of heat transfer in a highly loaded turbine guide vane. In *9th European Conference on Turbomachinery Fluid Dynamics and Thermodynamics (ETC 9)*. Istanbul, Turkey. 205

[66] GOURDAIN, N., GICQUEL, L.Y.M. & COLLADO, E. 2012 Comparison of RANS and LES for the prediction of the wall heat transfer in a highly loaded turbine guide vane. *AIAA J. Propulsion and Power* **28** (2). 35, 48, 49

[67] GOURDAIN, N., GICQUEL, L., MONTAGNAC, M., VERMOREL, O., GAZAIX, M., STAFFELBACH, G., GARCIA, M., BOUSSUGE, JF & POINSOT, T. 2009 High performance parallel computing of flows in complex geometries: I. Methods. *Computational Science & Discovery* **2**, 015003. 20, 22, 210

[68] GRANET, V., VERMOREL, O., LEONARD, T., GICQUEL, L., & POINSOT, T. 2010 Comparison of nonreflecting outlet boundary conditions for compressible solvers on unstructured grids. *AIAA J.* **48** (10), 2348–2364. 130, 178

[69] GRAVEMEIER, V. 2004 The variational multiscale method for laminar and turbulent incompressible flow. PhD thesis. 19

[70] GUEZENNEC, N. 2010 Contrôle actif de la combustion diphasique. PhD thesis, Institut National Polytechnique de Toulouse. 143

[71] GUEZENNEC, N. & POINSOT, T. 2009 Acoustically nonreflecting and reflecting boundary conditions for vorticity injection in compressible solvers. *AIAA J.* **47**, 1709–1722. 40

[72] GUHA, A. 2001 Performance and optimization of gas turbines with real gas effects. *Proceedings of the Institution of Mechanical Engineers, Part A: J. of Power and Energy* **215** (4), 507–512. 13

[73] HANSEN, J., SATO, M., RUEDY, R., KHARECHA, P., LACIS, A., MILLER, R., NAZARENKO, L., LO, K., SCHMIDT, GA, RUSSELL, G. *et al.* 2007 Dangerous human-made interference with climate: a GISS modele study. *Atmospheric chemistry and physics* **7** (9), 2312. 11

[74] HENSHAW, W.D. & SCHWENDEMAN, D.W. 2008 Parallel computation of three-dimensional flows using overlapping grids with adaptive mesh refinement. *J. Comput. Phys.* **227** (16), 7469–7502. 68

[75] HENSHAW, W. D. 2004 Part II: Composite Overlapping Grid Techniques. PhD thesis. PhD thesis, California Institute of Technology. 73

[76] HIRSCH, C. 2007 Finite volume method and conservative discretization with an introduction to finite element method. In *Numerical Computation of internal & external flows: Fundamentals of Computational Fluid Dynamics, second edition*, chap. 5, pp. 203–248. New York: John Wiley & Sons. 27, 125, 134, 206, 207

[77] HIRSCHFELDER, J., CURTIS, C. & BIRD, B. 1954 *Molecular Theory of Gases and Liquids*, 1954th edn. John Wiley & Sons. 200

[78] HOUZEAUX, G. & CODINA, R. 2003 An iteration-by-subdomain overlapping Dirichlet/Robin domain decomposition method for advection–diffusion problems. *J. of computational and applied mathematics* **158** (2), 243–276. 82

[79] HOUZEAUX, G. *et al.* 2002 *A Geometrical Domain Decomposition Methods in Computational Fluid Dynamics*. Universitat Politècnica de Catalunya. 97

[80] JAMESON, A. 1991 Time dependent calculations using multigrid, with applications to unsteady flows past airfoils and wings. *Tech. Rep.* AIAA-91-1596. AIAA 10th Computational Fluid Dynamics Conference. 37

[81] JAMESON, A., SCHMIDT, W. & TURKEL, E. 1981 Numerical solution of the Euler equations by finite volume methods using Runge-Kutta time stepping schemes. In *14th Fluid and Plasma Dynamic Conference* (ed. AIAA paper 81-1259). Palo Alto. 37, 144, 209

[82] JARRIN, N., BENHAMADOUCHE, S., LAURENCE, D. & PROSSER, R. 2006 A synthetic eddy method for generating inflow conditions for large eddy simulations. *Int. J. of Heat and Fluid Flow* **27**, (585–593). 16, 40, 41

[83] JARRIN, N., URIBE, J., PROSSER, R. & LAURENCE, D. 2008 Synthetic inflow boundary conditions for wall bounded flows. *Advances in Hybrid RANS-LES Modelling* pp. 77–86. 16, 18, 143

[84] JAURÉ, S., DUCHAINE, F., STAFFELBACH, G. & GICQUEL, L.Y.M. 2012 Scalable conjugate heat transfer solver based on large eddy simulation and application to an aeronautical combustion chamber. *submitted AIAA J.* . 73, 146, 189

[85] JIMÉNEZ, J., DEL ÁLAMO, J. C. & FLORES, O. 2004 The large-scale dynamics of near-wall turbulence. *J. Fluid Mechanics* **505**, 179–199. 20

[86] JIMÉNEZ, J. & MOIN, P. 1991 The minimal flow unit in near-wall turbulence. *J. Fluid Mechanics* **225**, 213–240. 38

[87] JOHNSON, M. W. 1994 A bypass transition model for boundary layers. *J. Turbomachinery* **116** (4), 759–764. 34

[88] KALITZIN, G., MEDIC, G., IACCARINO, G. & DURBIN, P. 2005 Near-wall behavior of RANS turbulence models and implications for wall functions. *J. Comput. Phys.* **204** (1), 265–291. 19

[89] KEELING, SL, TRAMEL, RW & BENEK, JA 1997 A theoretical framework for Chimera domain decomposition. In *Advances in Flow Simulation Techniques*. 69

[90] KIM, S., SCHLÜTER, J., WU, X., ALONSO, J.J. & PITSCH, H. 2004 Integrated simulations for multi-component analysis of gas turbines: RANS boundary conditions. *AIAA J.* **3415**. 154

[91] KING, R. & JOHNS, DJ 1976 Wake interaction experiments with two flexible circular cylinders in flowing water. *J. of Sound and Vibration* **45** (2), 259–283. 131

[92] KLAPDOR, E.V. 2011 Simulation of combustor-turbine interaction in a jet engine. PhD thesis, TU Darmstadt/Institut für Energie-und Kraftwerkstechnik. 12, 13, 175

[93] KOCH, H. & TATARU, D. 2001 Well-posedness for the Navier–Stokes equations. *Advances in Mathematics* **157** (1), 22–35. 18

[94] KOLMOGOROV, A.N. 1991 The local structure of turbulence in incompressible viscous fluid for very large Reynolds numbers. *Proceedings of the Royal Society of London. Series A: Mathematical and Physical Sciences* **434** (1890), 9–13. 16

[95] KOSTIC, ZG & OKA, SN 1972 Fluid flow and heat transfer with two cylinders in cross flow. *Int. J. Heat and Mass Transfer* **15** (2), 279–282. 131

[96] KRAICHNAN, R.H. 1970 Diffusion by a random velocity field. *Phys. Fluids* **13**, 22–31. 143

[97] KRAICHNAN, R. H. 1976 Eddy viscosity in two and three dimensions. *J. Atmos. Sci.* **33**, 1521–1536. 41

[98] KUZNETSOV, Y.A. 1994 Overlapping domain decomposition methods for parabolic problems. *Contemporary Mathematics* **157**, 63–63. 196

[99] KWON, O. J. & HAH, C. 1995 Simulation of three-dimensional turbulent flows on unstructured meshes. *AIAA J.* **33**. 27

[100] LABOURASSE, E. & SAGAUT, P. 2002 Reconstruction of turbulent fluctuations using a hybrid RANS/LES approach. *J. Comput. Phys.* **182** (1), 301–336. 203

[101] LAMARQUE, N. 2007 Schémas numériques et conditions limites pour la simulation aux grandes échelles de la combustion diphasique dans les foyers d'hélicoptère. Phd thesis, INP Toulouse. 37, 208

[102] LAX, P. D. & WENDROFF, B. 1960 Systems of conservation laws. *Commun. Pure Appl. Math.* **13**, 217–237. 144

[103] LÉONARD, T., DUCHAINE, F., GOURDAIN, N. & GICQUEL, L.Y.M. 2010 Steady/Unsteady Reynolds Averaged Navier-Stokes and Large Eddy Simulations of a turbine blade at high subsonic outlet Mach number. In *Proceedings of the ASME TURBO EXPO 2010 Gas Turbine Technical Congress & Exposit*. Glasgow, UK. 20, 27, 31

[104] LEYKO, M., MOREAU, STÉPHANE, NICOUD, F. & POINSOT, THIERRY 2010 Waves Transmission and Generation in Turbine Stages in a Combustion-Noise Framework. In *16th AIAA/CEAS Aeroacoustics Conference, Stocholm*, p. 14. 14

[105] LEYKO, M., MOREAU, S., NICOUD, F. & POINSOT, T. 2011 Numerical and analytical modelling of entropy noise in a supersonic nozzle with a shock. *J. of Sound and Vibration* . 158

[106] LIN, J.C., YANG, Y. & ROCKWELL, D. 2002 Flow past two cylinders in tandem: instantaneous and averaged flow structure. *J. of fluids and structures* **16** (8), 1059–1071. 121

[107] LIONS, P.L. 1988 On the Schwarz alternating method. I. In *First international symposium on domain decomposition methods for partial differential equations*, pp. 1–42. 67, 82, 100, 101

[108] LIU, Y. 2007 Aerodynamics and heat transfer predictions in a highly loaded turbine blade. *Int. J. of Heat and Fluid Flow* **28**, 932–937. 34, 56

[109] LUI, SH 2001 On Schwarz alternating methods for the incompressible Navier-Stokes equations. *SIAM J. on Scientific Computing* **22** (6), 1974–1986. 101

[110] LUMLEY, J. L. 1978 Computational modeling of turbulent flows. *Adv. Appl. Mech.* **18**, 123–176. 34

[111] LUO, J. & LAKSHMINARAYANA, B. 1997 Numerical simulation of turbine blade boundary layer and heat transfer and assessment of turbulence models. *J. Turbomachinery* **119**, 794–801. 33

[112] MAHIR, N. & ALTAÇ, Z. 2008 Numerical investigation of convective heat transfer in unsteady flow past two cylinders in tandem arrangements. *Int. J. Heat Fluid Flow* **29**, Pages 1309–1318. 137, 138, 140

[113] MARTELLI, F., ADAMI, P. & BELARDINI, E. 2003 Heat transfer modelling in gas turbine stage. *Tech. Rep. ADA419187 University of Florence* . 34

[114] MARTELLI, F., ADAMI, P., SALVADORI, S., CHANA, K.S. & CASTILLON, L. 2008 Aero-thermal study of the unsteady flow field in a transonic gas turbine with inlet temperature distortions. In *ASME Turbo Expo 2008: Power for Land, Sea and Air*. Berlin, Germany. 13

[115] MARTY, J., AUPOIX, B., SCHVALLINGER, M., SHARMA, VC & RAVAUD-RÉAU, R.R. 2008 Effet de la modélisation de la turbulence en proche pompage dans un compresseur multi-étages. In *43ème Colloque d'Aérodynamique Appliquée-AAAF*. 204

[116] MARY, I. & SAGAUT, P. 2002 Large eddy simulation of flow around an airfoil near stall. *AIAA J.* **40** (6), 1139–1145. 20

[117] MATTINGLY, J. D. 2005 *Elements of gas turbine propulsion*, 2nd edn. AIAA. 8

[118] MAYLE, R. E. 1991 The role of laminar-turbulent transition in gas turbine engines. *J. Turbomachinery* **113**, 509–537. 34

[119] MEDIC, G., KALITZIN, G., YOU, D., HERRMANN, M., HAM, F., VAN DER WEIDE, E., PITSCH, H. & ALONSO, J. 2006 Integrated RANS/LES computations of turbulent flow through a turbofan jet engine. In *Annual Research Briefs* , pp. 275–285. Center for Turbulence Research, NASA Ames/Stanford Univ. 151

[120] MEDIC, G., YOU, D. & KALITZIN, G. 2007 On coupling of RANS and LES for integrated computations of jet engines. In *Proceedings of the ASME Turbo Expo 2007*. Montreal, Canada. 14, 66, 72, 145, 154

[121] MENDEZ, S. & NICOUD, F. 2008 Large-eddy simulation of a bi-periodic turbulent flow with effusion. *J. Fluid Mechanics* **598**, 27–65. 37

[122] MENTER, F.R. 1994 Two-equation eddy viscosity turbulence model for engineering applications. *AIAA J.* **32** (8). 35, 37, 42

[123] MENTER, F.R., LANGTRY, R.B., LIKKI, S.R. & SUZEN, Y.B. 2006 A correlation-based transition model using local variables - Part 1: model formulation. *J. Turbomachinery* **128** (3). 35, 36, 37, 40, 45

[124] MICHELASSI, V., WISSINK, J. & RODI, W. 2002 Analysis of DNS and LES of flow in a low pressure turbine cascade with incoming wakes and comparison with experiments. *Flow, Turbulence and Combustion* **69**, 295–330. 33

[125] MOIN, P. 2002 Advances in large eddy simulation methodology for complex flows. *Int. J. Heat Fluid Flow* **23** (5), 710–720. 20, 34

[126] MOIN, P., SQUIRES, K. D., CABOT, W. & LEE, S. 1991 A dynamic subgrid-scale model for compressible turbulence and scalar transport. *Phys. Fluids* **A 3** (11), 2746–2757. 35, 205

[127] MOREAU, M. 2006 Modélisation numérique directe et des grandes échelles des écoulements turbulents gaz-particules dans le formalisme eulérien mésoscopique. Phd thesis, INP Toulouse. 117

[128] MORTON, K.W. & MAYERS, D.F. 2005 *Numerical solution of partial differential equations: an introduction*. Cambridge Univ Pr. 206

[129] MOUREAU, V., DOMINGO, P. & VERVISCH, L. 2011 From large-eddy simulation to direct numerical simulation of a lean premixed swirl flame: Filtered laminar flame-pdf modeling. *Combust. Flame* **158** (7), 1340–1357. 19

[130] MOUREAU, V., LARTIGUE, G., SOMMERER, Y., ANGELBERGER, C., COLIN, O. & POINSOT, T. 2005 Numerical methods for unsteady compressible multi-component reacting flows on fixed and moving grids. *J. Comput. Phys.* **202** (2), 710–736. 209

[131] M.P.ERRERA, QUÉMERAIS, E. & BAQUÉ, B. 2010 Approche Multi-Physique par Couplage de Codes. Application en Aérothermique. In *1er Colloque International Francophone d'Energétique et Mécanique*. Saly, Sénégal. 212

[132] NICOUD, F. 1998 Defining wave amplitude in characteristic boundary conditions. *J. Comput. Phys.* **149** (2), 418–422. 74, 75

[133] NICOUD, F., BAYA-TODA, H., CABRIT, O., BOSE, S. & LEE, J. 2011 Using singular values to build a subgrid-scale model for large eddy simulations. *Phys. Fluids* **23** (8). 20, 157, 205

[134] NICOUD, F. & DUCROS, F. 1999 Subgrid-scale stress modelling based on the square of the velocity gradient. *Flow, Turb. and Combustion* **62** (3), 183–200. 27, 36

[135] OLSSON, F. & PETERSSON, N.A. 1996 Stability of interpolation on overlapping grids. *Computers & fluids* **25** (6), 583–605. 146, 154

[136] PASSOT, T. & POUQUET, A. 1987 Numerical simulation of compressible homogeneous flows in the turbulent regime. *J. Fluid Mechanics* **181**, 441–466. 41

[137] PEIRÓ, J. & SHERWIN, S. 2005 Finite difference, finite element and finite volume methods for partial differential equations. *Handbook of Materials Modeling* pp. 2415–2446. 206

[138] PIERCE, C.D. & MOIN, P. 2004 Progress-variable approach for large-eddy simulation of non-premixed turbulent combustion. *J. Fluid Mechanics* **504** (1), 73–97. 20

[139] PIOMELLI, U. 2008 Wall-layer models for large-eddy simulations. *Prog. Aerospace Sci.* **44** (6), 437–446. 20

[140] PIOMELLI, U., MOIN, P. & FERZIGER, J. H. 1988 Model consistency in large eddy simulation of turbulent channel flows. *Phys. Fluids* **31** (7), 1884–1891. 20

[141] POINSOT, T. & LELE, S. 1992 Boundary conditions for direct simulations of compressible viscous flows. *J. Comput. Phys.* **101** (1), 104–129. 73, 74, 75, 76

[142] POINSOT, T. & VEYNANTE, D. 2005 *Theoretical and Numerical Combustion*. R.T. Edwards, 2nd edition. 34, 74, 75, 199

[143] POITOU, D., ELHAFI, M. & CUENOT., B. 2011 Analysis of radiation modeling for turbulent combustion : development of a methodology to couple turbulent combustion and radiative heat transfer in LES. *J. of Heat Transfer* **133** (6). 211

[144] POPE, S. B. 1983 Consistent modeling of scalar in turbulent flows. *Phys. Fluids* **2**, 404–408. 41

[145] POPE, S. B. 2000 *Turbulent flows*. Cambridge University Press. 17, 27, 34, 41, 147

[146] QUARTERONI, A., PASQUARELLI, F. & VALLI, A. 1992 Heterogeneous domain decomposition: principles, algorithms, applications. In *Fifth International Symposium on Domain Decomposition Methods for Partial Differential Equations*, pp. 129–150. SIAM, Philadelphia. 91, 101, 158

[147] QUÉMÉRÉ, P. & SAGAUT, P. 2002 Zonal multi-domain RANS/LES simulations of turbulent flows. *Int. J. for Num. Meth. in Fluids* **40** (7), 903–925. 21

[148] RICHARD, J. & NICOUD, F. 2011 Effect of the fluid structure coupling on the aeroacoustic instabilities of solid rocket motors. In *17th AIAA/CEAS AeroAcoustics Conference*. Portland, Oregon, USA. 211

[149] ROIDL, B., MEINKE, M. *et al.* 2012 A zonal RANS-LES method for compressible flows. *Computers & Fluids* . 158

[150] ROUX, A., GICQUEL, L. Y. M., REICHSTADT, S., BERTIER, N., STAFFELBACH, G., VUILLOT, F. & POINSOT, T. 2010 Analysis of unsteady reacting flows and impact of chemistry description in large eddy simulations of side-dump ramjet combustors. *Combust. Flame* **157**, 176–191. 20

[151] ROUX, S., CAZALENS, M. & POINSOT, T. 2008 Influence of outlet boundary condition for large eddy simulation of combustion instabilities in gas turbine. *J. Prop. Power* **24** (3), 541–546. 14

[152] SAGAUT, P. 2000 *Large Eddy Simulation for incompressible flows*. Springer-Verlag. 27, 34

[153] SAGAUT, P. & DECK, S. 2009 Large-Eddy Simulation for aeronadymics: status and perspectives. *Phil. Trans. R. Soc. Lond.* **367**, 2849–2860. 21, 27

[154] SARIC, W. S. 1994 Görtler vortices. *Ann. Rev. Fluid Mech.* **26**, 379–409. 58

[155] SAWYER, R.F. 2009 Science based policy for addressing energy and environmental problems. *Proceedings of the Combustion Institute* **32** (1), 45–56. 11, 12

[156] SCHLICHTING, H. & GERSTEN, K. 2000 *Boundary-layer theory*. Springer Verlag. 17

[157] SCHLÜTER, J.U. 2003 Advanced signal processing for integrated LES-RANS simulations: Anti-aliasing filters. In *Annual Research Briefs* , pp. 343–356. Center for Turbulence Research, NASA Ames/Stanford Univ. 14, 154

[158] SCHLÜTER, J., APTE, S., KALITZIN, G., VAN DER WEIDE, E., ALONSO, J. J. & PITSCH, H. 2005 Large-scale integrated LES-RANS simulations of a gas turbine engine. In *Annual Research Briefs* , pp. 111–120. Center for Turbulence Research, NASA Ames/Stanford Univ. 14

[159] SCHLUTER, J., PITSCH, H. & MOIN, P. 2002 Consistent boundary conditions for integrated LES/RANS simulations- LES outflow conditions. In *32 nd AIAA Fluid Dynamics Meeting, St. Louis, MO*. 73

[160] SCHLÜTER, J.U., PITSCH, H. & MOIN, P. 2005 Anti-Aliasing Filters for Coupled Reynolds-Average/Large-Eddy Simulations. *AIAA J.* **43** (3), 608–616. 117

[161] SCHLÜTER, J.U., PITSCH, H. & MOIN, P. 2005 Outflow conditions for Integrated Large Eddy Simulation/Reynolds-Average Navier-Stokes Simulations. *AIAA J.* **43** (1), 156–164. 66, 72, 129, 149, 154

[162] SCHLÜTER, J.U. & WU, X. 2004 On LES outflow conditions for integrated LES-RANS computations. In *Annual Research Briefs* , pp. 107–116. Center for Turbulence Research, NASA Ames/Stanford Univ. 14, 66

[163] SCHLÜTER, JU, WU, X., KIM, S., SHANKARAN, S., ALONSO, JJ & PITSCH, H. 2005 A framework for coupling Reynolds-averaged with large-eddy simulations for gas turbine applications. *J. Fluids Eng.* **127**, 806. 21, 73

[164] SCHØNFELD, T. & RUDGYARD, M. 1999 Steady and unsteady flows simulations using the hybrid flow solver AVBP. *AIAA J.* **37** (11), 1378–1385. 37, 65, 209

[165] SCHWARZ, H.A. 1890 *Gesammelte mathematische abhandlungen*, , vol. 1. J. Springer. 67

[166] SEHITOGLU, H. 1993 *Thermomechanical Fatigue Behavior of Materials*. ASTM. 11

[167] SELLE, L., NICOUD, F. & POINSOT, T. 2004 The actual impedance of non-reflecting boundary conditions: implications for the computation of resonators. *AIAA J.* **42** (5), 958–964. 76

[168] SERGENT, E. 2002 Vers une méthodologie de couplage entre la simulation des grandes echelles et les modèles statistiques. PhD thesis. 21

[169] SICOT, F. 2009 Simulation efficace des écoulements instationnaires périodiques en turbomachines. PhD thesis, Ecole Centrale de Lyon - École Doctorale Mécanique, Énergétique, Génie civil et Acoustique. 207, 209

[170] SINGH, SP & MITTAL, S. 2005 Flow past a cylinder: shear layer instability and drag crisis. *Int. J. for Num. Meth. in Fluids* **47** (1), 75–98. 137

[171] SMAGORINSKY, J. 1963 General circulation experiments with the primitive equations: 1. The basic experiment. *Mon. Weather Rev.* **91**, 99–164. 35, 36, 144, 203, 204

[172] SMIRNOV, E. & SMIRNOVSKY, A. 2009 Turbine vane cascade heat transfer predictions using a modified version of the $\mathrm{Re}_{\theta t}$ laminar-turbulent transition model. *Int. Symp. On Heat Transfer in Gas Turbine Systems* . 27, 34

[173] SMITH, B. R. 1990 The k-kl turbulence model and wall layer model for compressible flows. *AIAA Paper 1990-1483* pp. 21st AIAA Fluid Dynamics, Plasma Dynamics and Lasers Conference. 144

[174] STAFFELBACH, G., GICQUEL, L.Y.M., BOUDIER, G. & POINSOT, T. 2009 Large eddy simulation of self-excited azimuthal modes in annular combustors. *Proc. Combust. Inst.* **32**, 2909–2916. 20, 37, 79

[175] STEGER, J. L. & WARMING, R. F. 1981 Flux vector splitting of the inviscid gasdynamic equations with application to finite-difference methods. *J. Comput. Phys.* **40**, 263–293. 73

[176] STULL, D. R. & PROPHET, H. 1971 JANAF thermochemical tables, 2nd edition. *Tech. Rep.* NSRDS-NBS 37. US National Bureau of Standards. 201

[177] TANIDA, Y., OKAJIMA, A. & WATANABE, Y. 1973 Stability of a circular cylinder oscillating in uniform flow or in a wake. *J. Fluid Mechanics* **61** (04), 769–784. 131

[178] TENNEKES, H. & LUMLEY, J. L. 1972 *A first course in turbulence*. Cambridge: M.I.T. Press. 27, 34, 41

[179] TERRACOL, M., SAGAUT, P. & BASDEVANT, C. 2001 A multilevel algorithm for large-eddy simulation of turbulent compressible flows. *J. Comput. Phys.* **167** (2), 439–474. 21

[180] VON TERZI, DA & FRÖHLICH, J. 2007 Coupling conditions for LES with downstream RANS for the prediction of incompressible turbulent flows. In *Proceedings of Turbulence and Shear Flow Phenomena*, , vol. 5. 14, 21, 72

[181] VON TERZI, DA & FRÖHLICH, J. 2008 A statistically consistent approach to segregated LES-RANS coupling at tangential interfaces. In *Proc. of 7th Int. ERCOFTAC Symp. on Engineering Turbulence Modelling and Measurements ETMM-7*, pp. 28–33. 21

[182] TOURNIER, J.M. 1993 Turbulence et lois de paroi. Master's thesis, Institut National Polytechnique, CERFACS. 147, 148

[183] TRUFFIN, K. 2005 Simulation aux grandes échelles et identification acoustique des turbines à gaz en régime partiellement prémélangé. Phd thesis, INP Toulouse. 209

[184] TUCKER, PG 2011 Computation of unsteady turbomachinery flows: Part2 -LES and hybrids. *Progress in Aerospace Sciences* . 20

[185] TURNER, M.G., NORRIS, A. & VERES, J.P. 2004 High fidelity three dimensional simulation of the GE90. *Tech. Rep.*. NASA TM 2004-212981. 14

[186] VARADARAJAN, K. & BOGARD, D.G. 2004 Effects of hot streaks on adiabatic effectiveness for a film cooled turbine vane. In *ASME Turbo Expo 2004: Power for Land, Sea, and Air (GT2004)*. 12

[187] VERSTRAETE, T., ALSALIHI, Z. & DEN BRAEMBUSSCHE, R. A. VAN 2007 Numerical study of the heat transfer in micro gas turbines. *J. Turbomachinery* **129** (4), 835–841. 77

[188] VON KARMAN, T. 1948 Progress in the statistical theory of turbulence. *Proceedings of the National Academy of Sciences of the United States of America* **34** (11), 530. 18

[189] WHITE, F. M. 1991 *Viscous fluid flow*. New-York: McGraw-Hill. 57, 199

[190] WISSINK, J. & RODI, W. 2006 Direct numerical simulation of flow and heat transfer in a turbine cascade with incoming wakes. *J. Fluid Mechanics* **569**, 209–247. 33

[191] WLASSOW, F. 2012 Analyse instationnaire aérothermique d'un étage de turbine avec transport de points chauds: application à la maîtrise des performances des aubages. PhD thesis, Ecole Centrale de Lyon. 12, 60, 72, 154, 159

[192] WLASSOW, F., DUCHAINE, F., LEROY, G. & GOURDAIN, N. 2010 3D simulation of coupled fluid flow and solid heat conduction for the calculation of blade wall temperature in a turbine stage. *ASME Turbo expo (ed. GT2010-22513). Glasgow, UK* . 12, 159, 178

[193] XIA, JL, SMITH, BL, BENIM, AC, SCHMIDLI, J. & YADIGAROGLU, G. 1997 Effect of inlet and outlet boundary conditions on swirling flows. *Computers & fluids* **26** (8), 811–823. 14

[194] XIONG, Z. & LELE, S.K. 2007 Stagnation-point flow under free-stream turbulence. *J. Fluid Mechanics* **519**, 201–232. 33

[195] YARDI, N. R. & SUKHATME, S. P. 1978 Effect of turbulence intensity and integral scale of a turbulent free stream on forced convection heat transfer from a circular cylinder in cross-flow. , vol. 5, pp. 347–352. 32

[196] YOO, C.S. & IM, H.G. 2007 Characteristic boundary conditions for simulations of compressible reacting flows with multi-dimensional, viscous, and reaction effects. *Combust. Theory and Modelling* **11**, 259–286. 130

[197] YOON, S. & JAMESON, A. 1987 An LU-SSOR scheme for the Euler and Navier-Stokes equations. *25th AIAA Aerospace Science Meeting* . 37, 125, 134, 144

[198] ZDRAVKOVICH, MM 1977 Review of flow interference between two circular cylinders in various arrangements. *J. Fluids Eng.* **99**, 618–631. 131, 137

[199] ZHANG, Q., SCHRÖDER, W. & MEINKE, M. 2010 A zonal RANS-LES method to determine the flow over a high-lift configuration. *Computers & Fluids* **39** (7), 1241–1253. 151

Part III

Appendices

Appendix A

Simulation of the combustion chamber and NGV in LES

A.1 The study case: TURBOMECA propulsion system

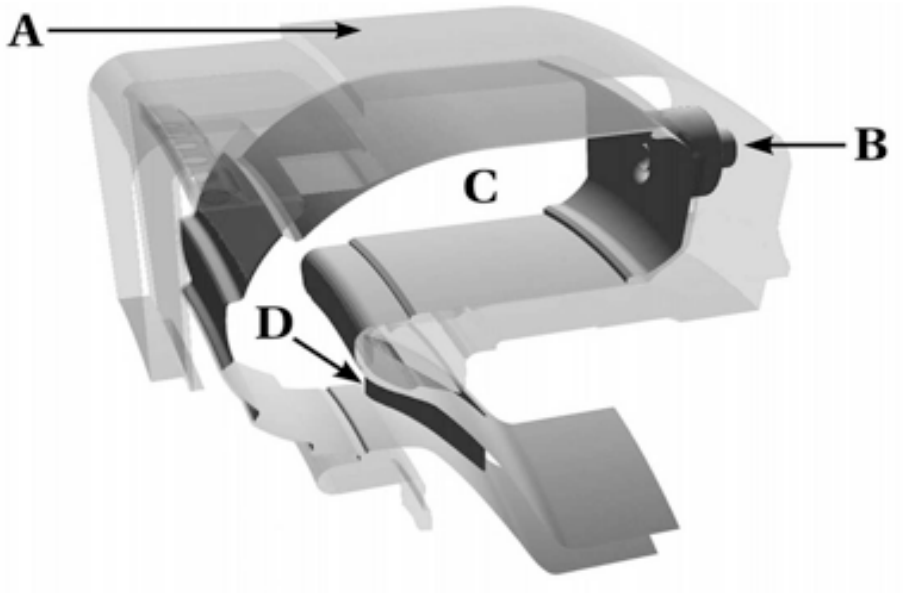

Figure A.1: View of the propulsion system geometry.

The aim of this study is to carry out a LES calculation, which integrates the chamber geometry as well as the one of the NGV of the turbine. A similar study is attempted with RANS codes in the dissertation of Klapdor [92]. This LES computation is the one to be used coupled to the RANS calculation in the turbine to determine the temperature of the high-pressure rotor, which is of prime importance for the efficiency and life expectancy of the whole propulsion system. Here, the objective

is to improve the combustion chamber overall predictions at its outlet so that the input for the turbine stage computation would be more accurate.

The configuration is a sector ($1/N$, N being the total number of injectors) of a helicopter combustion chamber, including the secondary air flow (**A**) and the NGV (**D**) like shown in Fig. A.1. The calculation takes into account all the components positioned between the outlet of the combustion chamber and the high-pressure rotor, as, for instance, the multiperforations. The novelty from this computation is the inclusion of the NGV in the LES prognosis. The flame tube (**C**) is fed with air through two contra-rotating swirlers and gaseous kerosene at the center (**B**). Cold air films along the walls assure the chamber cooling. The calculated operating point correspond to the normal flight operating point.

A.1.1 Mesh

The LES mesh is built with 11.9 10^6 tetrahedrical cells. It takes into account the secondary air flow as well as the cooling films and dilution jets, but only in the combustion chamber region. The mesh is refined in the primary zone, where the flame stabilizes in a conical zone. 5 10^6 cells are used for the combustion chamber (Fig A.2). The other half is used to refine the NGV vane (Fig A.3).

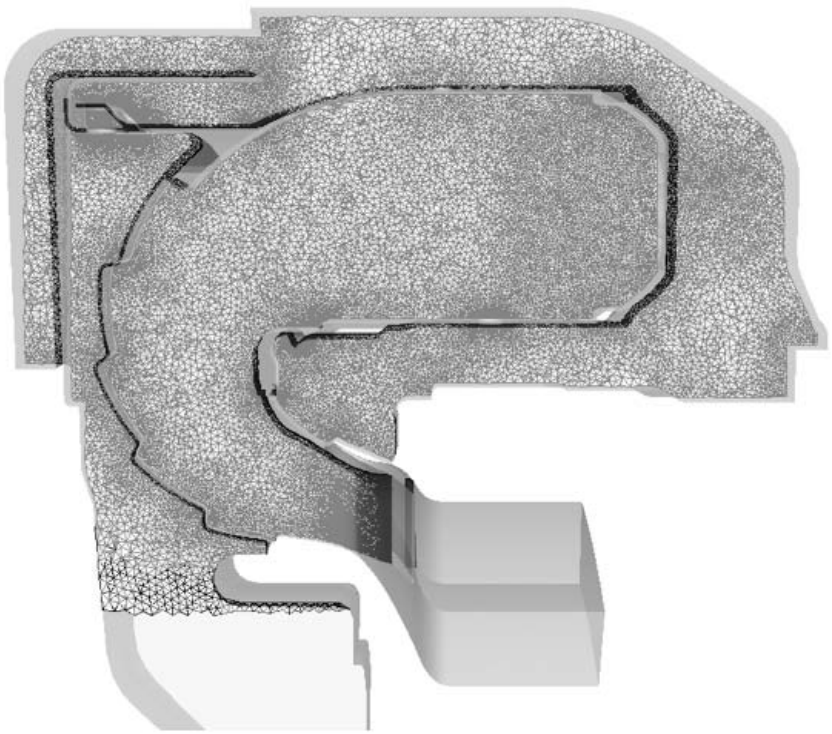

Figure A.2: View of the combustor mesh.

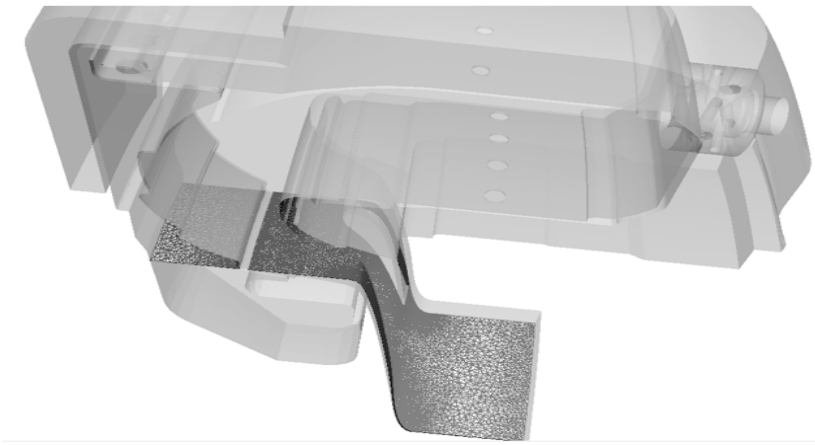

Figure A.3: View of the DHP mesh.

The original mesh comes from an isolated combustion chamber calculation. This mono-component mesh is the one used for the implementation of the NGV. Thus, the mesh had to change to adapt to the mesh used by RANS *elsA* simulation for the turbine stage. Indeed, Fig. A.4 shows the differences between the meshes. Results on the next section are shown only for the modified mesh.

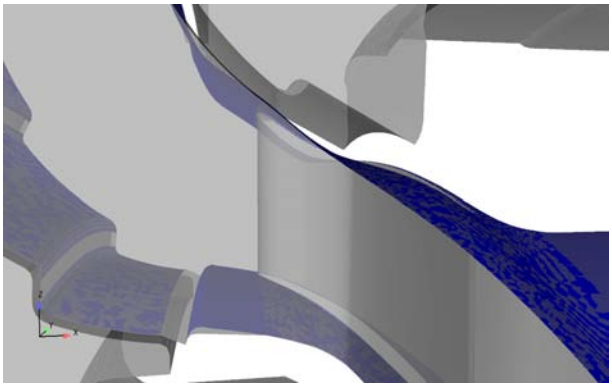

Figure A.4: View of the geometry change performed.

A.1.2 Numerical parameters

The LES is performed with the AVBP code. The numerical method employed for the integration is the second order Lax-Wendroff scheme. The sub-grid scale turbulent model used is the Smagorinsky model. The turbulent Schmidt and Prandtl numbers are equal to 0.6. The mean time step imposed by the CFL is of 2.2 10^{-8} s. The chemical kinetic scheme used for the kerosene is Kero-Luche, which reduces to 2 steps the global scheme [56]. A new specific correction for thickening flame model, which results are shown later in Fig. A.7 has been validated to improve the model of the second

reaction. Thermodynamic properties are tabulated so as to recover the correct temperature influence.

An algebraic adiabatic law of the wall is used for the walls of the geometry including the blade. In the outlet of the NGV, the pressure is fixed following the mean value obtained by a RANS computation in this plane for the turbine stage [192]. Some problems were encountered in the outlet limit of the computational domain. They were resolved by using the 3D approach for pressure [68] and the imposition of axisymmetric equal values. Obviously, to impose a constant pressure at the outlet of the computation domain is a limitation, no feedback from the rotor presence is taken. This constitutes one of the reason why the coupling strategy between AVBP and *elsA* is prone to. And a first step to achieve a coupled industrial computation is to perform a simulation taking into account a combustion chamber and a NGV at the same time, like this computation does; the NGV region being the overlap zone between LES and RANS computations in the future coupled simulation.

A summary of the numerical parameters used in the TURBOMECA engine computational case can be found in Table A.1.

Numerical scheme	LW
Sub-grid model	Smagorinsky
2nd order AV	0.2
4rth order AV	0.01
Time step	2.2 $10^{-}8$
Pr	0.739
Pr_t	0.6

Table A.1: Summary of the numerical parameters used for the calculation.

A.2 Numerical results

A.2.1 Average results

Figure A.5 (a) shows the mean axial velocity in the median plane, adimensionalized by the injection velocity. The recirculation zone, which is limited by a zero axial velocity contour, can be recognized. This contour extends from the injector nozzle to half the primary zone. The flow is not symmetric due to the curved geometry of the combustion chamber. Furthermore, the flow is strongly accelerated in the distributor, as it can be noticed in Fig. A.6 (b). The RMS axial velocity field emphasizes zones of high turbulence in Fig. A.5 (b). Close to the injection, there are shear zones and behind the central recirculation zone, the hot gas mix with the primary air jets.

Figure A.6 (a) displays the mean temperature, adimensionalized by the injection temperature T_{inj}. The hot primary zone reaches around the conical flame a maximum temperature of $4T_{inj}$. The flame

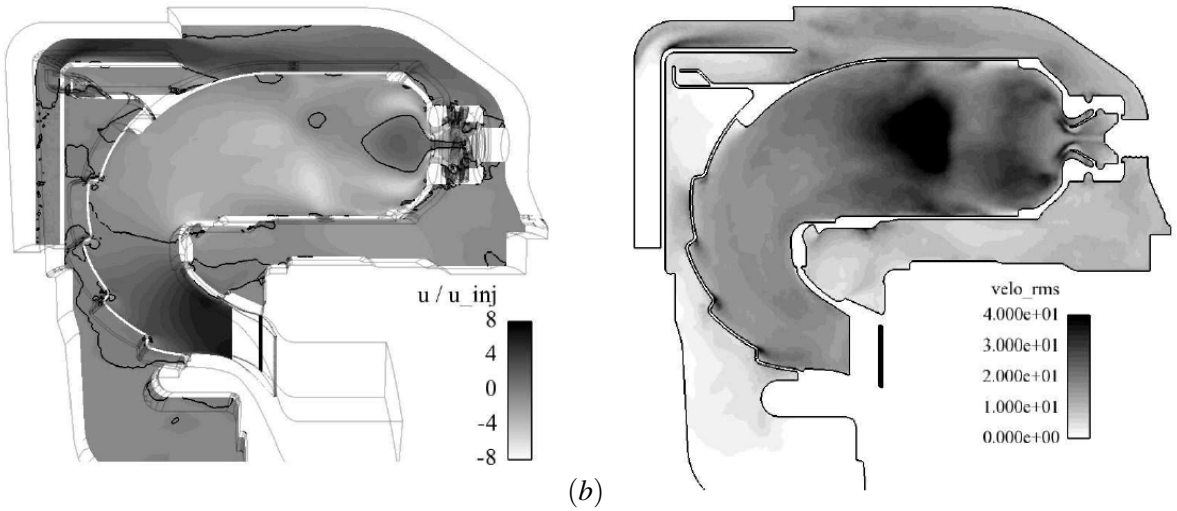

Figure A.5: Dimensionless mean axial velocity in the median plane with iso-contour of zero velocity (a) and RMS velocity (b).

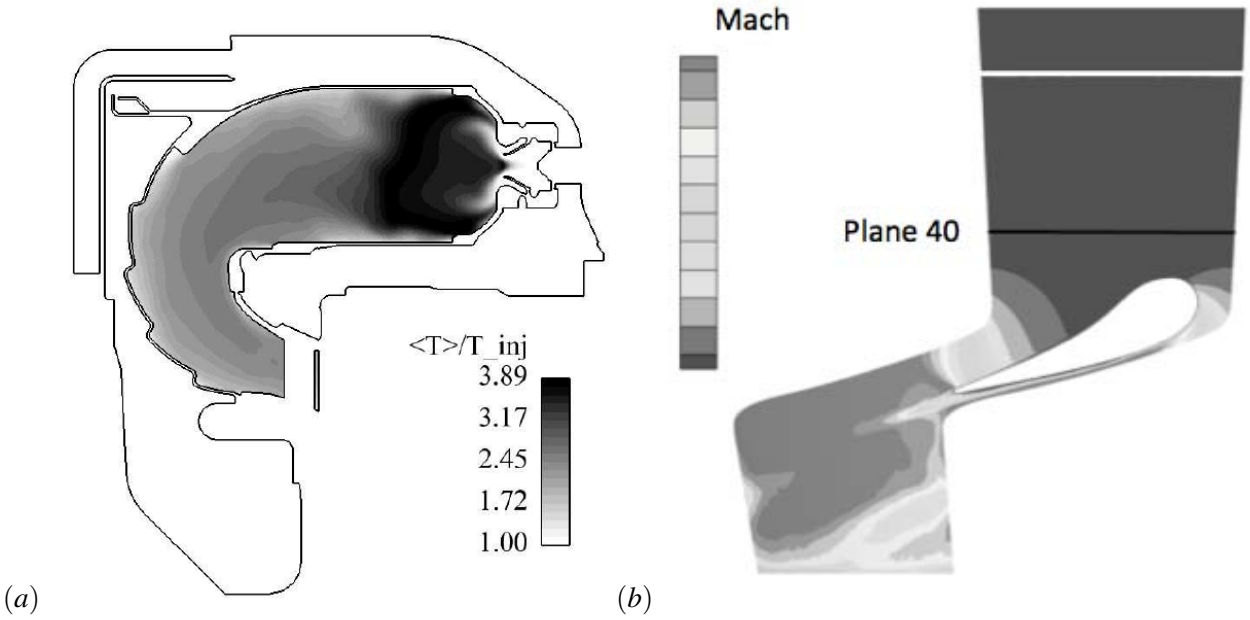

Figure A.6: Dimensionless mean static temperature in the median plane (a) and Mach number in the NGV vane (b).

is asymmetric as the hot zone is more extended on the internal side. In fact, the hot gases are cooled down abruptly by the cold air jets, down to a temperature around $2T_{inj}$. The temperature of the burnt gases gradually decreases downstream through the action of the cooling films along the chamber walls, reaching a value around $1.5T_{inj}$ near the blade. Although high turbulence levels in the dilution zone (Fig. A.5 (b)) increases mixing, the temperature is not homogeneous at the chamber exit.

A.2.2 Instantaneous results

The mesh refinement in such a computation does not allow to capture the real flame thickness, which is normally smaller than the mesh refinement. A thickened model [38] is introduced to replace the flame by an equivalent thicker flame resolvable with the mesh given.

The flame thickening can be seen in Fig. A.7 with an iso-surface of heat release (HR in the figure). The thickening procedure is only applied in the reacting zones. These results show that the model correction performed on the second equation is consistent with the physics expected in the recirculation zone.

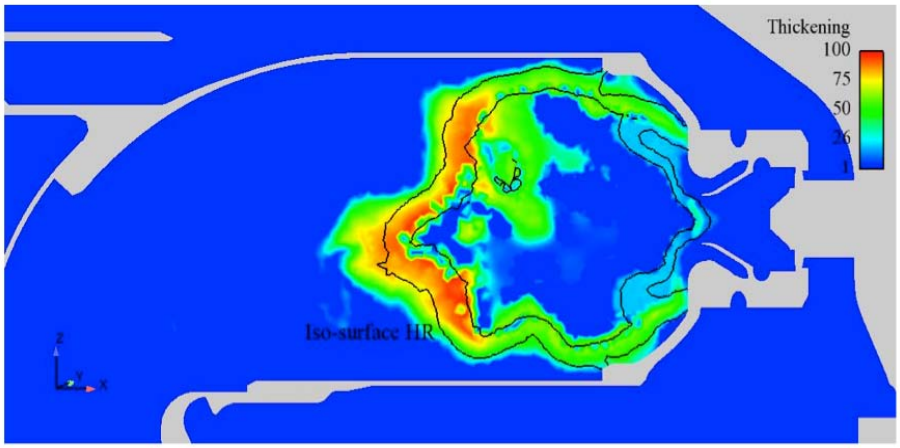

Figure A.7: Thickening field and iso-surface of HR in the median plane.

A.2.3 Effect of the NGV presence on aerodynamic magnitudes

Mean aerodynamic magnitudes are compared on a plane, which is 3 mm upstream of the leading edge of the NGV, for two cases:

- ◇ when there is not NGV in the computation,
- ◇ when there is a NGV in the computation domain.

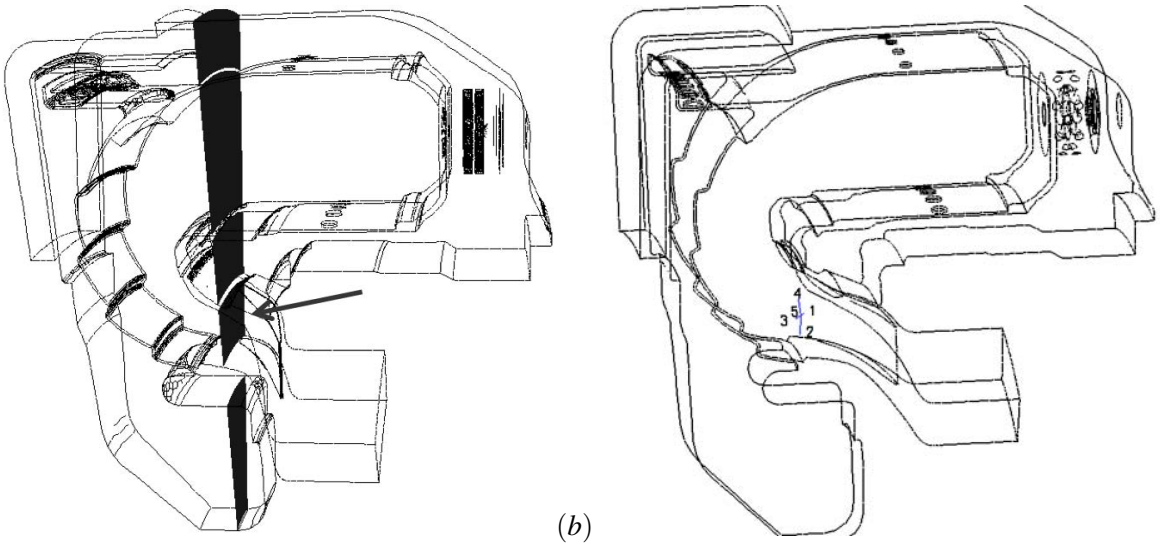

Figure A.8: (a) Location of the plane 40 and (b) view of the position of the probes in the plane 40 upstream of the NGV.

This plane, called plane 40, is shown in Fig. A.8 (a). Figure A.9 shows that the NGV has a great influence on all the quantities:

- U, V_t,V_r, the axial velocity, the tangential velocity and the radial velocity, respectively,
- *rho*, T, P, density, temperature and pressure, respectively.

The first consequence is that fields are more heterogenous in the azimuthal direction because of the NGV appearance. In the tangential velocity field, it can be noticed that velocity vectors have to adapt to the presence of a leading edge. Moreover, in the axial velocity and the pressure fields, the potential effects clearly appear: there is an acceleration on the suction side and a deceleration on the pressure side.

The two calculations have approximatively reached the same statistical values. Both of them have strictly the same set of numerical parameters (scheme, sub-grid model, average iteration step, ...). A negative iso-surface of axial velocity is taken in the whole volume in Fig. A.10 (a) for the computation without NGV and (b) with NGV. The influence of the NGV on the aerodynamic behavior of the chamber appears in a recirculation, in circles, before the leading edge of the NGV in hub and shroud. Nowadays, no boundary condition in *elsA* allows to have a negative axial velocity at the inlet. However, the coupling methodology proposed in this thesis allows a region at the inlet of the *elsA* computational domain where the velocity is negative, as shown in Section 5.3.

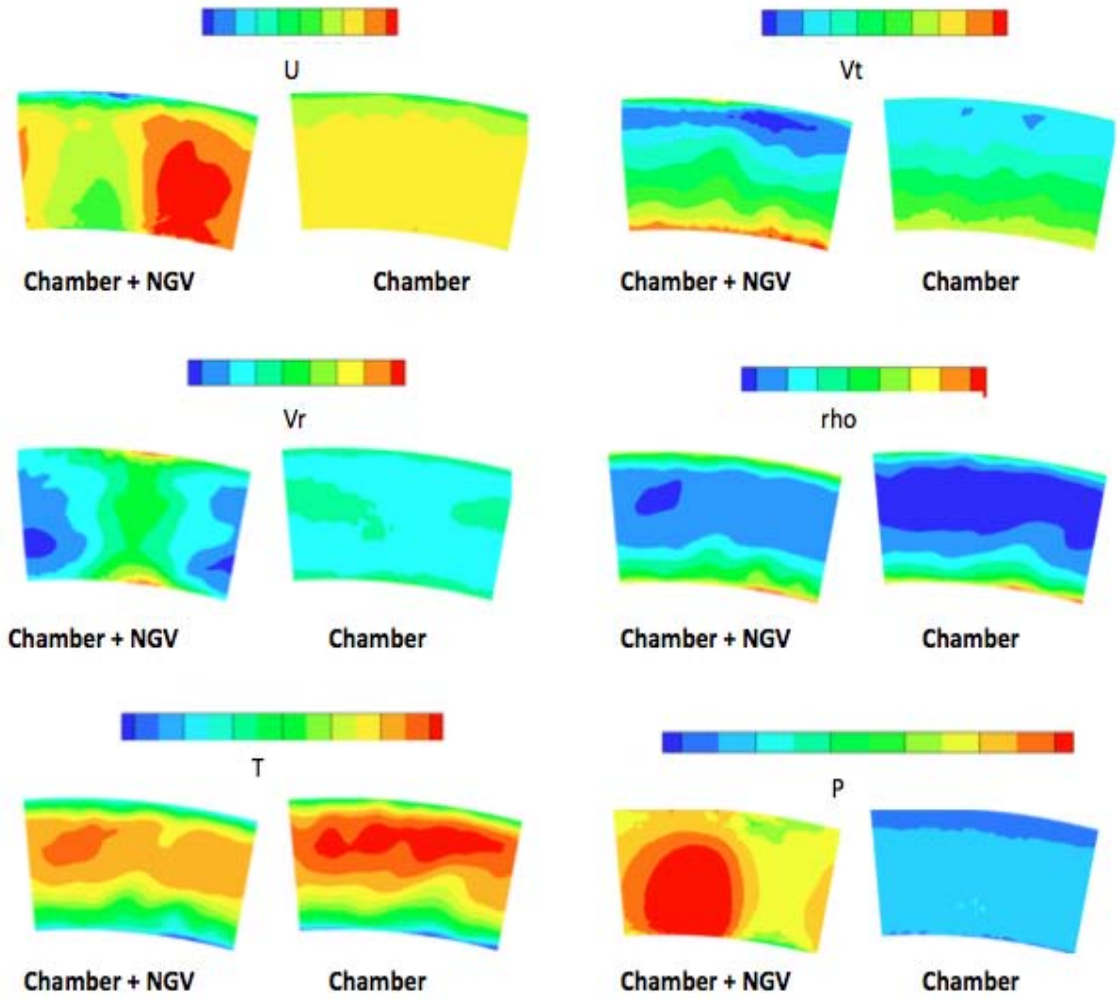

Figure A.9: Mean aerodynamic magnitudes with and without NGV in plane 40.

A.2.4 Unsteadiness upstream of the NGV

To characterize the unsteadiness at the inlet of the NGV vein, 5 probes have been placed in the plane 40. Their location is shown in Fig. A.8 (b). The temperature fluctuations are analyzed for the resolved LES field. The temperature fluctuations can be represented as a function of the time normalized by the revolution period of the high pressure rotor, like in Fig. A.11. It can be seen from the picture that during a rotor revolution, the upstream condition can vary radically, $T_{rms} \sim \pm 300K$, this phenomenon can affect the thermo-mechanical fatigue of the blades.

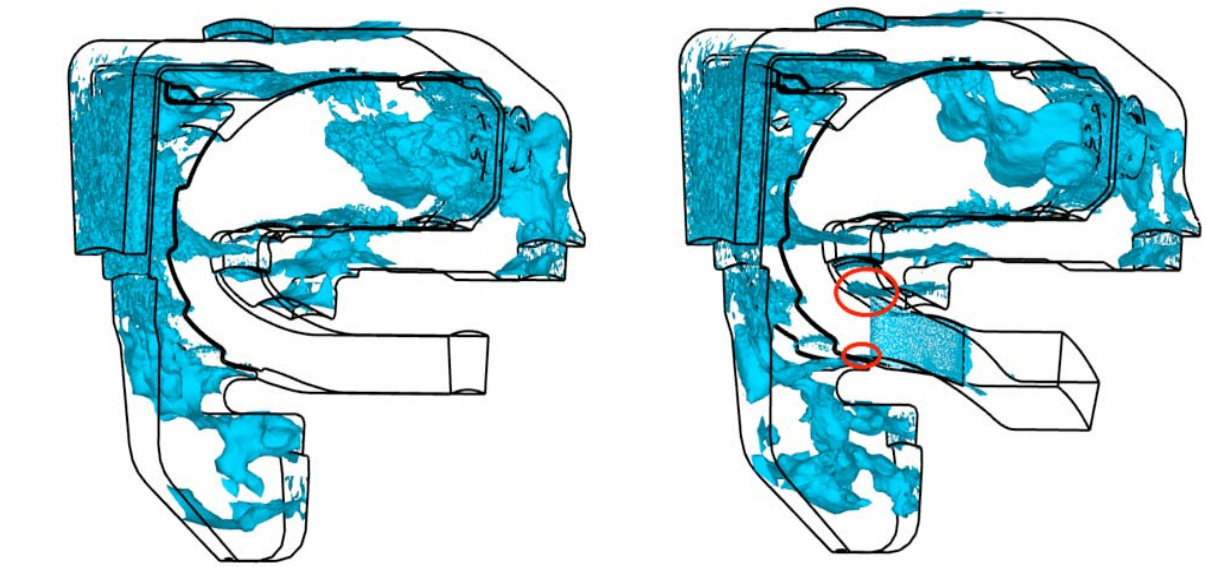

(a) (b)

Figure A.10: Isosurface of negative axial velocity in the calculation of the combustion chamber alone (a) and the combustion chamber with NGV (b).

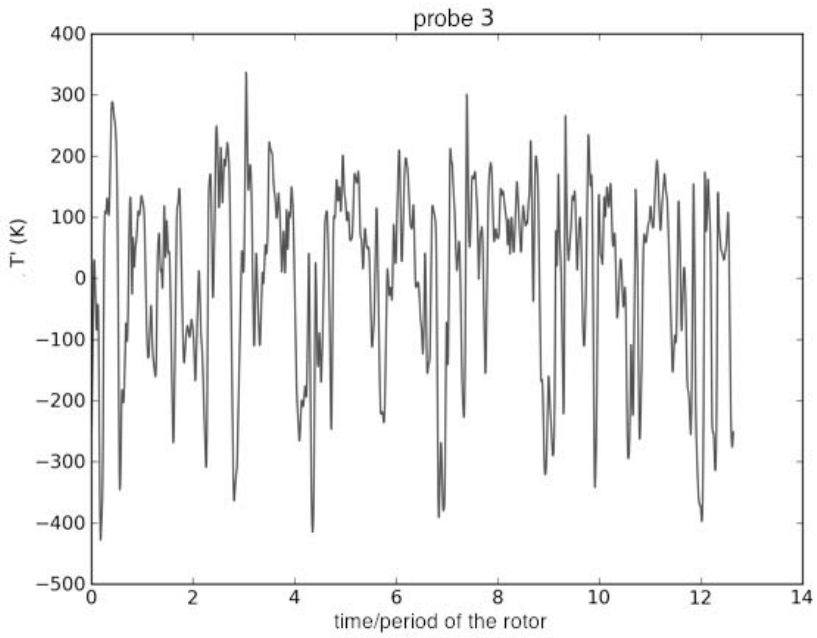

Figure A.11: Fluctuations of temperature in probe 3.

A.2.5 Radial Temperature Factor (RTF)

Engine manufacturers usually want to know the overheating of the combustion gases over the combustion chamber. That is the reason why they use a dimensionless profile of radial temperature to compare the heating capacity of engines. The RTF is computed at the perpendicular plane to the axis, plane 40 (Fig. A.8 (a)). The comparison of different RTF curves makes it possible for designers to analyze the homogeneity of the temperature field.

$$\dot{m}_{40} = \int_{A_{40}} \rho(r,\theta) u(r,\theta) dA \tag{A.1}$$

In Eq. (A.1), $\dot{m}_{40}$ represents the flow going through the plane 40, $u(r,\theta)$ and $\rho(r,\theta)$ are the axial velocity and the density in cylindric coordinates in the plane 40. The specific mean enthalpy value is shown in Eq. (A.2), $H(r,\theta)$ stands for the value of enthalpy in each point of the plane, it is a function of the total temperature $T(r,\theta)$ and the chemical composition.

$$\overline{H_{40}} = \frac{\int_{A_{40}} \rho(r,\theta) u(r,\theta) H(r,\theta) dA}{\dot{m}_4} \tag{A.2}$$

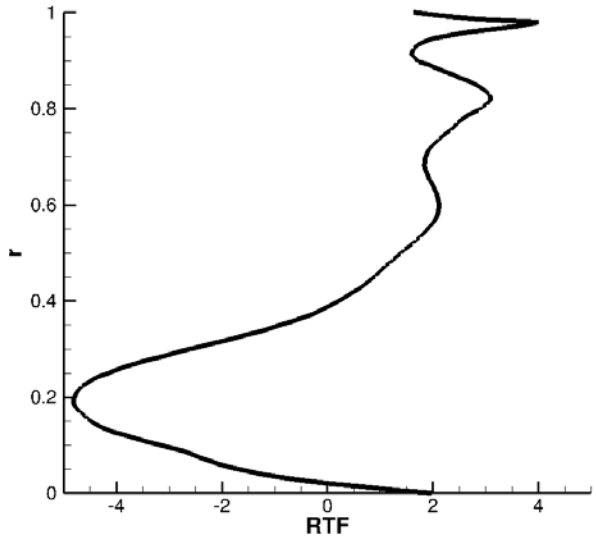

Figure A.12: Comparison of the Radial Temperature Factor of two calculations with/without NGV.

The relative increase of the enthalpy can be written as follows in Eq. (A.3) as a function of $\overline{H}_3$, the mean enthalpy of gases at the compressor outlet. The enthalpy is not a magnitude that can be easily extracted from the flow in experimental tests. The expression with enthalpies can be replaced by an

equation with temperatures, which can be taken out experimentally from the flow without difficulty. The local factor of temperature is defined in Eq. (A.4).

$$\frac{H(r,\theta)-\overline{H_{40}}}{\overline{H_{40}}-\overline{H_3}} \tag{A.3}$$

$$\frac{T(r,\theta)-\overline{T_{40}}}{\overline{T_{40}}-\overline{T_3}} \tag{A.4}$$

It should be noticed that the integral of the term in Eq. (A.3) is equal to zero by construction in the plane 40. On the contrary, the integral of the local factor of temperature in the Eq. (A.4) is not equal to zero, unless it is supposed that c_p and ρ are uniform in this plane. This hypothesis is accepted, the Radial Temperature Factor is defined by the formula in Eq. (A.5):

$$RTF(r)=\frac{\left(\frac{1}{2\pi}\int_{0\leq\theta\leq 2\pi}T(r,\theta)d\theta\right)-\overline{T_{40}}}{\overline{T_{40}}-\overline{T_3}} \tag{A.5}$$

The RTF of the actual computation is compared to the RTF of the combustion chamber alone and their difference is shown in Fig. A.12. The maximum discrepancy between the two curves is of 50K, which is the experimental error bars. For the moment, no supplementary conclusions can be drawn even if the azimuthal differences are evident in Fig. A.9. Indeed, the 1D RTF curve can not represent the azimuthal heterogeneity introduced by the NGV.

A.2.6 Concluding remark

The major conclusion extracted from this study is that the interaction between codes used for the separate combustor and turbine stage calculations has to be implemented, since as it has been seen that the NGV presence has a sizable influence on the flow upstream of its leading edge. Both solvers have to exchange information in order to improve the overall prediction, for instance, the LES code should be aware of the upstream potential effect of the NGV.

Appendix B

A multi-physics simulation of an industrial application

(a) 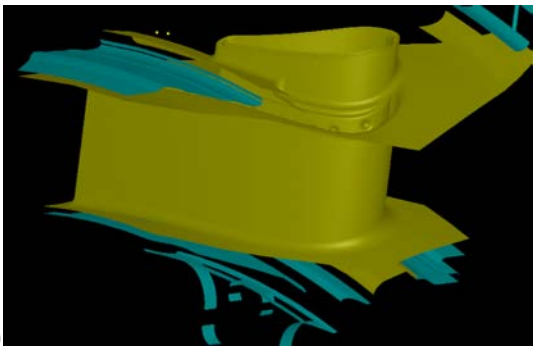 (b) 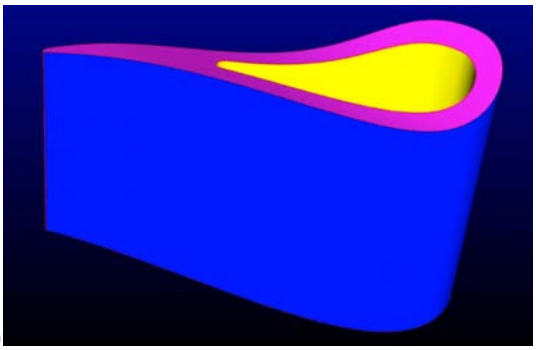

Figure B.1: (a) Real cooling system and (b) cooling system modeled inside the NGV.

A set of muti-physics coupled simulations (heat transfer and radiation) was pursued during the 2010 Summer Program in the Center for Turbulent Research on the configuration presented in Appendix A. The geometry studied is slightly different from the computation detailed above. The cooling system inside the stator blade has been modeled as shown in Fig. B.1 (b). The internal mesh is inspired on the true cooling system present in the real blade, Fig. B.1 (a). The mesh size of the NGV blade has been chosen non-coincident and of the same order as the cells of the fluid nearby as seen in the Fig. B.2. The physical properties chosen for the inner blade have been extracted from TURBOMECA experience. Amaya *et al.* [7] expose the conclusions from this study in the proceedings of the Summer Program 2010.

The main conclusion drawn from this work is that the temperature field in the fluid and in the NGV are sensitive to both heat conduction and radiation, and that these two phenomena must be included to accurately predict the blade temperature, as shown in Fig. B.3.

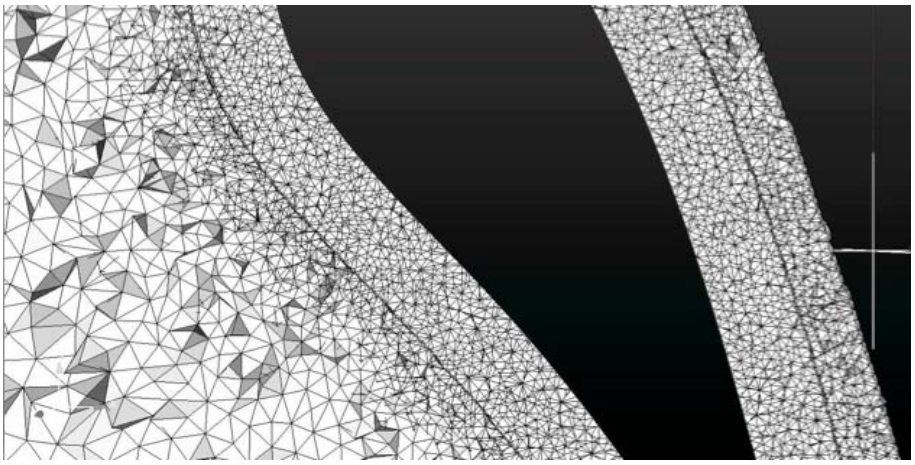

Figure B.2: Mesh of the NGV blade of the TURBOMECA engine.

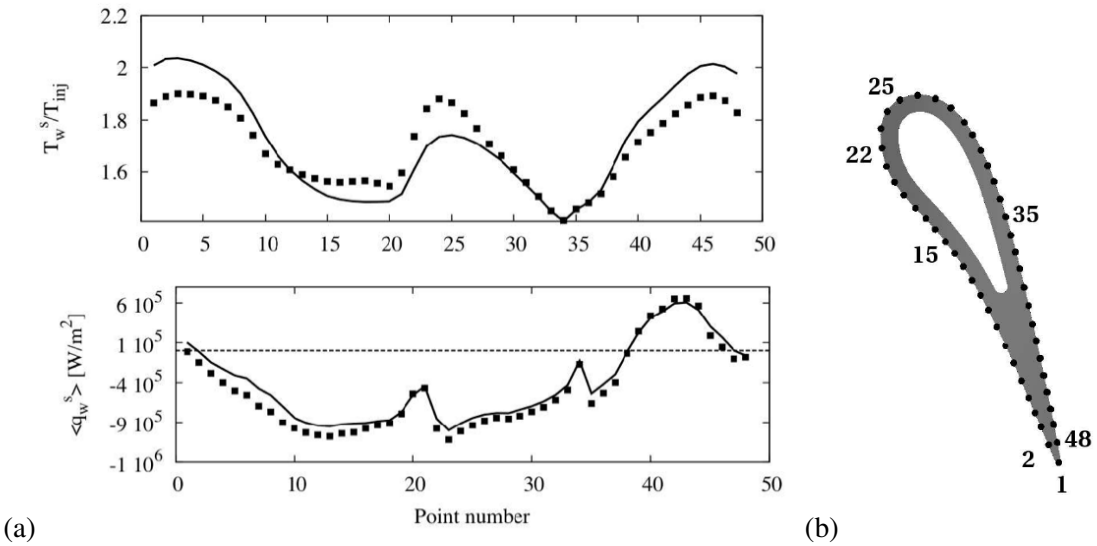

(a) (b)

Figure B.3: Profiles of dimensionless temperature on the surface $\frac{T_w^s}{T_{inj}}$ and convective heat q_w in the shroud for AVBP alone (solid lines) and AVBP coupled (symbols) with the radiation and the solid thermics, from [7].

Appendix C

Conjugate heat transfer: a mathematical analysis

In conjugate heat transfer, one parameter that greatly influences the thermodynamical fluid-structure interface behavior [36] is the thermal activity ratio defined as: $\beta = \sqrt{\frac{(\lambda\rho c_p)_f}{(\lambda\rho c_p)_s}}$ (f for fluid and s for solid). β drives the fluid/structure interaction in such a way that when $\beta \to \infty$ the wall temperature fluctuations tend to an isoflux boundary-condition behavior (maximum temperature fluctuations), whereas when $\beta \to 0$ the interface behaves like an isothermal wall with no temperature fluctuations. In our application test cases (turbine and combustion chamber), $\beta \to 0$. Therefore, the solid is usually considered in a steady state with respect to the fluid. Nevertheless, if LES results are used to couple to the thermal solver, the unsteady structures in the fluid domain can have an effect on the temporal variations of the fluid [84]. That's why one should not only analyze the fluid/solid interaction as an steady problem [37] but also in a unsteady context to incorporate, for instance, transient effects. The difference in the approach presented here with respect to the literature in unsteady problems for the conjugate heat transfer [45, 52, 62] is that we do not discretize the problem but treat the convergence towards a solution in the continuous form of the equations.

In this case, the PDE that describes the behavior of both domains is a parabolic equation. To solve the heat transfer coupling problem between fluid and solid, the methodology employed in Chapter 4 can be used to retrieve one of the most known results from literature [37, 45, 62]: to reach a stable thermal state, one should imposed a Dirichlet condition to the fluid and a Neumann or Robin condition to the solid.

The equation to be examined is the unsteady heat diffusion in each domain. Let's consider a 1D system of the form:

$$\tilde{F}T = \rho_i c_{pi} \frac{\partial T}{\partial t} - \lambda_i \frac{\partial^2 T}{\partial x^2} = 0 \qquad \text{for } i = 1,2 \text{ and} \qquad \forall x \in \Omega_i \tag{C.1}$$

since each domain has its own thermal conductivity λ_i ($W.m^{-1}.K^{-1}$), its own heat capacity c_{pi} ($J.kg^{-1}.K^{-1}$) and its own density ρ_i ($kg.m^{-3}$). 1 and 2 can designate the fluid or the solid subdomain.

After applying the Laplace transform with parameter $s \in \mathbb{C}$, $\Re(s) > 0$, one has:

$$FT = \rho_i c_{pi} T s - \lambda_i \frac{\partial^2 T}{\partial x^2} = 0 \qquad \text{for } i = 1,2 \text{ and} \qquad \forall x \in \Omega_i \tag{C.2}$$

The spatial domain is decomposed in two non-overlapping subdomains $\Omega_1 = (-l_1, 0_+)$ and $\Omega_2 = (0_-, l_2)$. There is no overlap, so $\delta = 0$ in this particular case. An iteration by subomain decomposition algorithm is used to solve system (C.2), given initial guesses T_1^0 and T_2^0, to find T_1^{k+1} and T_2^{k+1} such that:

$$\begin{cases} FT_1^{k+1} = 0 & \forall x \in \Omega_1, \\ T_1^{k+1} = T_{l1} & \text{at } x = -l_1 \\ \Phi_1(T_1^{k+1}) = \theta_1 \Phi_1(T_2^k) + (1-\theta_1)\Phi_1(T_1^k) & \text{at } x = 0_+, \end{cases} \tag{C.3}$$

$$\begin{cases} FT_2^{k+1} = 0 & \forall x \in \Omega_2, \\ T_2^{k+1} = T_{l2} & \text{at } x = l_2 \\ \Phi_2(T_2^{k+1}) = \theta_2 \Phi_2(T_1^{k'}) + (1-\theta_2)\Phi_2(T_2^k) & \text{at } x = 0_-, \end{cases} \tag{C.4}$$

where Φ_1 and Φ_2 are the linear functionals representing the transmission conditions at 0_+ and 0_- respectively. θ_1 and θ_2 are positive constants, called the relaxation parameters and k' is the iteration index which can be

$$k' = \begin{cases} k+1 & \text{for the sequential version,} \\ k & \text{for the parallel version.} \end{cases}$$

The geometry of the problem is plotted in Fig. C.1. It is assumed that the solution of problem (C.2) satisfies the transmission conditions, then the error $e_i^{k+1} = T_i^{k+1} - T$ verifies the following homogeneous system of equations for $k \geq 0$:

$$\begin{cases} Le_1^{k+1} = 0 & \forall x \in \Omega_1, \\ e_1^{k+1} = 0 & \text{at } x = -l_1 \\ \Phi_1(e_1^{k+1}) = \theta_1 \Phi_1(e_2^k) + (1-\theta_1)\Phi_1(e_1^k) & \text{at } x = 0_+, \end{cases} \tag{C.5}$$

$$\begin{cases} Le_2^{k+1} = 0 & \forall x \in \Omega_2, \\ e_2^{k+1} = 0 & \text{at } x = l_2 \\ \Phi_2(e_2^{k+1}) = \theta_2 \Phi_2(e_1^{k'}) + (1-\theta_2)\Phi_2(e_2^k) & \text{at } x = 0_-, \end{cases} \tag{C.6}$$

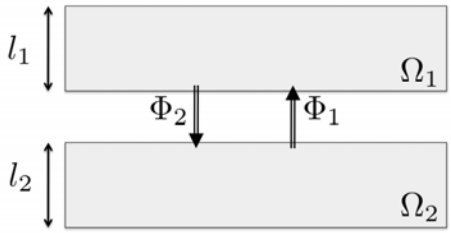

Figure C.1: Scheme of the simplified geometry considered to study the unsteady conjugate heat transfer between solid and fluid.

Three transmission conditions are of particular interest here:

$$\text{Dirichlet:} \quad \Phi_D(u) = T,$$

$$\text{Neumann:} \quad \Phi_N(u) = \lambda \frac{\partial T}{\partial x} n_x,$$

$$\text{Robin:} \quad \Phi_R(u) = \lambda \frac{\partial T}{\partial x} n_x + h\, T\, n_x,$$

n_x is the exterior normal which takes the values $n_x = 1$ and $n_x = -1$, for $x = 0_+$ and $x = 0_-$, respectively. h is the heat transfer convective coefficient of the fluid ($W.m^{-2}.K^{-1}$).

Solving Eqs. $(C.5)_1$ and $(C.6)_1$, the solution is of the form:

$$e_i^{k+1} = A_i^{k+1} exp(\tau_i x) + B_i^{k+1} exp(-\tau_i x)$$

where τ_i is given by:

$$\tau_i = \sqrt{\frac{\rho_i c_{pi}}{\lambda_i}} \sqrt{s} = \sqrt{\frac{s}{D_i}} \qquad \text{for } i = 1,2$$

where $D_i = \dfrac{\lambda_i}{\rho_i c_{pi}}$ is the thermal diffusivity of each one of the subdomains and A_i^{k+1} and B_i^{k+1} are constants depending on the boundary conditions given by $(C.5)_2$ and $(C.6)_2$. Since no discretization is introduced in this Appendix, we do not talk here about the fluid and solid time steps. A remark from researchers used to conjugate heat transfer problems can be that the s parameter is the same for both solid and fluid. Let's briefly recall the usual approach in literature [45]: instead of considering the same physical time, each subdomain is advanced of its characteristic time between a coupling iteration. Indeed, the characteristic time scales of fluid and structure are not the same in our application test cases: a few seconds are necessary for diffusion through a solid whereas the flow-through time along the solid can be of less than 1ms. When the steady state of the solid is aimed at, to gain

computational time, the coupling synchronization can be the same for the solid and the fluid. There is not consistency in the physical time. In our case, in a fully unsteady reasoning, the physical time is the same for both subdomains and thus, s is a global parameter.

Taking into account the previous boundary conditions, the errors can be expressed as:

$$e_1^{k+1} = C_1^{k+1} sinh(\tau_1(l_1 + x)),$$
$$e_2^{k+1} = C_2^{k+1} sinh(\tau_2(l_2 - x)).$$

C.1 Sequential system

Let's study the convergence analysis on the continuous problem for the unrelaxed sequential version. $k' = k+1$ and $\theta_1 = \theta_2 = 1$. No overlap is present in the solid/fluid decomposition domain, so that $\delta = 0$.

C.1.1 Dirichlet/Dirichlet

Dirichlet conditions are imposed at both $x = 0_+$ and $x = 0_-$. The transmission conditions give:

$$\Phi_1(e_1^{k+1}(0_+, s)) = C_1^{k+1} sinh(\tau_1 l_1))$$
$$\Phi_1(e_2^{k+1}(0_+, s)) = C_2^{k+1} sinh(\tau_2 l_2))$$

$$\Phi_2(e_1^{k+1}(0_-, s)) = C_1^{k+1} sinh(\tau_1 l_1))$$
$$\Phi_2(e_2^{k+1}(0_-, s)) = C_2^{k+1} sinh(\tau_2 l_2))$$

Substituting these equations into the equations for the error transmission Eq. (C.5)$_3$ and Eq. (C.6)$_3$, one can conclude that $|\rho| = 1$. The error at $k+1$ retains the initial error. The main conclusion is that imposing symmetric Dirichlet conditions is not enough to guarantee the strict convergence of the DDM problem.

C.1.2 Neumann/Dirichlet

A Neumann condition is imposed now at $x = 0_+$, $n_x = 1$ at this location. A Dirichlet condition is given at $x = 0_-$. The transmission conditions give:

$$\Phi_1(e_1^{k+1}(0_+, s)) = C_1^{k+1} \lambda_1 \tau_1 \; cosh(\tau_1 l_1)$$
$$\Phi_1(e_2^{k+1}(0_+, s)) = -C_2^{k+1} \lambda_2 \tau_2 \; cosh(\tau_2 l_2)$$

$$\Phi_2(e_1^{k+1}(0_-, s)) = C_1^{k+1} sinh(\tau_1 l_1)$$
$$\Phi_2(e_2^{k+1}(0_-, s)) = C_2^{k+1} sinh(\tau_2 l_2)$$

and

$$\rho = |\rho_1 \rho_2| = \left| \frac{\lambda_2 \tau_2}{\lambda_1 \tau_1} \frac{cosh(\tau_2 l_2)}{cosh(\tau_1 l_1)} \frac{sinh(\tau_1 l_1)}{sinh(\tau_2 l_2)} \right|$$

This last expression can be re-arranged as follows:

$$\rho_{N/D} = \left| \frac{\lambda_2 \tau_2}{\lambda_1 \tau_1} \frac{cosh(\tau_2 l_2)}{cosh(\tau_1 l_1)} \frac{sinh(\tau_1 l_1)}{sinh(\tau_2 l_2)} \right| = \left| \frac{\lambda_2 \tau_2}{\lambda_1 \tau_1} \frac{tanh(\tau_1 l_1)}{tanh(\tau_2 l_2)} \right|$$

The first fraction equals:

$$\frac{\lambda_2 \tau_2}{\lambda_1 \tau_1} = \frac{\lambda_2}{\lambda_1} \sqrt{\frac{D_1}{D_2}}$$

Since $tanh(x)$ is a monotonic increasing function, $|\rho_{N/D}| < 1$ as long as $\left| \frac{\lambda_2 \tau_2}{\lambda_1 \tau_1} \right| < 1$ and $\left| \frac{\tau_1 l_1}{\tau_2 l_2} \right| < 1$.

The solid thickness l_s is normally very small. Let's remind that we have applied the heat unsteady diffusion equation to the fluid (C.2), but this only stands in a little region near the solid where the heat transfer is prominent. For a $l > l_f$, the convective effects become dominant and the Eq. (C.2) is no longer valid. l_f is the thermic boundary layer thickness. It can be estimated as $\sim Pr^{1/3}.\delta_{conv}$, where δ_{conv} is the convective boundary layer and Pr is the Prandtl number. In our field of research, $Pr \sim 1$. As a consequence, $l_f \sim \delta_{conv}$ [34]. For the Reynolds number of the applications targeted, we have $\delta_{conv} \sim \frac{problem\ characteristic\ length}{\sqrt{Re}}$. As a consequence, we can express the hypothesis that l_f and l_s are of the same order of magnitude, i.e, if $l_1 \approx l_2$.

Thus, the last condition, $\left| \frac{\tau_1 l_1}{\tau_2 l_2} \right| < 1$, can also be expressed as $|D_2| < |D_1|$ if this approximation on the thickness of the subdomains is done. As an example, one can take the values in Table C.1 for the thermal characteristics of the subdomains. β, the thermal activity ratio defined in the introduction, can easily be calculated.

	Solid (650 K)	Hot gases (2300 K)
Thermal diffusivity D_i $(m^2.s^{-1})$	$3.36\ 10^{-6}$	$3.72\ 10^{-4}$
Thermal conductivity λ_i $(W.m^{-1}.K^{-1})$	12.97	0.140
$\frac{\lambda_i}{\sqrt{D_i}}$	$\sim 1\ 10^4$	~ 10

Table C.1: Thermal characteristics, from Duchaine *et al.* [46].

- On the one hand, if the fluid is in subdomain 1 and the solid is in 2, with the above values, one has:

$$\frac{\lambda_2}{\lambda_1} \approx 90,$$

$$\sqrt{\frac{D_1}{D_2}} \approx 10.$$

Thus, $\left|\frac{\lambda_2\tau_2}{\lambda_1\tau_1}\right| \gg 1$ and $|D_2| < |D_1|$, no convergence can be achieved if subdomain 1 is the fluid and subdomain 2 is the solid since $|\rho|$ would never be smaller than 1. *No convergence is possible if a Neumann condition is imposed to the fluid and a Dirichlet condition is imposed to the solid.*

- On the other hand, if the fluid is in subdomain 2 and the solid in 1:

$$\frac{\lambda_2}{\lambda_1} \approx 1\ 10^{-2},$$

$$\sqrt{\frac{D_1}{D_2}} \approx 1\ 10^{-1}.$$

Then $\left|\frac{\lambda_2\tau_2}{\lambda_1\tau_1}\right| \ll 1$ and $|D_2| > |D_1|$, so unconditional convergence is achieved for this type of coupling. *Imposing a Dirichlet condition to the fluid and a Neumann condition to the solid assures convergence since the rate of convergence is always smaller than 1.* The converging method is plotted in Fig. C.2.

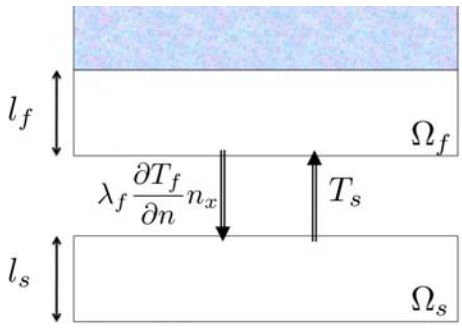

Figure C.2: Scheme of the converging method.

C.1.3 Robin/Dirichlet

A Robin condition is imposed now at $x = 0_+$. A Dirichlet condition is given at $x = 0_-$. The transmission conditions give:

$$\Phi_1(e_1^{k+1}(0_+,s)) = C_1^{k+1}[\lambda_1\tau_1\ cosh(\tau_1 l_1) + h\ sinh(\tau_1 l_1)]$$

$$\Phi_1(e_2^{k+1}(0_+,s)) = C_2^{k+1}[-\lambda_2\tau_2\ cosh(\tau_2 l_2) + h\ sinh(\tau_2 l_2)]$$

$$\Phi_2(e_1^{k+1}(0_-,s)) = C_1^{k+1} sinh(\tau_1 l_1)$$

$$\Phi_2(e_2^{k+1}(0_-,s)) = C_2^{k+1} sinh(\tau_2 l_2)$$

and

$$\rho = |\rho_1\rho_2| = \left| \frac{-\lambda_2\tau_2\ cosh(\tau_2 l_2) + h\ sinh(\tau_2 l_2)}{\lambda_1\tau_1\ cosh(\tau_1 l_1) + h\ sinh(\tau_1 l_1)} \frac{sinh(\tau_1 l_1)}{sinh(\tau_2 l_2)} \right|$$

Re-organising the equation, one has:

$$\rho_{R/D} = \left| \frac{-\lambda_2\tau_2 + h\ tanh(\tau_2 l_2)}{\lambda_1\tau_1 + h\ tanh(\tau_1 l_1)} \frac{tanh(\tau_1 l_1)}{tanh(\tau_2 l_2)} \right|$$

$\forall x$, $|tanh(x)| < 1$ and is a strictly increasing function, so

- if $|D_1| < |D_2|$, $|\tau_1| > |\tau_2|$ and $|tanh(\tau_1 l_1)| > |tanh(\tau_2 l_2)|$ with $l_1 \sim l_2$. The other term of the equation is easy to analyze, at most $tanh(\tau_2 l_2)$ or $tanh(\tau_1 l_1)$ are equal to 1.
  Typical values of h in turbomachinery have been plotted in Section 2.3.1. $h \sim 500\ W.m^{-2}.K^{-1}$. Remembering that $\tau_i = \sqrt{\frac{s}{D_i}}$, we can assure $\left| \frac{-\lambda_2\tau_2 + h\ tanh(\tau_2 l_2)}{\lambda_1\tau_1 + h\ tanh(\tau_1 l_1)} \right| < 1$, $\forall s > 0$. Indeed, substituting the expressions with the reference values given in Table C.1, this fraction can be easily plotted as a function of s to conclude that when subdomain 2 corresponds to the fluid and 1 to the solid, $|\rho| < 1$, $\forall s > 0$. For more information about the role played by h in conjugate heat transfer, one can refer to Chemin [37].

- On the contrary, the method where 1 is the fluid and 2 the solid is unconditionally divergent.

In fact, *the Robin/Dirichlet has the same convergence behavior that the Neumann/Dirichlet method*. The same conclusion was drawn in Chemin's thesis in what he called the Fourier/Dirichlet coupling (page 47 in [37]). Indeed, the Robin condition should be applied to the subdomain with the biggest thermal conductivity.

C.1.4 Relaxed sequential system

The methodology to deduce the rate of convergence of the relaxed sequential version has already been presented in Section 4.1.1.2. No addition is made in this Appendix. The reader is free to apply himself the conclusions of the aforementioned section and the limitations to the relaxation parameter induced. Some interesting results have already been deduced about relaxation on the conjugate heat transfer problem by Chemin [37], Duchaine *et al.* [45].

C.2 Concluding remarks

A brief literature survey of the conjugate heat transfer problems shows that main contributions center on stability, but lack on convergence analysis. This Appendix is just a draft of a methodology that should enable to define how many coupling iterations k are needed to solve an unsteady conjugate heat transfer coupling. Some of the aspects which have not been treated in this mathematical analysis and could be interesting are:

- ◇ other transmission conditions for the coupling can be studied, for instance, Robin/Neumann methods or Robin/Robin,
- ◇ the conjugate heat transfer could also be studied with a different modelization for the fluid (advection-diffusion, Navier-Stokes system, ...),
- ◇ a deeper investigation of the influence of discontinuous coefficients in the DDM convergence of parabolic equations [98],
- ◇ a 1D stability analysis, like the one performed in Giles [62], but for a fully symmetric (meaning both fluid and solid) unsteady problem,
- ◇ the generalization to 2D and 3D problems of convergence and stability criteria.

Appendix D

Numerical tools

D.1 *elsA* and AVBP

In the following sections, the equations governing the motion of the flow are described. In Section D.1.1, the RANS and LES governing equations (for averaged and filtered quantities) are derived. The CFD codes, *elsA* and AVBP, used to solve the equations are presented in Section D.1.2, with specific emphasis on the differences, that is the time-advancing scheme or spatial discretization. They are indeed important for understanding the modifications introduced concerning the coupling of codes.

D.1.1 Navier-Stokes equations

D.1.1.1 Conservation equations

Irrespectively of the turbulent modeling formalism adopted for the computation (*i.e.*, RANS or LES), the set of conservation equations describing the evolution of a compressible flow with chemical reactions of thermodynamically active scalars reads,

$$\frac{\partial \rho u_i}{\partial t} + \frac{\partial}{\partial x_j}(\rho u_i u_j) = -\frac{\partial}{\partial x_j}[P\delta_{ij} - \tau_{ij}], \tag{D.1}$$

$$\frac{\partial \rho E}{\partial t} + \frac{\partial}{\partial x_j}(\rho E u_j) = -\frac{\partial}{\partial x_j}[u_i(P\delta_{ij} - \tau_{ij}) + q_j] + S_E, \tag{D.2}$$

$$\frac{\partial \rho_k}{\partial t} + \frac{\partial}{\partial x_j}(\rho_k u_j) = -\frac{\partial}{\partial x_j}[J_{j,k}] + S_k. \tag{D.3}$$

Einstein's rule of summation is adopted for the description of the governing equations. Note however that the index k is reserved to refer to the k^{th} species and will not follow the summation rule unless specifically mentioned.

In Eqs. (D.1) to (D.3), which respectively correspond to the conservation laws for momentum, total energy and species, the following symbols (ρ, u_i, E, ρ_k) denote the density, the velocity vector, the total energy per unit mass and the density of the chemical species k. $\rho_k = \rho Y_k$ for k = 1 to N (where N is the total number of species). Y_k is the k^{th} species mass fraction, P denotes the pressure, τ_{ij} the stress tensor, q_i the heat flux vector and $J_{j,k}$ the vector of the diffusive flux of species k. The source term in the total energy equation (S_E in Eq. (D.2)) is composed of a chemical source term, $\dot{\omega}_T$. The source term in the species transport equations (S_k in Eq. (D.3)) contains contributions from chemical production or consumption of species, the net effect being noted $\dot{\omega}_k$.

It is common to distinguish between inviscid and a viscous terms. They are subsequently noted for the three conservation equations:

Inviscid terms:

$$\begin{pmatrix} \rho\, u_i\, u_j + P\, \delta_{ij} \\ (\rho E + P\, \delta_{ij})\, u_j \\ \rho_k\, u_j \end{pmatrix} \tag{D.4}$$

Viscous terms:

The components of the viscous flux tensor take the form:

$$\begin{pmatrix} -\tau_{ij} \\ -(u_i\, \tau_{ij}) + q_j \\ J_{j,k} \end{pmatrix} \tag{D.5}$$

The stress tensor τ_{ij} is detailed below in Eq. (D.6).

D.1.1.2 Transport coefficients

The stress tensor τ_{ij} is given by:

$$\tau_{ij} = 2\mu \left(S_{ij} - \frac{1}{3} \delta_{ij} S_{ll} \right) \tag{D.6}$$

where μ is the shear viscosity and where S_{ij} is the rate of strain tensor

$$S_{ij} = \frac{1}{2} \left(\frac{\partial u_j}{\partial x_i} + \frac{\partial u_i}{\partial x_j} \right) \tag{D.7}$$

In CFD codes, the molecular viscosity μ is often assumed to be independent of the gas composition and close to that of air so that the classical Sutherland law [189] can be used:

$$\mu = c_1 \frac{T^{3/2}}{T + c_2} \frac{T_{ref} + c_2}{T_{ref}^{3/2}} \tag{D.8}$$

where c_1 and c_2 must be determined so as to fit the real viscosity of the mixture. For air at T_{ref} = 273 K, c_1 = 1.71e-5 kg/m.s and c_2 = 110.4 K. The heat conduction coefficient of the gas mixture can then be computed by introducing the molecular Prandtl number of the mixture as:

$$\lambda = \frac{\mu C_p}{P_r} \tag{D.9}$$

with P_r supposed constant in time and space.

Furthermore, in multi-species flows the total mass conservation implies that:

$$\sum_{k=1}^{N} Y_k V_i^k = 0 \tag{D.10}$$

where V_i^k are the components in directions (i=1,2,3) of the diffusion velocity of species k. They are often expressed as a function of the species gradients using the Hirschfelder Curtis approximation:

$$X_k V_i^k = -D_k \frac{\partial X_k}{\partial x_i}, \tag{D.11}$$

where X_k is the molar fraction of species k : $X_k = Y_k W / W_k$ and D_k are the species diffusion coefficients. In terms of mass fraction, the approximation D.11 may be expressed as:

$$Y_k V_i^k = -D_k \frac{W_k}{W} \frac{\partial X_k}{\partial x_i}, \tag{D.12}$$

Summing Eq. (D.12) over all k shows that the approximation in Eq. (D.12) does not necessarily comply with Eq. (D.10) that expresses mass conservation. In order to achieve this, a correction diffusion velocity $\vec{V}^c$ is added to the convection velocity to ensure global mass conservation (see [142]) as:

$$V_i^c = \sum_{k=1}^{N} D_k \frac{W_k}{W} \frac{\partial X_k}{\partial x_i}, \tag{D.13}$$

and computing the diffusive species flux for each species k as:

$$J_{i,k} = -\rho \left(D_k \frac{W_k}{W} \frac{\partial X_k}{\partial x_i} - Y_k V_i^c \right), \tag{D.14}$$

Here, D_k are the diffusion coefficients for each species k in the mixture. The computation of the species diffusion coefficients D_k is a specific issue. These coefficients should be expressed as a function of the binary coefficients D_{ij} obtained from kinetic theory [77]. The D_{ij} are complex functions of collision integrals and thermodynamic variables. If a simplified chemical scheme is used, modeling diffusivity in a precise way is not needed. Therefore, a simplified approximation is used in AVBP for D_k. The Schmidt numbers $S_{c,k}$ of the species are supposed to be constant so that the binary diffusion coefficient for each species is computed as:

$$D_k = \frac{\mu}{\rho S_{c,k}} \tag{D.15}$$

Moreover, an additional heat flux term appears in the diffusive heat flux. This term is due to heat transport by species diffusion. The total heat flux vector then takes the form:

$$q_i = \underbrace{-\lambda \frac{\partial T}{\partial x_i}}_{\text{Heat conduction}} \underbrace{-\rho \sum_{k=1}^{N} \left(D_k \frac{W_k}{W} \frac{\partial X_k}{\partial x_i} - Y_k V_i^c \right) h_{s,k}}_{\text{Heat flux through species diffusion}} = -\lambda \frac{\partial T}{\partial x_i} + \sum_{k=1}^{N} J_{i,k} h_{s,k} \tag{D.16}$$

where λ is the heat conduction coefficient of the mixture and $h_{s,k}$ the sensible enthalpy of the species k.

D.1.1.3 Equation of state

To close the problem, a state equation relating $\rho.E$ and P is needed. For a bivariant fluid, the ideal gas law is usually:

$$P = \rho r T \tag{D.17}$$

where r is the gas constant of the mixture dependent on time and space: $r = \frac{\mathcal{R}}{W}$ where W is the mean molecular weight of the mixture obtained from:

$$\frac{1}{W} = \sum_{k=1}^{N} \frac{Y_k}{W_k} \tag{D.18}$$

The gas constant r and the heat capacities of the gas mixture depend on the local gas composition as:

$$r = \frac{\mathcal{R}}{W} = \sum_{k=1}^{N} \frac{Y_k}{W_k} \mathcal{R} = \sum_{k=1}^{N} Y_k r_k \tag{D.19}$$

$$C_p = \sum_{k=1}^{N} Y_k C_{p,k} \tag{D.20}$$

$$C_v = \sum_{k=1}^{N} Y_k C_{v,k} \tag{D.21}$$

where $\mathcal{R}$ = 8.3143 J/mol.K is the universal gas constant. The adiabatic exponent for the mixture is given by $\gamma = C_p/C_v$. Thus, the gas constant, the heat capacities and the adiabatic exponent are no longer constant if a reactive approach is taken. They depend on the local gas composition as expressed by the local mass fractions $Y_k(\mathbf{x},t)$:

$$r = r(\mathbf{x},t), \qquad C_p = C_p(\mathbf{x},t), \qquad C_v = C_v(\mathbf{x},t), \qquad \text{and} \qquad \gamma = \gamma(\mathbf{x},t) \tag{D.22}$$

D.1.1.4 Mono vs multi-species: determination of the temperature

AVBP and *elsA* both solve the compressible Navier-Stokes system previously detailed. On the one hand, AVBP has historically been developed to treat problems related to combustion chambers. Following this logic, the solver has a multi-species approach. The gas constant $\mathcal{R}$, γ and the heat capacities are not constant with temperature, the equations remain as established in Section D.1.1.1. The standard reference state used is P_0 = 1 bar and T_0 = 0 K. The sensible mass enthalpies ($h_{s,k}$) and entropies (s_k) for each species are tabulated for 51 values of the temperature (T_i with i = 1...51) ranging from 0 K to 5000 K with a step of 100 K. Therefore these variables can be evaluated by:

$$h_{s,k}(T_i) = \int_{T_0=0K}^{T_i} C_{p,k} dT = \frac{h^m_{s,k}(T_i) - h^m_{s,k}(T_0)}{W_k}, \qquad \text{and} \tag{D.23}$$

$$s_k(T_i) = \frac{s^m_k(T_i) - s^m_k(T_0)}{W_k}, \qquad \text{with i} = 1,51 \tag{D.24}$$

The superscript m corresponds to molar values. The tabulated values for $h_{s,k}(T_i)$ and $s_k(T_i)$ are obtained from the JANAF tables [176]. With this assumption, the sensible energy for each species can be reconstructed using the following expression;

$$e_{s,k}(T_i) = \int_{T_0=0K}^{T_i} C_{v,k} dT = h_{s,k}(T_i) - r_k T_i \qquad i = 1,51 \tag{D.25}$$

Note that the mass heat capacities at constant pressure $C_{p,k}$ and volume $C_{v,k}$ are supposed constant between T_i and T_{i+1} = $T_i + 100$ K. They are defined as the slope of the sensible enthalpy ($C_{p,k} = \frac{\partial h_{s,k}}{\partial T}$)

and sensible energy ($C_{v,k} = \frac{\partial e_{s,k}}{\partial T}$). The sensible energy varies continuously with temperature and is obtained by using a linear interpolation:

$$e_{s,k}(T) = e_{s,k}(T_i) + (T - T_i)\frac{e_{s,k}(T_{i+1}) - e_{s,k}(T_i)}{T_{i+1} - T_i} \tag{D.26}$$

The sensible energy and enthalpy of the mixture may then be expressed as:

$$\rho e_s = \sum_{k=1}^{N} \rho_k e_{s,k} = \rho \sum_{k=1}^{N} Y_k e_{s,k} \tag{D.27}$$

$$\rho h_s = \sum_{k=1}^{N} \rho_k h_{s,k} = \rho \sum_{k=1}^{N} Y_k h_{s,k} \tag{D.28}$$

The temperature is deduced from the the sensible energy, using Eqs. (D.26) and (D.27).

On the other hand, *elsA* has been developed to perform aerodynamical predictions around wings or blades of engines. From this background, the solver was conceived without adding multi-species equations. Hence, a contraction of the index k can be performed to deduce the system of equations solved by *elsA* and the internal energy can be expressed as:

$$e_s(T) = c_v T \tag{D.29}$$

where c_v does not change with the temperature of the gas. γ and c_p have no dependency on T.

The main characteristics of the two solvers used in this PhD are detailed in Table. D.1.

	elsA	AVBP
Historical Domain	Aerodynamics	Combustion
Equations	NS compressible	NS compressible
μ	Sutherland	Sutherland
Mixture	mono	multi
r	constant	$r(\mathbf{x},t,T)$
γ	constant	$\gamma(\mathbf{x},t,T)$
C_p	constant	$C_p(\mathbf{x},t,T)$
C_v	constant	$C_v(\mathbf{x},t,T)$
Temperature determination	Eq. (D.29)	Eq. (D.26)

Table D.1: *elsA* vs AVBP solver for Navier-Stokes equations.

D.1.1.5 Turbulence modeling

In the introduction of this manuscript, a comparison is provided of the different methods to deal with turbulence; it clearly identifies DNS of the above Navier-Stokes equations as being extremely costly due to the many different scales involved. If complexity of the system to be simulated is to be reduced, an operator has to be applied to the exact solution of the Navier-Stokes equations. Labourasse & Sagaut [100] defined the RANS averaging operator and the LES spatial filtering operator in the general framework of multilevel methods relying on different scale separation operators.

Succinctly, for RANS formalism, the mathematical operation introduced relies on the statistical ensemble of realizations of the same flow problem from which only the statistical ensemble means are of interest. As explained in Part I, in LES, the notion of separation of turbulent scales is introduced and distinguishes a separation between the resolved (large) turbulent scales and the modeled (small) scales.

For compressible LES and RANS, the spatial Favre filtering or ensemble means are used and the operation reduces for spatially, temporally invariant and localized filter functions to:

$$\overline{\rho}\,\widetilde{f} = \begin{cases} \text{RANS:} & \dfrac{1}{N}\displaystyle\sum_{1}^{N} \rho^n(\mathbf{x},t)\, f^n(\mathbf{x},t), \\ \text{LES:} & \displaystyle\int \rho(\mathbf{x}',t)\, f(\mathbf{x}',t)\, G(\mathbf{x}'-\mathbf{x})\, d\mathbf{x}', \end{cases} \tag{D.30}$$

where G denotes the filter function while n is the n^{th} realization of a statistical ensemble composed of N of such fields. The conservation equations for filtered quantities are obtained by filtering the instantaneous Eqs. (D.1), (D.2) and (D.3). In these new equations, there are now three types of terms to be distinguished: the inviscid terms, the viscous terms and the filtered terms. The inviscid terms are equivalent to the unfiltered equations except that they are now expressed in filtered quantities. The same conclusion is valid for the viscous terms. However, filtering the balance equations leads to unclosed quantities, which need to be modeled. These terms are:

$$\begin{pmatrix} -\overline{\tau_{ij}}^{t} \\ \overline{q_j}^{t} \\ \overline{J_{j,k}}^{t} \end{pmatrix} \tag{D.31}$$

The unresolved SGS stress tensor $\overline{\tau_{ij}}^{t}$ from LES and the equivalent Reynolds stress tensor appearing in RANS are usually modeled using the Boussinesq assumption [171]:

$$\overline{\tau_{ij}}^{t} - \frac{1}{3}\,\overline{\tau_{kk}}^{t}\,\delta_{ij} = -2\,\overline{\rho}\,\nu_t\,\widetilde{S}_{ij}\,, \tag{D.32}$$

$$\text{with } \widetilde{S}_{ij} = \frac{1}{2}\left(\frac{\partial \widetilde{u}_i}{\partial x_j} + \frac{\partial \widetilde{u}_j}{\partial x_i}\right) - \frac{1}{3}\frac{\partial \widetilde{u}_k}{\partial x_k}\,\delta_{ij}. \tag{D.33}$$

In Eq. (D.32), $\widetilde{S}_{ij}$ is the resolved or ensemble mean strain rate tensor and ν_t is the SGS or RANS turbulent viscosity. Normally for RANS a two-equations type of closure is adopted. There is a great number of different closures more or less suited for turbomachinery applications. For more information on the different kinds of RANS additional transport variables, one can consult [32, 115]. As highlighted above, filtering the transport equations yields a closure problem evidenced by the SGS turbulent fluxes. For the system to be solved numerically, closures need to be supplied in LES. Models for the subgrid-scale turbulent viscosity ν_t are an essential part of a LES: Smagorinsky [171] or WALE are some of the most used.

For AVBP , the subgrid scale diffusive species flux vector is:

$$\overline{J_{i,k}}^t = \overline{\rho}\left(\widetilde{u_i Y_k} - \widetilde{u}_i \widetilde{Y}_k\right), \tag{D.34}$$

$\overline{J_{i,k}}^t$ is modeled as:

$$\overline{J_{i,k}}^t = -\overline{\rho}\left(D_k{}^t \frac{W_k}{W}\frac{\partial \widetilde{X}_k}{\partial x_i} - \widetilde{Y}_k \widetilde{V}_i^{c,t}\right), \tag{D.35}$$

with

$$D_k^t = \frac{\nu_t}{S_{c,k}^t} \tag{D.36}$$

The turbulent Schmidt number $S_{c,k}^t$ is the same for all species. Note also that having one turbulent Schmidt number for all the species does not imply, $\widetilde{V}^{c,t} = 0$ because of the W_k/W term in Eq. (D.35). The correction diffusion velocities are then obtained from:

$$\widetilde{V}_i^c + \widetilde{V}_i^{c,t} = \sum_{k=1}^{N}\left(\frac{\overline{\mu}}{\overline{\rho} S_{c,k}} + \frac{\mu_t}{\overline{\rho} S_{c,k}^t}\right)\frac{W_k}{W}\frac{\partial \widetilde{X}_k}{\partial x_i}, \tag{D.37}$$

and where Eqs. (D.15) and (D.36) are used. The filtered diffusive species flux vector for non-reactive flows is:

$$\begin{aligned}\overline{J_{i,k}} &= -\overline{\rho\left(D_k \frac{W_k}{W}\frac{\partial X_k}{\partial x_i} - Y_k V_i^c\right)} \\ &\approx -\overline{\rho}\left(\overline{D}_k \frac{W_k}{W}\frac{\partial \widetilde{X}_k}{\partial x_i} - \widetilde{Y}_k \widetilde{V}_i^c\right),\end{aligned} \tag{D.38}$$

where higher order correlations between the different variables of the expression are assumed negligible.

At last, the subgrid scale heat flux vector is:

$$\overline{q_i}^t = \overline{\rho}(\widetilde{u_i E} - \widetilde{u}_i \widetilde{E}), \tag{D.39}$$

where E is the total energy.

$$\begin{aligned} \overline{q_i}^t &= -\overline{\lambda \frac{\partial T}{\partial x_i}} + \sum_{k=1}^{N} \overline{J_{i,k} h_{s,k}} \\ &\approx -\overline{\lambda} \frac{\partial \widetilde{T}}{\partial x_i} + \sum_{k=1}^{N} \overline{J_{i,k}} \widetilde{h}_{s,k} \end{aligned} \tag{D.40}$$

These forms assume that the spatial variations of molecular diffusion fluxes are negligible and can be modelled through simple gradient assumptions. In Eq. (D.40), $\widetilde{T}$ is the filtered temperature which satisfies the modified filtered state equation $\overline{p} = \overline{\rho}\, r\, \widetilde{T}$ [126]. The unclosed energy flux $\overline{q_i}^t$ is modeled using a turbulent heat conductivity obtained from ν_t by $\lambda_t = \overline{\rho}\, \nu_t\, \overline{c_p}/Pr_t$ where Pr_t is considered to be a constant turbulent Prandtl number even though it has been reported not to be so by Bhaskharan [18]. In the LS89 guide vane, values of the turbulent Prandtl number are reported to oscillate between 0.5 to 2. By our experience, this parameter has a minor influence in LES. To confirm this point, two simulations with $Pr_t = 0.6$ and $Pr_t = 0.9$ have been performed in the LS89 case. Results show that the predictions for the wall heat fluxes are identical.

To conclude, AVBP is an exclusively LES solver. Smagorinsky and WALE SGS models, among others, are implemented in AVBP. For more information on the SGS models and their application fields, one can search [30, 133]. In *elsA*, a large variety of turbulence models are available, ranging from eddy viscosity to Reynolds stress models, and including options for Detached Eddy Simulation (DES) and LES [63, 65].

	elsA	AVBP
RANS	✓	✗
DES	✓	✗
LES	✓	✓

Table D.2: *elsA* vs AVBP turbulent closures available.

D.1.2 Numerical methods

In this section, the numerical methods used by *elsA* and AVBP solvers are described. Aspects relevant for the developments carried out in the present work are discussed in details while elements like numerical schemes that are applied but not modified are briefly described. For more details, the reader is referred to the cited literature.

D.1.2.1 Spatial discretization

There is three major methods to resolve numerically the set of governing equations [137]. The first is Finite Difference (FDM), the flow variables are known at the mesh nodes. Schemes, based on Taylor expansions are used to calculate the derivates at these points [128]. The FDM uses a network of topological lines to construct the discretization of the partial differential equations (PDE). This is a limitation when working in complex geometries in multiple dimensions. This problem motivated the use of an integral form of the PDEs and the consequent development of the finite element and finite volume techniques. The second approach is Finite Elements (FEM); a numerical approach which finds approximate solutions of PDEs as well as integral equations. Galerkin methods are widely used in FEM for converting a continuous operator problem (such as a differential equation) to a discrete problem [51]. The last method is Finite Volume Method (FVM). In this method, the mean value of variables is taken on a control volume [76]. The theorem of Green is applied on the integral form of Navier-Stokes system of equations, so that integrals on surfaces can be obtained on the faces of each mesh cell. This method ensures conservativity and requires flux calculations.

Unstructured vs Structured: FVM can be applied on three kind of meshes, illustrated in Fig. D.1:

- Structured meshes: In 2D, it is made of quadrangles and of hexahedra in 3D. There is a regular connectivity between the mesh cells so that a 2 or 3 dimensions table with direct mapping is enough to store the mesh. One privileged direction per space dimension exists, which enables to associate mesh nodes to a triplet of integers (i, j, k) in three-dimension space. The major advantage of a structured mesh resides in this privileged direction that makes theses meshes nearly unbeatable when boundary layers are to be resolved. It is however almost impossible to discretize a whole complex geometrical domain with an only structured block. In practice, several blocks are necessary. The refinement in one location or direction is inherited by all the blocks in the domain. Fortunately, no-matching techniques [17] have been developed to relax this constraint. The major drawback of structured meshes is the generation of the mesh itself. It can be a difficult and long task especially for industrial applications.

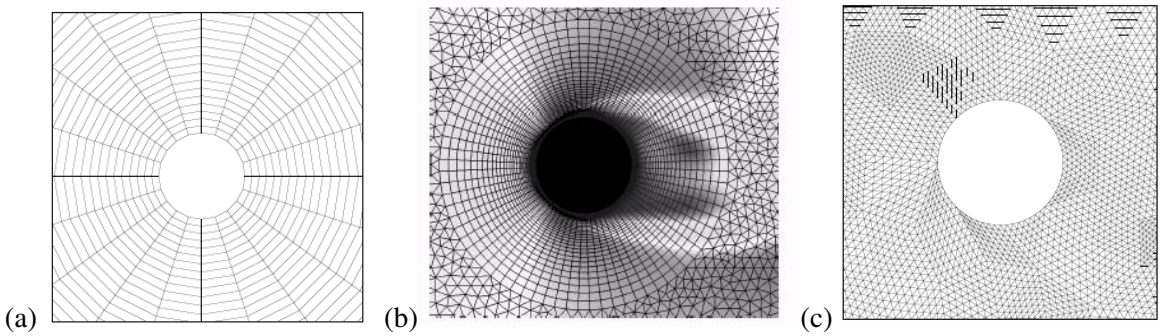

Figure D.1: 2D structured (a), hybrid (b) and unstructured (c) meshes (from [169]).

- ◇ Unstructured meshes: Any element can exist in an unstructured mesh. Normally, the major part is composed of triangles in 2D. The connectivity in unstructured meshes is not regular. The main drawback with respect to a structured approach is that all the connectivities between cells should be stored and demanding thereby much more memory and time for accessibility. Nevertheless, the unstructured method eases the mesh creation around complex geometries and handles local refinement quite naturally.

- ◇ Hybrid meshes take advantage of both type of meshes. A hybrid mesh is a mesh composed of several element shapes. Generally, they are structured near the wall to ensure proper capturing of boundary flows and unstructured in the rest of the domain.

elsA is a multi-block structured solver while AVBP is an unstructured/hybrid grid solver.

Cell-vertex vs Cell-centered: Once the spatial discretization treated, two different approaches to locate data can be defined. Indeed, *elsA* and AVBP share a FVM approach, but data is not located at the same place. The *cell-vertex* approach is a very common discretization method for FV schemes, the very popular alternative being the *cell-centered* formulation which is the most widespread technique for the discretization of the Navier-Stokes equations on structured grids [76]. While in the latter case, flow variables are stored at the center of the cells, they are stored at the grid nodes in the former as seen in Fig. D.2. The key difference is the computation of fluxes through cell boundaries. For cell-centered schemes, the flux through a cell boundary is based on the interpolation of variables situated on either side of the cell edge, i.e. from the *centers* of two neighboring cells. In a cell-vertex scheme, the flux is obtained from the values at the *vertices*, i.e. at either end of the cell edge. Here, vertices are to be understood as points that coincide with the grid nodes but are associated to a grid cell. This means that one grid node can coincide with several vertices, one for each grid cell the node is connected to.

The *cell-vertex* formalism corresponds to the one used in the AVBP solver and is described in detail by Lamarque [101]. The *cell-centered* formulation is the one used to solve the FV problem in *elsA*.

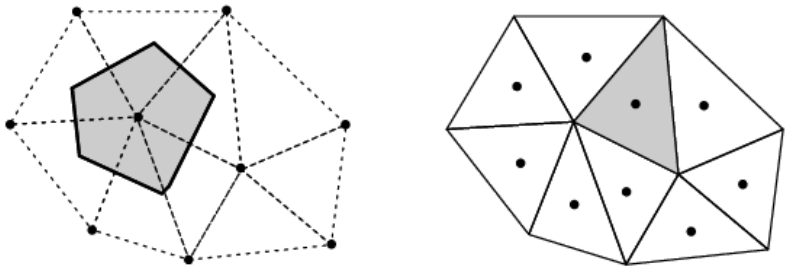

Figure D.2: Primary control volumes used in FVM. Left: vertex-centered. Right: cell-centered.

D.1.2.2 Temporal discretization

Irrespectively of the turbulent modeling formalism adopted for the computation (*i.e.*, RANS or LES), the initial governing equations are the unsteady compressible Navier-Stokes equations that describe the conservation of mass, momentum and energy. In conservative form, it can be expressed in three-dimensional coordinates as:

$$\frac{\partial \mathbf{U}}{\partial t} + div\,\mathbf{F} = 0 \tag{D.41}$$

where $\mathbf{U}$ in Eq. (D.41) is the vector of primary variables themselves function of time, t and space, $\mathbf{x}$. $\mathbf{F} = (\mathbf{f}-\mathbf{f_v}, \mathbf{g}-\mathbf{g_v}, \mathbf{h}-\mathbf{h_v})$ is the flux tensor; $\mathbf{f},\mathbf{g},\mathbf{h}$ are the inviscid fluxes and $\mathbf{f_v},\mathbf{g_v},\mathbf{h_v}$ are the viscous fluxes (including the potential contribution of models for turbulence through the addition of the so-called turbulent viscosity, ν_t). This is the compact form of Eqs. (D.1) & (D.2) & (D.3).

The advance of the solution in time in AVBP is originally based on a N-step low-storage Runge-Kutta explicit scheme [39]. One of the most crucial parameter in an unsteady calculation is the time step value Δt. Discretizations used in AVBP are conditionally stable, then one must ensure the time step is small enough to avoid numerical instabilities. Linear analyses have derived critical Courant-Friedrichs-Lewy (CFL) (for convection schemes) and Fourier (for diffusion schemes) numbers to be respected to ensure linear stability [64]. Therefore, the global time step, Δt_{max}, is determined by a CFL condition that limits the time step as a function of the spatial discretization. In practice, this introduces an important constraint because excessively small grid cells, Δx_{min} (even if they occur only very locally and in small numbers) can considerably increase the computational cost of the entire computation.

$$\Delta t_{max} < CFL \frac{\Delta x_{min}}{(|\vec{V}| + c)_{max}} \tag{D.42}$$

where $|\vec{V}|$ is the velocity vector and c the propagation speed.

In *elsA*, if the flow solution targeted is stationary so the temporal derivative in Eq. (D.41) is null, to converge the initial solution of the computation to the stationary solution, iterations are done over a pseudo-time t^* so that actual system solved reads:

$$\frac{\partial \mathbf{U}}{\partial t^*} + div\,\mathbf{F} = 0 \tag{D.43}$$

With this technique there is no need to assure a temporal consistency between all cells, as in an unsteady computation, so each cell can have a difference pseudo-time. The local time step hence equals:

$$\Delta t = CFL \frac{\Delta x_{cell}}{(|\vec{V}| + c)_{cell}} \tag{D.44}$$

Convergence is achieved when the residuals resulting from the spatial discretization of convective and diffusive terms tend to zero.

Otherwise, when the computation is unsteady, all the cells of the domain must have the same physical time, i.e., the global time step equals the littlest of all, given by Eq. (D.42). Use of an implicit temporal method allows to release the constraint on the time step for a given grid resolution. The resulting implicit system to solve becomes however non-linear for each time step and the resolution can be done by a direct Newton method or a Dual Time Stepping (DTS) approach like in Eq. (D.45). For the latter, at each t, a loop on t^* is advanced. The first term of Eq. (D.45) tends to zero and only the unsteady equation remains, becoming Eq. (D.41). The resolution of this system of equations for each time step allows the use of a bigger time step if compared with classical methods [81]. To retrieve more information on DTS, one can refer to the thesis of Sicot [169].

$$\frac{\partial \mathbf{U}}{\partial t^*} + \frac{\partial \mathbf{U}}{\partial t} + div\,\mathbf{F} = 0 \tag{D.45}$$

D.1.3 *elsA* vs AVBP

The AVBP solver is a property of CERFACS and IFPEn (`http://www.cerfacs.fr/~avbp`). It was originally created by the Oxford University Computing Laboratory and CERFACS in 1993. Nowadays, the AVBP solver is the basis of several industrial collaborations with national and international research programs. The code is written in Fortran. It allows to study both academic configurations [183] as well as industrial configurations (piston engines, aeronautical combustion chambers) with interesting results [60, 130, 164]. As said, the solver relies on the *cell-vertex* approach and FVM on unstructured or hybrid meshes.

elsA (**e**nsemble **l**ogiciel pour la **s**imulation en **A**érodynamique) solver was developed by ONERA in 1997 to integrate in a standalone solver the knowledge disseminated in several solvers to resolve problems in subsonic and transonic flows in turbomachinary, planes as well as supersonic flow in rockets. *elsA* can also treat multi-physics applications as aeroelasticity and aeroacoustics. Since 2001, CERFACS participates to the development of the numerical routines. The last status on the solver has been done by Cambier & Veuillot [32]. As mentioned before, *elsA* uses FVM on structured meshes and Euler, RANS, URANS, DES as well as LES are integrated in the solver. *elsA* is object-oriented written in C++ with the low level routines written in Fortran to improve computation performance. The user interface is in Python.

No information is given in this manuscript about the numerical performance and parallelism characteristic of the solvers used at CERFACS, for more information, one can read Gourdain *et al.* [67]. A table summing up the major numerical features of AVBP and *elsA* is presented below:

	elsA	AVBP
Meshes	structured	unstructured/hybrid
Spatial discretization	FVM cell-centered	FVM cell-vertex
Temporal discretization	implicit	explicit
CFL	> 1	< 1

Table D.3: *elsA* vs AVBP numerical methods.

D.2 OpenPALM

Most of the CFD problems, not only combustion chamber-turbine interaction, deal simultaneously with mechanisms involving different physics. Their modelization needs to be linked to different physical description in time and space. Instead of developing a new numerical tool which will enable the resolution of the global problem, one can benefit from years of development on each dedicated solver. To do so, an independent and performing coupling solver is needed. The major advantage of implementing a coupling methodology is that each code can evolve independently of the coupling strategy.

In 1996, the MERCATOR project faced the problem to set-up a tool for Data Assimilation in an evolving configuration. Instead of hard-coding data assimilation routines in the model, a coupled tool for the model, observations and algebra were imagined in a flexible and computationally effective way. PALM (Projet d'Assimilation par Logiciel Multi-méthode) was created [1]. Nowadays,

PALM has become open-source, OpenPALM, and its application domain extends to multiple scientific applications. It has been tested in numerous CFD problems handling multi-physics: flow and structure [45, 148]; flow and radiation [6, 143]; flow, structure and radiation [7].

D.2.1 The software

The coupler is a software tool allowing the concurrent execution and the intercommunication of programs not having been especially designed for it. Furthermore, the coupler takes care of a number of other services, such as intermediate computations on the exchanged data, grid to grid interpolations, parallel data redistribution. The codes may run in parallel, especially if the coupling takes place in the iterative process of the computational entities. The main qualities of the OpenPALM coupler are its easy set-up, its flexibility, its performances, the simple updates and evolutions of the coupled application and the many side services and functions that it offers.

OpenPALM applications are implemented via a graphical user interface called PrePALM. In this interface, the programmer initially defines the coupling algorithm: number of components, sequential and parallel sections, loops and conditional executions, resources management. Indeed, an OpenPALM application can be described as a set of computational units arranged in a coupling algorithm [29]. The communications between units are described at this level as well as all synchronization, memory management and parallel computing options. Computing resources such as the required memory and the number of concurrent processors, are handled by the OpenPALM coupler too. The different units are controlled conditionally and iteratively and belong to algorithmic sequences called computational branches. The possible communications between OpenPALM units are assured by PALM_Put and PALM_Get primitives written in the source codes. The PALM_Puts and PALM_Gets are connected through the graphical interface PrePALM, which really creates the communications based on MPI protocols.

A branch is structured like a program in a high level programming language: it allows the definition of sequential algorithms. Inside a branch, the coupled independent programs, the units, are invoked as if they were subroutines of the branch program. For two coupled solvers, each solver has a branch which is drawn in the PrePALM canvas and the units are inserted in each branch. The resulting PrePALM application for AVBP/*elsA* coupling, presented in Part II, is plotted in Fig. D.3. One can see the two branches with one unit each.

To find more information on communications and OpenPALM environment, one can refer to Buis *et al.* [29] or look at the very complete web (`http://www.cerfacs.fr/globc/PALM_WEB/`). Moreover, a complete description of the methodology that should be followed to instrument the codes and include them as computational units in OpenPALM can be found in Amaya [5].

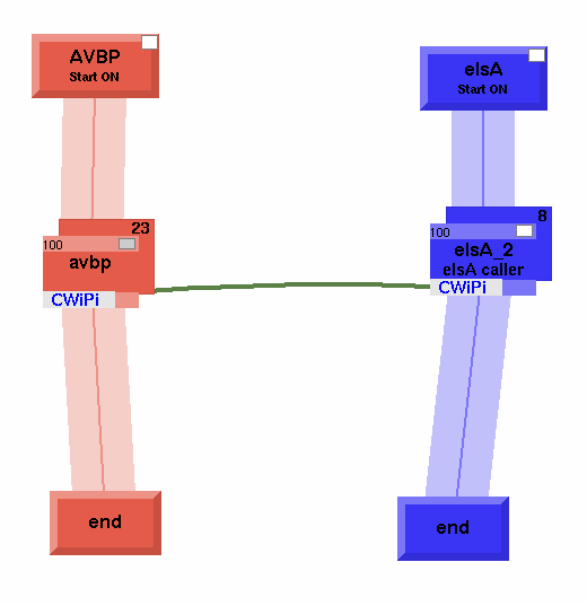

Figure D.3: OpenPALM AVBP/*elsA* coupled application.

D.2.2 The CWIPI functionnality

Coupling With Interpolation Parallel Interface (CWIPI) [14, 131] is a library that enables the coupling between *n* parallel codes with MPI communications. It was created by EDF and it is now developed by ONERA and CERFACS. Coupling is made through an exchange zone that can be discretized in a different way on any coupled code. Linear, surface or volume couplings are available. CWIPI takes into account all types of geometrical elements (polygon, polyhedral); there is no requirement about the mesh nature. CWIPI contains the following functionalities:

- ◇ control of coupled processes,
- ◇ geometrical location,
- ◇ interpolation,
- ◇ field exchange,
- ◇ visualization file building.

The application programming interface is available in Fortran and C/C++. CWIPI can thus couple codes written in different languages, as it is the case for AVBP and *elsA*. The coupled applications must be launched in the same MPI environment, cf Fig. D.4. During the initialization phase, CWIPI creates an internal communicator for each code. For every coupling defined by the user, inter communicators are created between coupled codes. From the user point of view, the inter-application communications become completely transparent even if the applications are parallel.

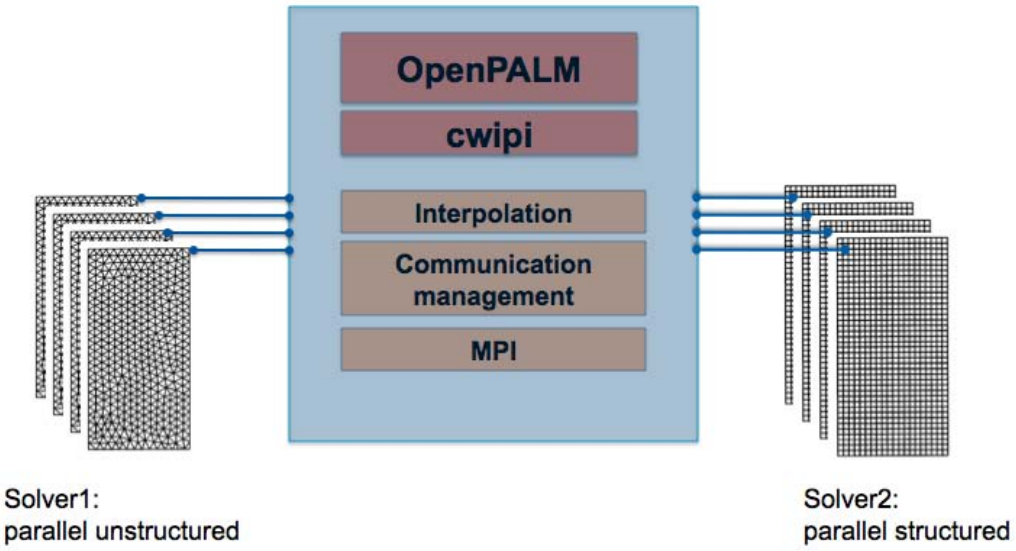

Figure D.4: Schematic OpenPALM interface application.

The user can define coupling algorithms by the use of the control parameters. These parameters are global variables that are synchronized and shared between coupled codes. For example, one can define some control parameters to exchange the convergence state or the simulation time, for instance like in the AVBP/*elsA* coupling, a coupling frequency to determine the rhythm of exchanges between the codes.

In order to improve the interoperability of the different codes, instead of implementing all coupling routines (communication, search, and interpolation) in all solvers separately, theses tasks are assured by CWIPI. The idea is to take away some of the workload from the solvers. CWIPI performs all searches and interpolations. In order to be able to perform these tasks, the coupler requires the meshes and the solutions of the solvers. In the case of the AVBP/*elsA* coupling, the field projection is based on a linear interpolation. CWIPI exports all results to EnsightTM gold format files to visualize exchanged interpolated fields which makes debug much more easy. All these CWIPI functionalities are directly accessible in the PrePALM canvas.

This thesis provides an example in Part II of the application of OpenPALM using the library CWIPI to construct a fluid-fluid coupled application. For more information, on the use of CWIPI, one can refer to Duchaine et al. [47, 48].

Nomenclature

Latin characters

Symbol	Description	Unit
a	Advection factor	$[m/s]$
c	Propagation velocity	$[m/s]$
C	Blade chord	$[m]$
C_w	WALE model constant	$[-]$
C_v	Heat capacity at constant volume	$[J/(kgK)]$
C_p	Heat capacity at constant pressure	$[J/(kgK)]$
c_p	Pressure coefficient	$[-]$
D	Diameter	$[m]$
D	Thermal diffusivity	$[m^2/s]$
e, E	Sensible, specific energy	$[J]$, $[J/kg]$
e_i, E_i	Error	$[-]$
f	Frequency	$[Hz]$
$\mathbf{F}$	Flux tensor of the conservative variables	
$\mathbf{f}$	Convective part of the flux tensor of the conservative variables	
$\mathbf{f_v}$	Viscous part of the flux tensor of the conservative variables	
G	Filter function	$[-]$
H	Heat transfer coefficient	$[W/(m^2K)]$
h, H	Sensible, specific enthalpy	$[J]$, $[J/kg]$
i, j, k	Mesh nodes triplets	$[-]$
$J_{j,k}$	Diffusive flux vector of species k	$[kg/(m^2s)]$
k	Kinetic turbulent energy	$[J]$
k	Coupling iteration index	$[-]$
k	RANS $k-l$ model specific dissipation	$[m^2/s^2]$
l	RANS $k-l$ model specific length	$[m]$
$L(\,)$	Laplace transform	$[-]$
L_e	Most energetic turbulence length scale	$[m]$
L_0	Inlet turbulence length scale	$[m]$
$\dot{m}$	Mass flux	$[kg/s]$
P	Pressure	$[N/m^2]$
q	Heat flux	$[J/(m^2s)]$
Q	Volumetric flow rate	$[m^3/s]$
Q_{ij}	Vorticity tensor	$[1/s]$
r, θ	Cylindrical coordinates	
r	Mixture gas constant	$[J/(kgK)]$
$\mathcal{R}$	Universal gas constant	$[J/(kgK)]$
R	Radius	$[m]$
s	Sensible entropy	$[J/K]$
s	Laplace transform variable	$[1/s]$

Symbol	Description	Unit
S	Curvilinear abscissa	$[m^2]$
S_{ij}	Boussinesq tensor (rate of strain tensor)	$[m/s^2]$
S_t	Strouhal number	$[-]$
$\mathbf{S}$	Vector of source terms	$[kg/(m^3 s)]$
t	Time	$[s]$
T	Gaseous temperature	$[K]$
$\mathbf{T}$	Iteration matrix	$[-]$
T_i	Period	$[s]$
u, U, V	Velocity	$[m/s]$
$\mathbf{U}$	Vector of conservatives variables	
V_i	Species diffusion velocity vector	$[m/s]$
$\mathbf{W}$	Vector of characteristic variables	
W	Molecular weight	$[kg/mol]$
x	Spatial coordinate	$[m]$
X	Molar fraction	$[-]$
y	Distance to the wall	$[m]$
Y	Mass fraction	$[-]$

Greek characters

Symbol	Description	Unit
β	Thermal activity ratio	$[-]$
γ	Adiabatic exponent of the mixture	$[-]$
δ	Overlap half length	$[m]$
δ_v	Wall characteristic length	$[m]$
$\Delta x, \Delta y, \Delta z$	Grid extension sizes	$[m]$
Δ	Cut-off scale of the filter G	$[m]$
Δp	Pressure drop	$[N/m^2]$
Δt	Time step	$[s]$
ε	Dissipation rate	$[m^2/s^3]$
η	Kolgomorov length scale	$[m]$
λ	Thermal conductivity	$[J/(mK)]$
λ_i	Eigenvalues	$[-]$
μ	Molecular viscosity	$[kg/(ms)]$
ν	Kinematic viscosity	$[m^2/s]$
ρ	Gaseous density	$[kg/m^3]$
ρ_i	Convergence rate in the mathematical context	$[-]$
τ_{ij}	Stress tensor	$[N/m^2]$
θ	Momentum thickness	$[-]$
θ_i	Relaxation parameters	$[-]$
Φ_i	Linear functions for the transmission conditions	$[-]$
$\dot{\omega}$	Chemical source term	$[kg/(m^3 s)]$
Ω_i	(Sub)domain	$[-]$

Dimensionless numbers

Symbol	Description
M	Mach number
Nu	Nusselt number
Pe	Pèclet number
Pr	Prandtl number
Pr_t	Turbulent Prandtl number
R	Reaction number
Re	Reynolds number
Sc	Schmidt number
Tu	Turbulent intensity

Indices and superscripts

Symbol	Description
$\bar{}$	Time-averaged or Favre filtered value
$\sim$	Resolved value
$+$	Superscript of quantities written in wall units
$'$	Superscript for fluctuating quantity
k	Iteration superscript
0	Index for free-stream quantities
BL	Index of quantities in the liquid column boundary layer
cpl	Index for coupling quantities
j	Index of a grid node
f	Index of fluid quantities
k	Species quantity
is	Index for isentropic quantities
n	Index for normal quantities
r	Index for radial quantities
s	Index of solid quantities
SGS,t	Index for modeled (SGS or turbulent) value
t	Index for tangential quantities
w	Index of variables located at the wall

Acronyms

Symbol	Description
AV	Artificial Viscosity
BC	Boundary Condition
CFL	Courant-Friedrichs-Lewy
CFD	Computational Fluid Dynamics
CWIPI	Coupling With Interpolation Parallel Interface
DES	Detached Eddy Simulation
DDM	Domain Decomposition Method
DNS	Direct Numerical Simulation
FDM	Finite Difference Method
FEM	Finite Elements Method
FFT	Fast Fourier Transform
FST	Free-Stream Turbulence
FVM	Finite Volume Method
LES	Large Eddy Simulation
LUSSOR	Lower-Upper Symmetric Successive Over-Relaxation
MPI	Message Passing Interface
NGV	Nozzle Guide Vane
NSCBC	Navier-Stokes Characteristic Boundary Condition
ODE	Ordinary Differential Equation
PDE	Partial Differential Equation
PSD	Power Spectrum Density
RANS	Reynolds-Averaged Navier-Stokes
RMS	Root Mean Square
RTF	Radial Temperature Factor
SEM	Synthetic Eddy Method
SGS	Sub-Grid Scale
STT	Shear Stress Transport
VKI	Von Karman Institute
WALE	Wall-Adapting Local Eddy

Abstract

This PhD dissertation, conducted as part of a CIFRE research project between TURBOMECA and CERFACS, deals with improving performance of axial turbines from helicopter engines. One of the main difficulties with such an objective is the control of the temperature prediction around the blades, especially the temperature of the high pressure rotor.

The work of this thesis focusses on two axes:

- First concerns the analysis of Large Eddy Simulation (LES) predictions around blades: a numerical LES approach on unstructured meshes is compared to Reynolds Averaged Navier-Stokes (RANS) results on structured meshes as well as to LES on structured meshes. LES on unstructured meshes demonstrates its capacity of taking into account the phenomena which have an impact on wall heat flux around blades.
- The second axis deals with the development of a numerical tool for coupling and transferring information between a reactive LES code, used in combustion chambers, and a non-reactive RANS solver, employed by industrial actors for modeling the turbine stage. This tool is validated on a number of test cases which show the potential of this methodology for multi-component predictions.

Keywords: Combustion chamber-turbine interaction, heat transfer, numerical simulation, coupling.

Résumé

Ce travail de thèse, mené dans le cadre d'une convention CIFRE entre TURBOMECA et le CERFACS, s'inscrit dans un contexte d'amélioration des performances des turbines de type axial équipant les turboréacteurs d'hélicoptère. L'une des principales difficultés rencontrée dans cette démarche concerne la maîtrise de la température que voient les pales de ce composant, notamment la roue haute pression.

Les travaux de cette thèse s'articulent autour de deux axes principaux:

- ◇ Le premier traite l'analyse de la Simulations aux Grandes Echelles (SGE) autour de pales. Une approche numérique SGE sur des maillages non-structurés est comparée aux résultats Reynolds Averaged Navier-Stokes (RANS) sur des maillages structurés, usuels dans ce type de configuration, ainsi qu'à une approche SGE sur maillages structurés. La SGE sur maillage non-structuré démontre sa capacité à prendre en compte les phénomènes qui ont un impact sur les flux de chaleur pariétaux.
- ◇ Le second axe de recherche a pour objectif de développer un outil numérique de couplage pour assurer le transfert d'information entre un code SGE réactif sur maillage non-structuré, employé dans les chambres de combustion, et un code non-réactif en RANS, utilisé par les industriels pour modéliser l'étage turbine. Cet outil a été validé sur plusieurs cas tests qui montrent le potentiel de cette méthodologie pour le couplage multi-composant.

Mots clés: Interaction chambre de combustion-turbine, transfert de chaleur, simulation numérique, couplage.

–Buena está – dijo Sancho – firmela vuestra merced.
–No es menester firmarla – dijo Don Quijote –,
sino solamente poner mi rúbrica.

El Ingenioso Caballero Don Quijote de la Mancha,
Miguel de Cervantes